Unveiling Dark Matter through Gamma Rays: Spectral Features, Spatial Signatures and Astrophysical Backgrounds

Dissertation with the aim of achieving a doctoral degree
at the Faculty of Mathematics, Informatics and Natural
Sciences

DEPARTMENT OF PHYSICS OF
UNIVERSITÄT HAMBURG
and
DEPARTMENT OF PHYSICS OF
UNIVERSITÀ DEGLI STUDI DI TORINO

submitted by

Francesca Calore

Hamburg 2013

– corrected version –

Day of oral defense: 18th of September, 2013

The following evaluators recommend the admission of the dissertation:
Dr. Torsten Bringmann
Dr. Fiorenza Donato

Zusammenfassung

Obwohl die Existenz der Dunklen Materie (DM) durch zahlreiche unabhängige Ergebnisse auf verschiedenen Skalen gestützt wird, sind die Details ihrer eigentlichen Beschaffenheit weit davon entfernt, durch gegenwärtige Möglichkeit der Detektion offengelegt zu werden. Die vorliegende Arbeit konzentriert sich auf die indirekte Suche nach DM schwach wechselwirkenden massiven Teilchen (Weakly Interacting Massive Particles - WIMPs) mithilfe der γ-Strahlung.

Um die spektrale DM-Verteilung sorgfältig zu modellieren, führen wir die erste allgemein gültige Berechnung der führenden elektroschwachen Korrekturen zur Paarvernichtungsrate supersymmetrischer Neutralino-DM durch und zeigen, dass diese Korrekturen die totale Photonenausbeute signifikant erhöhen, was zum Teil dadurch bedingt wird, dass einige der Beiträge bisher nicht beachtet worden sind. Ferner erwartet man, dass DM neben den spektralen Signaturen auch spezifische räumliche Besonderheiten bewirkt, da Ergebnisse von N-Körper-Simulationen vorhersagen, dass der primäre galaktische Halo DM-Subhalos unterschiedlicher Größe und Masse beherbergt. Wir berechnen das winkelabhängige Leistungsspektrum der γ-Strahlung galaktischer DM unter Ausnutzung der neuesten Ergebnisse von N-Körper-Simulationen. Zusätzlich heben wir die theoretischen Unsicherheiten dieser Berechnung, die sich als relevant für gegenwärtige Suchen nach DM mithilfe von Anisotropien der γ-Strahlung herausstellen kann, hervor.

Eine angemessene Strategie zur Detektion von DM sollte sowohl die Methoden als auch die Auswahl der Zielobjekte optimieren. Wir zeigen, dass traditionelle Methoden der Spektralliniensuche für γ-Strahlung, die die auf astrophysikalische Hintergrundflüsse zurückzuführenden Unsicherheiten stark reduziert, erfolgreich erweitert werden können, um spezifische Merkmale des Spektrums für Energien nahe der Masse der DM-Teilchen zu entdecken und dass die projizierten Einschränkungen des Wirkungsquerschnitts der DM-Paarvernichtung in Hinblick auf die Tscherenkow-Teleskope der nächsten Generation im Vergleich zur heutigen Eingrenzung erheblich verbessert werden können. Außerdem weisen wir nach, dass der isotrope diffuse γ-Strahlungshintergrund (isotropic diffuse γ-ray background - IGRB) eines der vielversprechendsten Objekte ist, um DM indirekt nachzuweisen, sobald die Unsicherheiten des unvermeidbaren astrophysikalischen Hintergrunds durch weitere Messdaten reduziert worden sind. Tatsächlich können wir zeigen, dass der wichtigste astrophysikalische Beitrag zum IGRB von der unbekannten Menge der sogenannten schlecht ausgerichteten aktiven galaktischen Kerne stammt. Unter Beachtung dieses zusätzlichen Beitrags können thermisch produzierte WIMPs mit Massen von bis zu einigen TeV stark eingeschränkt werden.

Abstract

Although the existence of Dark Matter (DM) is supported by multiple unrelated evidences at different scales, its intimate nature is far from been unveiled by current detection strategies. This thesis focuses on indirect searches of DM Weakly Interacting Massive Particles (WIMPs) through γ-rays.

In order to accurately model the spectral DM distribution, we perform the first fully general calculation of leading electroweak corrections to the annihilation rate of supersymmetric neutralino DM and we demonstrate that these corrections significantly enhance the total photon yield, partially because of contributions that have been overlooked so far. Besides spectral signatures, DM is expected to show distinctive spatial features because of DM subhalos of various sizes and masses hosted by the main galactic halo as predicted by N-body simulations. We compute the γ-ray angular power spectrum of galactic DM by exploiting the results of recent N-body simulations. Notably, we emphasize the theoretical uncertainty associated to such a calculation which may turn out to be relevant for current DM searches by means of γ-ray anisotropies.

A good DM detection strategy should optimize methods and choice of targets. We demonstrate that traditional methods for γ-ray line searches, which greatly reduce the uncertainties related to astrophysical background fluxes, can successfully be extended to look for any spectral feature at photon energies close to the DM particle mass and that projected constraints on the DM annihilation cross section by means of the next generation of Cherenkov telescopes turn out to be considerably improved with respect to current limits. Moreover, we prove the isotropic diffuse γ-ray background (IGRB) to be one of the most promising targets for testing the WIMP hypothesis once the uncertainties on the unavoidable astrophysical background will be reduced by further data. We indeed show that the most important astrophysical contribution to the IGRB is due to the unresolved population of mis-aligned active galactic nuclei. Taking into account this additional contribution to the IGRB, thermally produced WIMPs may be severely constrained for masses up to several TeV.

Acronyms

AGN	Active Galactic Nuclei
APS	Angular Power Spectrum
BB	Back-to-Back (system)
BL Lacs	BL Lacertae objects
CDM	Cold Dark Matter
CMB	Cosmic Microwave Background
CMS	Center of Mass System
CR	Cosmic Ray
DM	Dark Matter
EBL	Extragalactic Background Light
EC	External Compton
EM	Electromagnetic
EW	Electroweak
FR (I/II)	Fanaroff Riley (I/II)
FSR	Final State Radiation
FSRQ	Flat Spectrum Radio Quasar
GC	Galactic Center
IACT	Imaging Atmospheric Cherenkov Telescope
IC	Inverse Compton
ID	Indirect Detection
IGRB	Isotropic (Diffuse) γ-ray Background
ISR	Initial State Radiation
KK	Kaluza Klein
LHC	Large Hadron Collider
LSP	Lightest Supersymmetric Particle
MAGN	Mis-Aligned Active Galactic Nuclei
MSP	Milli-second Pulsar
MSSM	Minimal Supersymmetric Standard Model
SF	Star Forming
SM	Standard Model
SSC	Self Synchrotron Compton
SUSY	Supersymmetry
VIB	Virtual Internal Bremsstrahlung
WIMP	Weakly Interacting Massive Particle
UED	Universal Extra-Dimensions

Contents

List of Publications

My research activity during the former three years has been focused on Astroparticle Physics, namely on the indirect detection of Dark Matter (DM) through γ-rays. My main contribution in this field deals with the modeling of the expected spectral and angular DM signal as well as with the possibility to constrain the DM annihilation cross section by means of targets as different as the isotropic diffuse γ-ray background and the galactic center region. Moreover, I also participated in assessing the contribution to the isotropic diffuse γ-ray background of the unresolved population of mis-aligned active galactic nuclei. My research results in the following publications and e-print submissions:

[P1] F. Calore, V. De Romeri and F. Donato, "Conservative upper limits on WIMP annihilation cross section from *Fermi*-LAT γ-rays," Phys. Rev. D **85** (2012) 023004 [arXiv:1105.4230 [astro-ph.CO]].

[P2] T. Bringmann, F. Calore, G. Vertongen and C. Weniger, "On the Relevance of Sharp Gamma-Ray Features for Indirect Dark Matter Searches," Phys. Rev. D **84** (2011) 103525 [arXiv:1106.1874 [hep-ph]].

[P3] M. Di Mauro, F. Calore, F. Donato, M. Ajello and L. Latronico, "Diffuse γ-ray emission from misaligned active galactic nuclei," *submitted to the Astrophysical Journal* [arXiv:1304.0908 [astro-ph.HE]].

[P4] T. Bringmann, F. Calore, M. Di Mauro and F. Donato, "Constraining dark matter annihilation with the isotropic γ-ray background: updated limits and future potential," *submitted to Phys. Rev. D* [arXiv:1303.3284 [astro-ph.CO]].

[P5] T. Bringmann and F. Calore, "Significant Enhancement of Neutralino Dark Matter Annihilation," *submitted to Phys. Rev. Letter* [arXiv:1308.1089].

Furthermore, the following work is in preparation:

[WP1] F. Calore, V. De Romeri, M. Di Mauro, F. Donato, J. Herpich, A. V. Maccio', L. Maccione and G. Stinson, "Uncertainties on γ-ray anisotropy from dark matter in the Milky Way."

List of Figures

List of Tables

Chapter 1

Introduction

On cosmological scale Dark Matter (DM) contributes a fraction of about 25% of the total energy density of the universe and its evidence derives from several unrelated observations at different scales. A well motivated class of candidates is represented by Weakly Interacting Massive Particles (WIMPs), which can account for the observed DM abundance. Several strategies for WIMP DM detection have been attempted: direct detection of the recoil energy after the scattering off nuclei, indirect searches through astrophysical and cosmological signals, and collider searches for DM with mono-jet, mono-photon and mono-Z events. Chapter 2 is dedicated to a general introduction to DM: evidence, candidates and detection strategies.

Notably, the DM indirect detection (ID) relies on the possibility to detect the final stable products of DM pair annihilation or decay (e.g. γ-rays, antimatter, neutrinos). Disentangling a potential signal over the unavoidable astrophysical background constitutes its main challenge. In this context, γ-rays show several advantages with respect to other messengers: they propagate unperturbed throughout the halo so that they do not suffer from uncertainties due to cosmic rays (CRs) propagation; being unaffected by gas and magnetic fields they walk along straight lines (at galactic scale) and they thus point toward their source; moreover, they show unambiguous spectral features which make them suitable for the detection of a signal rather than for only placing constraints on the DM parameter space. For all the above mentioned reasons, γ-rays can be considered the "golden channel" of indirect searches and this represents the prime topic of our work. A general overview of the current status of DM searches through γ-rays will be given in chapter 3.

The expected γ-ray flux from DM pair annihilation depends on the underlying particle physics content which determines the spectral distribution of the signal, and on the DM density in astrophysical targets which instead encodes the spatial and angular distribution of the same signal. Predicting spectral and spatial DM signatures is thus a fundamental ingredient for indirect searches.

In chapter 4 we will present the first fully general calculation of leading electroweak corrections to the annihilation rate of supersymmetric neutralino DM, due to the unavoidable emission of an additional $SU(2)$ gauge boson occurring whenever DM annihilates into two-body final state. In particular, we expect that the annihilation into two fermions will lift the helicity suppression, occurring at tree-level, when an additional gauge boson is radiated (as it has been firstly shown to happen for photon bremsstrahlung). Moreover, electroweak bremsstrahlung can be phenomenologically important even for processes that do not lift the helicity suppression, like the radiation off final fermion legs. We will discuss the effects of electroweak corrections both on total cross sections and spectra of final stable photons which are directly connected to observational perspectives. We will identify new enhancement mechanisms and show that electroweak corrections can significantly improve the discovery potential of neutralino DM with current and upcoming CR experiments. The chapter is accompanied by a series of Appendices illustrating the method applied for the computation (Appendices A – D).

Besides the spectral distribution, DM is expected to show distinctive spatial features because of its density distribution modeled according to the outcome of N-body simulations. Those simulations predict the formation of DM halos of different sizes and masses: at large scale galaxies and clusters of galaxies form, whereas at small scales primary halos can host several, less massive subhalos. Focusing on galactic scales, DM distribution of galactic sized halos (i.e. comparable to the Milky Way) is composed by two separate components: a smoothly distributed phase, i.e. the main halo, and a clumpy component in the form of virialized substructures, i.e. the subhalos. DM annihilating in a such a lumpy distribution produces photons that are expected to track the position of their sources and imprint this information in the γ-ray angular power spectrum (APS). Discussing the theoretical uncertainties related to DM searches through γ-rays anisotropies will be the topic of chapter 5, where we will explore (i) the intrinsic uncertainty due to the extrapolation to short distances of the DM distribution determined from numerical simulations and (ii) the statistical fluctuations implied by the mass and space distribution of subhalos. We will consider only the DM distribution in our galaxy, whereas we will neglect the contribution coming from external galaxies as well as standard astrophysical backgrounds.

Data from the last generation of γ-ray experiments have led to a deep insight into the nature of the different targets which are suitable for DM ID searches, i.e. the Galactic Center (GC) and halo, the isotropic diffuse γ-ray background (IGRB), Milky Way satellite dwarf galaxies, globular clusters, external galaxies, and galaxy clusters. Each target requires an optimized analysis properly treating the astrophysical background and assessing the uncertainties of the derived constraints.

Understanding in details the astrophysical background may unveil the great potential of the IGRB, recently measured by the *Fermi* Large Area Telescope (LAT) at high latitudes, as one of the most promising targets for DM searches. This faint emission is believed to arise from the superposition of contributions from (mainly) unresolved galactic and extragalactic point-sources and, to a lesser extent, from astrophysical diffuse processes. Probing its origin is a delicate issue in astrophysics. Typically, the contribution to the diffuse γ-ray emission due to an unresolved point-source population is computed through the so-called γ-ray luminosity function, i.e. the number of sources per unit of comoving volume and luminosity. This function is built either from data, if the statistics is large enough, or by adopting a phenomenological approach which exploits the knowledge we have of the statistical properties of the source class in other wavelengths. Chapter 6 will show that the dominant contribution to the IGRB arises from the unresolved population of radio-loud mis-aligned Active Galactic Nuclei (MAGN) that have been established as a γ-ray emitting class by *Fermi*-LAT. Given the poorness of the *Fermi*-LAT sample, we will predict the expected diffuse γ-ray flux of such a source class by correlating the radio and γ-ray luminosity of sources detected in both wavelengths. We will conclude that this faint but numerous population gives a sizable diffuse γ-ray flux that, when added to the contribution from the other populations, could even saturate the observed IGRB. Nonetheless, the prediction will turn out to be affected by an important uncertainty which originates mostly from the correlation between the radio and γ-ray luminosity.

The determination of this additional contribution to the IGRB impacts not only on astrophysics but also on DM ID. Indeed, the IGRB measurements represent a powerful tool to constrain the DM parameter space. Taking into account the unavoidable astrophysical background is mandatory when constraining the DM γ-ray flux through the IGRB. Modeling the emission of unresolved γ-ray sources may leave very little room for more exotic sources, such as DM in the halo of our galaxy as we will show in chapter 7, Sec. 7.1. We will derive constraints on the WIMP DM annihilation cross section that result to be competitive with current limits and can likely be improved significantly by reducing even slightly the uncertainty on the astrophysical fluxes. Notably, if MAGN contribute even at 90% of the maximal level consistent with our prediction, thermally produced WIMPs would be severely constrained as DM candidates for masses up to several TeV.

Besides background studies, optimizing methods and choice of targets is crucial for DM searches. Indeed, we will illustrate in Sec. 7.2 how well looking for pronounced spectral features, other than lines, at the high-energy end of the signal can improve the sensitivity of current and future γ-ray telescopes to the DM signal. We will present a general method to search for DM spectral features which greatly reduces the uncertainties related to astrophysical background fluxes and can considerably improve DM searches, as we will demonstrate with a concrete application to Imaging Atmospheric Cherenkov Telescopes (IACTs) for observations of the GC region.

Finally, our findings are summarized and an outlook for future developments of the topics discussed in this thesis is given in chapter 8. The results presented here are based on several coauthored works, listed in the "List of Publications", which have been published or submitted to refereed journals.

Chapter 2

Dark Matter Primer

A large "invisible" matter component has been identified in our universe, on different scales and by different experimental techniques. The standard picture of modern cosmology sees the universe very close to being flat, with about 25% of its content in the form of a cold dark matter (CDM) component, responsible for structure formation, while the remaining 70% is thought to be made of an exotic dark energy component. Baryons account 4%-5%, much less than the CDM amount. This fact points toward a non-baryonic origin of DM and suggests that our understanding of the Standard Model (SM) of particle physics is likely incomplete.

After a brief introduction to the matter-energy content of the universe, Sec. 2.1, this first chapter aims to make the reader familiar with DM: evidence and inferred properties (Secs. 2.2 – 2.3), particle candidates (Sec. 2.4) and strategies for detection (Sec. 2.5).

2.1 The matter-energy content of the universe

We present here a short introduction to Cosmology which provides some preliminary notion, useful for the understanding of the following sections. The content of this section is based mostly on "The Early Universe (Frontiers in Physics)" (Kolb & Turner, 1990).

In the cosmological Standard Model the universe is described in terms of the Friedmann-Robertson-Walker (FRW) solution of Einstein equations of General Relativity with a perfect fluid energy-momentum tensor. The fundamental assumption of homogeneity and isotropy for the universe has been confirmed by the uniformity of the temperature of the Cosmic Microwave Background (CMB) (Komatsu et al., 2011; Ade et al., 2013) and by the large scale structure of the universe (Abazajian et al., 2009).

The metric of a FRW solution is a maximum spatially symmetric solution, whose line element writes as:

$$ds^2 = -dt^2 + a(t)\left[\frac{dr^2}{1-kr^2} + r^2(d\theta^2 + \sin^2\theta d\phi^2)\right] , \tag{2.1}$$

where $a(t)$ is the cosmological scale factor and k is the curvature constant of the 3-dimensional subspace ($k = -1, 0, +1$ corresponding to an open, spatially flat and closed universe respectively). The coordinates r, θ and ϕ constitute the so called co-moving reference frame. Co-moving coordinates assign constant spatial coordinates values to observers who moves along with the Hubble flow. The time coordinate t is the proper time measured by an observer at rest in the co-moving frame. The metric is not time independent, due to the overall scale factor $a(t)$. The motion with respect to this reference frame is usually addressed as peculiar motion.

Friedmann equations describe the evolution of the scale factor across the cosmic time:

$$H^2(t) \equiv \frac{\dot{a}^2}{a^2} = \frac{8\pi G}{3}\rho - \frac{k}{a^2} + \frac{\Lambda}{3} , \tag{2.2}$$

$$\frac{\ddot{a}}{a} = -\frac{4\pi G}{3}(\rho + 3p) + \frac{\Lambda}{3} , \tag{2.3}$$

where $H(t)$ is the Hubble parameter, ρ is the total (matter and radiation) average energy density of the universe, p is the pressure of the fluid and Λ refers to the so-called cosmological constant, introduced originally as a repulsive force and now invoked to explain the observed acceleration of the expansion of the universe. The nature of this "dark energy" component of the universe is still controversial although the existence of an accelerating component is probed by the latest measurements of the distance-redshift relation of Type Ia supernovae (Riess et al., 1998; Perlmutter et al., 1999).

In an Einstein-De Sitter universe ($k = 0$ and $\Lambda = 0$) the energy density equals the so-called critical density, ρ_c, i.e. :

$$\rho_c(t) \equiv \frac{3H^2(t)}{8\pi G}. \tag{2.4}$$

Usually, we express the abundance of a substance in the universe (matter or radiation) in units of ρ_c, by means of a dimensionless and time dependent parameter:

$$\Omega_i = \frac{\rho_i}{\rho_c} \tag{2.5}$$

for each species i with density ρ_i.

Eq. 2.2 can be written in terms of the density parameter as:

$$(\Omega_m - 1 + \Omega_\Lambda)H^2(t) = \frac{k}{a^2(t)} , \tag{2.6}$$

where $\Omega_\Lambda \equiv \Lambda/3H^2$ and Ω_m is due to the matter density in the form of radiation (negligible today), baryonic (from now on indicated by Ω_b) and non-baryonic (more or less exotic) matter. The values of $k = -1, 0, +1$ correspond to $\Omega_{\text{tot}} < 1$, $\Omega_{\text{tot}} = 1$ and $\Omega_{\text{tot}} > 1$ respectively, with $\Omega_{\text{tot}} \equiv \Omega_m + \Omega_\Lambda$.

The time evolution of the density parameter is linked to the equation of state[i] of the different components. Cosmological density parameters today (hereafter with a superscript 0) refer to the present epoch, in which the value of the Hubble constant has been measured to be $H_0 = 72 \pm 3$(statistical)± 7(systematic) km $\text{s}^{-1}\text{Mpc}^{-1}$ by the Hubble Space Telescope Key Project (Freedman et al., 2001). We notice that this measurement is in agreement with the seven-year WMAP data (Komatsu et al., 2011) and with the determination of cosmological parameters by the latest results of the Planck mission (Ade et al., 2013). The Planck result at 68% C. L. is: $H_0 = (67.4 \pm 1.4)$ km s^{-1} Mpc^{-1}.

2.2 The density parameter and evidence for Dark Matter

A well-established component of the density parameter Ω_{tot} is the standard baryonic matter. Strong limits on the amount of baryonic matter arise from the primordial cosmological nucleosynthesis (BBN), namely from the light elements (D, ^3He, ^4He and ^7Li) abundances today:

$$0.011 \leq \Omega_b^0\, h^2 \leq 0.025 \,\text{(Burles, Nollett \& Turner, 2001)} \qquad (2.7)$$

where $h = 0.072$ is the present Hubble constant (Freedman et al., 2001), expressed in units of 100 km s^{-1} Mpc^{-1}. Although the mechanism of the primordial nucleosynthesis is well explained in the context of the standard cosmological model, some tensions are present (e.g. the lithium problem in metal-poor stars (Cayrel, Steffen, Bonifacio, Ludwig & Caffau, 2008)). Ω_b^0 is also determined independently and more accurately by measuring the relative height of the acoustic peaks of the CMB temperature fluctuations power spectrum:

$$\Omega_b^0\, h^2 = 0.02207 \pm 0.00033\,, \qquad 68\%\ \text{C. L.}\ \text{(Ade et al., 2013)} \qquad (2.8)$$

The two values are well in agreement.

---

[i] In natural units, the equation of state relates the pressure and the density as $p = w\rho$, where w is a dimensionless parameter specific for each component, e.g. $w_m \sim 0$,$w_{\text{rad}} = 1/3$ and $w_\Lambda = -1$.

By now, a large amount of astronomical and cosmological observations at different scales indicate that there is more matter than what can be associated with standard baryons, meaning that a new matter component should participate in determining the total matter density Ω_m^0.

On galactic scales, rotation curves of spiral galaxies show that the orbital velocity of stars and gas as a function of the distance from the galactic center is constant sufficiently far from the center, while, according to Kepler's third law, the orbital velocities should decrease with the distance as $v_{\rm orb} \propto r^{-1/2}$ for distances beyond the visible galaxy disk. This was firstly observed by Vera Rubin and collaborators in 1980 (Rubin, Ford & Thonnard, 1980). This flattening is interpreted in terms of a new massive source of gravity that does not emit any "observable" radiation, therefore called DM. The rotation curves are compatible with expectations if the galaxy cores are surrounded by a dark halo, with $\rho_{DM} \propto r^{-2}$ over some intermediate range of r[ii] (Salucci & Borriello, 2003) (the inner profile is a delicate issue of the DM distribution and we will discuss it in Sec. 3.2). To quantify the luminous matter density in galaxies, the mass-to-light ratio is usually adopted, i.e. the ratio of the mass (in units of the mass of the Sun) to the luminosity (in units of the luminosity of the Sun). This quantity depends a lot on the type of galaxy studied: for common spiral galaxies (e.g. the Milky Way) the mass-to-light ratio is ~ 10 (Faber & Gallagher, 1979), whereas for specific galaxies, i.e. dwarf spheroidal galaxies, this ratio can reach ~ 100 since those are objects without active stellar formation (Aaronson, 1983). High mass-to-light ratios reveal that a new dark, i.e. non-luminous, component should dominate the dynamics of such objects.

Galaxy clusters give the first firmly established hints of non-baryonic DM. The mass of a cluster can be determined through different methods. In 1933, F. Zwicky, while studying of the Coma cluster (otherwise known as Abell 1656) argued that inferring the mass of galaxy clusters from the detection of the luminous component and internal rotation can only lead to a mass lower limit (Zwicky, 1933). On the contrary, he proposed a method, based on the virial theorem, to infer the value of the total cluster mass from the measured velocity dispersion of the galaxies belonging to the cluster itself. This approach remains valid (at least as an order of magnitude estimate) even if the hypothesis of equilibrium for the cluster is relaxed. The value Zwicky found for the mass of the Coma cluster was ~ 200 times larger than what usually assumed considering only the luminous component. Thus, he claimed the existence of a new form of non-luminous matter able to explain the larger mass value he had found. Today, dynamical estimates are consistent with a value $\Omega_m^0 \simeq 0.2 - 0.3$ on cluster scales (see e.g. (Bertone, Hooper

---

[ii] A constant velocity, $v^2 = GM(r)/r$, requires that $M(r) \propto r$. Since $4\pi \int_0^r r^2 \rho(r) dr \equiv M(r)$, the distribution of the DM component $\rho_{DM}(r) \propto r^{-2}$ assures $v \propto$ const at large distance from the center where DM dominates.

& Silk, 2005) and references therein). Similar results come from gravitational lensing e.g. (Falco, Kochanek & Munoz, 1998; Tyson, Kochanski & dell'Antonio, 1998) and from the profile of the X-ray emission of the hot emitting gas, see (Bertone et al., 2005) for a review.

Another resort to get an estimate of Ω_m^0 on even larger scales is to study the distribution of peculiar velocities of galaxies and clusters. On these scales, there are measurements, (Willick, Strauss, Dekel & Kolatt, 1997), that indicate a lower value for the overall matter density in the range:

$$\Omega_m^0 \simeq 0.2 \div 0.5 \,. \tag{2.9}$$

Again, this result is in good agreement with the other proofs coming from smaller scales.

Additionally, the linear mass power spectrum derived from observations of the Lyman-α forest[iii] and combined with the observed mass function of galaxy clusters (i.e. by comparing the measurement of the linear power spectrum to the predictions of cluster-normalized models) also requires a substantial amount of DM (Weinberg, Croft, Hernquist, Katz & Pettini, 1999).

Another piece of gravitational evidence for DM on clusters scale is the cluster merging system 1E0657-558 (z = 0.296), commonly known as "Bullet Cluster" because of the characteristic cone-like shape of the hot colliding gas.

This galaxy cluster is believed to be composed by two merging dynamical systems which are spatially segregated during the collision: a dissipationless stellar component and a fluid-like X-ray emitting plasma which experiences strong dissipation. Gravitational lensing of deep background objects traces the gravitational potential of the total mass of the system. Its center results to be significantly offset from the center of the hot plasma, i.e. the dominant baryonic mass component (Clowe et al., 2006). Such a displacement supports the fact that the majority of the matter is not interacting electromagnetically and such a phenomenon cannot be explained by modifications of gravitational laws. Moreover, the "Bullet Cluster" shows evidence that the material in clusters is weakly enough interacting to suffer no significant disruption when clusters pass through each other. Together with another clear example of a Bullet-like configuration (Bradač et al., 2008), the "Bullet Cluster" phenomenon provides a direct evidence for a DM component on large cluster scales[iv].

[iii] The Lyman-α forest is a phenomenon of absorption in the spectra of high-redshift quasistellar objects (quasars): clouds of neutral hydrogen between the emitting objects and the observer absorb ultraviolet light at the wavelength of the Lyman-α line of hydrogen at a wavelength of 122 nm. Quasars also emit a strong Lyman-α line and absorption lines are all on the shorter wavelength side of the quasar emission line since the absorbing clouds are situated at smaller redshifts giving origin to the so-called "forest".

[iv] While this excludes baryonic DM, it does not set very stringent constraints on the self-interactions of DM candidates.

On the largest scales, observations of the temperature fluctuations of the CMB witness the existence of a large amount of DM and allow to derive the cosmological parameters with a high level of precision through a multi-parameters likelihood analysis.

Fluctuations in the temperature distribution of the order of $\sim 10^{-5}$ reflect initial matter density deviations from the mean density in the early universe. The CMB is thus a snapshot of the universe at the time of last scattering giving details about the fluctuations in the energy density at that time. The CMB temperature fluctuations measure the density contrast in baryons at the CMB formation epoch, indicating that a DM component is required in order to reproduce the observations. Indeed, according to the standard theory of cosmic structure formation (see (Lucchin & Coles, 1992) as a reference text book), the cosmic structures in the universe were formed as a consequence of the growth of primordial tiny fluctuations (for example seeded in the inflationary epochs) by gravitational instability in an expanding frame. Without a non-baryonic matter component the growth of structures via gravitational instability would have been too slow to reproduce structures as they are today on the scales tested by the CMB. Non-baryonic DM helps since it would cause the baryonic perturbations to grow faster and to form the observationally seen large scale structure.

From the power spectrum of temperature fluctuations it is possible to infer the details of our cosmology: the overall amplitude of the peaks depends on the total amount of matter Ω_m^0, whereas the relative height of the peaks is affected by the amount of baryons. The latest data of the Planck satellite are well fitted by a minimal six-parameters flat ΛCDM model. The abundances' parameters for this model, using the Planck data are: $\Omega_b^0 h^2 = 0.02207 \pm 0.00033$, $\Omega_{CDM}^0 h^2 = 0.1196 \pm 0.0031$ (68% C. L.). The improved constraint (at the 68% C. L.) on the total matter density turns out to be $\Omega_m^0 h^2 = 0.1423 \pm 0.0029$, (Ade et al., 2013).

For the sake of completeness, with regard to Ω_Λ, there are today several observations which indicate that the cosmological constant is indeed present and non-zero. Notably, the study of the relation between the luminosity distance $d_L(z)$ and the red-shift z for a Type Ia supernovae sample at $z = 1$ prefers a flat universe with positive cosmological constant (Riess et al., 1998; Perlmutter et al., 1999). The Planck estimate is $\Omega_\Lambda^0 = 0.686 \pm 0.020$ (Ade et al., 2013).

2.3 Summary: Dark Matter properties

We have seen that the DM-to-baryon ratio is ~ 5 on cosmological scales and it can vary significantly on smaller scales. From CMB measurements we know with precision the amount of DM on cosmological scales and we can infer its general properties from several observations at different scales. Here we summarize which are the main characteristics the new matter component has to satisfy in order to fulfill the astrophysical and cosmological observational constraints:

- *Stable on cosmological timescales*: the lifetime of DM must exceed the present age of the universe, H_0^{-1} so that DM abundance is significant today. In many proposed extensions of the SM, the stability of the DM particle is guarantied by imposing a new symmetry that forbids the decay of DM into SM particles.

- *Neutral*: the fact that the DM is not emitting any "visible" light told us it must be electrically neutral. Moreover, its $SU(3)$ color charge must be zero as well, since, otherwise, it would lead to the production of "dark" hadrons which, in turn, would interact so strongly with baryons to affect the cosmic history from the BBN till the structures formation.

- *Non-baryonic*: the baryon fraction of the matter density in the universe is accurately and independently determined by BBN – by comparing predictions to measurements of the abundance of different elements – and by the CMB power spectrum. The discrepancy between Ω_m^0, measured at different scales, and Ω_b^0 implies that non-baryonic DM has to dominate the energy density by a large factor[v]. Moreover, in order to reconcile CMB and cosmic structures observations non-baryonic DM is required.

- *Non-relativistic at the time of structure formation*: damping effects should be taken into account when discussing the evolution of density perturbations. Besides the Silk (or collisional) damping due to the imperfect coupling between baryons and photons at recombination (Silk, 1968), collisionless species (e.g. neutrinos, DM, axions), after their decoupling from the heat bath, move in the universe from overdense regions to underdense regions and participate in washing out density perturbations. No clustering occurs for scales below the free-streaming scale which depends on the velocity of the collisionless species at the time perturbations start to grow. Species which are relativistic at the

---

[v] We notice that the light element abundances require the existence of baryonic DM, which is still most likely several times more abundant than luminous baryonic matter. Possible candidates are objects like brown dwarfs or planets: these objects are known as MACHOs, for MAssive Compact Halo Objects (Longair, 1998).The signature of these objects is the occasional amplification of the light from extragalactic stars by the gravitational lens effect. Other possible astrophysical objects, contained in the halo, are the relics of stars, dim stars such as white dwarfs, neutron stars, or even black holes. Nevertheless, those candidates could not be the dominant component of the galactic dark halo as constrained by gravitational microlensing measurements (Gates, Gyuk & Turner, 1995).

time of structure formation have large free-streaming scales and thus erase small-scale structures. This kind of component is known as Hot Dark Matter (HDM) and it is disfavored by observations from the Sloan Digital Sky Survey (Reid et al., 2010). Furthermore, HDM models predict that small structures form by fragmentation of larger ones (top-down scenario), while the observed distribution of galaxies at different redshifts as measured by the largest surveys – e.g. 2dF Galaxy Redshift Survey (Abazajian et al., 2009) – favors a so called bottom-up scenario as actual paradigm of hierarchical structure formation. In this hierarchical scenario, the small primordial density fluctuations grow due to non-linear gravitational evolution and become the first virialized structures (halos) which subsequently form larger structures during merger processes. On the other hand, DM particles with non-relativistic velocities at the time of structure formation can clump on smaller scales and provide the kind of structure formation scenario preferred by observations, i.e. small clumps merging in larger ones, forming galaxy halos and successively larger structures.

- *Collision-less*: the typical feature DM must satisfy to explain the “Bullet Cluster” phenomenon is being collisionless, i.e. DM should not interact or very weakly interact with baryonic matter. On the other hand, constraints on DM self-interactions are not too strong.

What is DM made of? DM can be explained either by invoking modifications to gravity which would mimic a matter component on large scales or by considering the DM as a new, unknown particle. So far, in the former scenario, Modified Newtonian Dynamics (MOND) theories (Milgrom, 1983) are able to explain some local feature of DM and individual observations but the Bullet Cluster (whose interpretation requires anyhow the existence of a new dark matter component). Given the weakness of this kind of models, a particle DM candidate seems to be more likely. We remind that a good DM candidate should not only satisfy the astrophysical and cosmological constraints, it must also be well-motivated from the point of view of particle physics. A wide range of DM candidates can be found in the literature, each of them proposed to solve the DM problem or at least some issues related to it.

In the following we will focus on the class of Weakly Interacting Massive Particles (WIMPs) and we point the reader to (Bertone et al., 2005; Bertone, 2010) for a discussion on other candidates, e.g. neutrinos, axions, sterile neutrinos, etc.

2.4 Particle Dark Matter

Particle DM is a viable solution to the DM issue not only because of the weakness of MOND theories but also since it requires the existence of new unknown particles that can be motivated by some new fundamental theories of particle physics. Indeed, the SM of particle physics does not provide any suitable DM candidate. Although for some time neutrinos were considered good DM candidates, it was then realized that they can not be the dominant DM component because of their very small masses. From CMB measurements, the bound on the neutrinos relic density, $\Omega_\nu^0 h^2 = \sum m_\nu/(93.5\,\mathrm{eV}) \sim 0.01$ (derived by the 95% C.L. limit on $\sum m_\nu$ from Planck using WMAP polarization)(Ade et al., 2013), implies that they cannot fulfill the DM cosmological abundance measurement. Moreover, as explained before, neutrinos, being relativistic at the time of the matter-radiation equality, would lead to a top-down hierarchical scenario in the formation of cosmic structure which is disfavored by current cosmological observations. Therefore, a particle DM candidate requires an extension of the SM with some new particle content. The urgency of a physics beyond the SM is not only supported by the DM issue, but it is also required in order to address still not solved problems in particle physics which, in turn, may motivate good DM candidates. In this regard, particle DM represents a fundamental link between astrophysical/cosmological observations and particle physics and makes the DM issue a leading topic of astroparticle physics.

Since a good particle DM candidate has to be well motivated from a particle physics point of view, we briefly review the current picture of SM physics, its open problems (the most relevant for DM) and viable DM candidates that can be motivated by solutions to these problems.

The gauge hierarchy problem is one of the main difficulties of the SM. The physical value of the Higgs mass in an electroweak symmetry broken theory is expected to be about the weak scale – ~ 100 GeV – and it receives quantum corrections from loop-level diagrams connected with the well higher fundamental Planck scale, $M_{Pl} \sim 10^{19}$ GeV. If no physics beyond the SM is present up to M_{Pl}, quantum corrections must cancel with high accuracy (Weinberg, 1976; Susskind, 1979) in order to lead to the correct physical Higgs mass. This fine-tuning can be cured by new physics at the weak scale – ~ 1 TeV – and thus a solution to the hierarchy problem may motivate DM candidates with masses of the order of $m_{\mathrm{weak}} \sim 10$ GeV – TeV such as WIMPs and SuperWIMPs, i.e. particles with interactions weaker than weak and produced in late decays of WIMPs (J. L. Feng, Rajaraman & Takayama, 2003b, 2003a).

The new physics at the weak scale can in turn generate a series of problems in the flavor sector in respect to e.g. baryon and lepton number conservation, flavor and CP symmetry. This “new physics flavor problem” motivates DM candidates as e.g. light gravitino in gauge-mediated supersymmetry breaking models (Pagels & Primack, 1982) and some hidden sector DM models as e.g. mirror baryons (Hodges, 1993).

Furthermore, a minimal extension of the SM is required in order to allocate a massive neutrino since observations of neutrino flavor oscillations require at least two massive neutrinos. Nevertheless, a minimal modification of the SM would not explain the relative sizes of observed neutrino masses with respect to those of charged leptons and quarks. A viable solution to this problem is provided by the see-saw mechanism, where right-handed neutrinos are added. Those new particles, called sterile neutrinos since they cannot have any interaction with other particles but gravitational, turn out to be good DM candidates, see (Dodelson & Widrow, 1994) and (Abazajian et al., 2012) for an extensive review.

Finally, the SM QCD predicts contribution to CP-violating flavor conserving observables (i.e. the electric dipole moment of the neutron) which are severely constrained by observations. The fact that QCD does not seem to violate the CP symmetry is known as the strong CP problem and motivates axions as DM candidates, (Gates et al., 1995; Abbott & Sikivie, 1983; Dine & Fischler, 1983; Preskill, Wise & Wilczek, 1983).

We remind that other unsolved problems, as e.g. the grand unification problem, support the need of physics beyond the SM.

In the following, we will not discuss all the DM candidates presented above, e.g. sterile neutrinos and axions, but we will focus on WIMPs, notably on supersymmetric WIMPs, since the work of this thesis has been developed in such a framework.

2.4.1 Weakly Interacting Massive Particles

WIMPs are found in many theories beyond the SM and they represent the most studied candidates as non-baryonic, cold DM. They are produced rather independently on the initial conditions in the history of the universe, they naturally can achieve the correct relic density (the so called "WIMP miracle") and they represent new physics at the weak scale being motivated by the naturalness problem explained above.

We describe here the standard WIMP production mechanism, i.e. the thermal freeze-out, as explained in (Jungman, Kamionkowski & Griest, 1996). The early universe can be treated as a system in equilibrium characterized by the temperature. It is possible to show that time and temperature in the radiation dominated epoch satisfy the relation: $t \sim T^{-2}$. In the radiation-dominated era, at sufficiently large temperatures, WIMPs, as every other particle, are generated during the collisions among particles of the thermal plasma and they are kept in chemical equilibrium by the following reaction

$$\chi\bar{\chi} \leftrightarrow \ell\bar{\ell}\,, \tag{2.10}$$

where χ indicates the WIMP and ℓ any other particle in the heat bath. Such a process is effective in both directions when the temperature of the universe is greater than the WIMP mass, then, as the universe cools down, WIMPs become non-relativistic and they can be no longer produced efficiently.

The evolution of the WIMP number density, $n(t)$, as a function of cosmological time t, is described by the standard Boltzmann equation:

$$\frac{dn}{dt} = -3Hn - \langle \sigma_{\rm ann} v \rangle \left(n^2 - n_{\rm eq}^2 \right) , \tag{2.11}$$

where $\langle \sigma_{\rm ann} v \rangle$ is the average over the thermal distribution of initial particles. In the case of non-relativistic particles, the thermally averaged cross section can be parametrized with a non-relativistic expansion in powers of v:

$$\langle \sigma_{\rm ann} v \rangle = a + b \left\langle v^2 \right\rangle + O(\left\langle v^4 \right\rangle) \simeq a + \frac{b}{x} , \tag{2.12}$$

with $x = m_\chi / T$ and $T \sim \langle v \langle^2$ for non relativistic particles; $n_{\rm eq}$ is the equilibrium density of WIMPs in the plasma at temperature T. The first term in the right hand side of the Eq. 2.11 takes into account the dilution of the number density due to the expansion of the universe. Instead, the second term takes into account the evolution of the particles number density due to the annihilation (depletion rate proportional to n^2) and pair production (with rate proportional to $n_{\rm eq}^2$).

At the value $x_f \equiv m/T_f$[vi] the number density n leaves the equilibrium number density $n_{\rm eq}$ and the WIMPs' comoving density remains constant. WIMPs undergo the so called chemical decoupling or freeze-out.

This happens when the rate of the direct annihilation reaction, $\Gamma(T) = n(T) \langle \sigma_{\rm ann} v \rangle$, falls below the expansion rate of the universe, $H(T)$, and particles can no longer interact since the causal horizon is larger than their mean free path.

Depending on the WIMP mass, the freeze-out of WIMPs is predicted to take place at a temperature of a few GeV or above, much earlier than any of the processes which can be directly tested through cosmological observations. The expected relic abundance of a non-relativistic particle which thermalizes in the early universe can be computed by solving the Boltzmann equation, Eq. 2.11. The relic density today for a generic non-relativistic WIMP χ, whose annihilation cross section is weakly energy dependent, is:

$$\Omega_\chi h^2 \approx \frac{1.07 \times 10^9 {\rm GeV}^{-1}}{M_{Pl}} \frac{x_f}{\sqrt{g_*(x_f)}} \frac{1}{a + b/x_f} \approx \frac{3 \times 10^{-27} {\rm cm}^3 {\rm s}^{-1}}{\langle \sigma_{\rm ann} v \rangle} , \tag{2.13}$$

where $g_*(x_f)$ counts the relativistic degrees of freedom at the decoupling and M_{Pl} is the Planck mass. From Eq. 2.13, we can derive the so called "thermal"

[vi] x_f depends on the WIMP mass and typical values when requiring to fulfill the observed relic density are $x_f \sim 1/25$.

cross section of $\langle\sigma_{\mathrm{ann}}v\rangle \sim 3 \cdot 10^{-26}$ cm^3 s^{-1}, that results in the correct DM relic density in the simplest WIMP scenarios (i.e. velocity-independent annihilation and no co-annihilations with other particles close in mass to the WIMP[vii]). For a detailed discussion and complete calculation of WIMP relic density we refer to (Gondolo & Gelmini, 1991; Edsjö & Gondolo, 1997).

Finally, it is worth noting the fundamental assumption that particles are in thermal equilibrium in the early universe applies to thermal relics only. Instead, it can be evaded by species which are non-thermally produced. In fact, it is possible that DM particles did not experience the thermal history depicted above and that, for example, they inherit the appropriate relic density through the decay of a more massive species, that has earlier decoupled from the thermal bath (e.g. SuperWIMP, axions). Several production mechanisms can act together to produce a given species, hence its relic abundance receives contributions from each of them. Moreover, non-standard cosmological scenarios which predict possible modifications of the expansion rate at the time of DM freeze-out or later, may lead to measurable consequences on the WIMPs' relic abundance which, in turn, may increase by several orders of magnitude (Catena, Fornengo, Masiero, Pietroni & Schelke, 2008). Therefore, the calculation depends on the details of the particle physics and cosmological models adopted.

As we have seen WIMPs arise naturally as new physics at the weak scale which can relieve the hierarchy problem.

The lightest WIMP should be stable over the cosmological time in order to be a DM candidate. This is guaranteed if WIMPs satisfy an additional discrete symmetry preventing the decay of the lightest new physics particle which will then represent a good DM candidate.

Fortunately, some new symmetry at the TeV scale is required in particle physics in order to solve the so called "post-LEP little hierarchy problem". The new physics at the weak scale is in tension with electroweak precision measurements and flavor sector observations. These tensions cannot be solved by any known SM symmetry and they can be relieved if the scale of the new physics is larger than few TeV (Barbieri, 1999). New symmetries at the TeV scale have been therefore proposed to make the new physics consistent with electroweak precision data and still allow to cut the quadratically divergent corrections to the Higgs mass off. Notably, whereas SM particles are neutral with respect to this new symmetry, the lightest new physics state must be charged under it, meaning that the new symmetry introduces

---

[vii] Co-annihilations are processes that deplete the number of WIMPs and occur when another particle is close in mass to the WIMP, i.e. mass difference of the order of the temperature. In this case the scattering process can convert the WIMP in the slightly heavy particle, since the energy barrier that would otherwise prevent it (i.e. the mass difference) is easily overcome. The subsequent decay and reaction of those heavier particle can then effect the disappearance of WIMPs (Gondolo & Gelmini, 1991; Edsjö & Gondolo, 1997).

a new stable particle which can be a viable DM candidate. The most known new symmetries are R-parity (Farrar & Fayet, 1978) in the context of Supersymmetry (SUSY), which motivates the neutralino as the most likely DM candidate, and Kaluza-Klein (KK) parity (H.-C. Cheng, Matchev & Schmaltz, 2002a) in universal extra dimensions (UED) (Appelquist, Cheng & Dobrescu, 2001).

We will now discuss briefly these two DM candidates, neutralino and KK particles. This discussion is not meant to be exhaustive but it contains the most general features of such candidates relevant for DM indirect searches.

2.4.2 Neutralino Dark Matter

In the context of SUSY, neutralino is the most studied WIMP DM candidate. We will devote Appendix E to an introduction to the Minimal Supersymmetric extension of the Standard Model (MSSM) (Fayet, 1979, 1976, 1977) and its general structure. Nonetheless, we mention here briefly its main motivations and features related to the DM issue.

SUSY can elegantly alleviate the hierarchy problem and stabilizes the scale of electroweak symmetry breaking by means of introducing new particles with opposite spin-statistics with respect to the SM ones and with masses at the TeV scale (Witten, 1981). Moreover, unification of gauge SM couplings is possible in the context of SUSY, by including sparticles in the renormalization group equations, (Ellis, Kelley & Nanopoulos, 1991; Giunti, Kim & Lee, 1991) and (Boer, 1994) for a review on the topic. Finally, a general SUSY prediction is a relatively light Higgs boson (Ellis & Ross, 2001) which agrees with electroweak precision measurements. This prediction is going to be proved by the recent discovery of the neutral scalar particle with $m \sim 125$ GeV (most likely the Higgs boson) by means of two Large Hadron Collider (LHC) experiments (Aad, Abajyan et al., 2012; Chatrchyan et al., 2012a).

The lack of observational evidence of superparticles forces SUSY to be a broken symmetry (exact supersymmetry would require the mass of superpartners to be the same as the SM particles). SUSY is broken explicitly and "softly" in order to not spoil the SUSY's solution to the hierarchy problem as we will discuss in Appendix E.

Up to now no evidence for SUSY at the weak scale has been discovered. After a two-year data taking, the LHC experiments have pushed the mass limit for new physics above the TeV scale for gluinos and squarks, making the naturalness of SUSY a challenge.

We notice that the strongest bound on new physics at the weak scale come from low-energy flavor and CP violation measurements which exclude large effects from new physics beyond the SM. We will not address here the problem of the naturalness of SUSY and its phenomenological implications on the parameter space. For a review we point the reader to (J. L. Feng, 2013).

The new particle content has many implications for cosmology and any new stable, neutral and weak interacting particle can potentially be a good DM candidate, e.g. sneutrinos, gravitino, neutralinos (Goldberg, 1983; Ellis, Hagelin, Nanopoulos, Olive & Srednicki, 1984). To make stable the lightest supersymmetric particle (LSP) a new symmetry is required. This new discrete symmetry is called R-parity and it has been originally introduced to get rid off terms violating lepton or baryon number in the SUSY superpotential (Farrar & Fayet, 1978). Such a symmetry assigns even R-parity to SM particles and odd R-parity to SUSY partners so that supersymmetric particles can only be produced in pairs and can decay only into lightest SUSY particles. By consequence, the LSP is stable.

In the MSSM the most promising LSP candidate is the lightest neutralino. It arises from the linear combination of the neutral wino $\tilde{W}^3$, the U(1) bino $\tilde{B}$, and the two neutral higgsinos $\tilde{H}_1^0$ and $\tilde{H}_2^0$:

$$\tilde{\chi}_1^0 = N_{11}\,\tilde{B} + N_{12}\,\tilde{W}^3 + N_{13}\,\tilde{H}_1^0 + N_{14}\,\tilde{H}_2^0\,. \tag{2.14}$$

Accordingly to its composition, i.e. to its gaugino fraction, $Z_g \equiv |N_{11}|^2 + |N_{12}|^2$, $\tilde{\chi}_1^0$ may be more bino-like, wino-like or higgsino-like. The tree-level mass is determined by four parameters: the masses of the $SU(2)_L$ and $U(1)$ gauge fields, $M_{2,1}$, the Higgs mixing parameter μ, and the ratio of the vacuum expectation values of the neutral components of the Higgs doublet, $\tan\beta \equiv v_2/v_1$, as we will see in Appendix E. Neutralino as DM candidate must fulfill the correct DM relic density which depends on the concrete MSSM model parameters. On the other hand, the parameter space can be constrained by imposing the correct relic density. The MSSM has 124 free parameters. Typically, making some assumptions, e.g. about SUSY symmetry breaking, will result in models with much fewer free parameters. An example of gravity mediated soft SUSY breaking is the constrained MSSM (Drees & Nojiri, 1993). It includes the minimum additional particle content and depends on five free parameters: m_0, the universal scalar mass, $M_{1/2}$, the universal gaugino mass (both defined at $M_{\rm GUT} \sim 2 \cdot 10^{16}$ GeV), A_0, related to the cubic scalar particles interaction, and parameters defining the Higgs boson potential, $\tan\beta$ and sign(μ). In general, large scans over the parameter space are required in order to constrain models. Nevertheless, besides regions of the parameter space excluded by the requirement that the LSP must be neutral and by the absence of electroweak symmetry breaking, it is possible to individuate different cosmological regions constrained by the DM abundance.

We here briefly present several regions of the parameter space that can accommodate the correct abundance of neutralino CDM. For more details we refer to the overview in (Baer, Barger & Mustafayev, 2012) and references therein.

The case of neutralino annihilation into lepton pairs via t-channel slepton exchange, with slepton masses in the 30 – 80 GeV range (Baer & Brhlik, 1998), has long been excluded by the LEP-2 results on direct slepton pair searches (Heister et al., 2002).

The remaining regions during the post-LEP2 era were:

- the stau co-annihilation region at larger $M_{1/2}$ and relatively small m_0, where neutralinos co-annihilate with lighter staus in the early heat bath;
- for specific values of A_0 neutralino can annihilate with light stops, i.e. stop co-annihilation region[viii];
- for $m_0 \geq 1$ TeV, the hyperbolic branch/focus point region provides neutralinos which are mostly higgsino-like with annihilation rate dominated by scattering into WW, ZZ, hh and Zh channels (J. L. Feng, Matchev & Wilczek, 2000);
- in the A-funnel region at high $\tan\beta \sim 50$ the mass of the CP-odd Higgs is small and neutralino pair annihilation is enhanced by the presence of a broad s-channel A-resonance e.g. (Drees & Nojiri, 1993);
- the h-resonance region at low $M_{1/2}$ where neutralinos have an enhanced annihilation rate via the narrow s-channel h resonance (Nath & Arnowitt, 1993).

Gluino and squark searches at the LHC strongly constrain the allowed parameter space (mass limits of $m_{\tilde{g}} \geq 1.4$ TeV when $m_{\tilde{q}} \sim m_{\tilde{g}}$ and $m_{\tilde{g}} \geq 0.9$ TeV when $m_{\tilde{q}} \gg m_{\tilde{g}}$ (Aad, Abbott et al., 2012; Chatrchyan et al., 2011)) and exclude already the whole h-resonance annihilation region, some portions of the stau and stop co-annihilation regions and the lowest m_0 and $M_{1/2}$ portions of the A-resonance annihilation region (Baer et al., 2012, 2013).

Additionally, depending on the quantity of fine tuning considered acceptable, the impact of a SM-like Higgs boson with mass ~ 125 GeV would be to leave open only the focus point region at high m_0 (Baer et al., 2012).

In chapter 4, we will further discuss the MSSM parameter space in light of the calculation of electroweak corrections to neutralino DM annihilation.

Neutralino DM shows distinctive features which allow such a candidate to be particularly well suitable for searches with direct and indirect detection techniques that must be complemented by direct searches for new physics with accelerator-based experiments (i.e. fixed target experiments or particle colliders), as we will see in what follows.

[viii] Co-annihilations could give rise to reasonable values of the relic density even at very large values of $M_{1/2}$, at both low and high $\tan\beta$ (Ellis, Falk & Olive, 1998; Ellis, Falk, Olive & Srednicki, 2000; Arnowitt, Dutta & Santoso, 2001).

2.4.3 Kaluza Klein Dark Matter

The solution of the hierarchy problem can be embedded in theories with extra dimensions. The first attempts of physics beyond the SM with extra dimensions date back to the beginning of the XX century with the work of Kaluza and Klein (Kaluza, 1921; Klein, 1926). KK extra dimensions are compactified in a volume R^n and fields can propagate through them. A tower of four-dimensional particles with increasing masses corresponds to every particle propagating in one of the extra-dimensional directions.

A specific class of extra dimensional models is UED (Appelquist et al., 2001), where all fields are assumed to propagate in a flat space-time $\mathcal{M}_4 \times X$, where X is a compact space, compactified on a circle.

The momentum along the extra-dimension is discretized as a consequence of the compactification and, in the four-dimensional effective theory, a tower of KK resonances in the particle spectrum occurs. Each SM particle, which is identified with the lowest-lying ("zero") mode, has a tower of KK-partners with increasing masses, $m^n_{KK} \sim n/R$. Differently from SUSY, the mass spectrum of KK particles is strongly degenerate and mass splittings arise from radiative corrections (H.-C. Cheng, Matchev & Schmaltz, 2002b). The mass of the first KK-excitation is inversely proportional to the radius of the extra dimension. This size strongly depends on the extra dimensions model and can be constrained by the fact that we do not see KK partners of ordinary particles.

KK number is no longer conserved when Lorentz invariance is broken, e.g. when introducing orbifold boundaries, and thus KK states are not stable and can decay into SM particles. To prevent such a decay, KK parity is imposed as a new discrete symmetry at TeV scale which solves the little hierarchy problem and make the lightest KK mode stable (LKP) (H.-C. Cheng, Matchev & Schmaltz, 2002a). Therefore, for models at the TeV scale the LKP is stable, "weakly" interacting and can thus be a viable DM candidate.

In minimal UED models, the absence of all higher-dimensional operators at the cutoff scale Λ[ix] is assumed (Carena, Tait & Wagner, 2002). Under this assumption, the only free parameters of the model are the compactification scale R^{-1} and the cutoff scale Λ.

Currently strong lower limits on the compactification scale in minimal UED come from LHC data giving a bound of $R^{-1} \gtrsim 550$ GeV if the recently discovered boson with $m \sim 125$ GeV is a UED Higgs boson (Bélanger, Belyaev, Brown, Kakizaki & Pukhov, 2013), whereas upper bounds follow from the relic density of the dark matter candidate although they strongly depend on the KK mass spectrum (Bélanger, Kakizaki & Pukhov, 2011).

Usually in minimal UED, the LKP is $B^{(1)}$, the first excitation of the weak hypercharge gauge boson (Servant & Tait, 2003). By computing its

---

[ix] The theory is non-renormalizable and must therefore be considered as an effective theory with a cutoff Λ.

relic density it is possible to constrain the viable $B^{(1)}$ mass of about 1.3 TeV (Bélanger et al., 2011). While present direct detection experiments are not sensitive enough to probe KK DM (Arrenberg, Baudis, Kong, Matchev & Yoo, 2008), such a candidate is suitable for indirect searches due to its spectral energy distribution as we will see in chapter 7.

2.5 Hunting Dark Matter

The thermal history of WIMPs together with the typical strength of their interactions not only gives a motivation for new physics beyond the SM at the weak scale, but has also an impact on the phenomenology of such a candidate and on how it may be detected. Indeed, the fact that WIMPs were annihilating in the early universe into standard particles, $\chi\chi \to SMSM$, and that the reversed process acted during the chemical equilibrium phase, tell us that also the process $\chi SM \to \chi SM$ should be possible and the strength of WIMP interactions implies that these three reactions are still possible today and can be exploited to build experiments aiming to detect DM.

Different techniques and experimental methods have been developed and optimized to look for DM, new dedicated detectors have been built or ongoing experiments (mainly astrophysical mission) have been exploited. The main techniques are the direct and indirect detection of DM but searches at colliders have also started delivering important results. Searches for DM are deeply connected and have to be combined in a coherent way to lead to a complete picture of the status of DM detection. They indeed investigate complementary aspects of the DM issue and their combined results can help in breaking the degeneracies in the phenomenological parameter space of DM. We will review the main detection techniques in what follows.

2.5.1 Direct Detection

Direct detection (DD) experiments can probe directly the existence of DM with several and complementary techniques.

DD is based on the scattering of the WIMP with the nuclei of a sensitive detector stored in an underground site (to shield it from CRs which penetrate the atmosphere). If the galaxy is filled by WIMPs, then many of them should pass through the Earth and interact with matter. The result of this interaction can be looked for by e.g. recording the recoil energy of nuclei as WIMPs elastic scatter off them (Goodman & Witten, 1985) (and also the direction in directional experiments). The relevant quantity to be calculated and compared with the experimental measurements is the differential detection rate, which theoretically depends on the nucleus and WIMP mass, on the velocity distribution of WIMP in the halo, on their local density and on the WIMP-nucleus cross section. The latter is determined by the particle physics model in which WIMPs are embedded and by the nucleus composition. Spin-dependent and spin-independent terms contribute to the total cross section. Moreover, inelastic scattering may contribute to the WIMP-nucleus cross section. Therefore, the rate turns out to be subject to large uncertainties from particle and nuclear physics as well as from astrophysics. We refer the reader to chapter 17 in (Bertone, 2010) for an introductory review.

The interaction of slow halo DM particles with the detector produces the recoil of a nucleus with energy E_R of the order of few keV. The recoil energy can be measured by means of various experimental techniques (e.g. cryogenic detectors, noble liquids, superheated liquids, scintillators and ionization detectors) using different nuclear species, like Ge, NaI, Xe, CaF_2, TeO_2. They all require a great effort in the complex procedures of discriminating electromagnetic signals from recoil events and the delicate subtractions meant to separate putative WIMP signals from neutron- or other background-induced events.

WIMP DD experiments – e.g. CDMS-II (Ahmed et al., 2010), CoGENT (Aalseth et al., 2011), XENON100 (Aprile et al., 2011), CRESST (Angloher et al., 2012) – can thus constrain the DM parameter space and hopefully detect a positive DM signal. Presently the strongest bounds are set by XENON100, which works with a liquid xenon target (Aprile et al., 2011). In tension with these strong limits, claims for detection of light DM ~ 10 GeV have been made by other experiments, CoGENT (Aalseth et al., 2011) and CRESST-II (Angloher et al., 2012). Recently, also the CDMS-II has reported three WIMP-candidate events that can be due to the background with a 5.4% probability (Agnese et al., 2013).

The interpretation of such results is complicated by the 8.9σ C.L. detection of annual solar modulation claimed the DAMA/NaI and DAMA/LIBRA experiments (with a total exposure of 0.82 ton yr) (Bernabei et al., 2010, 2008). The annual modulation of the detection rate during the orbital motion of the Earth around the Sun is a typical signature of DM in DD experiments. The change of the direction of the relic particle velocities with respect to the detector induces a time dependence in the differential detection rate, which may be a clear DM signature (Drukier, Freese & Spergel, 1986). The signal can be interpreted as due to relic neutralino DM interactions, e.g. (Bottino, Donato, Fornengo & Scopel, 2004, 2008; Scopel, Fornengo & Bottino, 2013), although it can not be easily accommodated in standard SUSY (Cumberbatch, López-Fogliani, Roszkowski, Ruiz de Austri & Tsai, 2011). It is worth mentioning that also the CoGENT experiment found a modulation in the rate of low energy nuclear recoil events with a significance of 2.8σ (Aalseth et al., 2011).

This puzzling picture of the status of DM DD is presently an issue of debate although theoretical efforts have been made in order to alleviate the tensions among different observations, e.g. (Schwetz & Zupan, 2011).

2.5.2 Indirect Detection

ID of DM is the technique of observing the stable particles produced by DM annihilations in different astrophysical environments:

- annihilations in the galactic halo or external galaxies would lead to the direct or indirect (via hadronization and decays) production of neutrinos, photons and rare components in CRs (positrons, antiprotons, antideuterons)[x]. The detection rate is proportional to $\rho_\chi^2 \cdot \sigma_{\mathrm{ann}}$, where ρ_χ is the DM distribution in the astrophysical object.

- annihilations taking place in the interior of celestial bodies (Earth and the Sun), where DM particles have been captured and accumulated as they lose energy through scattering with nucleons, would give rise to a neutrino signal. In this case, the annihilation rate is proportional to the product $\rho_\chi \cdot \sigma_{DM}^{\mathrm{nucleon}}$.

By comparing predictions with current experimental data it is possible to look for DM and, in the case of null result, to constrain DM models and the astrophysical properties of the DM candidate. Different channels may be explored via different techniques; a multi-messenger and multi-wave-length approach is thus fundamental in understanding the properties of DM in a coherent and consistent picture. It is worth noticing that, despite of DD experiments which are DM-purposed instruments, ID experiments are only partially dedicated to DM searches.

We here present a brief overview of the channels relevant for ID searches, namely neutrinos and antimatter. We instead postpone the discussion of DM searches through γ-rays, the most likely promising method for DM ID, to the next chapter 3, which will be completely devoted to this topic, since it is one of the main subjects of this thesis.

A neutrino signal may come from celestial bodies, Earth and Sun, where DM particles have been gravitationally captured (after elastic collisions with nuclei) and accumulated during the lifetime of the celestial body (Berezinsky et al., 1996). Pair annihilations of the accumulated DM particles generate a final flux of high-energy neutrinos that can escape the dense medium with minimal absorption.

Neutrino telescopes look for an excess of up-going muons above the muon flux originated from atmospheric neutrinos. Muons are produced by the macroscopic charged-current conversion of the muon neutrino component of

---

[x] DM annihilations produce also matter. Nevertheless, a good detection strategy is characterized by the possibility to reduce the most the background from ordinary astrophysical processes. That is the basic reason why searches for charged particles focus on fluxes of antiparticles which are much less abundant than the corresponding particles.

the signal and then traverse the detector upwardly. The different angular behavior of the signal with respect to the atmospheric neutrino background, which has a rather flat distribution as a function of the zenith angle, is the handle for the signal-to-background discrimination. Current operating neutrino telescopes are Super-Kamiokande (Desai et al., 2004), AMANDA (Ackermann et al., 2006), Antares (J. Aguilar et al., 2004) and IceCube (Achterberg et al., 2006). Limits on DM in the Sun have been recently released by the IceCube Collaboration by including the DeepCore subarray and turn out to be the most stringent spin-dependent WIMP-proton cross section limits to date (Aartsen et al., 2013).

As direct detection experiments do, DM searches through neutrinos depend on the local DM density and its velocity distribution, but, despite of ID with γ-rays and CRs, they do not rely on the DM distribution in the galaxy and on the properties of magnetic and radiation fields.

When DM annihilation takes place directly in the galactic halo (of the Milky Way or in external galaxies), besides neutrinos, other signals are expected. A possible signature of WIMPs annihilation is a non-negligible flux of antimatter, i.e. antiprotons, antideuterons and positrons. The aim of the search is to disentangle a non-standard component in CRs from the astrophysical background generated by the interactions of high-energy CRs with gas in the interstellar medium. The spectrum of CRs extends for several decades in energy and flux and it is studied by means of several experiments (ballons in the atmosphere, space-based satellite and large-area detectors on the ground).

Primary CRs are believed to be produced in astrophysical sources such as supernova remnants or pulsars. They mainly consist of protons and electrons, helium, as well as of other nuclei synthesized in stars. The interaction of primary CRs with the interstellar medium (ISM) lead to the production of secondary CRs: lithium, beryllium, and boron (not abundant products of stellar nucleosynthesis) as well as an antimatter component, i.e. antiprotons, positrons and antideuterium. As far as a DM origin is concerned, antimatter can be originated in the decay and hadronization of the final state particles of the DM annihilation processes.

After being produced, antimatter propagates inside the galaxy and experiences both diffusion in the galactic magnetic field and energy losses due to ionization, scattering, and collisions. The propagation of antinuclei in the galaxy is described by the well known propagation-diffusion equation (Berezinskii, Bulanov, Dogiel & Ptuskin, 1990) which can be solved exploiting semi-analytical models of the galaxy (Maurin, Donato, Taillet & Salati, 2001) or through full numerical methods (Evoli, Gaggero, Grasso & Maccione, 2010; Moskalenko & Strong, 1998). For positrons and electrons the main propagation mechanisms are diffusion and energy losses due to synchrotron radiation in the galactic magnetic fileds and inverse Compton (IC) scattering off the CMB and starlight. Moreover, the interstellar positron and electron fluxes experience strong effects due to solar modulation: CR positrons and electrons lose energy due to solar winds while diffusing in the solar system before reaching Earth (Gleeson & Axford, 1968). Solving the diffusion equation is the big challenge of CRs physics and it is affected by several uncertainties which reflect our little knowledge about the astrophysics of the galaxy (e.g. gas distribution, structure of the spiral arms, height of the diffusive halo, etc.). Antiprotons propagation is instead dominated by convection and spallation. It is worth mentioning that the charged CRs DM flux is mildly dependent on the DM spatial profile, since particles reaching the Earth are produced relatively close to us and therefore they do not strongly feel the quite uncertain galactic center mass distribution.

Secondary antiprotons of astrophysical origin are produced by spallation of high-energy CRs on ISM (Donato et al., 2001) and predictions of antiproton flux from astrophysical processes suffer from a relatively small uncertainty; see (Donato, Fornengo, Maurin, Salati & Taillet, 2004; Bringmann & Salati, 2007; Evoli, Cholis, Grasso, Maccione & Ullio, 2012) for a discussion of the astrophysical antiproton flux in the context of DM searches. Extremely precise data of the antiproton flux from PAMELA (and very recently from AMS-02) result in a strong constraining power on DM. Indeed, secondary astrophysical antiprotons may well explain experimental data in the whole energetic range, so that little space is left for antiproton deriving from DM annihilations (or any other primary source), see e.g. (Bottino, Donato, Fornengo & Salati, 1998; Donato, Maurin, Brun, Delahaye & Salati, 2009; Bringmann & Salati, 2007; Evoli et al., 2012).

A promising channel to look for an exotic source of CRs is represented by antideuteron (a bounded state of an antineutron and an antiproton). Indeed, the astrophysical background rapidly decreases for kinematical reasons at low energies (Duperray et al., 2005; Donato, Fornengo & Maurin, 2008), where the DM contribution may show up (Donato, Fornengo & Salati, 2000). The expected antideuteron flux at Earth from DM annihilation has been predicted (Ibarra & Wild, 2013; Fornengo, Maccione & Vittino, 2013) in view of the results of new experiments such as AMS-02 (Ahlen et al., 1994).

Secondary positrons are produced mostly by the decay of produced pions when protons collide with the ISM. Locally there can be also sources of primary positrons and electrons. Pulsar and Milli-second pulsars (MSPs) are indeed though to be leptons accelerators and a flux of $e^{\pm}$ is expected to come from their directions (Shen, 1970). Moreover, DM can lead to an $e^{\pm}$ flux both from the decay and hadronization chain of DM annihilation and from direct annihilation into $e^{\pm}$ pairs. The branching ratio for this process is usually very small for SUSY candidates, but occurs frequently for KK DM (H.-C. Cheng, Feng & Matchev, 2002). Also annihilations into ZZ or $W^{+}W^{-}$ can produce a positron flux (Kamionkowski & Turner, 1991).

It is generally believed that a substantial fraction of electrons comes from primary sources while all CRs positrons are of interstellar origin. As a consequence, the positron fraction, i.e. the ratio of the positron flux to the combined positron and electron fluxes, should continuously and smoothly decrease with energy (Moskalenko & Strong, 1998). Recently, the positron fraction results from the AMS-02 mission have been published (M. Aguilar et al., 2013). With unprecedented statistical accuracy, they cover the energy range of $0.5 - 350$ GeV and show a rise in the positron fraction at ~ 10 GeV, which confirms the previous outcomes from PAMELA (Adriani et al., 2010) and *Fermi* (Abdo, Ackermann, Ajello, Atwood, Axelsson et al., 2009a) experiments and it is compatible with an extra-source with an exponential power-law spectrum. The discrepancy at low energies ≤ 10 GeV among the different set of data is well explained by solar modulation (Maccione, 2013), whereas the origin of the rise is an open issue. Several solutions have been proposed invoking DM, e.g. (Bergström, Bringmann & Edsjö, 2008; Arkani-Hamed, Finkbeiner, Slatyer & Weiner, 2009; Nomura & Thaler, 2009), and astrophysics (local pulsars and MSPs), e.g. (Profumo, 2012; Di Bernardo et al., 2011; Hooper, Blasi & Dario Serpico, 2009; Delahaye et al., 2009). Since PAMELA results the list of scientific papers about viable solutions grew incredibly. It is worth saying that to derive some final conclusions about the DM contribution to the positron flux, a better knowledge of the standard mechanisms of production and propagation of the CRs in the galaxy is mandatory. So far, AMS-02 positron data set the strongest constraints on DM annihilation or decay into light leptons for masses up to ~ 300 GeV by exploiting spectral features which survive the propagation (Bergstrom, Bringmann, Cholis, Hooper & Weniger, 2013).

We also make notice that $e^{\pm}$ propagating in the galactic magnetic fields produce synchrotron radiation that can be observed in the radio wavelength. By computing the total synchrotron power emitted by the distribution of DM-induced electrons and positrons, constraints on the annihilation cross section can be set via radio observations e.g. of the GC (Bertone, Sigl & Silk, 2002; Bergström, Bertone, Bringmann, Edsjö & Taoso, 2009; Bertone, Cirelli, Strumia & Taoso, 2009; Fornengo, Lineros, Regis & Taoso, 2012).

2.5.3 Dark Matter searches at colliders

New physics at the weak scale is expected to show up at the energies (~ 14 TeV) at which LHC will be operating after the current shutdown. The production of DM particles is not directly detectable since DM produced pairs are invisible. Nonetheless, a photon or a gluon can be emitted by the initial annihilation legs (initial state radiation) and can be detectable as mono-photon, mono-jet (Birkedal, Matchev & Perelstein, 2004) or mono-Z (Bell et al., 2012). Although those searches are affected by irreducible backgrounds, they can set competitive bounds on new physics (e.g. (Chatrchyan et al., 2012b) for DM searches of DM and large extra dimensions in mono-jet events).

Typically, LHC experiments look for the production of physics beyond the SM. For example SUSY searches are based on the pair production of sparticles (dominantly squarks and gluinos via the strong interaction) which then decay via cascades into the stable LSP (e.g. neutralino). The signature of such a process would be multiple, high energetic jets and transverse missing momentum in the energy-momentum balance of the collisions. This strategy is generally promising for searches of new physics and can be used to constrain pair production of neutralinos as well as extra dimensions models. Even if there is no evidence for physics beyond the SM, strong constraints can be placed on neutralino properties as for example the neutralino-nucleon scattering cross section that can be complementary to DD experiments (Chatrchyan et al., 2012b).

Of course, the detection of new physics and missing particles at LHC experiments can not be claimed as a DM discovery. Indeed, the new physics must fulfill all the requirements imposed by astrophysical and cosmological observations in order to be identified as DM. Notably, its relic density should be compatible with the latest Planck results. Collider experiments may provide a way to predict and test fundamental properties of new discovered particles. Nonetheless, comparing such predictions with cosmological observations would be a very compelling task.

2.5.4 Complementarity

Any claim of a relic DM signal requires some distinctive feature to be convincing and even a direct discovery will leave open questions about the nature of DM and its connection with the weak scale and the electroweak symmetry breaking. Moreover, each strategy must face its fundamental limitations and be complemented in this respect by other detection techniques. Hence a cross-correlation between different detection methods (direct, indirect, accelerator) will be crucial when combining different experiments with the aim of drawing a complete phenomenological interpretation of results and hints. DM searches at the colliders are devoted to constrain and, eventually, characterize the new WIMP as the same particle that will be found in astrophysical/cosmological experiments. Presently, the high accuracy reached by both particle physics and astrophysical/cosmological experiments requires to analyze and combine data from different observations and to dispose of common tools being complementary in the search for DM. Exploiting the complementarity of the different detection techniques can help in achieving a convincing identification of the DM nature and in breaking the degeneracies in the phenomenological parameter space of DM that would be present when considering only one detection strategy at a time (Serpico & Bertone, 2010; Bertone, Cerdeño, Fornasa, Ruiz de Austri & Trotta, 2010;

Bergström et al., 2011).

Chapter 3

Dark Matter indirect detection: a closer look to γ-rays

The main topic of the present thesis deals with DM searches through γ-rays. This chapter will introduce all the notions required by the following discussion which will be devoted to specific aspects of γ-ray DM ID. γ-rays are particularly suitable for DM detection since they propagate unperturbed throughout the halo so that they do not suffer from propagation uncertainties like charged CRs; being unaffected by gas and magnetic fields they walk along straight lines (at galactic scale) and they thus point toward the source where they have been originated, allowing directional searches. Moreover, in the case of γ-ray searches is relevant not only the number of particles (i.e. photons) produced by DM but also the spectral energy distribution of the signal which greatly can help in disentangling a DM signal from the unavoidable standard astrophysical background. Finally, they are produced rather quite abundantly. Due to all these reasons they have a great discovery potential.

Furthermore while it is possible that the LHC will provide evidence for physics beyond the SM and DM, or that future direct DM detection experiments will detect a clear signature of nuclear-recoil events produced by DM, γ-ray observations provide a unique tool to measure the DM halo spatial profiles and to elucidate the role of DM in structure formation. Effectively, γ-ray DM searches are more sensitive to the features of the DM distribution in the galactic halo than all the above cited detection techniques (direct and indirect).

As for other DM messengers, γ-rays are final stable products of DM annihilation or decay. In the following we will discuss only DM annihilation, whereas we do not explore the case of decaying DM.

The predicted γ-ray flux $\mathrm{d}\Phi_\gamma/\mathrm{d}E_\gamma$ from DM annihilating particles is defined as the number of photons collected by a detector per unit of time, area, solid angle, and observed energy E_γ. Pointing towards the direction ϕ, θ (longitude and latitude in galactic coordinates) in the sky, by an experiment with spatial resolution α and under a solid angle $\Delta\Omega = 2\pi\,(1 - \cos\,\alpha)$, it reads:

$$\frac{\mathrm{d}\Phi_\gamma}{\mathrm{d}E_\gamma}(E_\gamma, \phi, \theta, \Delta\Omega) = \frac{1}{4\pi}\,\frac{\langle\sigma v\rangle}{2m_\chi^2} \cdot \sum_i B_i\,\frac{dN_\gamma^i}{dE_\gamma} \int_0^{\Delta\Omega} \mathrm{d}\Omega \int_{\mathrm{l.o.s}} \rho^2(R(s,\phi,\theta))ds\,, \tag{3.1}$$

where m_χ is the mass of the DM particle χ, $\langle\sigma_{\mathrm{ann}} v\rangle$ is the annihilation cross section times the relative velocity averaged over the DM velocity distribution, B_i is the branching ratio into some final state i and $dN_\gamma^i(E_\gamma)/dE_\gamma$ is the photon spectrum per annihilation which is summed over all annihilation channels. Eq. 3.1 can be factorized into two terms: the first one depends on the particle physics model through the m_χ and $\langle\sigma_{\mathrm{ann}} v\rangle$ parameters and the photon spectrum; the second one, often referred to as "J-value", is linked to the geometrical distribution of DM in the halo and it corresponds to the integration of the squared DM density $\rho(R)$ (R being the galactocentric distance) at a distance s from the Earth in the direction along the line of sight (l.o.s.), and in the observational cone of solid angle $\Delta\Omega$.

After presenting the mechanisms of γ-ray production from DM annihilation (Sec. 3.1), in Sec. 3.2 we explain how DM is believed to be distributed in the galaxy and at cosmological distances. We then provide a broad overview of DM searches through γ-rays: operating experiments, promising targets and astrophysical backgrounds, Sec. 3.3. In particular, we focus on the IGRB and on its contributions originating from various astrophysical source classes, Sec. 3.4. Finally in Sec. 3.5, we report about the present status of γ-ray searches and their results.

3.1 γ-ray production from Dark Matter annihilation

γ-rays of DM origin can be "prompt" (in the sense that they are directly produced by the annihilation and its subsequently hadronization and decaying processes) or originate from the interaction of DM electrons and positrons with ambient photons that are upscattered to higher energies, i.e. IC scattering.

DM particles in the galactic halo (as well as in the halo of external galaxies) undergo annihilation giving rise to final fluxes of different species, $e^\pm, p, \bar{p}, \bar{d}, \nu, \gamma$. At tree level, the possible annihilation channels, if kinematically allowed, are into quarks, leptons, Higgs and weak gauge bosons pairs. Branching ratios depend on the underlying particle physics model.

The tree level annihilation of DM pairs suffers from two suppression mechanisms: the velocity and the helicity suppressions, that we explain in what follows. The velocity of DM particles moving in the halo, being about $10^{-3}c$, makes DM annihilate essentially at rest. In this velocity (i.e. non-relativistic) regime, the expansion of the scattering amplitude as a sum of angular momentum components (partial waves decomposition) is possible:

$$\langle \sigma_{ann} v \rangle = a + b\, v^2 + O(v^4)\,. \tag{3.2}$$

Thus, in the limit of low velocities the L^{th} partial wave contribution is proportional to v^{2L}, with L the orbital momentum. The first term in the expansion, a, receives contribution from s-wave annihilation, while the second term, $b\, v^2$, comes from both s- and p-wave annihilation. Given the small velocity of DM today, all the L^{th} partial waves but $L = 0$ are velocity suppressed. From Eq. 3.2, it follows that the unsuppressed s-wave, if present, dominates the $\langle \sigma_{\rm ann} v \rangle$.

For Majorana fermions, the Fermi-Dirac statistics imposes that the total wave function is antisymmetric. Therefore, the two-particle spin state of the (velocity) unsuppressed s-wave contribution (i.e. $L = 0$) must be 0 (i.e. singlet spin state). Consider the angular momentum quantum numbers $|J, M; L, S>$ where J is the total angular momentum, M is the component of total angular momentum along any fixed axis, L is the orbital angular momentum and S the total spin angular momentum: for a pair of annihilating non-relativistic Majorana fermions, only the state $|J = 0, M = 0; L = 0, S = 0>$ exists[i]. We remind that, in this kinematical limit, for a Majorana fermion pair parity and charge conjugation are defined as $P = -1$ and $C = +1$. Thus, the annihilating DM pair acts as a pseudo-scalar particle $J^{PC} = 0^{-+}$ decaying at rest with energy in the center of mass system equal to twice of the mass of the DM candidate, m_χ. The initial state of the two incoming particles is ${}^1S_0$[ii].

In the case the annihilating state has total angular momentum $J^P = 0^-$, as it is for Majorana fermion pairs annihilating at rest, the s-wave contribution suffers from the helicity suppression of fermion pair final states, in analogy with the helicity suppression of the charged pion decay, $\pi^\pm \to \mu^\pm \nu_\mu$. Indeed, angular momentum conservation and assumed (C)P invariance impose that also the final fermion-antifermion state has $J^{PC} = 0^{-+}$ quantum numbers and for highly relativistic final states (i.e. light fermions, except eventually $t\bar{t}$) which are relatively light compared to the energy scale of the process, $2\, m_\chi$, the rate is suppressed by a factor $\simeq (m_f/m_\chi)^2$. [iii]

---

[i] We notice that for a Dirac fermion the spin allowed states correspond to $S = 0, 1$, i.e. $|J = 0, M = 0; L = 0, S = 0>$ and $|J = 1, M = 0; L = 0, S = 1>$ in terms of angular momentum quantum numbers.

[ii] The angular momentum quantum numbers of a two-particle state can be expressed by the "term symbol" ${}^{2S+1}L_J$, where L is the orbital angular momentum and the letter S indicates $L = 0$, J is the total angular momentum of the system and S is the spin.

[iii] In the massless fermion limit, $m_f = 0$, the weak interaction V-A coupling determines

Pair produced particles are unstable (except for $e^{\pm}$ pairs) and subsequently decay and fragment in showers (hadronization) mainly through the π^0 decay into two photons. Fluxes of final stable particles are produced. Those processes can be simulated by Monte Carlo event generators as Pythia (Sjöstrand, Mrenna & Skands, 2006) and then interpolated with numerical codes such as DarkSUSY(Gondolo et al., 2004) or fitted via analytical parametrizations (Fornengo, Pieri & Scopel, 2004; Cembranos, de La Cruz-Dombriz, Dobado, Lineros & Maroto, 2011). The spectra of "secondary photons" from two-body final states are slightly channel-dependent, almost featureless since they present a universal soft cutoff at the high-energy limit $E_\gamma \sim m_\chi$ and mildly model-dependent (through the dependence on m_χ). Discriminating such a featureless DM signal over a dominating, poorly controlled background represents a challenge for DM searches.

Additional contributions to the spectrum are expected from higher order corrections to the tree level process. In general their contribution is $\mathcal{O}(\alpha)$ suppressed but they can dominate over the two-body annihilation rate in the case the tree label process results to be suppressed. First order corrections are represented by electromagnetic, electroweak and strong radiative corrections. Whenever charged particles pairs are produced, an additional gauge boson (γ, Z, $W^{\pm}$ or gluon) can be emitted by the initial legs (Initial State Radiation, ISR), by the exchanged particle which mediates the interaction (Virtual Internal Bremsstrhalung, VIB) and by the final legs (Final State Radiation, FSR). We postpone the detailed discussion of radiative corrections to chapter 4 and we here present the general contributions to the γ-ray spectrum originating from leading order corrections. Generically, $\mathcal{O}(\alpha_{\rm em})$, $\mathcal{O}(\alpha_{\rm ew})$, and $\mathcal{O}(\alpha_{\rm s})$ radiative corrections give origin to different final spectra:

- Electromagnetic corrections have been show to give rise to an enhancement of the γ-ray yield at the kinematical endpoint $E_\gamma \sim m_\chi$ (Bringmann, Bergström & Edsjö, 2008). It is a general prediction of many models, that the emission of an additional photon causes the spectrum to show a sharp cutoff at energies of about m_χ. In this respect, FSR gives rise to a rather universal step-like spectrum (Birkedal, Matchev, Perelstein & Spray, 2005) which dominates e.g. the spectrum of KK DM (Bergström, Bringmann, Eriksson & Gustafsson, 2005b), while VIB yield is highly model-dependent and it can produce a pronounced bump-like spectrum which is slightly similar to a distorted line (Bergström, Bringmann, Eriksson & Gustafsson, 2005a; Bringmann et al., 2008).

---

the left chirality for fermion, f_L, and right chirality for antifermion, $\bar{f}_R$. The final state has thus $S = 1$ and it is forbidden for helicity conservation. When fermions are massive, states of total zero spin are possible. Nonetheless, the coupling is still between same chirality spinors (remember that the chirality of antiparticle's spinor is opposite to the chirality of the antiparticle, $\bar{f}$) and the final squared amplitude is proportional to $\simeq (m_f/m_\chi)^2$.

- Electroweak corrections are expected to contribute to the lifting of the helicity suppression and to affect the low-energy tail of the signal (Kachelrieß & Serpico, 2007; Bell, Dent, Jacques & Weiler, 2008; P. Ciafaloni, Comelli et al., 2011). Indeed, emitted weak gauge bosons undergo decay and hadronization processes which would populate the spectrum with low-energy photons.

- Strong corrections originate from DM annihilating into colored fermions. In the case of massless quarks, only t-channel diagrams are present and the cross section in the zero-velocity limit for the $q\bar{q}g$ process coincides with the one for $q\bar{q}\gamma$ after having replaced $Q^2\alpha_{\rm em}$ (Q being the quark charge) by $4/3\alpha_s$ (Asano, Bringmann & Weniger, 2012; Garny, Ibarra & Vogl, 2011).

The most striking spectral feature (i.e. an abrupt change in the spectral energy distribution) comes from the loop-suppressed direct annihilation into γX, where $X = \gamma, Z, H$ (Bergström, Ullio & Buckley, 1998). In this cases the signal is expected to be a monochromatic line centered at $E_\gamma = m_\chi(1 - m_X^2/4m_\chi^2)$. The limited energy resolution of detectors makes the line broaden and represents the most fundamental limitation for line searches. Moreover, this process is usually expected to be subdominant since it is $\mathcal{O}(\alpha_{\rm em}^2)$ suppressed although some models with enhanced line signals have been proposed e.g. (Dudas, Mambrini, Pokorski & Romagnoni, 2009; Gustafsson, Lundström, Bergström & Edsjö, 2007; Arina, Hambye, Ibarra & Weniger, 2010).

Fig. 3.1 displays the different contributions to the γ-ray spectrum and the effect of energy resolution. Spectral features represent a powerful tool to discriminate a DM signal from the dominant, poorly understood background and, in this respect, they are very different from "secondary photons". We will expand such a discussion in the light of DM searches techniques and perspectives in chapter 7.

We finally mention that in models with a high branching ratio into $e^\pm$ pairs a significant γ-ray flux from IC scattering of those particles on starlight and CMB is expected, e.g. (Baltz & Wai, 2004). Although it increases the number of expected photons, IC is highly affected by the uncertainties on propagation parameters and on the distribution of the radiation fields.

3.2 Astrophysical and cosmological Dark Matter distribution

The spatial distribution of the signal depends on the DM density in the target where annihilations take place and traces it directly.

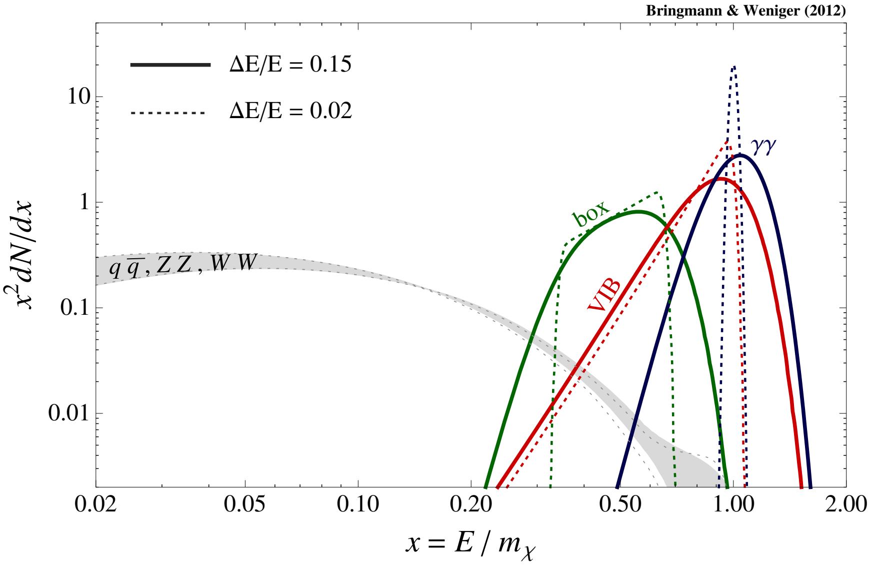

Figure 3.1: γ-ray spectra dN_γ/dx ($x = E_\gamma/m_\chi$) from DM annihilation ($m_\chi =$ 100 GeV), normalized to $N(x \geq 0.1) = 1$. Secondary photons from two-body final states are represented by the grey band. They slightly depend on the annihilation channel. Spectral features are displayed as well together with the smearing due to the energy resolution of the instrument. Figure taken from (Bringmann & Weniger, 2012).

3.2.1 Galactic Dark Matter distribution

The existence of DM halos is a general prediction of ΛCDM (Peebles, 1982). Structures as clusters, galaxies and stars are the result of highly non-linear processes that can be simulated with numerical methods. Numerical collisionless N-body simulations follow the hierarchical structure formation and provide robust predictions for the structural and substructure properties of the DM distribution within virialised halos (Diemand, Moore & Stadel, 2005; Navarro, Frenk & White, 1996; Bullock et al., 2001; Diemand et al., 2008; Springel et al., 2008). N-body simulations suggest the existence of a universal DM profile. Typically, the DM profile is assumed to be spherically symmetric and it is parametrized as follows (Zhao, 1996):

$$\rho(R) = \rho_\odot \left(\frac{r_\odot}{R}\right)^\gamma \left[\frac{1 + (r_\odot/r_s)^\alpha}{1 + (R/r_s)^\alpha}\right]^{(\beta-\gamma)/\alpha} , \qquad (3.3)$$

where $r_\odot \sim 8.5$ kpc is the distance of the Sun from the GC, r_s is the typical scale length of the profile and $\rho_\odot \sim 0.4$ GeV cm^{-3} is the local DM density, which can span the generous range 0.2 - 0.7 GeV cm^{-3} (Salucci, Nesti, Gentile & Frigerio Martins, 2010). The parameters (α, β, γ) define the specific halo profile: $(\alpha, \beta, \gamma) = (1,\ 3,\ 1)$ correspond to the Navarro-Frenk-White (NFW) profile which is divergent for $r \to 0$ (Navarro, Frenk

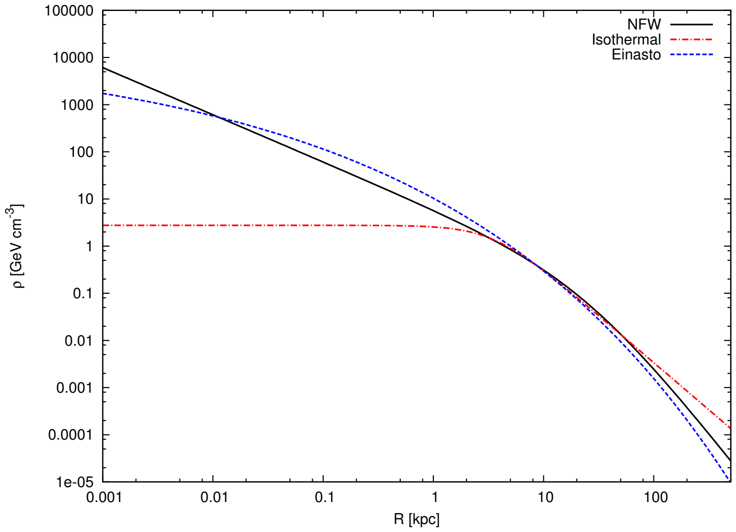

Figure 3.2: DM density distribution in the Milky Way, normalized to $\rho_\odot = 0.4$ GeV cm^{-3} at $r_\odot = 8.5$ kpc. The black solid line refers to a NFW profile with $r_s = 25$ kpc, the red dot-dashed line represent the isothermal profile with $r_s = 3.5$ kpc and the blue dashed curve to an Einasto profile with $r_{-2} = 15$ kpc.

& White, 1996), whereas a cored isothermal profile is given by $(\alpha, \beta, \gamma) = (2,\ 2,\ 0)$. Fig. 5.3 shows the superposition of the different DM halo profiles: important differences arise at small distances from the GC, $R \leq 5$ kpc. A direct consequence is that γ-rays coming from the GC are very sensitive to the inner part of the galaxy where differences among several halo profiles turn out to be relevant. Instead, signals coming from high galactic latitudes are not dependent (or mildly dependent) on the critical behavior of the DM density about the GC.

The most recent simulations indicate that the DM spatial profile is not proportional to any power of the distance from the GC at small radii (Navarro et al., 2004). Indeed, the DM distribution is well described by an Einasto profile (Einasto, 1965) according to which the logarithmic slope of the profile flattens in approaching the GC. In Fig. 5.3, such a non-singular profile is also shown. Its distribution function is in the form:

$$\rho(R) = \rho_{-2} \exp\left\{-\frac{2}{\alpha}\left[\left(\frac{R}{r_{-2}}\right)^{\alpha} - 1\right]\right\}\ , \tag{3.4}$$

where r_{-2} is the radius where the logarithmic slope, $\delta(R) \equiv -d(\ln \rho(R))/d(\ln R) \approx R^{-\alpha}$, is $\delta = -2$, and $\rho_{-2} \equiv \rho(r_{-2})$.

Recently, a new functional form for the fitting function of the density profile has been proposed (Stadel et al., 2009):

$$\rho(R) = \rho_0 \exp\left\{-\lambda \left[\ln\left(1 + R/r_\lambda\right)\right]^2\right\}\ . \tag{3.5}$$

Below r_λ the profile approaches the central maximum density ρ_0 as $R \to 0$ and it shows a linearly varying logarithmic density gradient. In the following, we will refer to this profile as Moore & Stadel profile.

Despite pure DM N-body simulations, kinematic observations of rotation curves of low-surface-brightness spiral galaxies suggest the presence of shallow, or even flat, cores in the innermost part of the galaxies, e.g. (Gentile, Salucci, Klein & Granato, 2007; Salucci & Burkert, 2000; Oh, de Blok, Brinks, Walter & Kennicutt, 2011). Typically, those observations are well fitted by a Burkert profile in the form:

$$\rho(R) = \frac{\rho_0}{(1 + R/r_0)\,(1 + (R/r_0)^2)}\,, \tag{3.6}$$

with ρ_0 the central DM density and r_0 the scale radius. Moreover, these two parameters have been discovered to be nearly constant and independent of galaxy luminosity (Donato, Gentile et al., 2009). Astrophysical observations and N-body numerical simulations are thus in disagreement as soon as the sub-kiloparsec scale of the DM distribution is considered. Nonetheless, for both predictions there are caveats that can somehow alleviate the contradictions between them; astrophysical observations suffer from systematic biases e.g. (Spekkens, Giovanelli & Haynes, 2005; Simon, Bolatto, Leroy, Blitz & Gates, 2005; Valenzuela et al., 2007), whereas N-body simulations are fundamentally limited by the resolution of the simulation and every extrapolation below the simulation resolution has to be used cautiously. This tension between N-body simulations and observations about the inner density DM profile is known as the “cusp/core” problem.

A solution to such an issue is suggested by hydro-dynamical simulations, where the effect of baryonic matter is introduced. Indeed, pure DM N-body simulations make the structures evolve only via gravitational interactions although gas and stars are concentrated in the inner part of galaxies. At small scales baryons can be gravitationally dominant. The effect of baryonic infall and star formation on the DM profile is still an open issue of debate. To a first approximation, the gravitational potential of baryons attracts DM particles during galaxy formation and the dark component increases its central density. Hydro-dynamical simulations predicting such an “adiabatic contraction” (Blumenthal, Faber, Flores & Primack, 1986; Gnedin, Kravtsov, Klypin & Nagai, 2004) fail in reproducing the observed rotation curves because of too centrally concentrated stellar and DM profiles. Thus, opposite mechanisms of expansion of the DM inner profile have to take place (Gnedin, Weinberg, Pizagno, Prada & Rix, 2007; Dutton et al., 2011). An expansion of the DM halo can result from gas bulk motions. For example, supernova-driven winds can expel a large fraction of the baryonic component from a galaxy disk in regions of high star formation activity and the subsequent energy loss of gas clouds transfers energy to the central DM component (Navarro, Eke & Frenk, 1996; Ogiya & Mori, 2011). Moreover, gravitationally induced fluctuations (Mashchenko, Couchman & Wadsley, 2006; Mashchenko, Wadsley & Couchman, 2008) and small starbursts in the centre of the protogalaxy (Pontzen & Governato, 2012) may induce the flattening of the DM profile. Recently, it has been demonstrated that also simulated Milky Way-like galaxies show a cored DM distribution when a reasonable baryonic feedback is considered,(Macciò et al., 2012) and references therein. Finally, also active galactic nuclei (AGN) feedback can contribute in flattening the innermost DM distribution (Martizzi, Teyssier & Moore, 2013). It is worth saying that at present there is neither a clear prescription about the baryonic feedback nor a commonly adopted simulation code.

Given the uncertainties involving observed and simulated halo profiles, a reasonable approach is to consider the DM profile's slope at small radii as a free parameter and discuss the prospects of DM ID for the different models proposed in the literature.

3.2.2 Enhancement factor I: galactic Dark Matter substructures

The latest numerical simulations of Milky Way-sized DM halos, i.e. the *Aquarius* (Springel et al., 2008) and *Via Lactea II* (Diemand & Moore, 2011) numerical simulations, show that the DM distribution of galactic sized halos is composed by two separate components: a smoothly distributed phase, i.e. the main halo, and a clumpy component in the form of virialized substructures, i.e. the subhalos. The CDM scenario indeed predicts the formation of these small virialized structures with a lower mass cutoff ranging roughly $M_{\rm cut} \sim 10^{-11} - 10^{-3}{\rm M}_{\odot}$, depending on the particle physics nature of the DM candidate and on its kinetic decoupling, see e.g. (Green, Hofmann & Schwarz, 2004, 2005; Bringmann, 2009). The presence of subhalos in the galaxy would enhance the expected DM signal due to inhomogeneities along the l.o.s. and lead to a spatial signature much more striking than the one from the smooth halo alone.

The two simulations were able to resolve substructures down to masses $\sim 10^5 M_{\odot}$ and to study the properties of the subhalo distribution. They both find the substructure distribution to be *antibiased* with respect to the smooth distribution, meaning that fewer structures are expected in the innermost region of the galaxy than in the outer part. This result implies the possibility of resolving some substructure at high latitudes that would be discovered as unidentified source with no counterpart in other wavelengths e.g. by *Fermi* (Zechlin, Fernandes, Elsässer & Horns, 2012; Zechlin & Horns, 2012).

The mass resolution constitutes a fundamental limitation for modeling the properties of galactic substructures down to the minimal mass of bounded DM structures, $M_{\rm cut}$, and severe extrapolations of the N-body simulation results are adopted introducing large theoretical uncertainties that we will discuss in details in chapter 5, where we compute the expected spatial signal from the galactic substructure DM distribution.

3.2.3 Enhancement factor II: extragalactic Dark Matter

Halos and subhalos form outside our galaxies at all redshifts (up to the structure formation epoch). Thus, a γ-ray flux arises from DM annihilating at cosmological distances. The contribution to the IGRB can span from 1% up to 100% of the measured flux because of the theoretical uncertainties, e.g. the distribution of halos and subhalos (Bergström, Edsjö & Ullio, 2001; Ullio, Bergström, Edsjö & Lacey, 2002), their concentration and evolution with redshift (Abdo, Ackermann, Ajello, Baldini et al., 2010; Serpico, Sefusatti, Gustafsson & Zaharijas, 2012). Moreover, the spatial signature of extragalactic DM in the IGRB anisotropy has been extensively discussed, e.g. (Ando & Komatsu, 2006), and recent predictions of the DM induced anisotropy signal show that the extragalactic component is generally affected by about two orders of magnitude uncertainty (Fornasa et al., 2013). Therefore, depending on the particular assumptions made in the extrapolation of the unresolved (sub)halo distributions, the extragalactic spectrum might be or not the dominant component of the total energy spectrum and, in the same way, we cannot tell whether the anisotropy signal can receive a significant or a negligible contribution from extragalactic (sub)structures (Fornasa et al., 2013).

3.3 Dark Matter searches through γ-rays

As we already pointed out, γ-rays represent probably the best channel for DM ID. We bring the reader's attention to a nice review about searches through γ-rays (Bringmann & Weniger, 2012), while we here briefly discuss the main searches techniques and their possible outcomes.

DM annihilations give origin to spectral and spatial γ-ray signatures that can highly help in disentangling the DM signal from the astrophysical background and in identifying an eventual DM excess.

Searches are sensitive to both normalization and end-point features of the DM flux. Besides the contribution of "secondary photons", it is crucial that (*i*) we consider radiative corrections to the tree-level process when predicting the expected DM signal (see chapter 4 for the first fully general calculation of leading order electroweak corrections to neutralino annihilation), and (*ii*) we optimize DM searches by including spectral features which can significantly improve the sensitivity of γ-ray telescopes to DM signals (see chapter 7, namely (Bringmann, Calore, Vertongen & Weniger, 2011)). While a convincing claim of DM detection based exclusively on secondary photons is rather demanding and such a kind of signal has for now only constrained the DM parameter space, the dedicated search of pronounced spectral signatures (originating from loop and electromagnetic corrections) has provided some hints of detection as we discuss in Sec. 3.5. Searches of spectral features show a great potential for the discrimination of the signal over the background and they are basically background-free since the background can always be locally approximated by a power-law (Bringmann et al., 2011).

Looking for the spatial signature expected from the DM distribution in the galaxy and in cosmological environments represents a powerful method of detection. Indeed, γ-rays trace the morphology of the DM distribution. Besides the differences in the signal due to the modeling of the inner DM profile of the main halo, the inhomogeneous DM distribution in the Milky Way and in external galaxies as predicted by N-body simulations gives origin to a typical γ-ray APS. Theoretical predictions of the DM γ-ray anisotropy signal is highly uncertain and we will discuss this topic in details in chapter 5. The first anisotropy measurements of the γ-ray sky have been released only very recently by the *Fermi*-LAT Collaboration and are still affected by the poor statistics and systematics effects (Ackermann, Ajello, Albert, Baldini, Ballet et al., 2012). The detectability of DM substructures with current and future experiments is an open issue of debate, e.g. (Ando & Komatsu, 2006, 2013; Fornasa et al., 2013; Ripken, Cuoco, Zechlin, Conrad & Horns, 2012), although such a signature represents a promising way to probe the DM distribution and it carries complementary information to spectral searches.

3.3.1 γ-ray experiments

Typically, a continuum DM signal (depending on the DM mass) is expected to range in the GeV – TeV energy band showing a cutoff at the WIMP mass. Thus, we are interested in high-energy γ-rays (GeV – TeV) while we neglect here the discussion of other wavelengths.

To observe cosmic γ-rays directly, observations must be made from the outer space because in the energy range we are most interested in (GeV to TeV) photons interacting with the atmosphere via $e^{\pm}$ pair production cannot reach ground-based telescopes. Indeed, at GeV energies the photon interaction length of approximately 38 g cm^{-2} is shorter than the thickness of the Earth's atmosphere (1030 g cm^{-2}) (Bertone et al., 2005). Nevertheless, new techniques have been developed in order to observe γ-rays indirectly with ground-based experiments.

Space-based telescopes detect γ-rays by recording the characteristics of $e^{\pm}$ pairs produced in the interaction of the incident γ-ray with the detector. The first high-energy (above GeV) γ-ray space telescope was the Energetic Gamma-Ray Experiment Telescope (EGRET), on board the Compton γ-ray observatory (Sreekumar et al., 1998). Its successor is the LAT on board of the *Fermi*γ-ray space satellite, which has been operating since 2008 unveiling new aspects of the γ-ray sky in the GeV energy band (Atwood et al., 2009).

The LAT is "an imaging, wide field-of-view, high-energy γ-ray telescope, covering the energy range from below 20 MeV to more than 300 GeV" (Atwood et al., 2009), including the previously unexplored energy band 10 – 100 GeV. The limitation of the telescope performances at high energies, due mainly to the limited collection area, makes the complementarity with other experiments crucial in the overlapping energy range.

Ground-based experiments detect photons interacting in the atmosphere and producing an electromagnetic cascade of secondary particles. These instruments are IACTs, observing the Cherenkov light originating from their passage through the Earth's atmosphere and using advanced image reconstruction techniques to characterize primary photons. Current operating experiments are: MAGIC[iv], HESS II[v] and VERITAS[vi]. They are characterized by a good angular resolution for single γ-rays ($\sim 5'$ above 1 TeV), energy resolution of $\sim 15\%$ depending on the energy range, a limited field-of-view ($\sim 5°$) and a relatively poor duty cycle (with about 1000 hours of useful observations obtainable per year) (Bugaev, 2011); those characteristics make them suitable for pointed observations.

Although current IACTs have improved their performances and data quality, they cannot still be competitive with *Fermi*-LAT at low energies and overlap with it. The new generation of IACTs will provide such a complementarity. The planned Cherenkov Telescope Array (CTA) will consist of two Cherenkov arrays, situated in the Northern and Southern hemispheres, and aims to improve the performances of current IACTs (Actis et al., 2011). Namely, an expected sensitivity at the milli-Crab level for 50 hour of observation time at energies of a few TeV (obtained by increasing the effective area) would represent a gain by a factor of 10 compared to currently operating arrays; a lower energy threshold down to about 30 GeV will provide a substantial overlap with *Fermi*-LAT and improve observations currently affected by threshold effects ($\sim$ 100 GeV for HESS); finally, a larger field-of-view ($\sim 8°$) may help in improving the angular resolution and increases the exposure.

For an extensive and interesting discussion about the performances of CTA and *Fermi*-LAT in the overlapping energy range we refer to (Funk & Hinton, 2013).

3.3.2 Promising targets and astrophysical backgrounds

We review here the main astrophysical targets suitable for DM detection, see e.g. (Baltz et al., 2008). We highlight the relevance of the background in each of these targets; the background might be of both astrophysical and instrumental origin (mainly due to the discrimination of γ-rays from

---

[iv] https://www.magic.mppmu.mpg.de

[v] http://www-hfm.mpi-hd.mpg.de/HESS

[vi] http://veritas.sao.arizona.edu

other particle species). We do not discuss the systematics effects due to the different instruments, but we focus on the unavoidable astrophysical background.

- *Galactic Center.* In an ideal background-free galaxy, the region around the GC would represent the most interesting target for DM searches. Indeed, the controversial shape of the inner DM profile predicts fluxes which can span several orders of magnitude and can produce a potentially visible signal. Moreover, a DM signal from the GC would help in solving the "cusp/core" problem giving some insight into the innermost DM distribution. Despite of this great potential and the very good statistics, the GC region is dominated by poorly known backgrounds of standard astrophysical origin. Firstly, the GC lies inside the galactic disk ($|b| \leq 10^{\circ}$) where the uncertainties due to the contamination from the galactic diffuse emission (GDE), i.e. γ-rays originated by the interactions of CRs with gas of the ISM and of the low energy photons with the interstellar radiation field, strongly contaminates the data. Secondly, closely to the GC astrophysical point-like sources have been detected. Notably, the very high energy γ-ray point source observed by the H.E.S.S. (Aharonian et al., 2004, 2009), MAGIC (Albert et al., 2006), VERITAS (Kosack et al., 2004) and CANGAROO (Tsuchiya et al., 2004) collaborations has been identified with either the bright compact radio source Sgr A* or with the pulsar wind nebula G359.95-0.04 (Braun et al., 2008). It has also been noticed (Bringmann & Weniger, 2012) that a possible displacement of the highest DM density point from the dynamical center of the galaxy may be due to the effect of baryons and recent N-body simulations show first hints for such a displacement (Guedes, Callegari, Madau & Mayer, 2011; Kuhlen, Guedes, Pillepich, Madau & Mayer, 2013).

- *Dwarf Spheroidal Galaxies.* They represent excellent target for γ-ray DM detection. They are located outside the galactic disk and thus their emission is not contaminated by the GDE. Dwarf spheroidal galaxies (dSphs) are DM-dominated systems with mass-to-light ratio is $\sim \mathcal{O}(100)$, without active star formation or detected gas content probably because star formation only occurs above some threshold mass and supernovae-driven winds may have expelled baryons from the galaxies (Mateo, 1998; Grcevich & Putman, 2009). The density profile of the DM distribution is reconstructed by measurements of the velocity dispersion of stars in these systems, e.g. (Walker, Combet, Hinton, Maurin & Wilkinson, 2011; Strigari et al., 2008) and, despite of the uncertainties, integrated fluxes are rather robust (Ackermann et al., 2011). For those reasons, dSphs represent an outstanding target to derive robust constraints on DM taking into account that the combined analysis of multiple dwarf galaxies further increases the sensitivity for DM signals.

- *Galaxy Clusters.* Galaxy clusters forming at the present epoch (e.g. Coma and Fornax) have been indicated as good targets for DM detection. They are the most massive virialized objects dominated by DM and they are expected to host a hierarchical structure of subhalos (Colafrancesco, Profumo & Ullio, 2006; Jeltema, Kehayias & Profumo, 2009). Although the signal-to-noise ratio might also exceed the one from dwarfs in some optimistic scenarios (Gao, Frenk, Jenkins, Springel & White, 2012), predictions on DM γ-ray flux are affected by great uncertainties which make the ensuing limits not so robust.

- *Galactic Halo.* A diffuse, almost isotropic, DM emission is expected to come from the whole galactic halo, even at high latitudes. Observing the region above $|b| = 10^\circ$ avoids the main uncertainties due to the GDE and point-like sources (which are mainly concentrated along the galactic disk) and it is less sensible to the inner DM profile. In spite of these advantages, the astrophysical background in this region arises from a superposition of galactic and extragalactic unresolved sources whose fluxes are affected by large uncertainties. Sec. 3.4 will be dedicated to a detailed discussion of the contributions to the IGRB whose determination is fundamental for DM searches.

  We notice that the anti-biased spatial distribution of galactic subhalos implies that observable satellites are located mostly at high galactic latitudes. This implies a potential discovery of DM substructures as point-like sources at high latitudes. Up to know, no DM subhalos have been identified with unasssociated *Fermi*-LAT sources (Zechlin et al., 2012; Zechlin & Horns, 2012).

3.4 The *Fermi*-LAT isotropic γ-ray background

Among other important results of the *Fermi*-LAT, the spectrum of the IGRB at high latitudes was measured (Abdo & al., 2010).

This faint emission was firstly discovered by the SAS-2 satellite (Fichtel et al., 1975), whose results indicated that this residual and apparently isotropic emission was not associated with the galaxy and, thus, it was believed to have an extragalactic origin. This first detection was later confirmed, extended and improved by EGRET (Sreekumar et al., 1998), which measured an isotropic γ-ray emission in the $\simeq 30$ MeV – 100 GeV range, well fitted by a power-law with spectral index $\alpha \simeq 2.1$.

The *Fermi*-LAT measured IGRB shows a high degree of isotropy and its energy spectrum is compatible with a simple power-law with spectral index, $\alpha = 2.41 \pm 0.05$ and integrated intensity I(>100 MeV) = $(1.03 \pm 0.17) \cdot 10^{-5}$

$\mathrm{cm}^{-2}\mathrm{s}^{-1}\mathrm{sr}^{-1}$. It has been obtained by subtracting from data the galactic γ-ray foreground (which represents the main systematic uncertainty in that analysis), the emission from point-like sources detected by the telescope, the background from CRs in the detector and solar photons.

The origin of such a residual component is still unknown, though it is usually considered to arise from the superposition of contributions from (mainly) unresolved point-sources and, to a lesser extent, from astrophysical diffuse processes.

The origin of the IGRB is a delicate issue in astrophysics. Most likely unresolved point-source populations represent the dominant component. Nevertheless, other astrophysical processes contribute to the γ-ray emission. We review here the main classes of γ-ray emission which lead to a guaranteed γ-ray diffuse flux and compete in giving origin to the IGRB.

In general, the contribution to the diffuse emission due to a point-source population is computed as follows:

$$\frac{dN}{dE_\gamma d\Omega} = \frac{1}{4\pi}\int_0^{z_m} \frac{dV_c}{dz}\int_{L_m}^{\infty} \frac{dN}{dV dL}\frac{dN}{dE_\gamma}(z) dL\, dz\,, \tag{3.7}$$

where $\frac{dN}{dE_\gamma}$ is the intrinsic γ-ray flux derived from observations of single sources belonging to the same class, z is the redshift, $\frac{dV_c}{dz}$ is the cosmological volume element, L_m is the total luminosity of the weakest source and the luminosity function $\frac{dN}{dVdL}$ is the number of sources per unit of comoving volume and luminosity. The latter quantity is called γ-ray luminosity function and it is built either from data, if the statistics is high enough, or by correlating the γ-ray emission to other wavelengths.

Active Galactic Nuclei. A nucleus of a galaxy strongly shining from the radio to the γ-ray waveband is called AGN. General models of AGN structure (Urry & Padovani, 1995) concentrate on the possibility of a supermassive black hole lying at the center of the object and accreting matter onto an accretion disk, which brightly emits in ultraviolet and eventually in soft X-rays wavelengths. Around it, “broad-line clouds” (clouds of high temperature gas close to the black hole) emit lines in optical and UV, however this radiation may be obscured from transverse l.o.s. by a torus or warped disk. A large amount of gravitational energy is released and flows away through powerful collimated radio-emitting jets, i.e. streams of particles coming from the central source beamed relativistically in the forward direction. Part of the energy in this hot plasma is emitted as X-rays and γ-rays.

The observed properties and spectral characteristics of AGN lead to an empirical classification. We follow the taxonomy in (Urry & Padovani, 1995). Firstly, AGN can be classified depending on their radio loudness (radio to optical flux ratio) in radio-quiet (e.g. Seyfert low luminosity galaxies and QSO quasars) and radio-loud (e.g. Fanaroff-Riley radio galaxies and blazars). About 15% – 20% of AGN are radio-loud. Secondly, the optical spectra (namely the presence/absence and width of line emission) determine the AGN's type (1, 2 or 0) depending on the obscuration of the nucleus.

Since the intrinsic spectra of radio-quiet AGN cut off around 100 keV, these objects are not expected to be important contributors to the γ-ray IGRB. In the following we thus focus on radio-loud AGN. As mentioned before, radio-loud AGN can be classified according to their optical properties. Radio-loud Type 1 AGN are called Broad-Line Radio Galaxies (BLRG) at low luminosities and either Steep Spectrum Radio Quasars (SSRQ) or Flat Spectrum Radio Quasars (FSRQ) at high luminosities (depending on radio continuum shape). AGN with weak continua or only narrow emission lines are of Type 2, the radio-loud population is referred to as Narrow-Line Radio Galaxies (NLRG). This class includes two distinct morphological types: Fanaroff-Riley type I (FRI) (low luminosity galaxies with often symmetric radio-jets) and Fanaroff-Riley type II (FRII) (high luminosity galaxies with well defined lobes and prominent hot spots) radio galaxies (Fanaroff & Riley, 1974). Finally, radio-loud AGN with no line emission include BL Lacertae (BL Lac) objects.

Among the classes above, BL Lac objects and FSRQ are characterized by strong and variable optical polarization, superluminal motion of radio cores and significant time variability at most wavelengths. BL Lac objects and FSRQ are called blazars.

Because of their anisotropic emission (by either relativistic beaming or obscuration), radio-loud AGN observations depend strongly on their orientation with respect to the observer. This complex zoology has been interpreted within the so called Unified Scheme for Radio-Loud AGN (Urry & Padovani, 1995). AGN are classified as radio galaxies (FRI and FRII) or blazars (BL Lac objects and FSRQ) according to the orientation of the jet-emission with respect to the l.o.s.: blazars jets are oriented along the l.o.s., whereas objects with an emission at angles larger than 14° are dubbed as "non-blazars" (Barthel, 1989). In this respect, mis-aligned AGN (MAGN) must constitute the so called "parent population" of AGN. MAGN have weaker luminosities but are expected to be more numerous by a factor 2 Γ_L^2 (where Γ_L is the Lorentz factor) (Urry & Padovani, 1995).

Blazars are the most luminous radio-loud AGN because of relativistic Doppler boosting effects of the collimated jets pointing along the l.o.s..

Their spectral energy distribution consists typically of two broad bumps: a low energy component is commonly believed to arise from the synchrotron emission of ultra-relativistic particles confined in the jets by magnetic fields, while a high energy component would result from IC emission on various underlying radiation fields (i.e. synchrotron photons produced by the same population of relativistic electrons in the case of synchrotron self-Compton models (T. W. Jones, O'dell & Stein, 1974; Ghisellini & Maraschi, 1989) or UV photons generated by the accretion disk surrounding the black hole in the case of external radiation Compton (Sikora, Begelman & Rees, 1994; Dermer & Schlickeiser, 2002). Typically the external Compton (EC) and synchrotron self-Compton (SSC) scenarios require that the IC γ-rays originate relatively close to the centre, within the central parsecs. A detailed analysis of the spectral energy distribution of the *Fermi*-LAT detected blazars as been reported (Abdo, Ackermann, Agudo et al., 2010).

Observations of the *Fermi*-LAT (Abdo, Ackermann, Ajello, Allafort et al., 2010; Nolan et al., 2012) indicate that blazars constitute the class of γ-ray emitters with the largest number of identified members. Therefore, unresolved blazars are expected to give a sizable contribution to the IGRB, as pointed out already after EGRET results (Sreekumar et al., 1998). Studies of the spectral and statistical properties of the resolved *Fermi*-LAT blazars show that their unresolved counterpart is a sizable component, able to explain up to 20% − 30% of the IGRB (Abdo, Ackermann, Ajello, Antolini et al., 2010). The two blazars classes FSRQ and BL Lacs objects are found to follow a power-law spectrum with a softer ($\alpha_{FSRQ} = 2.45 \pm 0.03$) and harder ($\alpha_{BLLacs} = 2.23 \pm 0.03$) spectral index respectively. We notice that this estimate does not take into account the extragalactic background light absorption, which is important starting from about 100 GeV and depletes the flux due to cascade emission at lower energies. We notice that the result is also affected by the spectral energy distribution of the sources. Indeed, by using a new determination of the spectral energy distribution and luminosity function FSRQs contribution to the diffuse γ-ray flux has been re-evaluated and found to not follow a power-law anymore (Ajello et al., 2012). The predicted flux represents no more than 10% of the IGRB in the 0.1 − 100 GeV and becomes negligible for E $\sim$ 20 GeV.

Mis-aligned AGN. Radio-loud AGN with jets pointing at larger or intermediate angles, $\sim 15° - 40°$ (Urry & Padovani, 1995) are usually referred to as mis-aligned AGN (or mis-pointed). This class includes radio galaxies, mis-aligned non-thermal dominated AGN with no broad emission lines and large emission angles, and SSRQ, mis-aligned non-thermal dominated AGN with broad emission lines (Abdo, Ackermann, Agudo et al., 2010). The presence/absence of broad emission lines is though to be due to the jet orientation angle: the larger the angle is, the more hidden the emission lines are by the torus.

Fanaroff and Riley (Fanaroff & Riley, 1974) classified radio galaxies in two categories according to the different radio morphology: FRI are preferentially present in rich clusters and located in weak-line galaxies, they have a low radio luminosity and show a two-sided jets dominated emission; FR II are instead found in isolated galaxies or in poor galaxy clusters and hosted by strong emission-line galaxies, their high luminosity radio emission is concentrated in the extended region of the lobes and shows one-sided jets with prominent hot spots. A prescription to discriminate FR galaxies in terms of their multi-wavelength properties is given in (Ledlow & Owen, 1996). This consists in finding a correlation between radio and optical emission, which implies that in a luminous galaxy more radio power is needed for FRII radio sources with respect to FRI and may indicate that the environment plays a crucial role in determining the source structure.

As for blazars, the spectral energy distribution of radio galaxies shows two peaks associated with synchrotron emission (at low energies) and with IC processes (at higher energies). In general, IC photons range from X- to γ-rays, up to the TeV range. The origin of the seed photons is today unclear and is thought to be driven by the same mechanisms producing γ-rays in blazars: SSC or EC radiation. The debate about the origin of the γ-ray emission is today still open, whereas the radio emission is typically attributed to synchrotron emission of highly relativistic electrons moving in a compact blob down the jet.

Being radio galaxies the "parent population" of blazars, they could contribute significantly to the IGRB. Indeed, although they are less luminous given the lack of beaming effects, their expected number in the entire sky is higher than for blazars. Differently from blazars, the sample of detected MAGN in γ-rays is too little to allow a statistical estimate of the γ-ray luminosity function which is required for computing the diffuse flux. Nevertheless, a phenomenological approach can be followed. As it has been suggested formerly for blazars, a correlation between radio and γ-ray luminosity would provide a tool for computing the contribution to the IGRB of the unresolved counterpart of radio galaxies. We will discuss the meaning and powerfulness of the radio-γ correlation and its implications for the IGRB in chapter 6.

Normal and Starburst Forming Galaxies. Star forming (SF) galaxies are an additional class of sources that may significantly contribute to the IGRB as they are abundant in the universe and are known to emit at all observable γ-ray energies. Though their number density is larger than the blazars one, SF galaxies are more difficult to detect in γ-rays because of their less intense luminosities. Thus, a reliable estimate of the contribution of SF galaxies to the IGRB relies in the determination of the γ-ray luminosity function, describing the evolution of their space density and luminosity with cosmic epoch.

Different emission processes make SF shine in several wavelengths. Notably, the thermal emission of the interstellar dust in the infrared band (IR) is thought to be correlated with the SF rate (SFR). Moreover, the CR population of electrons and positrons present in SF galaxies produces photons through synchrotron emission and thermal bremsstrahlung in the radio continuum band (the latter being subdominant), whereas scattering of CRs off gas (bremsstrahlung) or off interstellar radiation field (inverse Compton scattering) lead to a diffuse γ-ray emission closely correlated with the radio flux since it originates from the same electrons/positrons population. Finally, the hadronic interaction of CRs protons with ambient gas nuclei produces γ-ray from the decay of the produced π^0 and from the secondary CR leptons originating from the decay of charged pions.

Starburst and luminous infrared galaxies (LIG) constitute a class of high luminosity SF galaxies due to the intense SF activity (a factor of ten higher than in the Milky Way). They are often identified by their high IR luminosities.

Several authors claim, since the EGRET era, that SF galaxies can compete with blazars in originating the IGRB, (Pavlidou & Fields, 2002; Thompson, Quataert & Waxman, 2007; Fields, Pavlidou & Prodanović, 2010; Makiya, Totani & Kobayashi, 2011; Stecker & Venters, 2011). Notably, the maximum contribution of SF galaxies has been shown to range between $63\% - 19\%$ of the IGRB, depending on the evolution of SF galaxies over cosmic time (Fields et al., 2010). The cumulative γ-ray emission from starburst galaxies was estimated modeling the interactions of CR protons with interstellar medium in starburst galaxies and it was found that starbursts may account for a significant fraction of the IGRB ($\leq 20\%$) (Thompson et al., 2007) .

Recently, the flux emitted by galaxies in formation has been computed (Ackermann, Ajello, Allafort et al., 2012). Based on three-year *Fermi*-LAT data, a sample of 64 SF galaxies beyond the Local Group was analyzed and four objects were detected: two typical star-burst galaxies (M82 and NGC 253) and two hosting Syfert 2 nuclei (NGC 1068, NGC 4945) (Ackermann, Ajello, Allafort et al., 2012). None of the remaining 60 candidate sources showed an excess above the background. By following the approach outlined in (Stecker & Venters, 2011), the contribution of SF galaxies to the IGRB was evaluated by exploiting the correlation between IR, radio and γ-ray luminosities. The correlations of the sample between luminosities in γ-ray and IR $8 - 1000\,\mu$m, and γ-ray and radio 1.4 GHz were found to be robust and revealed a connection between γ-ray luminosity and the SFR. The γ-ray luminosity function was indeed computed starting from the IR luminosity function of (Rodighiero et al., 2010) which describes the evolution in redshift of the density of SF galaxies within different luminosity classes. In order to compute the diffuse flux, the differential photon flux of an individual galaxy has to be modeled. Due to the lack of statistics, the γ-ray average spectral properties of SF galaxies are difficult to firmly establish. Therefore, differences in the spectra of quiescent and star-burst galaxies are expected to be present and the expected contribution from multiple-type SF galaxies is reproduced by assuming two possible γ-ray spectra (Ackermann, Ajello, Allafort et al., 2012). The first one refers to Milky Way-like SF galaxies (model MW), the second one assumes a power-law spectrum in accordance to the properties of the *Fermi*-LAT detected star-burst galaxies (model PL).

The predictions differ in particular above 5 GeV, where the MW model gets significantly softer. At 100 GeV the PL model over predicts the MW one by one order of magnitude. The estimate spans $4\% - 23\%$ of the IGRB intensity above 100 MeV.

Milli-second Pulsars. A further interesting class of high-energy γ-ray sources at high latitude is represented by MSPs. The population of MSPs is thought to be originated by the recycling process in binaries (Bhattacharya & van den Heuvel, 1991) or from accretion-induced collapse of white dwarfs in a binary (Du, Xu, Qiao & Han, 2009). They are old neutron stars with low magnetic field and short spin period ($\simeq 20$ ms).

Since the first observation of an emitting MSP in 1982 (Backer, Kulkarni, Heiles, Davis & Goss, 1982), the mechanisms of high-energy pulsed and unpulsed emission have been investigated. Presently, two competing γ-ray emission models are at stake: the polar cap (Daugherty & Harding, 1994) and outer gap model (K. S. Cheng, Ho & Ruderman, 1986). They primarily differentiate by the location of the acceleration of charges in the magnetosphere. In these objects primary and secondary electrons are accelerated and then experience cooling via curvature and synchrotron radiation, which are the processes participating in the γ-ray emission. The ensuing spectral distribution results in: (*i*) a curvature radiation of primary electrons which dominates from few GeV up to 100 GeV, (*ii*) a synchrotron radiation from primary and secondary electrons dominating up to about 100 MeV, and (*iii*) a weaker IC radiation from primary electrons which peaks at 1 TeV (Harding, Usov & Muslimov, 2005; Bulik, Rudak & Dyks, 2000; Du, Qiao & Chen, 2013).

As a result of their short periods, typical MSPs may be brighter in the γ-rays and much older than ordinary pulsars (Faucher-Giguère & Loeb, 2010). While young, energetic ordinary pulsars are concentrated close to the galactic plane, MSPs are expected to be more prevalent at high latitudes since their ages generally exceed the oscillation time across the galactic disk by a large factor. Thus, a non-negligible contribution of such a population to the IGRB at high latitudes is expected. One of the first estimates of the contribution to the diffuse γ-ray background of the Milky Way due to MSPs dates back to 1991 (Bhattacharya & Srinivasan, 1991). As far as also the pulsar population is concerned, (Harding & Stecker, 1981) used a calculation of the pulsar γ-ray emission spectrum together with a statistical analysis of data on 328 known radio pulsars to determine of the pulsar contribution to galactic γ-ray emission. They also re-examined the contributions from diffuse interstellar CRs induced production mechanisms to the total emission and conclude that pulsars may account for a significant fraction of galactic γ-ray emission ($\simeq 15 - 20\%$). Recently, (Faucher-Giguère & Loeb, 2010) illustrated the potential contribution of pulsars and MSPs to the γ-ray background. The contribution to IGRB at high latitudes (based on EGRET data) turns out to be a relatively small fraction, $\simeq 10^{-3}$ for ordinary pulsars, whereas MSPs could contribute a significant fraction of the measured high-latitude intensity ($\simeq 5\% - 15\%$) since, as a result of their short periods, a typical MSP may be brighter in the γ-rays than a typical ordinary pulsar.

It is important to notice the dramatic increase in the number of known γ-ray MSPs: after the first eight-month of data taking, eight γ-ray MSPs were detected (Abdo, Ackermann, Ajello, Atwood, Axelsson et al., 2009b); presently, more than 40 MSPs have been discovered (Guillemot et al., 2012) and their number is going to increase with future observations. Such a discovery offers the opportunity to study the population of these high-energy objects and allows for more detailed predictions of their contribution to the IGRB. For a study of the *Fermi*-LAT detected MSPs population we refer to (Grégoire & Knödlseder, 2013).

Other Source Populations and Truly Diffuse Processes. We list here other γ-ray sources which can lead to a diffuse γ-ray emission, though their contribution has not been found to be as important as the classes of sources quoted above.

- Clusters of galaxies are self-gravitating systems of mass $\simeq 10^{15}$ $M_{\odot}$ and size of few Mpc^3. Their are made of DM ($\simeq 80\%$, on average), hot diffuse intra-cluster plasma ($\leq 20\%$) which is revealed observationally through thermal bremsstrahlung emission in the X-ray band, and a small fraction of stars, dust, and cold gas, mostly caught in galaxies, (Diaferio, Schindler & Dolag, 2008). High-energy γ-rays can be produced in these objects mainly from (*i*) interaction of CR protons with the gas of the cluster and subsequent production/decay of neutral pions and (*ii*) up-scattering of CMB photons to γ-ray energies, through IC scattering of high energy electrons (Blasi, Gabici & Brunetti, 2007; Waxman & Loeb, 2000). As discussed in (Blasi et al., 2007), the contribution from clusters of galaxies could yield about $1\% - 10\%$ of the EGRET γ-ray diffuse emission. Although a detection of extended cluster emission at GeV energies is yet to be made (Ackermann et al., 2010b), point-like emission from two bright clusters of galaxies, NGC 1275 and M 87 in the Perseus and Virgo clusters respectively (Abdo, Ackermann, Ajello, Asano et al., 2009; Abdo, Ackermann, Ajello, Atwood, Baldini et al., 2009), is seen and there is considerable potential for improving our understanding of this class of objects using future GeV data.

- γ-ray bursts are short and powerful stellar explosions which probably represent the most energetic events in the universe. They generally have large redshift and occurred in an epoch of active star formation. An estimate for the contribution of the γ-ray bursts emission to the GeV extragalactic diffuse γ-ray flux (EGRET data) is given in (Casanova, Dingus & Zhang, 2007). By modeling the emission from γ-ray bursts as due to a low energy synchrotron spectrum and a higher energy IC scattering spectrum, the resulting γ-ray diffuse background is only a small fraction of what is observed. Analogously, (Ando, Nakar & Sari, 2008) shows that γ-ray bursts can contribute at least 0.01% and most likely 0.1% to the EGRET measured diffuse flux.

Besides unresolved point sources, truly diffuse processes participate in originating the γ-ray background. Among diffuse processes arising from extended sources we find:

- Emission produced by interactions of primary ultra high energy CRs with relic photons (Berezinsky, Gazizov, Kachelrieß & Ostapchenko, 2011; Kalashev, Semikoz & Sigl, 2009). Photons and positrons from $p+\gamma_{CMB} \to p+e^{+}+e^{-}$ pair-production start electromagnetic cascades on CMB and infrared photons, dumping all the energy injected into cascade particles below the pair-production threshold at $\simeq$ 100 GeV. This mechanism leads to a background of diffuse isotropic γ radiation typically extending up to the GeV – TeV band. The estimated contribution to the IGRB spans from few percents up to 50% and it starts to be competitive with other emission processes at energies about 100 GeV (Calore et al., 2012).

- Possible signature of large scale structure formation. Highly relativistic electrons, produced during cluster mergers and large scale structure formation as a consequence of gravitationally induced shock waves, up-scatter CMB photons to GeV energies. A contribution to the γ-ray background is produced in filaments, sheets, and extended γ-ray halos associated with massive cluster (Keshet, Waxman, Loeb, Springel & Hernquist, 2003). Analogously, (Gabici & Blasi, 2003) finds that CRs of cosmological origin can account for about 10% of the γ-ray background.

- γ-ray emission from CRs interacting in populations of small solar system bodies (Moskalenko & Porter, 2009; Moskalenko, Porter & Digel, 2006).

3.5 Current results

We conclude the chapter by presenting an overview of the most recent findings and limits on DM through γ-rays and commenting on future perspectives of this research domain.

The measure of the total number of photons above the detector threshold is typically used to constrain the DM parameter space, namely the annihilation rate $\langle \sigma_{\rm ann} v \rangle$ as a function of the DM mass. In placing limits on DM, the prompt γ-ray component is usually assumed to originate from DM annihilating into a fixed channel (typically $b\bar{b}$) with 100% branching ratio in order to be rather model-independent. Moreover, the expected γ-ray flux can be computed by including also IC scattering from DM produced $e^{\pm}$. This inclusion results in a larger DM flux and in stronger upper bounds, although the DM flux in this case is affected by more uncertainties than the prompt flux. Strongest constraints can then be derived if the distribution of substructures in the galaxy and extragalactic DM are added to the total DM flux. Even in this case, an improvement of limits results in a larger uncertainty, i.e. in less robust bounds.

Different selected targets as well as different background estimation techniques make constraints less easily comparable. Therefore, comparisons among limits in the literature have to be made cautiously. Presently, the strongest constraints on $\langle \sigma_{\rm ann} v \rangle$ for high WIMP masses ($\sim$ 1 TeV) come from the GC observation with the HESS telescope (Abramowski et al., 2011), whereas masses $10 - 500$ GeV are severely constrained by observations of nearby dwarf galaxies with *Fermi* (Abdo, Ackermann, Ajello, Atwood et al., 2010; Ackermann et al., 2011; Geringer-Sameth & Koushiappas, 2011; Mazziotta, Loparco, de Palma & Giglietto, 2012). We notice that by modifying the DM distribution inside the dwarf galaxy (J. Han et al., 2012) limits can be less stringent and comparable to those coming from the GC (Hooper & Linden, 2011; Hooper, Kelso & Queiroz, 2012) and globular clusters (L. Feng, Yuan, Yin, Bi & Li, 2012) observed by *Fermi*. DM can be constrained also by looking at galaxy clusters (Huang, Vertongen & Weniger, 2012; Zimmer, Conrad, for the Fermi-LAT Collaboration & Pinzke, 2011) and external galaxies (Lavalle et al., 2006). Finally, the IGRB has been shown to lead to competitive bounds that can be even stronger when a detailed, yet conservative, modeling of the astrophysical background is considered, see chapter 7 and (Abdo, Ackermann, Ajello, Baldini et al., 2010; Ackermann, Ajello, Albert, Baldini, Ballet et al., 2012; Calore et al., 2012; Bringmann, Calore, Di Mauro & Donato, 2013).

With *Fermi* it is possible to look for γ-ray anisotropies in the IGRB. The *Fermi*-LAT indeed already reported the detection of some angular power above the noise level in the multipole range $\ell \sim 155 - 504$ with a significance ranging from 7.2σ between 2 and 5 GeV to 2.7σ between 10 and 50 GeV, which is consistent with a constant value within each energy bin (Ackermann, Ajello, Albert, Baldini, Ballet et al., 2012). Possible contributors to the IGRB anisotropy are well established astrophysical sources: blazars (Ando, Komatsu, Narumoto & Totani, 2007; Miniati, Koushiappas & Di Matteo, 2007), SF galaxies (Ando & Pavlidou, 2009), and MSPs (Siegal-Gaskins, Reesman, Pavlidou, Profumo & Walker, 2011) as well as annihilating or decaying DM in galactic subhalos (Siegal-Gaskins, 2008; Ando, 2009) and extragalactic structures (Lee, Ando & Kamionkowski, 2009; Ando et al., 2007). Predictions of the APS[vii] in the range $\ell \sim 100 - 500$ for those source classes, but DM, are consistent with the Poisson noise term which describes the anisotropy from an unclustered population of point sources and is almost constant in multipole. The APS of DM annihilation or decay is instead predicted to be smooth and relatively featureless, with the angular power generally falling off more quickly with multipole than Poisson angular power (Ando et al., 2007; Ando, 2009). Shape and amplitude of the predicted anisotropy vary among source classes and identifying the various contributions represents the main challenge for such a kind of search that should be complemented by spectral analysis (Hensley, Siegal-Gaskins & Pavlidou, 2010). So far, the energy independence of the anisotropy signal indicates that it might originate from one or more unclustered populations of point sources and strong constraints have been placed on DM models and their small-scale distribution in the galaxy, e.g. (Fornasa et al., 2013; Ando & Komatsu, 2013).

The non-detection of γ-ray lines by *Fermi* when looking at GC (Ackermann, Ajello, Albert, Baldini, Barbiellini et al., 2012), dSphs (Geringer-Sameth & Koushiappas, 2012), and galaxy clusters (Huang, Yuan, Yin, Bi & Chen, 2012) places limits on DM annihilation into two photons far from WIMP expectations and starts to constrain some model predicting strong line signals. Nevertheless, there have been recently some hints for a detection of a line-like signal from the GC region in the *Fermi* data which are highly debated and not yet definitive. *Fermi*-LAT data from the GC region have unveiled the feature of a narrow line close to 130 GeV (Bringmann, Huang, Ibarra, Vogl & Weniger, 2012; Weniger, 2012; Tempel, Hektor & Raidal, 2012; Finkbeiner, Su & Weniger, 2013), with an angular distribution consistent with WIMP DM and a statistical significance of at least 3σ after trials factor correction and more than 5σ when taking into account both spectral and spatial information of the incoming events (Finkbeiner et al., 2013). A corresponding analysis of the *Fermi*-LAT Collaboration shows less optimistic perspectives although the analysis is performed for different target regions (Bloom et al., 2013; Fermi-LAT Collaboration, 2013). Interpreted in terms of DM, the signal is compatible with both a VIB signal (with mass $m_\chi \sim 149$ GeV) and a line-like signal ($m_\chi \sim 130$ GeV) with an annihilation cross section into photons larger than typically expected for thermally produced DM. So far, neither realistic alternative astrophysical explanation (Aharonian, Khangulyan & Malyshev, 2012) nor compelling instrumental and systematic effects (Finkbeiner et al., 2013; Whiteson, 2012) have been proposed as viable solutions. A larger exposure is required to clarify the na-

---

[vii] We refer the reader to chapter 5 for a better introduction and discussion about this topic.

ture of this potential signal and its statistical robustness; with the proposed new observation strategy for *Fermi* this could be achievable until the end of 2014 (Weniger, Su, Finkbeiner, Bringmann & Mirabal, 2013; Weniger et al., 2013).

Current experiments will keep taking data, improving the collected statistics and performances (as e.g. the new phase of HESS, the HESS II telescope). In the next decade, *Fermi*-LAT dSphs limits are expected to improve by a factor up to ten, allowing to constrain DM masses of $\sim$ 600 GeV (for $b\bar{b}$ annihilation channel). With the upcoming generation of ground-based telescopes, i.e. CTA (Doro et al., 2013), GC limits will go down by about an order of magnitude. Moreover, future space telescopes, e.g. GAMMA-400 (Galper et al., 2013), will strengthen limits e.g. from dSphs in the background limited low energy regime because of the better angular and energy resolution but a smaller effective area compared to *Fermi*. All this searches are (and will be) highly complementary to techniques exploiting also other messengers, as for example IceCube and AMS-02. Finally, we notice that γ-ray searches for DM signal will inevitably face a fundamental reach due to irreducible systematics effects but this limit is far from being achieved and still impressive improvements are possible, see (Bringmann & Weniger, 2012) for some estimates on limits from dSphs and on γ-ray lines.

Chapter 4

Particle physics content: the role of radiative corrections

In chapter 3 we have shown that the DM expected flux depends both on the DM astrophysical distribution in the specific target and on the predicted spectrum of final stable particles. Therefore, modeling the DM signal is a fundamental ingredient for ID strategies.

In this chapter we present the first fully general calculation of leading electroweak corrections to the annihilation rate of supersymmetric neutralino DM due to the unavoidable emission of a gauge boson (γ, Z or $W^{\pm}$) occurring whenever DM annihilates into two-body final state. Although also the emission of colored gauge bosons (gluons) is expected as an $\mathcal{O}(\alpha_s)$ correction to the tree-level process, such a calculation is beyond the scope of the present work and we will mention it very briefly. After an introductory section, Sec. 4.1, about the importance of radiative corrections for DM annihilation and the current state of the literature, we discuss the method followed for computing the squared matrix, the spectra of final state particles, cross sections and the spectra of final stable particles, notably of photons (Sec. 4.2). The most of the technical details can be found in the accompanying Appendices A – D. Finally, results and conclusions are extensively discussed in Sec. 4.3. Every calculation is performed within the framework of neutralino DM annihilating into fermion-antifermion pairs and one gauge boson. The concrete particle physics model is the MSSM, which we dedicate Appendix E to. The content of this chapter is based on (Bringmann & Calore, 2013).

4.1 The importance of radiative corrections

The strength of the interaction of DM particles is expressed by the annihilation cross section averaged over the velocity distribution of DM particles, $\langle \sigma_{\rm ann} v \rangle$. In Sec. 3.1, we have explained that DM annihilation today experiences, at tree-level, two suppressions: the velocity and the helicity suppressions which reduce the interaction rate and the hope to be sensitive to DM indirect signals. The small velocity of DM particles today ($v \simeq 10^{-3}c$) makes all the partial wave contributions to the annihilation rate but the s-wave suppressed. Moreover, since Majorana pairs annihilating in the zero velocity limit act as a pseudo-scalar particle $J^{PC} = 0^{-+}$ decaying at rest with energy in the center of mass system equal to twice of the mass of the DM candidate, the annihilation into relativistic fermion-antifermion final states is helicity suppressed because of angular momentum conservation and assumed (C)P invariance.

In this regard, an important role is played by the unavoidable quantum corrections to the tree-level process, namely by radiative corrections due to the emission of an additional gauge boson. Indeed, the annihilation into charged particles is always accompanied by the emission of γ, Z or $W^{\pm}$ and colored gauge bosons. Higher order corrections to the tree-level annihilation process are generically suppressed by a factor $\alpha/\pi \simeq 10^{-3}$. Nevertheless, they may dominate the annihilation rate in the cases in which the two-body process is suppressed (as it is for light fermion-antifermion pairs), by lifting the helicity suppression.

Physically, the radiative $2 \to 3$ process is unsuppressed because the additional particle carries away a unit of angular momentum, so that the mismatch between the allowed two-particle spin state of the fermion-antifermion pair and their chirality is no longer present.

The phenomenological effects of the emission of a photon (i.e. of electromagnetic (EM) bremsstrahlung) have been longer explored in the literature, e.g. (Bergström, 1989; Flores, Olive & Rudaz, 1989; Baltz & Bergström, 2003; Bergström et al., 2008; Bringmann et al., 2008). Notably, the photon radiated either from the final legs (FSR) or from the virtual charged particles (VIB) could strongly enhance the photon yield and lead to spectral features at the high-energy end of the spectrum.

It has been shown that FSR is dominated by infrared and collinear singularities in the propagator of the virtual (i.e. $q^2 \to m_f^2$) final state particles. The corresponding spectrum shows a universal logarithmic enhancement and it can be parametrized in an almost model-independent way (Birkedal et al., 2005; Bergström et al., 2005b). Collinear singularities in QED occur when photons are emitted in the forward direction (i.e. at small angles) from relativistic particles, e.g. fermions. In this case, the radiative correction is enhanced by a logarithmic factor but is naturally regularized by the mass of the emitting particle. In this regime, it is possible to factorize the long-distance sub-process of the photon emission and the short-distance sub-process via the so called Weizäcker-Williams equivalent photon approximation. The differential cross section for the process $\chi\chi \to X\bar{X}\gamma$, where

$X, \bar{X}$ is a pair of relativistic charged particles, is dominated at high energies by the photons that are approximately collinear with either X or $\bar{X}$. The cross section is factorized in terms of the tree-level process, $\sigma_{\chi\chi\to X\bar{X}}$, times a universal collinear factor:

$$\frac{d\sigma_{\chi\chi\to X\bar{X}\gamma}}{dx} \simeq \frac{\alpha_{\rm em}Q_X^2}{\pi} F_X(x) \ln\left(\frac{s(1-x)}{m_X^2}\right) \sigma_{\chi\chi\to X\bar{X}} \,, \tag{4.1}$$

where $x = 2E_\gamma/\sqrt{s}$, Q_X is the electric charge of the particle X, $F_X(x)$ is a splitting function which depends on the spin of X (f stays for fermion and s for scalar), e.g. :

$$F_f(x) = \frac{1+(1-x)^2}{x}\,, \qquad F_s(x) = \frac{1-x}{x}\,. \tag{4.2}$$

The logarithm of Eq. 4.1 enhances the three-body cross section in the limit of $x \to 1$, i.e. high photon energies.

Such a purely kinematic effect can dominate the high-energy end of total photon yield e.g. in the case of KK DM (Bergström et al., 2005b). It is worth noticing that FSR is not expected to lift the helicity suppression since the symmetry of the two- and three-body process is the same given the fact that the virtual final state particles are almost on mass-shell.

On the other hand, VIB, although being highly model-dependent, is efficient in lifting the helicity suppression and can lead to even more important contribution to the spectrum than FSR (Bringmann et al., 2008). VIB is expected to be dominant in the case of (i) annihilation into fermions when the t-channel exchanged sfermions are degenerate in mass with the neutralino and (ii) di-boson final state for heavy neutralinos (i.e. bosons are light compared to m_χ) when the annihilation is dominated by t-channel diagrams with t-channel exchanged particles degenerate in mass with the neutralino (Bergström et al., 2005a). In this case, it is possible to understand the enhancement of the annihilation rate by looking at the t-channel propagator. For non-relativistic DM incoming particles, it writes as:

$$D_t(q) \propto ((p_1-k_i)^2 - m_{\tilde{X}}^2)^{-1} \simeq (m_\chi^2 + m_i^2 - m_{\tilde{X}}^2 - 2m_\chi E_i)^{-1}\,,\ \mathrm{i} = 1,\, 2 \tag{4.3}$$

where $\tilde{X}$ is the t-channel exchanged particle, p_1 and k_i the momenta of the incoming and outgoing particles respectively. When $\tilde{X}$ and the DM particle are degenerate in mass, the rate is enhanced at small E_i, namely at high E_γ. The lifting of the helicity suppression happens at order $\mathrm{O}((m_\chi^2/m_{\tilde{X}}^2)^4)$ at the cross section level (due to the presence of two $\tilde{X}$ propagators for VIB diagrams).

In the case of EM bremsstrahlung the lifting of the helicity suppression translates in an enhancement of the annihilation rate and thus of the total photon yield notably at high energies (observationally most interesting) where the typically expected spectra show sharp features distinguished from the featureless two-body energy distribution.

While the most striking spectral signatures are expected from EM corrections, electroweak (EW) bremsstrahlung (i.e. emission of an additional $SU(2)$ gauge boson) might alter significantly the low-energy spectra of final particles, entailing relevant implications for predictions of fluxes of γ-rays and antimatter originating from DM annihilations and leading to a *multi-messenger* signal for ID DM searches. Indeed, besides photons, Z and $W^{\pm}$ produce $e^{\pm}, p, \bar{p}, \nu$ via hadronization and decays and populate the low energy tail of the spectrum with more final stable particles. Therefore, observations of different CRs species can be simultaneously used to derive constraints on the DM properties. The main advantage of EW bremsstrahlung is therefore the enhancement of photon yield at low energies as well as of lepton and hadron fluxes originating by the subsequent decay of the gauge bosons and leading to correlated multi-messenger signals.

As for photons, EW gauge bosons are emitted by the final legs (FSR) or by the virtual exchanged particles (VIB). Additionally, $SU(2)$ gauge bosons can be radiated by initial legs (incoming DM particles) leading to the so called ISR. Such an emission takes place whenever the DM candidate is charged under $SU(2)_L$ as it is for $SU(2)_L$ doublets (in the MSSM this would correspond to neutralino in the higgsino limit) or triplets (e.g. wino-like DM) DM.

For hard processes (i.e. $m_\chi \gg m_W$) the emission of soft EW bosons radiated off highly relativistic particles (FSR) is enhanced by (i) $\ln(s/m_W^2)$ when collinear divergences are present[i] and (ii) $\ln^2(s/m_W^2)$ in the case of both collinear and infrared divergences (P. Ciafaloni, Cirelli et al., 2011b). Differently from unbroken gauge symmetries like QED and QCD, the (spontaneously) broken EW sector of the SM manifests a double log-enhanced contribution $\ln^2(s/m_W^2)$ in the spectra of final stable particles (P. Ciafaloni & Comelli, 1999; M. Ciafaloni, Ciafaloni & Comelli, 2000). These corrections correspond to collinear and infrared divergences that in massive gauge theories do not cancel as in the case of physical scattering processes in QED and QCD (this cancellation is known as “Bloch-Nordsieck Theorem” (Bloch & Nordsieck, 1937)). As in the case of EM corrections, the EW FSR can be factorized in terms of the two-body process by means of partonic splitting functions (P. Ciafaloni, Comelli et al., 2011). Although single and double logarithm enhancements are already effective at $\mathrm{O}((m_\chi^2/m_{\tilde{X}}^2)^2)$ via FSR diagrams, the annihilation still proceed through p-wave and thus the enhancement is not sufficient to lift the helicity suppression (P. Ciafaloni,

---

[i] This is similar to the case of photons and gluons from FSR, since the hard scale of the process $m_\chi \gg m_W$ is such that the $SU(2)$ gauge bosons masses can be safely neglected

Comelli et al., 2011; P. Ciafaloni, Cirelli et al., 2011b).

Analogously to the case of EM corrections, models whose rates are suppressed at tree-level because of helicity arguments may lift the suppression when an additional $SU(2)$ boson is emitted by the internal legs (VIB). This is expected to be notably enhanced when the neutralino mass is degenerate with the sfermions exchanged in the t- and u-channel as it is illustrated by Eq. 4.3. In this case, if the neutralino is degenerate with the exchanged sfermion the propagator diverges for energies of the fermion (antifermion) close to $m_f/2m_\chi$ $(m_{\bar{F}}/2m_\chi)$. This is a feature of models e.g. in the co-annihilation region.

Finally, it has been shown that ISR (not present in the case of EM corrections) gives origin to a non-vanishing s-wave, preventing the helicity suppression by altering the axial-vector structure of the initial current (P. Ciafaloni, Cirelli et al., 2011a; Garny, Ibarra & Vogl, 2012).

In general it is not possible to distinguish among those contributions (i.e. FSR, ISR and VIB) in a gauge invariant way, since only all of them are a set of a gauge invariant diagrams. In this respect, the above statements are gauge invariants in specific toy-models in which the Lagrangian does not allow all the topologies while preserves gauge invariance.

The main differences between $SU(2)$ and $U(1)$ corrections originate mostly from the much larger number of diagrams involved in the former case, which results in a rich and complex phenomenology. Indeed, as we will discuss in the next sections, $SU(2)$ gauge bosons emitted also from the initial legs participate in lifting the helicity suppression and may efficiently enhance the annihilation rate, while this does not occur for EM bremsstrahlung. Moreover, the interplay among s-channel diagrams results in important interference effects that may deplete or further enhance the rate. Furthermore, the non-zero mass of the $SU(2)$ gauge bosons changes the allowed kinematical range, reduces the phase space for low neutralino masses and, most importantly, allows the production of longitudinally polarized vectors. In this case, the cross section is enhanced and a harder spectrum for the vector boson is produced[ii] (Garny et al., 2012). Phenomenologically, the total photon yield is expected to be altered differently by these two kind of corrections: EM corrections are expected to modify the high-energy end of the spectrum by originating spectral features at $E_\gamma \sim m_\chi$, while EW corrections are expected to change the low-energy tail of the spectrum. Indeed, the additionally emit-

---

[ii] The production of longitudinally polarized vector boson takes place when the full mass content of the theory is considered, namely when the mass splitting between charged and neutral sfermions is non-vanishing. In this case, the total cross section is enhanced by the production of longitudinal degrees of freedom (Garny et al., 2011). Indeed, the coupling of charged and neutral sfermions with the longitudinal component of the $W^\pm$ is related to the coupling to the Goldstone bosons that give mass to the W, according to the equivalence theorem, and such a coupling turns out to be proportional to the sfermions mass splitting. Therefore, in the degenerate case the longitudinal W component does not contribute, while it enhances the cross section when the mass difference is non-zero.

ted gauge bosons produce hadrons and mesons that then decay and fragment leading to a considerable amount of less energetic "secondary" photon; since a few energetic particles are converted in a great number of less energetic particles, the low-energy end of the spectrum would be enhanced.

We also mention that in the case DM annihilates into colored fermions, additional gluons are emitted in the process. In the case of massless quarks, only t-channel diagrams are present and the cross section in the zero-velocity limit for the $q\bar{q}g$ process coincides with the one for $q\bar{q}\gamma$ after having replaced $Q^2\alpha_{\rm em}$ (Q being the quark charge) by $4/3\alpha_s$. The enhancement is important when squarks are degenerate in mass with the neutralino and the ensuing antiproton (but also γ-ray) fluxes may give rise to stringent constraints for masses below $\sim 45 - 80$ GeV (Asano et al., 2012; Garny et al., 2011).

The first discussion of s-wave suppressed Majorana DM annihilation into fermion antifermion pairs in the context of supersymmetric DM dates back to 80's (Goldberg, 1983). Afterward a lot of effort has been spent in computing the effect of radiative corrections on DM annihilation in concrete models as well as in rather model-independent ways. Bremsstrahlung from photons has long been known to lift the helicity suppression and to dominate the two-body process (Bergström, 1989; Flores et al., 1989; Baltz & Bergström, 2003; Bergström et al., 2008; Bringmann et al., 2008). Besides some preliminary exploring work (Kachelrieß & Serpico, 2007; Bell et al., 2008; Dent, Scherrer & Weiler, 2008), EW corrections have been extensively studied in the last few years highlighting the great impact of such corrections on the predicted DM spectra (Kachelrieß, Serpico & Solberg, 2009; Bell, Dent, Jacques & Weiler, 2011b, 2011a; Bell, Dent, Galea et al., 2011; P. Ciafaloni & Urbano, 2010; P. Ciafaloni, Comelli et al., 2011; P. Ciafaloni, Cirelli et al., 2011b, 2011a; P. Ciafaloni, Comelli, De Simone, Riotto & Urbano, 2012; Garny et al., 2011, 2012). The above mentioned literature provides a deep insight into the problem, although EW corrections have always been computed in specific toy models – which correspond to some MSSM neutralino DM limit (e.g. bino-, wino- or higgsino-like DM) and can make use of effective field theory operators – or in a completely model-independent way which generalizes partonic splitting functions to massive partons (P. Ciafaloni, Comelli et al., 2011). Notably, the latter approach is valid in the regime of high DM masses (i.e. $\gtrsim$1 TeV) and takes into account only the effect of EW fragmentation from the final legs. Additional contributions to the prompt γ-ray emission (i.e. from VIB and ISR) can only be computed in the framework of a precise DM model because one needs to know the higher order QED annihilation/decay diagrams and are not covered by such a model-independent approach.

Stimulated by this plethora of previous works, which have shown how important modeling higher order radiative corrections to two-body DM annihilation can be, we study EW corrections to neutralino DM annihilation. Moreover, the lack of a complete and full treatment in concrete DM models motivates our choice to report here the first fully general calculation for MSSM neutralino DM annihilation, by keeping not only all relevant diagrams but also the full mass dependence of both fermions, gauge bosons and other involved particles. In this respect, our work is model-dependent and, for this same reason, it should be able to embrace the most of the possible effects and implications for neutralino DM ID.

4.2 Computing EW corrections to neutralino DM annihilation

We here present the method we follow in performing the fully general computation of EW corrections to neutralino MSSM DM annihilation in the zero velocity limit. We focus only on the annihilation into a fermion-antifermion pair and a vector boson, since, in this case, the two-body final state is suppressed for helicity arguments and the three-body final state may enhance the annihilation rate. The enhancement due to EW corrections should indeed be more relevant for those channels that suffer from some suppression mechanism. The particular kinematical limit ($v \to 0$) in which we work allows us to simplify the computation since only the singlet state ($\mathrm{J}^P = 0^-$) of the neutralino pair contributes. In this case, we can make use of the ${}^1S_0$ projector for the initial state. In order to calculate the squared matrix we extend to three-body final state processes the *helicity amplitude* method which has proven very useful for the numerical analysis of neutralino annihilation into two-body final states (Edsjö & Gondolo, 1997).

4.2.1 From Feynman rules to amplitudes

We generate all the diagrams with FeynArts (Hahn, 2001). For this purpose, we modify the supplied generic MSSM model file in order to accommodate the generic couplings adopted in DarkSUSY (Gondolo et al., 2004). We then use FeynCalc (Hahn, 2008) to produce the symbolical expressions of each matrix element.

Fig. 4.1 shows in a schematic form all Feynman diagrams contributing to neutralino annihilation into two fermions and one gauge boson. We consider the process of neutralino annihilation into $\bar{F}fV$, where F equals f for Z-boson emission ($V = Z$) and (F, f) are the two components of an $SU(2)_L$ doublet for W-boson emission ($V = W^{\pm}$). In Fig. 4.1 dotted lines indicate scalar (neutral A, h, H and charged $H^{\pm}$) or vector ($Z, W^{\pm}$) mediators. Diagrams in the first (second) row derive from tree-level s-channel diagrams

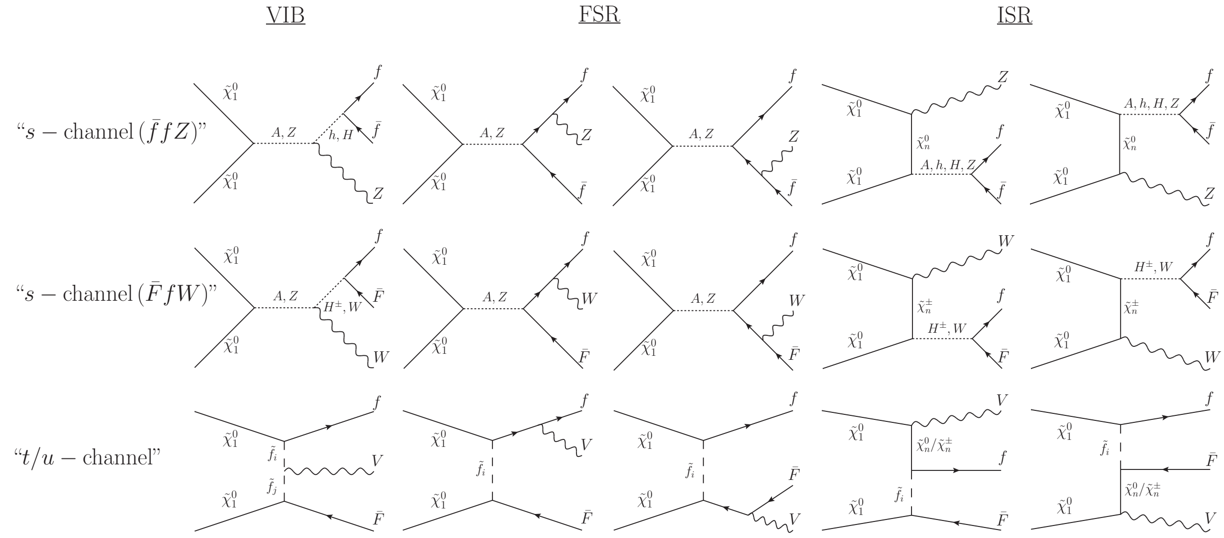

Figure 4.1: Feynman diagrams for neutralino annihilation into $\bar{F}fV$, where $F = f$ for Z-boson emission ($V = Z$) and (F, f) are the two components of an $SU(2)_L$ doublet for W-boson emission ($V = W^\pm$). Dotted lines indicate scalar (neutral A, h, H and charged $H^\pm$) or vector ($Z, W^\pm$) mediator fields. Diagrams obtained through fermion-line crossing are not displayed.

for the processes $\bar{f}fZ$ ($\bar{F}fW$). The third row refers instead to t-channel diagrams; diagrams derived from tree-level u-channel are not shown explicitly and for $v \to 0$ result in the *same* amplitudes as the t-channel case. The diagrams can then be classified according to the leg which the electroweak gauge boson is radiated off, i.e. whether it is emitted by the virtual particles mediating the interaction at tree-level (VIB, first column), by one of the final fermions (FSR, second and third column), or by one of the initial neutralino legs (ISR, column 4 and 5). We notice that we here take into account for the first time s-channel diagrams and initial state radiation diagrams, which have been little explored in literature so far (P. Ciafaloni, Cirelli et al., 2011a; Garny et al., 2012). In total we deal with 46 diagrams for the process $\bar{F}fW$ and 88 for $\bar{f}fZ$.

4.2.2 From amplitudes to the squared matrix element

The symbolical expressions for the amplitudes can be simplified exploiting the fact that the initial Majorana pair is annihilating at rest. In this case, it is possible to apply the Lorentz-invariant projector

$$P_{^1S_0} = \frac{\gamma_5}{\sqrt{2}} \left(m_\chi - \not{p}/2 \right) , \tag{4.4}$$

whith p being the total momentum of the system. This projector actually replace the pair of external Majorana spinors in the amplitude. We refer the reader to Appendix B where we work out the derivation of the projector from the explicit expression of the four-component spinors and we explain how to apply the projector to amplitudes.

In order to derive the total squared matrix element, we then apply the *helicity amplitude* method and we extend it to three-body final states. Such a method has been adopted to compute two-body processes implemented in DarkSUSY (Edsjö & Gondolo, 1997) and turned out to be efficient for the computation of matrix elements involving a great number of diagrams. We apply to the process $\chi\chi \to f\bar{F}V$.

The matrix element for the process $\chi(p_1)\chi(p_2) \to f(k_1)\bar{F}(k_2)V(k_3)$ is generically expressed in terms of fermion chains and the polarization vector, $\epsilon^*_\mu(\lambda)$ – with μ Lorentz index and λ indicates the polarization –. The typical structure of the amplitude for an s-channel topology is written as:

$$\mathcal{M}_s \propto \bar{v}_i(p_2)\,(\Gamma_{\text{initial}})_{ij}\,u_j(p_1)\bar{u}_m(k_1)\,(\Gamma_{\text{final}})_{mn}\,v_n(k_2)\epsilon^*_\mu(k_3)\,, \tag{4.5}$$

where $\Gamma_{\text{initial}}/\Gamma_{\text{final}}$ are the sequences of couplings and propagators, written according to the Feynman rules. In this case (i.e. s-channel), the subscripts “initial” and “final” indicate initial and final fermion chains of the two incoming neutralinos and the outgoing fermion-antifermion pair respectively. In the t- and u-channel, the structure of the amplitude is slightly different from Eq. 4.5 and is not possible to distinguish between “initial” and “final” chains[iii].

By applying the $P_{^1S_0}$ projector as described in Appendix B, it is possible to replace the pair of external Majorana spinors. Independently of the topology, the resulting amplitude is then in the form:

$$\mathcal{M} \propto \bar{u}_r(k_1)\Gamma_{rs}v_s(k_2)\epsilon^*_\mu(k_3)\,, \tag{4.6}$$

where in the case of s-channel Γ corresponds to Γ_{final} (we here explicit only spinor indices whereas we omit Lorentz indices).

The idea of the *helicity amplitude* method is to replace $\bar{u}_r(k_1)\Gamma_{rs}v_s(k_2)$ with a linear combination of *helicity* vectors, which represent an orthonormal basis of $\mathcal{R}^4$. After having reduced $\bar{u}_r(k_1)\Gamma_{rs}v_s(k_2)$ to a combination of fundamental Dirac field bilinears, each bilinear can be written as a linear combination of helicity vectors by operating a standard basis transformation from the $\mathcal{R}^4$ canonical basis to the helicity basis (we here explicit Lorentz indices whereas we omit spinor indices):

$$\bar{u}\,\Gamma^{\mu\ldots\nu}\,v = \sum_{\alpha\ldots\beta} C^{\alpha\ldots\beta} e^\mu_\alpha \ldots e^\nu_\beta = \sum_{\alpha\ldots\beta} C'^{\alpha\ldots\beta} e'^\mu_\alpha \ldots e'^\nu_\beta\,, \tag{4.7}$$

[iii] A way to get such a separation would be to apply Fierz transformations. We will see that however they are not needed in this context.

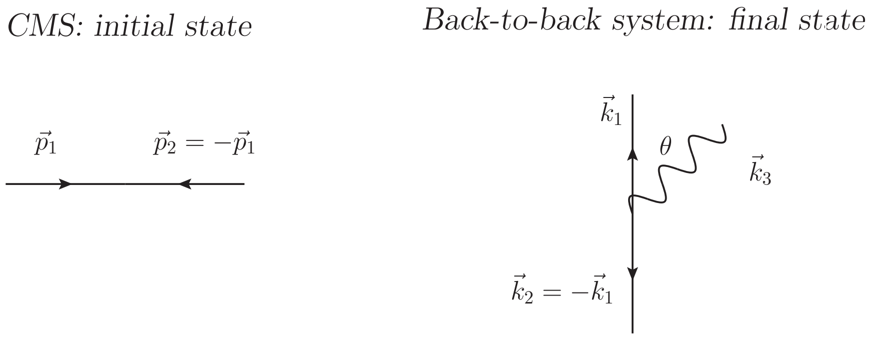

Figure 4.2: Kinematics for the process $\chi(p_1)\chi(p_2) \to f(k_1)\bar{F}(k_2)V(k_3)$. In the CMS of the initial state (left panel): $\vec{p}_1 = -\vec{p}_2$ ($|\vec{p}_1| = |\vec{p}_2|$) and in the zero-velocity limit $|\vec{p}_1| = m_\chi$. The back-to-back (BB) system (right panel) is defined such that $\vec{k}_1 = -\vec{k}_2$ ($|\vec{k}_1| = |\vec{k}_2| \equiv |\vec{k}|$), where the outgoing particle, f, has momentum k_1 and mass m_1, whereas the outgoing antiparticle $\bar{F}$ has momentum k_2 and mass m_2. The vector boson is emitted with momentum k_3, at an angle θ with respect to the direction of k_1.

where e'^{μ}_{α} is an element of the canonical basis:

$$B = \{(1,0,0,0),(0,1,0,0),(0,0,1,0),(0,0,0,1)\}\,, \tag{4.8}$$

and e'^{μ}_{α} is an element of the helicity vector basis:

$$B' = \{(1,0,0,0),\frac{1}{\sqrt{2}}(0,-1,-i,0),\frac{1}{\sqrt{2}}(0,1,-i,0),(0,0,0,1)\}\,. \tag{4.9}$$

Such a decomposition leads to manageable expressions if the two-particle fermion-antifermion system has definite spin, i.e. *helicity*, configurations in the center of mass system (CMS) of the two particles, where the direction of the fermion momentum corresponds to the quantization axis of the third component of the spin operator. For the final state, we thus work in a particular reference frame where the fermion and antifermion are emitted back-to-back (BB) and the vector boson is radiated with a certain angle with respect to the direction of the fermion momentum (see Fig. 4.2 for an illustrative picture of the kinematics and the assignation of momenta for the three-body process). The possible two-body helicity states of the particle-antiparticle system are four, one for the total spin singlet $S = 0$ and three for the total spin triplet $S = 1$. Such configurations are labelled by the indices (s,η), where s is the total spin and η the eigenvalue of the operator S_z.

Each Dirac field bilinear with specified helicity configuration can thus be decomposed as follows:

$$(\bar{u}\,\Gamma^{\mu\ldots\nu}\,v)_{(s,\eta)} = \sum_{\alpha\ldots\beta}\left(\left(C'^{\alpha\ldots\beta}\right)_{(s',\eta')}\,e'^{\mu}_{\alpha}\ldots e'^{\nu}_{\beta}\right)\delta^{s',\eta'}_{s,\eta}\,. \tag{4.10}$$

We remind the interested reader of the definition of helicity states in terms of the four-component spinors with definite helicity and of the decomposition of fundamental Dirac bilinears in terms of helicity basis vectors in Appendix C.

Moreover, for each fermion-antifermion helicity configuration three definite polarization states of the emitted boson exist, $\lambda = 0, +, -$. By specifying the vector components of the polarization vectors $\epsilon^*_\mu(\lambda)$ it is possible to work out the vector-contractions among helicity vectors, polarization vectors and kinematical quantities (see Appendix D). By applying those contractions to the manipulated amplitudes, we end up with 4 × 3 helicity amplitudes $\mathcal{M}^{(h,\lambda)}$, where h refers to the helicity of the fermion-antifermion pair in the back-to-back system and λ to the polarization states of the emitted vector boson. We notice that $\mathcal{M}$ refers to the sum over all the involved diagrams: $\mathcal{M} = \mathcal{M}_s + \mathcal{M}_t + \mathcal{M}_u$.

Finally the standard total squared amplitude (averaged over initial spins and summed over final degrees of freedom) is:

$$\overline{|\mathcal{M}|}^2 \equiv \frac{1}{4} \sum_{r,s,r',s',\lambda} \left| \mathcal{M}_{\chi\chi\to\bar{F}fV} \right|^2 \equiv \tag{4.11}$$

$$\frac{1}{4} \sum_{h,\lambda} \left| \sum_{\text{diag.}} \mathcal{M}^{(h,\lambda)}_{\chi\chi\to\bar{F}fV} \right|^2, \tag{4.12}$$

where $r, s(r', s')$ refer to spins of initial (final) particles, λ to the polarization states of the emitted vector boson and h to the helicity of the fermion-antifermion pair in the back-to-back system.

4.2.3 Cross sections and particles yields

The relevant quantities for ID DM searches are cross sections and total yields of final stable particles. Starting from the expression of the helicity amplitudes we implement numerically in DarkSUSY the computation of the total squared matrix, the spectra of final state particles, cross sections and the spectra of final photons. We distinguish 12 times 2 final state channels corresponding to the 12 possible two-body final fermion-antifermion pairs and the 2 $SU(2)$ vector bosons (Z and $W^\pm$)[iv]. All matrix elements and cross sections will be available with the next DarkSUSY public release. The code is flexible in the sense that all quantities are computed channel-wise and then added to give the total result, so that the user can select the single $SU(2)$ channel.

[iv] Given the CP invariance for the processes $f_{\rm up}\bar{F}_{\rm down}W^-$ and $f_{\rm down}\bar{F}_{\rm up}W^+$ for all fermion final states, we effectively only implement 6 final state channels corresponding to the W^- emission and we then set the $\langle\sigma_{\rm ann}v\rangle_{f_{\rm down}\bar{F}_{\rm up}W^+}$ equal to $\langle\sigma_{\rm ann}v\rangle_{f_{\rm up}\bar{F}_{\rm down}W^-}$.

The total cross section is obtained by integrating over the three-body phase space the double differential cross section:

$$\frac{d(\sigma v)}{dE_1 dE_2} = \frac{1}{16\, m_\chi^2} \frac{1}{(2\pi)^3} \overline{|\mathcal{M}|}^2 \,, \tag{4.13}$$

where E_1 and E_2 are the CMS energies of any two final state particles[v].

Then, the spectrum of any of the final state particles p is obtained by integrating Eq. 4.13 over the energy of the other involved particle:

$$\frac{dN_p^{\bar{F}fV}}{dE_p} = \frac{1}{\sigma v_0^{\mathrm{tree}}} \int_{E_{p'}^{\mathrm{min}}(E_p)}^{E_{p'}^{\mathrm{max}}(E_p)} \frac{d(\sigma v)}{dE_p dE_{p'}} dE_{p'} \,. \tag{4.14}$$

We normalized the spectrum to the *total* tree-level annihilation rate $\sigma v_0^{\mathrm{tree}}$. Expressions for the integration limits are quoted in Appendix D.

Final state particles then undergo fragmentation or decay processes leading to a flux of final stable particles, e.g. $e^\pm, p, \bar{p}, \nu$. The spectrum of a potentially observable stable particle P, resulting from a given annihilation channel $\chi\chi \to \bar{F}fV$ and normalized to the total two-body annihilation rate $\sigma v_0^{\mathrm{tree}}$, is thus given by:

$$\frac{dN_P^{\bar{F}fV}}{dE_P} = \sum_{p=F,f,V} \int_{E_p^{\mathrm{min}}}^{E_p^{\mathrm{max}}} \frac{1}{2} \frac{dN_P^{\bar{p}p\to P+X}}{dE_P} \frac{dN_p^{\bar{F}fV}}{dE_p} dE_p \,, \tag{4.15}$$

where $dN_P^{\bar{p}p\to P+X}/dE_P$ is the Monte Carlo simulated number of stable particles P resulting from the two-body inclusive annihilation process $\bar{p}p \to P + X$ with CMS energy of $2E_p$. Those spectra are implemented in DarkSUSY (Gondolo et al., 2004) and based on Pythia (Sjöstrand et al., 2006) runs.

We implement in DarkSUSY the computation of the total photon yield ($P = \gamma$) from the $SU(2)$ corrections:

$$\frac{dN_\gamma^{SU(2)}}{dE_\gamma}(E_\gamma) = \sum_{i\in\{\bar{F}fV\}} \frac{dN_\gamma^i}{dE_\gamma}(E_\gamma) \,, \tag{4.16}$$

where, again, $f = \{\nu_l, l, q\}$ and F is equal to f (for Z-boson emission, $V = Z$) or to the $SU(2)_L$ partner of f (for W-boson emission, $V = W^\pm$).

As a cross-check of the correctness of our method, we analytically reproduce the differential cross section for $\chi\chi \to f\bar{f}\gamma$ (Bringmann et al., 2008),

---

[v] The decay process into a three-body final state depends on two independent variables. Indeed, the nine components of the final three-vectors are constrained by four energy-momentum conservation equations and, furthermore, the final state is independent on the three Euler angles describing its orientation as a whole since the initial state is isotropic in the rest frame of the incoming particles (see Appendix D for details).

for all diagrams and $m_f \neq 0$, considering the correct limit of our expressions for $\bar{f}fZ$ final states. We checked also our results against the toy-model limits considered in (Garny et al., 2012), i.e. $m_f \equiv 0$ and χ being a pure bino or higgsino. This work extends previous partial results of (Bell, Dent, Galea et al., 2011; Bell, Dent, Jacques & Weiler, 2011a). We also explicitly test the CP invariance of the cross section for the processes $f_{\rm up}\bar{F}_{\rm down}W^-$ and $f_{\rm down}\bar{F}_{\rm up}W^+$ for all fermion final states. If not otherwise specified, we refer to $(f\bar{F}W^- + F\bar{f}W^+)$ as $2\,f\bar{F}W$.

4.3 Results

We report here the main results of the full computation of EW corrections for neutralino DM. We refer the interested reader to the corresponding publication (Bringmann & Calore, 2013). The results are based on a large scan over the parameter space of two MSSM simplified models: the constrained MSSM (cMSSM) and a phenomenological MSSM-7. We apply all bounds and SM parameter estimates from accelerator measurements implementing limits recommended by the Particle Data Group (Amsler et al., 2008), with 2009 partial update, and we impose that models fulfill the neutralino relic density as measured by Planck, $\Omega_m^0 h^2 = 0.1423 \pm 0.0029$ (Ade et al., 2013), within 3σ. About $4 \cdot 10^5$ models are left after this selection. We refer to Appendix E for further details on the MSSM theory.

4.3.1 Spectra of final state particles

From Eq. 4.14, the spectrum of each final state particle can be computed. Although this quantity is not directly observable, it shows some interesting effects of such a full computation. Namely, the inclusion of s-channel diagrams opens the possibility of hitting resonances that would not occur otherwise. This effect is evident by looking at the energy distribution of final state particles, whereas it is completely smeared out in the spectrum of final stable photons.

S-channel resonances occur whenever the real part of the propagator of one of the virtual particles is singular. From kinematical arguments it is easy to individuate where (in energy) the resonances can appear. By inspecting the propagators of diagrams in Fig. 4.1, we find that resonances may originate from s-channel VIB and ISR and from s-, t- and u-channel FSR.

In the case of VIB and ISR, virtual exchanged particles can lead to resonances in the spectral distribution of the vector boson. Fig. 4.3 highlights the kinematics of the VIB (left panel) and ISR (right panel) diagrams leading to the resonance of the particle X. The figure encodes both $\bar{f}fZ$ and $\bar{F}fW$ processes according to Fig. 4.1. The direction of the momentum flow is

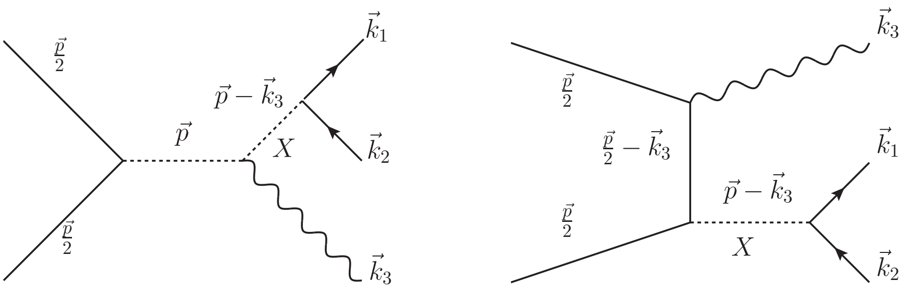

Figure 4.3: Schematic representation of VIB (left panel) and ISR (right panel) diagrams that lead to the resonance of particle X. We here emphasize the assignation of particles' momenta. The direction of the momentum flow is always assumed to be from right to left (and from top to bottom) if not otherwise specified.

always assumed to be from right to left (and from top to bottom) if not otherwise specified. The s-channel propagator o the virtual particle X reads:

$$D_X(E_V) \propto [(p-k_3)^2-m_X^2+im_X\Gamma_X]^{-1} \simeq [4\,m_\chi^2+m_V^2-4\,m_\chi\,E_V-m_X^2+im_X\Gamma_X]^{-1}\,. \tag{4.17}$$

It is easy to determine the position of the resonance:

$$z_V^{\rm res} \equiv E_V^{\rm res}/m_\chi = 1+\frac{m_V^2-m_X^2}{4m_\chi^2} \tag{4.18}$$

where we have introduced the definition of the dimensionless quantity $z_i = E_i/m_\chi$ with $i=f,\bar{F},V$ (see Appendix D for further details about the kinematics of the process). Notice that Γ_X is the width of the exchanged particle.

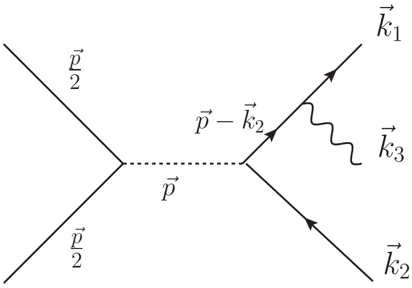

Figure 4.4: Schematic representation of FSR diagram that leads to the resonance of the antifermion (the FSR diagram in which the vector boson is emitted from the other leg leads instead to the resonance of the fermion). We here emphasize the assignation of particles' momenta. The direction of the momentum flow is always assumed to be from right to left (and from top to bottom) if not otherwise specified.

From the same kinematical argument, also resonances in the spectrum of the final state fermions and antifermions might appear. Fig. 4.4 illustrates

Table 4.1: For each class of diagrams (VIB, ISR and FSR) and process ($f\bar{f}Z$ and $f\bar{F}W^{\pm}$) we list the virtual particles which can give origin to the resonances in the energy distribution of the final state particles.

Diagrams	X ($f\bar{f}Z$)	X ($f\bar{F}W^{\pm}$)
VIB	h, H	$W^{\pm}, H^{\pm}$
ISR	Z, h, H, A	$W^{\pm}, H^{\pm}$
FSR	$f, \bar{f}$	$f, \bar{F}$

the momenta involved in the process that gives origin to a resonance in the spectral energy distribution of the antifermion. The FSR diagram in which the vector boson is emitted from the other leg leads instead to a resonance in the fermion spectrum. As above, the direction of the momentum flow is always assumed to be from right to left (and from top to bottom) if not otherwise specified. Namely, from the virtual fermion (antifermion) propagator:

$$D_X(E_i) \propto [(p-k_i)^2 - m_i^2 + i m_i \Gamma_i]^{-1} \simeq [4\, m_\chi^2 - 4\, m_\chi\, E_i + i m_i \Gamma_i]^{-1}\,, \quad (4.19)$$

where the index i stays for the particle considered, i.e. $i = 1$ indicates the fermion f and $i = 2$ the antifermion $\bar{F}$. The corresponding energy at which the real part of the propagator vanishes is:

$$z_i^{\rm res} \equiv E_i^{\rm res}/m_\chi = 1\,. \quad (4.20)$$

This corresponds to the standard collinear/IR divergence.

Tab. 4.1 summarizes the resonances present in the annihilation process into $f\bar{F}V$. Depending on the kinematics of the process each resonance can fall either inside or outside the allowed kinematical range. Tab. 4.2 quotes the (dimensionless) energies at which resonances can appear together with the kinematical limits for the corresponding energies. From Tab. 4.2 it is possible to have an idea of under which kinematical conditions those resonances occur inside the kinematical range. The spectrum of the corresponding final state particle turns out to be enhanced by the resonance even if it occurs slightly outside the allowed kinematical range. It is thus possible that for specific models multiple resonances appear in the kinematical allowed range.

To give an example of such resonances, Fig. 4.5 displays the spectrum of the final vector boson for an MSSM-7 model in the case of annihilation into light/heavy quarks and either Z or $W^{\pm}$. The model parameters are: $\mu = 0.12 \cdot 10^4$, $M_2 = 0.65 \cdot 10^4$ GeV, $m_A = 0.53 \cdot 10^3$ GeV, $\tan\beta = 0.52 \cdot 10^2$,

Table 4.2: The resonance of the particle X for different processes/diagrams (see Tab. 4.1) can occur at z_i^{res} (i stays for 1, 2 or V) in the spectrum of the final state particle f, $\bar{F}$ or V respectively. We also quote the minimal/maximal allowed (dimensionless) energies z_i according to expressions in Appendix D.

Particle	i	z_i^{res}	z_i^{min}	z_i^{max}
f	1	1	$\frac{m_1}{m_\chi}$	$1+\frac{m_1^2-(m_V+m_2)^2}{4m_\chi}$
$\bar{F}$	2	1	$\frac{m_2}{m_\chi}$	$1+\frac{m_2^2-(m_V+m_1)^2}{4m_\chi}$
V	V	$1+\frac{m_V^2-m_X^2}{4m_\chi^2}$	$\frac{m_V}{m_\chi}$	$1+\frac{m_V^2-(m_1+m_2)^2}{4m_\chi}$

$m_0 = 0.1 \cdot 10^5$ GeV, $A_t/m_0 = -0.204$ and $A_b/m_0 = 0.103$ (see definition of parameters in Appendix E). For this model, $m_\chi = 1210$ GeV, $Z_g = 3 \cdot 10^{-4}$, $m_h = 124$ GeV and $m_H = 532$ GeV. The possible resonances in the spectrum of the vector boson are:

$$z_V^H = 0.952 \tag{4.21}$$
$$z_V^h = 0.998 \tag{4.22}$$
$$z_V^Z = 1 \tag{4.23}$$

for the process $f\bar{f}Z$, and

$$z_V^{H^\pm} = 0.949 \tag{4.24}$$
$$z_V^W = 1 \tag{4.25}$$

for $f\bar{F}W$. The superscript label indicates the particle on resonance. The energies at which the resonances may occur are indicated by vertical lines. From the figure, the resonances of the heaviest neutral Higgs H and the charged $H^\pm$ are clearly distinguishable whereas the one due to the lightest Higgs occurs closely to the vector boson resonance which is not visible. Indeed, from the width of the resonance at $z_V \sim 1$ we can argue that it corresponds to the lightest Higgs which gives origin to a very narrow resonance due to its small width. In the case of annihilation into $t\bar{b}W$ the resonance at $z_V = 1$ lies outside the kinematical boundaries and the spectrum fall down before $z_V = 1$.

4.3.2 Spectra of final stable particles: the differential photon yield

Predictions for the spectra of final stable particles are an important ingredient of DM ID. We focus here only on γ-rays and we postpone the discussion of other channels to a future work. The total number of photons per annihilation enters in the expression of the DM photon flux Eq. 3.1.

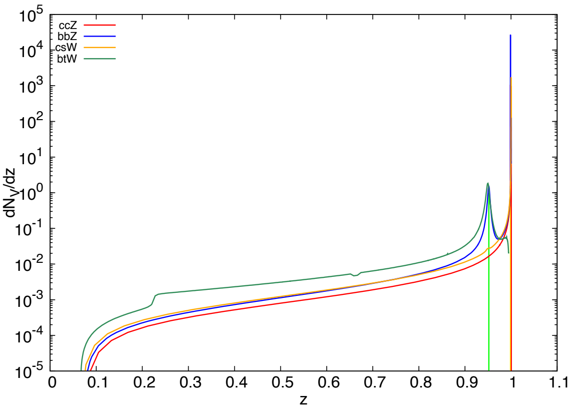

Figure 4.5: Spectrum of final state vector boson in case of annihilation into $c\bar{c}Z$ (red solid line), $b\bar{b}Z$ (blue solid), $c\bar{s}W$ (orange solid), and $t\bar{b}W$ (see-green solid). Resonances due to the heaviest and charged Higgs occur at $z_V \sim 0.5$ (green solid). The lightest Higgs and the exchanged vector boson give origin to a resonance at $z_V \sim 1$, although the latter is not visible because hidden by the former.

The total photon yield takes contribution from "secondary photons" originating from the hadronization and subsequent decay, mostly from the π^0 decay, of any unstable final state particle, namely from two- and three-body final states. Besides "secondary photons" originating from the two-body process, DM γ-rays arise from $\mathcal{O}(\alpha)$ corrections to the tree-level process, namely EM, EW and strong corrections and photons directly produced from DM annihilation via loop diagrams and suppressed by $\mathcal{O}(\alpha^2)$ (see chapter 3 for an introduction to the γ-ray spectrum and its contributions).

Typically, the spectrum of "secondary photons" from two-body final states drops softly at energy $\sim m_\chi$ and it is almost featureless. Higher order corrections may enhance the total photon yield and produce spectral features at the high energy end of the spectrum. The most striking signature is the line-like signal coming from loop suppressed processes. Moreover, it has been shown that also EM corrections from VIB diagrams can lead to a bump-like feature at high energies which is phenomenologically similar to a line. On the other hand, EM FSR leads to a logarithmic enhancement of the photon yield that is almost universal although less striking.

EW corrections are expected to alter sensibly the low-energy tail of the spectrum of final photons because more particles are produced from the hadronization and decay of additionally emitted $Z, W^\pm$ and, by consequence, more "secondary photons". As an example, let's consider the tree-level annihilation into neutrinos: no γ-ray flux is expected from such a two-body final state and this channel thus does not contribute to the "secondary photon" spectrum from two-body final states, while, if an additional gauge boson is emitted, then also neutrinos final state can give a contribution to the γ-ray

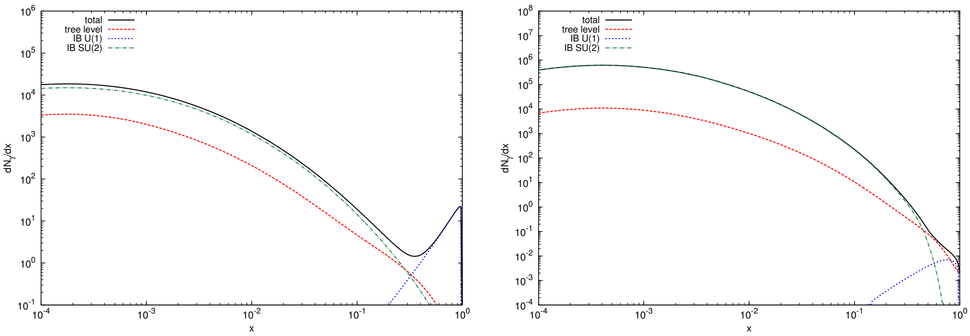
(a) BM1 (b) BM2

Figure 4.6: Differential total photon yield (solid black line) for two different models whose parameters are quoted in Tab. 4.3. Contributions from the tree-level (dashed red line) spectrum, the spectrum from EW corrections only (dash-dotted sea-green line) and EM corrections (dotted blue line) are plotted separately.

flux. EW corrections thus modify the spectrum at low energies and represent a strong constraint for the low-energy part of a possible signal since this continuous contribution must not exceed the astrophysical background.

In this respect, EM and EW corrections act on different energy ranges: EM corrections modify the high-energy end of the spectrum giving rise to spectral features, whereas EW corrections change the strength of the signal in the low-energy tail.

In order to appreciate such differences we display in Fig. 4.6 the total differential photon yield for two cMSSM models. The quantity depicted here is the number of photons per annihilation in function of the dimensionless variable $x \equiv E_\gamma/m_\chi$. We refer to the two models as BM1 and BM2 and we summarize their model parameters in Table 4.3.

Table 4.3: cMSSM model parameters for two models whose spectra are shown in Fig. 4.6. We quote the neutralino mass m_χ, the gaugino fraction Z_g, the mass of the lightest stau $m_{\tilde{\tau}}$ and the relic density Ωh^2.

Model	m_0 [GeV]	$m_{1/2}$ [GeV]	$\tan\beta$	A_0 [GeV]	sgn (μ)	m_χ [GeV]	Z_g	$m_{\tilde{\tau}}$ [GeV]	Ωh^2
BM1	168	871	4.61	-292	-1	362.5	0.999	364.3	0.113
BM2	576	402	4.85	-2132	-1	168.2	0.999	590.5	0.128

The left panel refers to a typical bino-like cMSSM model in the $\tilde{\tau}$-coannihilation region, while in the right panel the spectrum for a model with $m_\chi \lesssim m_t$ is shown. In the latter case, $\bar{t}t$ final states are kinematically not allowed or strongly suppressed, thus leading to a strong enhancement of the

$t\bar{b}W$ three-body final state.

In both plots the full spectrum including EW corrections corresponds to the black solid line and it results in an overall enhancement of the tree-level spectrum (dashed red line) whereas at high energies, if present, the contribution from EM corrections dominates (dotted blue line).

As expected, the effect of EW corrections is relevant at the lower-end of the energy spectrum, which appears almost featureless and similar to the secondary photons from two-body final states. Thus, EW corrections result in an important change at the level of both the total photon flux and spectral form. We notice that commonly adopted model-independent expressions for FSR (P. Ciafaloni, Comelli et al., 2011) would lead to a result close to the tree-level one.

4.3.3 Cross sections and total photon yields

Cross sections and total photon yields are important quantity for DM ID; if they are enhanced by some mechanism (e.g. EW and EM bremsstrahlung) the ensuing DM flux of final stable particles turns out to be larger and, hopefully, detectable. Fig. 4.7 shows the strong correlation existing between cross section and photon yield, by displaying the photon yield enhancement $N_\gamma^{\bar{F}fV}/N_\gamma^{\rm tree}$ as a function of the cross section enhancement $\langle\sigma_{\rm ann}v\rangle_{f\bar{F}V}/\langle\sigma_{\rm ann}v\rangle_{\rm tree}$. Different symbols represent models characterized by a different gaugino fraction: $Z_g > 0.99$ (mostly bino-like neutralino), $Z_g < 0.01$ (higgsino-like) or $0.01 \leq Z_g \leq 0.99$ (mixed).

In Fig. 4.8, we report the comparison between the total annihilation rate into three-body final states with the emission of an additional $SU(2)$ gauge boson and the one from electromagnetic corrections[vi]. In the left panel we emphasize the dominant $SU(2)$ annihilation channel (i.e. single channel contributing more than 50%), whereas in the right panel we indicate the gaugino fraction.

By observing Fig. 4.8, we see that EW corrections are in general larger than EM corrections and a correlation between the two is not so clear. In what follow, the mechanisms that can enhance the annihilation rate and produce such a structure are discussed qualitatively.

As expected, a clear correlation between the two contributions is the orange strip with $\ell^+\ell^-Z$ and $\ell^\pm\nu W^\mp$ final states dominating the EW corrections. Those models lie in the cMSSM co-annihilation region (mostly the

---

[vi] In the case of electromagnetic corrections, infrared divergencies arise naturally when $E_V \to 0$ because of the vanishing mass of the photon. Those divergencies are cancelled, when computing inclusive observables like cross sections, by the addition of vertex corrections. Since at low-energy secondary photons from two-body final states dominate over photons from EM corrections, the cross section for the process $\bar{f}f\gamma$ is computed by integrating with $E_\gamma > 0.5\, m_\chi$. This is equivalent to consider the annihilation into hard photons only. In the case of EW corrections, instead, the infrared divergence is regularized by the electroweak mass of the $SU(2)$ gauge bosons.

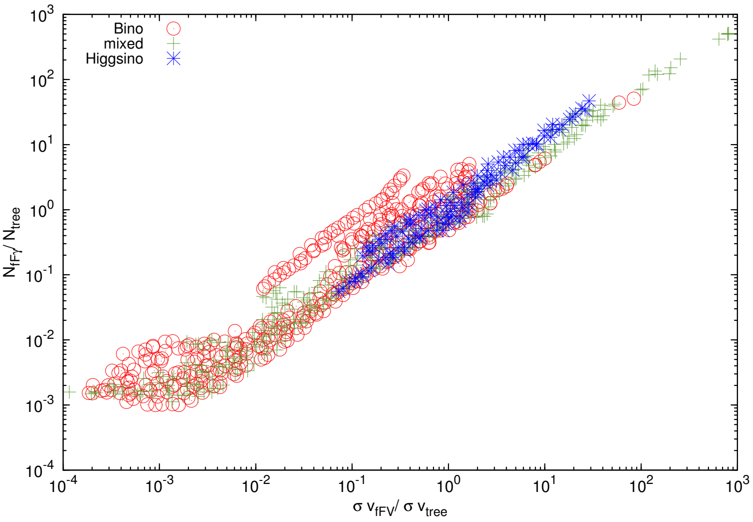

Figure 4.7: Correlation between the photon yield enhancement $N_\gamma^{\bar{F}fV}/N_\gamma^{\rm tree}$ as a function of the cross section enhancement $\langle\sigma_{\rm ann}v\rangle_{f\bar{F}V}/\langle\sigma_{\rm ann}v\rangle_{\rm tree}$. Symbols indicate models where the neutralino is mostly bino ($Z_g > 0.99$), higgsino ($Z_g < 0.01$) or mixed ($0.01 \leq Z_g \leq 0.99$).

$\tilde{\tau}$ co-annihilation region) where the EM corrections have proven to be enhanced by the small mass splitting among the sfermion and the neutralino and EW corrections are expected to undergo the same enhancement mechanism as we have seen previously. In the case of EW bremsstrahlung, the effect is somewhat suppressed due to destructive interference with s-channel diagrams.

In the vertical strip with dominantly $\bar{q}qZ$ final states lie models corresponding to binos in the s-channel A resonance region. For those models, FSR cannot lift the helicity suppression and this explains why the $U(1)$ contribution is so small here. Those happen to be models with a small neutralino mass, i.e. $m_\chi < m_t$. Moving toward the top of the strip, the higgsino fraction of the neutralino increases (see right panel of Fig. 4.8). For higgsinos ISR channels contribute to the squared matrix and thus potentially can largely enhance the cross section due to a lifting of the helicity suppression.

Models dominated by $\bar{q}qW$ final states annihilate mostly through Z mediated s-channel diagrams where the ISR dominates and they correspond to models in which the otherwise dominating $t\bar{b}W$ channel is kinematically suppressed, i.e. $2m_\chi < m_t + m_W$.

The largest enhancements appear indeed for $t\bar{b}W$ final states. One of the strongest enhancement mechanisms that we identify is a threshold effect for $m_\chi \lesssim m_t$, where $\bar{t}t$ final states are kinematically not allowed or strongly suppressed. Moreover, some of those models are dominated by the

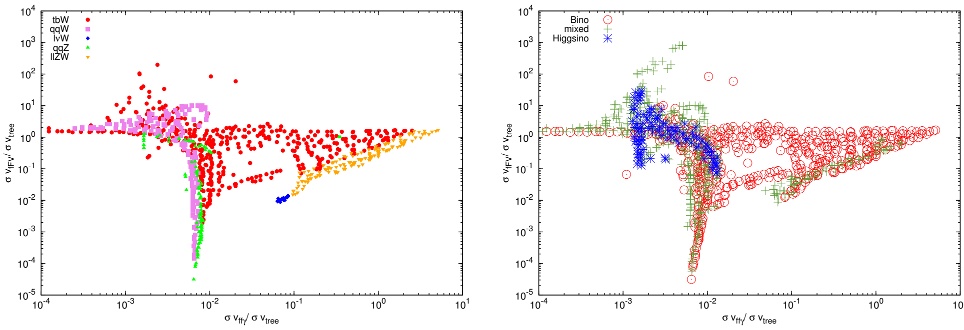

Figure 4.8: Total annihilation cross section of thermally produced neutralino DM into any fermion pair and a photon (with $E_\gamma > 0.5\, m_\chi$) or an EW gauge boson, normalized to the total cross section at tree-level. In the left panel, different colors indicate the $SU(2)$ annihilation channel which dominates the three-body rate. q represents light quarks (i.e. excluding the top). $t\bar{t}Z$ channel never dominates. The right panel shows instead the neutralino composition according to the gaugino fraction; symbols indicate models where the neutralino is mostly bino ($Z_g > 0.99$), higgsino ($Z_g < 0.01$) or mixed ($0.01 \leq Z_g \leq 0.99$).

A mediated s-channel diagrams and the amplitude turns out to be directly proportional to the large top mass. Indeed, in the case of pure bino, only VIB and FSR (with the CP odd Higgs mediating the interaction) participate in the process and it is possible to show analytically that the s-channel VIB + FSR (for the process $f\bar{F}W$) leading term in $|M|^2$ is $\propto m_f^2/m_W^2$. Finally, it is worth mentioning that whenever also the two-body cross section into $t\bar{t}$ is large, meaning an importance of the FSR for the $t\bar{b}W$ process, a careful subtraction of the top decay should be performed in order to avoid double counting. We do not address here the solution of this delicate issue that we postpone to a future work.

Fig. 4.9 displays the enhancement of the photon yield (with $E_\gamma >$100 MeV) as a function of both the full annihilation rate $\langle\sigma_{\rm ann} v\rangle_{\rm tree}$ at tree level (left panel) and the mass (right panel). Such a quantity is the most relevant one for ID searches, although we have seen that cross section and photon yield enhancements are strongly correlated.

The enhancement of the photon count can reach up to two orders of magnitude and, interestingly, models with very little discussion in the literature (i.e. with a neutralino mostly being mixed or higgsino) show the largest rising of the total number of produced photons for a tree-level cross section close to the "thermal" value of $\langle\sigma_{\rm ann} v\rangle\sim 3 \cdot 10^{-26}$ cm^{3}s^{-1}.

This suggests that EW corrected spectra for neutralinos as heavy as several hundred GeV will be testable by *Fermi*. Moreover, since the enhance-

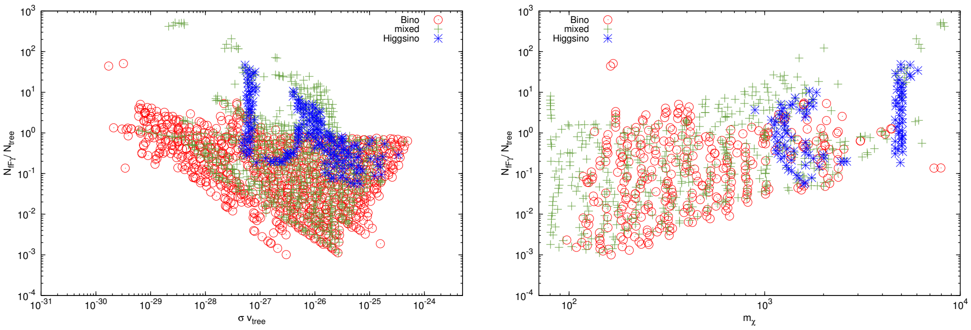

Figure 4.9: Photon yield enhancement (for $E_\gamma > 100\,\mathrm{MeV}$) from neutralino DM annihilation due to EW radiative corrections in function of both the full annihilation rate $\langle\sigma_{\rm ann}v\rangle_{\rm tree}$ at tree level in units of $\mathrm{cm}^{-3}\mathrm{s}^{-1}$ (left panel) and the mass in units of GeV (right panel). Symbols indicate models where the neutralino is mostly bino ($Z_g > 0.99$), higgsino ($Z_g < 0.01$) or mixed ($0.01 \leq Z_g \leq 0.99$).

ment occurs also for TeV neutralinos (as one can appreciate from the right panel of Fig. 4.9), even currently operating Air Cherenkov telescopes, which have an higher energy threshold at about 100 GeV, can constraints those models. EW radiative corrections will be then even more important when searching for DM with lower targeted threshold instruments, e.g. CTA.

We finally notice that, while we have limited the above discussion to γ-rays, the flux of other CR species is expected to be enhanced by EW corrections and, in particular, prospects for indirect DM searches with antiprotons or positrons through the AMS experiment will be also significantly improved.

Chapter 5

Astrophysical distribution: the role of galactic substructures

Besides the number of photons emitted by the annihilation process, the γ-ray DM flux of Eq. 3.1 depends crucially on the DM distribution in the targets where annihilations take place. The J-value, introduced in chapter 3, can span several orders of magnitude depending on how the galactic and extragalactic DM distribution is modeled. As a consequence, limits on DM cross section may turn out to be more or less stringent.

Notably, such a theoretical uncertainty is crucial when the angular distribution of the DM signal is studied and its anisotropy signal is predicted. Indeed, besides the constraints coming from spectral analysis of the DM signal (see chapter 7), the expected level of anisotropy coming from DM substructures as predicted by CDM N-body simulations can be constrained by the measurement of the γ-ray anisotropy of the IGRB, which appears isotropic on large angular scales but may contain fluctuations on small angular scales (Ackermann, Ajello, Albert, Baldini, Ballet et al., 2012).

Discussing the theoretical uncertainties related to DM searches through anisotropies in γ-rays is the topic of the present chapter, which is based on the preliminary results of (Calore et al., 2013) (work in preparation). Notably, we discuss in details (*i*) the intrinsic uncertainty due to the extrapolation to short distances of the DM distribution determined from numerical simulations and (*ii*) the statistical fluctuations implied by the mass and space distribution of subhalos.

We here consider only the DM distribution in our galaxy, whereas we neglect the contribution coming from external galaxies. Although, well-known astrophysical source populations are expected to contribute to the γ-ray anisotropy[i], they will not be discussed in the context of this thesis.

---

[i] Astrophysical source populations that have been considered as possible contributors

The chapter is organized as follows. In Sec. 5.1 we introduce the galactic DM distribution and how it is simulated by analytic Monte Carlo methods. We dedicate Sec. 5.2 to the computation of the APS of γ-ray anisotropy from annihilating DM in the galaxy and we discuss there its main theoretical uncertainties.

5.1 The galactic Dark Matter distribution

In section 3.2, we have seen that the modeling of the DM distribution relies on the results of numerical N-body simulations. Structures as clusters, galaxies and stars are indeed the result of highly non-linear processes that can be simulated with numerical methods. In N-body simulations, the evolution of structure formation is approximated by the non-linear gravitational clustering from specified initial conditions of the density fluctuations and by the modeling of effects of e.g. gas dynamics and radiative transfer. A general prediction of N-body simulations is the formation of DM halos of different sizes and masses: at large scales galaxies and clusters of galaxies form, whereas at small scales primary halos can host several, less massive subhalos. The capability of N-body simulations to faithfully reproduce the gravitational clustering is measured by the mass and length resolution. The smallest mass of virialized objects measures the mass resolution of the simulation, while the spatial resolution is limited by the softening scale for the computation of the gravitational force[ii]. For a recent review on numerical simulations we remind the reader of (Kuhlen, Vogelsberger & Angulo, 2012).

The latest numerical simulations of Milky Way-sized DM halos, i.e. the *Aquarius* (Springel et al., 2008) and *Via Lactea II* (Diemand & Moore, 2011) numerical simulations, show that the DM distribution of galactic sized halos is composed by two separate components: a smoothly distributed phase, i.e. the main halo, and a clumpy component in the form of virialized substructures, i.e. the subhalos. Given the high resolution, those simulations were able to resolve substructures down to masses $\sim 10^5 M_\odot$ and to study the properties of the subhalo distribution. They are in agreement with each other, although they adopt a slightly different cosmology and different subhalo finder algorithms. Namely, they both find more DM substructures in the outer region of the galaxy than in the center. Subhalos dominate the mass profile at large distances from the GC and their spatial distribution is

---

to the anisotropy of the IGRB are e.g. blazars (Ando et al., 2007; Ando, Komatsu, Narumoto & Totani, 2007; Miniati et al., 2007), star forming galaxies (Ando & Pavlidou, 2009), and galactic MSPs (Siegal-Gaskins, Reesman, Pavlidou, Profumo & Walker, 2011).

[ii] The gravitational force between two colliding particles presents a singularity when the distance of the two particles approaches zero, leading to infinities. The singularity may be avoided by introducing a softening length that is by modifying the gravitational interaction at small scales. The softening length is a typical distance below which the gravitational interaction is suppressed.

antibiased with respect to the smooth component.

The mass resolution constitutes a fundamental limitation for modeling the properties of galactic substructures down to the minimal mass of bounded DM structures, $M_{\rm cut}$. Therefore, studying the subhalo distribution has to rely on severe extrapolations of the N-body simulation results.

Monte Carlo simulations can be performed in order to reproduce the DM density by means of analytic distributions that model the results of current N-body simulations.

In modeling the components of the galactic halo, we follow the method outlined in (Pieri, Lavalle, Bertone & Branchini, 2011), which extrapolates the description of the subhalo distribution down to mass scales smaller than the simulation mass resolution. We use a Monte Carlo algorithm to create several realizations of this clumpy distribution based on the results of the *Aquarius* (Springel et al., 2008) simulation, namely of the Aq-A-1 realization[iii].

In the following, R refers to the galactocentric radial coordinate, while r is the "clump-centric" radial coordinate. Spherical symmetry is always assumed. We reserve the subscript *sm* for the smooth component, while *sh* (and *cl*) will be used for quantities related to substructures. $M_{\rm MW}$ indicates the mass of the Milky Way (i.e. Milky Way-sized halo).

The total DM density profile is given by the sum of the smooth component and the subhalo component (i.e. the spatial distribution of DM substructures): $\rho_{\rm tot}(R) = \rho_{\rm sm}(R) + \rho_{\rm sh}(R)$. We notice that this sum is the quantity that usually is considered to have a "NFW or Einasto or whatever shape" and the two addenda need not to have the same shape as their sum. The *Aquarius* total DM distribution is consistent with an Einasto profile

$$\rho_{\rm tot}(R) = \rho_s \exp\left\{-\frac{2}{\alpha}\left[\left(\frac{R}{r_s}\right)^{\alpha} - 1\right]\right\} \tag{5.1}$$

with $\alpha = 0.17$ and $r_s = 20$ kpc ; ρ_s is determined by imposing that

$$4\pi \int_0^{R_{\rm vir}} dR\, R^2\, \rho_{\rm tot}(R) \;= M_{\rm MW} \;. \tag{5.2}$$

where $R_{\rm vir}$ is the virial radius.

Once the spatial distribution of DM substructures and the total DM density are known, the smooth component is obtained by difference

$$\rho_{\rm sm}(R) = \rho_{\rm tot}(R) - \rho_{\rm sh}(R) \;. \tag{5.3}$$

On the contrary, the DM density profile within a substructure, $\rho_{\rm cl}(r)$, is assumed to be the same as the one of the total halo

$$\rho_{\rm cl}(r) = \rho_{s,\rm cl} \exp\left\{-\frac{2}{\alpha}\left[\left(\frac{r}{r_{s,\rm cl}}\right)^{\alpha} - 1\right]\right\} \;. \tag{5.4}$$

[iii] Our Monte Carlo code includes also the substructure distribution as given by the *Via Lactea II* (Diemand & Moore, 2011) simulation.

with $\alpha = 0.17$ and where the parameters $\rho_{s,\mathrm{cl}}$ and $r_{s,\mathrm{cl}}$ depend on mass and position of the specific clump, as we will see in what follows. Indeed, *Aquarius* results indicate that Einasto model fits subhalos profiles better than NFW and Moore & Stadel models and that this conclusion is insensitive to varying α in the range $\sim 0.16 - 0.20$.

The subhalo mass density profile (i.e. subhalo density per unit subhalo mass) is defined as:

$$\frac{d\rho_{\mathrm{sh}}(M_{\mathrm{sh}}, R)}{dM_{\mathrm{sh}}} = \rho_{\mathrm{sh}}(R)\mathcal{F}(\mu, M_{\mathrm{sh}}) \;, \tag{5.5}$$

with $\mathcal{F}(\mu, M_{\mathrm{sh}}) = \mathcal{F}_0(M_{\mathrm{sh}}/M_\odot)^{-\mu}$ the normalized mass distribution function with $\mu = 1.9$. Our surveyed mass range is $M_{\mathrm{min}} = M_{\mathrm{cut}} = 10^{-6}M_\odot$[iv] and $M_{\mathrm{max}} = 10^{-2}M_{\mathrm{MW}}$, which corresponds to the highest virialized substructure of *Aquarius*. $\mathcal{F}_0$ is derived by normalizing to unity the mass distribution function in the surveyed mass range $M_{\mathrm{min}} - M_{\mathrm{max}}$.

The spatial (radial) distribution of substructures is $\rho_{\mathrm{sh}}(R)$

$$\rho_{\mathrm{sh}}(R) = \rho_a \exp\left\{-\frac{2}{\alpha_a}\left[\left(\frac{R}{r_a}\right)^{\alpha_a} - 1\right]\right\} \;, \tag{5.6}$$

with $\alpha = 0.678$ and $r_a = 199$ kpc (corresponding to the scale radius of the distribution). *Aquarius* thus finds that the number density of subhalos increases towards the halo center but much more slowly than the total DM density. This results in more subhalos of a given mass lying in the outer part of the halo, i.e. $R \gtrsim 100$ kpc.

The substructure distribution is normalized such that:

$$4\pi \int_0^{R_{\mathrm{vir}}} dR\, R^2\, \rho_{\mathrm{sh}}(R) \int_{M_1}^{M_2} dm\, m\, \mathcal{F}(\mu, m) = f\, M_{\mathrm{MW}} \;, \tag{5.7}$$

where f is the fraction of subhalos resolved by the simulation between $M_1 - M_2$ as quoted in Tab. 5.1.

The fraction of the total mass found in substructures in the whole surveyed mass range $M_{\mathrm{min}} - M_{\mathrm{max}}$ is f_{tot} and it is derived as follows:

$$f_{\mathrm{tot}} = f \times \frac{\int_{M_{\mathrm{min}}}^{M_{\mathrm{max}}} dm\, m\, \mathcal{F}(\mu, m)}{\int_{M_1}^{M_2} dm\, m\, \mathcal{F}(\mu, m)} \;. \tag{5.8}$$

[iv] We assume $M_{\mathrm{cut}} = 10^{-6}\, M_\odot$, as it is typically done in the literature. As an example, in the case of neutralino DM, M_{cut} can vary between $10^{-3}\, M_\odot$ and $10^{-11}\, M_\odot$ depending on the particle physics model. Indeed, the particle nature of the DM determines the small-scale cutoff in the matter power spectrum of density fluctuations from which the minimum mass M_{cut} is inferred (Green et al., 2004, 2005; Bringmann, 2009). Even larger cutoff values are possible if the WIMPs couple to light force carriers (Aarssen, Bringmann & Goedecke, 2012).

Table 5.1: Numerical values of the parameters of the DM distribution based on *Aquarius* results.

R_{vir} (kpc)	433
M_{MW} ($M_\odot$)	2.5×10^{12}
M_{res} ($M_\odot$)	$10^{4.5}$
α	0.17
r_s (kpc)	20
ρ_s ($10^6 M_\odot$ kpc^{-3})	2.8
$R_a(kpc)$	199
α_a	0.678
μ	1.9
f	0.132
M_1 (M_{MW})	1.8×10^{-8}
M_2 (M_{MW})	10^{-2}
M_{min} ($M_\odot$)	10^{-6}
M_{max} (M_{MW})	10^{-2}
$\mathcal{F}_0$ ($M_\odot^{-1}$)	3.6×10^{-6}
N_{sub}	1.1×10^{15}
$M_{\mathrm{sub}}^{\mathrm{tot}}(< R_{\mathrm{vir}})$ ($M_\odot$)	4.2×10^{11}
$f_{\mathrm{tot}}(< R_{\mathrm{vir}})$	0.17
ρ_a ($M_\odot$ kpc^{-3})	2840

Finally, the mass and spatial probability distribution functions (i.e. normalized to unity) are:

$$\frac{dP_M}{dM_{\mathrm{sh}}} = \mathcal{F}(\mu, M_{\mathrm{sh}}) \, , \tag{5.9}$$

$$\frac{dP_R}{dV} = \frac{\rho_{\mathrm{sh}}(R)}{f_{\mathrm{tot}}\, M_{\mathrm{MW}}} \, . \tag{5.10}$$

The numerical values of the parameters used are summarized in Tab. 5.1.

The parameters $r_{s,\mathrm{cl}}$ and $\rho_{s,\mathrm{cl}}$ of the individual substructure profile are derived, for each clump, from clump's virialized mass, M_{cl} and position R as extracted from the subhalo mass probability distribution through Monte Carlo methods[v]. $\rho_{s,\mathrm{cl}}$ is obtained by normalizing $\rho_{\mathrm{cl}}(r)$ over the volume of the subhalo to give its virialized mass. The virial radius, which determines

---

[v] The constraint the simulated subhalos must fulfill is that $\sum_i M_{\mathrm{cl},i} = f_{\mathrm{tot}} M_{\mathrm{MW}}$, where i runs over the simulated subhalos.

the size of the halo, is defined as:

$$r_{\mathrm{vir,cl}} = \left(\frac{3M_{\mathrm{cl}}}{4\pi 200 \rho_{\mathrm{cr}}} \right)^{\frac{1}{3}} , \tag{5.11}$$

where ρ_{cr} is the critical density of the universe $\rho_{\mathrm{cr}} = 3H_0^2/(8\pi G)$. The equation above defines the so-called r_{200}, i.e. the radius (measured from the center of the clump) which encloses an average DM density equal to 200 times the critical density.

The scale radius $r_{s,\mathrm{cl}}$ for the Einasto profile is derived in analogy with the NFW profile through the concentration:

$$c_{200,\mathrm{cl}} = \frac{r_{200,\mathrm{cl}}}{r_{s,\mathrm{cl}}} . \tag{5.12}$$

The concentration depends in general on the clump mass and on the position in the halo. According to numerical simulations it can be parameterized as (Pieri et al., 2011)

$$c_{200}(M_{\mathrm{cl}}, R) = \left(\frac{R}{R_{\mathrm{vir}}} \right)^{-\alpha_R} \times \left[C_1 \left(\frac{M_{\mathrm{cl}}}{M_\odot} \right)^{-\alpha_1} + C_2 \left(\frac{M_{\mathrm{cl}}}{M_\odot} \right)^{-\alpha_2} \right] , \tag{5.13}$$

where $\alpha_R = 0.237, C_1 = 232.15, C_2 = -181.74, \alpha_1 = 0.0146$, and $\alpha_2 = 0.008$.

The above discussion includes also an extrapolation of the substructures profiles in the GC region which is poorly explored by simulations due to limited spatial resolution (for *Aquarius* the resolution is $\sim$ 200 pc). Indeed, the actual distribution might be different from the extrapolated one, due to the presence of external tides that cause mass losses to the subhalos close to the GC. To account for this effect, the so called Roche criterion is applied: a substructure is destroyed when its scale radius $r_{s,\mathrm{cl}}$ is larger than the tidal radius r_{tid}, i.e. the radius at which the tidal forces of the host potential are as intense as the self-gravity of the subhalo:

$$r_{\mathrm{tid}}(R) = \left(\frac{M_{\mathrm{cl}}}{3M_{\mathrm{MW}}} \right)^{1/3} R . \tag{5.14}$$

The Monte Carlo algorithm, within the Milky Way virial radius and until the total substructure mass is not reached, dials the position and the mass of a substructure according to Eq. 5.5. Then, if the substructure survives tidal disruption, its concentration is computed and its scale radius is inferred. Finally, all the other relevant clumps parameters are derived and stored.

Fig. 5.1 shows the mass and spatial distribution for a realization of the Monte Carlo simulation. The left panel displays the histogram of the mass distribution (in unit of the $\log_{10}$) for the subhalos. As expected, few structures with masses above $10^8 M_\odot$ are created, whereas the most of the substructures accumulates at small masses. In the right panel the histogram of

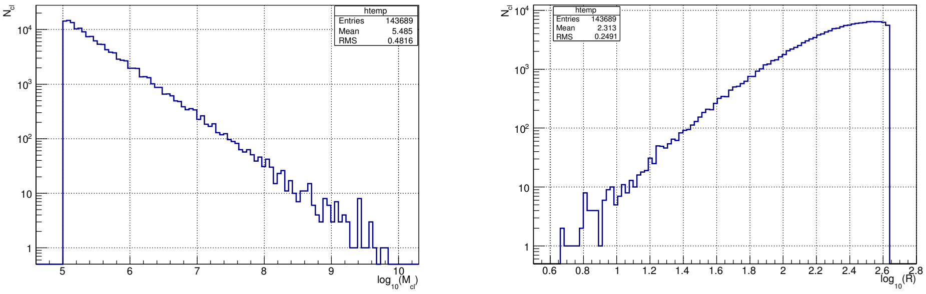

Figure 5.1: Example of subhalo mass (left panel) and radial (right panel) distribution for a halo realization of the Monte Carlo simulation described in Sec. 5.1.

the distance of the subhalos from the GC R is shown. The radial distribution of substructures is *antibiased* with respect to the smooth halo and more structures are found in the outermost region of the galaxy (the radial edge for the simulation has been assumed equal to the virial radius of the galaxy, $R_{\rm vir}$).

5.2 Dark Matter anisotropy signal

The good angular resolution ($\lesssim 0.15°$ for $E \gtrsim 10$ GeV) of the *Fermi*-LAT has allowed the measurement of the APS of the IGRB (Ackermann, Ajello, Albert, Baldini, Ballet et al., 2012), which is consistent with a constant value within each energy bin, as explained in chapter 3.

Besides standard astrophysical contributions, also DM is expected to leave its imprint in the γ-ray APS as a consequence of WIMPs annihilation or decay.

The study of the APS is interesting because it is complementary to the analysis of the intensity energy spectrum, i.e. the IGRB measured flux, it can unveil the spatial distribution of sources and even help in disentangling contributions to the IGRB originating from different source populations (Hensley et al., 2010).

If the APS is DM-induced, it consists of: an extragalactic contribution, a smooth galactic contribution, characterized by an intrinsic anisotropy, and a galactic subhalos contribution.

Pioneering works emphasized the importance of galactic DM as a contribution to the γ-ray anisotropy e.g. (Siegal-Gaskins, 2008; Ando, 2009), as well as the effect of including extragalactic substructures (Lee et al., 2009; Ando et al., 2007). Nevertheless, estimates of the APS have always been affected by great uncertainty due to the modeling of the DM distribution at galactic and cosmological scales.

Analytic Monte Carlo approaches (similar to the one followed by our analysis) have shown that the contribution of the galactic signal is in general expected to dominate the extragalactic DM component, although highly depending on the adopted model for the substructure distribution (Fornasa, Pieri, Bertone & Branchini, 2009).

A very exhaustive discussion about the energy spectrum and the APS due to galactic and extragalactic DM sources has been provided (Fornasa et al., 2013). In that work the authors used the results of the detailed cosmological structure formation N-body simulation *Millennium-II* (Boylan-Kolchin, Springel, White, Jenkins & Lemson, 2009) and of the *Aquarius* (Springel et al., 2008) simulation to compute both the energy spectrum and the APS for annihilating and decaying DM. In contrast with previous works, these observables were computed by directly using the results of the numerical N-body simulations instead of analytic Monte Carlo simulations or other hybrid methods.

As far as uncertainties on the galactic contribution are concerned, we individuate, besides the ones discussed in (Fornasa et al., 2013), at least two other sources of uncertainty that must be taken into account. First of all, computing the power spectrum at $\ell \gtrsim 100$ requires to extrapolate the DM profile down to very small scales, much below the resolution of current numerical simulations. Furthermore, the substructures with large mass ($M \gtrsim 10^8\ M_\odot$) are expected to be only a few and hence the statistical fluctuations associated to their distribution can be large.

In the next sections we present the framework of our analysis which relies on both N-body simulations and analytic Monte Carlo studies of the subhalo galactic population and we then compute the APS for galactic DM by emphasizing the theoretical uncertainties affecting the predictions. Results presented here are still preliminary.

We here consider only the galactic DM distribution, whereas we have not included any contribution from DM in extragalactic structures. In fact, as discussed in (Fornasa et al., 2013), the contribution from extragalactic DM halos and subhalos that are not resolved by N-body simulations leads to about two orders of magnitude uncertainty on the predicted level of the extragalactic energy spectrum, which may result as the dominant or the subdominant component of the total energy spectrum. Similarly, the APS can receive a significant or a negligible contribution from extragalactic (sub)structures. We have therefore chosen to focus on the properties of the APS for the galactic DM emission.

5.2.1 The angular power spectrum of γ-ray anisotropies

The APS C_ℓ of an intensity map $I(\Psi)$, where Ψ is a direction in the sky, depends on the statistical properties of the fluctuations of the map around its mean. The *intensity* APS is given by the coefficients

$$C_\ell = \frac{1}{2\ell+1}\left(\sum_{|m|<\ell}\langle|a_{\ell m}|^2\rangle\right) \tag{5.15}$$

with the $a_{\ell m}$ determined by expanding the map in spherical harmonics $Y_{\ell m}$, after subtracting the average value of the intensity over the region of the sky considered:

$$I(\Psi) = \frac{\mathrm{d}\Phi}{\mathrm{d}E}(\Psi) - \langle\frac{\mathrm{d}\Phi}{\mathrm{d}E}\rangle = \sum_{\ell=0}^{\infty}\sum_{m=-\ell}^{m=\ell} a_{\ell m}Y^*_{\ell m}(\Psi). \tag{5.16}$$

The *intensity* APS indicates the dimensionful size of intensity fluctuations and can be compared with predictions for astrophysical sources whose collective intensity is known or assumed (Siegal-Gaskins et al., 2011). Moreover, the *intensity* APS is an additive quantity: the *intensity* APS of a sum of maps is equivalent to the sum of the *intensity* APS of each map, provided that the maps are uncorrelated (i.e. that the product $a_i a_j^* = 0$). The C_ℓ roughly corresponds to the correlation between two points on the sky separated by an angle $\theta \sim \pi/\ell$. However, it is possible to define also another quantity, the so-called *fluctuation* APS, by dividing the *intensity* APS C_ℓ of a map by the mean sky intensity squared $\langle \mathrm{d}\Phi/\mathrm{d}E\rangle^2$. The *fluctuation* APS characterizes the angular distribution of the emission independently of the intensity normalization and it is dimensionless.

To obtain the *fluctuation* APS of a sum of maps, it is necessary to multiply each coefficient by the relative emission of each map with respect to the total, squared:

$$C_\ell^{\mathrm{fluct}} = \sum_i f_i^2 C_{\ell,i}^{\mathrm{fluct}}\,, \tag{5.17}$$

where $f_i = \frac{\langle \mathrm{d}\Phi^i/\mathrm{d}E\rangle}{\langle \mathrm{d}\Phi/\mathrm{d}E\rangle}$ and in the case of zero cross products[vi].

In the case of annihilating DM $I(\Psi)$ is the intensity averaged map of the γ-ray flux in the direction Ψ as given by Eq. 3.1, where $\cos(\Psi) = \cos(\psi)\cos(\theta)$ with ψ and θ being the longitude and the latitude respectively.

5.2.2 Sky-maps generation

The γ-ray intensity maps and their power spectra are generated by using the HEALPix software[vii] (Górski et al., 2005). Maps with the same angular

---

[vi] In the case of two correlated components Eq. 5.17 writes as: $C_\ell^{\mathrm{fluct}} = \sum_{i=1}^{2} f_i^2 C_{\ell,i}^{\mathrm{fluct}} + 2f_1f_2C_{\ell,1\times 2}^{\mathrm{fluct}}$.

[vii] `http://healpix.sourceforge.net`

resolution as *Fermi* are created by setting the map order parameter $k = 9$[viii]. The resolution of the map corresponds to an angular area of approximately 4×10^{-6} sr for each pixel. Presently, the analysis is extended up to $\ell_{\rm max} = 520$, although we are currently testing the extension to higher multipoles in order to make predictions for the next generation of γ-ray telescopes, i.e. CTA (angular resolution $\Delta\theta \sim 0.05°$).

The γ-ray intensity maps are computed according to Eq. 3.1, by integrating the DM distribution ρ along every direction Ψ in the sky. The units of the γ-ray maps are thus $\rm cm^{-2}s^{-1}sr^{-1}\ GeV^{-1}$.

The particle physics factor represents an overall normalization of the map once a DM benchmark set of parameters has been chosen. We here consider annihilation into 100% $b\bar{b}$ (the spectrum for the prompt emission dN/dE follows the parameterization given in (Cembranos et al., 2011)), a DM mass of 200 GeV and $\langle\sigma_{\rm ann}v\rangle \sim 3\cdot 10^{-26}\rm cm^3s^{-1}$. The γ-ray flux has been obtained at 4 GeV, in analogy with (Fornasa et al., 2013) to allow a more easy comparison among the results. We do not consider the ICS component.

The galactic DM distribution, ρ, is composed by the main galactic halo and the substructures. The population of subhalos is simulated by means of the analytic Monte Carlo described in section 5.1 for a mass range $M^{MC}_{\rm min} = 10^5 M_\odot$ and $M^{MC}_{\rm max} = 10^{10} M_\odot$.

According to Eq. 3.1, the J-value, i.e. the term $J(\psi, \theta, \Delta\Omega)$, corresponds to the integration of the ρ^2 along the l.o.s. in the observational cone of solid angle $\Delta\Omega$:

$$J(\psi, \theta, \Delta\Omega) = \int_0^{\Delta\Omega} {\rm d}\Omega \int_{\rm l.o.s} \rho^2(s, \psi, \theta)\ \ {\rm d}s\ , \tag{5.18}$$

where $\rho(s, \psi, \theta)$ is the DM density at distance s from Earth in the direction ψ, θ (longitude and latitude in Galactic coordinates).

In our calculations, however, we will make the observational solid angle very small, such that we will compute the following quantity

$$J(\psi, \theta) = \frac{1}{\Delta\Omega} J(\psi, \theta, \Delta\Omega) \simeq \int_{\rm l.o.s} \rho^2(s, \psi, \theta)\ \ {\rm d}s\ . \tag{5.19}$$

[viii] The order of the map, k, is related to the number of pixels in the map by the relation: $N_{\rm pix} = 12\,(2^k)^2$ and the parameter which gives information about the resolution of the map is $N_{\rm side} = 2^k$. The maximal allowed multipole up to which the decomposition in sherical harmonics is reliable is $\ell_{max} \sim 2N_{\rm side}$.

Hence, the J-value writes as:

$$
\begin{aligned}
J &= \int_{\text{l. o. s.}} \left(\rho_{\text{sm}}(s) + \sum_i \rho_{\text{cl},i}(s) \right)^2 ds \\
&= \int_{\text{l. o. s.}} \left(\rho_{\text{sm}}(s)^2 + \sum_i \rho_{\text{cl},i}(s)^2 + 2\, \rho_{\text{sm}}(s) \cdot \sum_i \rho_{\text{cl},i}(s) + \sum_i \sum_{j \neq i} \rho_{\text{cl},i}(s) \cdot \rho_{\text{cl},j}(s) \right) ds \\
&= J_{\text{sm}} + J_{\text{cl}} + J_{\text{cl,sm}} + J_{\text{cl,cl}}
\end{aligned}
\tag{5.20}
$$

where

$$J_{\text{sm}} = \int_{\text{l. o. s.}} \rho_{\text{sm}}(s)^2\, ds \tag{5.21}$$

$$J_{\text{cl}} = \int_{\text{l. o. s.}} \sum_i \rho_{\text{cl},i}(s)^2\, ds \tag{5.22}$$

$$J_{\text{cl,sm}} = 2 \int_{\text{l. o. s.}} \sum_i \rho_{\text{sm}}(s) \cdot \rho_{\text{cl},i}(s)\, ds \tag{5.23}$$

$$J_{\text{cl,cl}} = \int_{\text{l. o. s.}} \sum_i \sum_{j \neq i} \rho_{\text{cl},i}(s) \cdot \rho_{\text{cl},j}(s)\, ds \tag{5.24}$$

with *sm* referring to the smooth component and *cl* to the subhalos contribution.

The dominant terms are J_{sm} and J_{cl}, whereas we find the interference terms subdominant and computationally very time-consuming. In order to speed up the calculations, we compute them according to a simplified procedure. As far as $J_{\text{cl,sm}}$ is concerned, the integral is evaluated by taking into account the emission from the clump up to a radial distance from its center equal to N times the virial radius, with $N = 4$. We have tested the impact of varying N on both the intensity maps and the power spectrum, up to $N = 10$. By varying N, the power spectra differ by less than few percent at low multipoles and are equivalent from $\ell = 5$ on.

The interference term $J_{\text{cl,cl}}$ is evaluated by considering non-zero the product $\rho_{\text{cl},i}\rho_{\text{cl},j}$ only if the following two conditions are satisfied (i) the relative distance between the two clumps is less than ten times the sum of the two virial radii, (ii) the distance from the l.o.s. to the center of each clump is equal to 4 times its virial radius. Although we checked that varying the two conditions impacts less than few percent on the total intensity maps for a limited subhalo mass range, the computation of such an interference term in the whole mass range turns out to be too time-consuming to be included in this analysis. A confirmation of its sub-dominance at small angular scales with respect to the main contributions is reported in (Ando, 2009). We anyhow postpone the detailed study of the impact of the interference term $J_{\text{cl,cl}}$ on the APS to a future work.

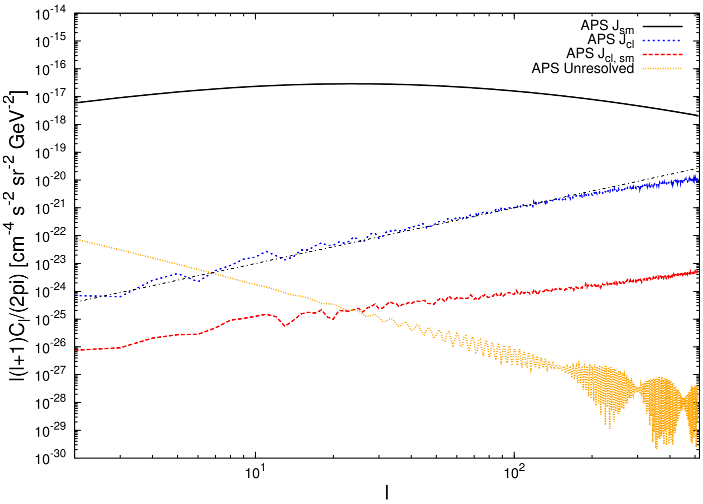

Figure 5.2: *Intensity* APS for the different components of the galactic DM distribution for a single halo Monte Carlo realization. The displayed contributions are: smooth halo (solid black); subhalos (dotted blue); unresolved subhalos, i.e. $M = 10^{-6} - 10^{5} M_\odot$ (dotted orange) and the interference term $J_{\rm sm}$ (dashed red). The dot-dashed black line indicate an APS growing as ℓ^2, i.e. a Poissonian APS independent on multipole, and normalized to the subhalos contribution at $\ell = 100$.

As we have explained previously, the subhalo mass density profile has been derived from a fit to the current simulations' results and it is strictly valid only down to the mass resolution limit of the simulations. Yet, substructures with smaller mass could be present and we need to evaluate their contribution. In order to extrapolate the distribution of substructures in a mass range below the simulation resolution, we assume that both mass and space probability distributions are the same as for the resolved substructures, and we compute the contribution of "unresolved" substructures from 10^{-6} $M_\odot$ up to 10^{5} $M_\odot$ as follows.

From the spatial and mass probability distribution functions of Eqs. 5.9 – 5.10 we compute the average contribution from the unresolved clump distribution:

$$\langle J_{\rm cl}^{\rm unres} \rangle = N_{\rm tot} \int_{\rm l.\,o.\,s.} \frac{dP_{\rm R}}{dV}\, dl \int_{M_{\rm min}}^{M_{\rm max}} \mathcal{L}(M)\, \frac{dP_{\rm M}}{dM}\, dM\,, \tag{5.25}$$

where $\mathcal{L}(M)$ is the luminosity of a single clump:

$$\mathcal{L}(M) = \int_{V_{\rm cl}} \rho_{\rm cl}(r)^2 dV = 4\,\pi \int_0^{R_{\rm vir,cl}} \rho_{\rm cl}(r)^2\, r^2\, dr\,. \tag{5.26}$$

and $M_{\rm min} = 10^{-6} M_\odot$ and $M_{\rm max} = 10^{5} M_\odot$. Increasing the number of small structures should have the effect of making the sky more isotropic and thus we expect a subdominant contribution of the smallest halos. Notice moreover that we here compute only an average contribution assuming small statistical fluctuations. Our results are compatible with (Fornasa et al., 2009). We here neglect the cross correlation term between unresolved substructures and the main smooth halo which has been shown to be highly subdominant (Fornasa et al., 2009). On the other hand, the cross correlation between unresolved substructures and "resolved" ones (i.e. $M \gtrsim 10^5 M_\odot$) is expected to vanish since a resolved subhalos at a given location excludes the presence of an unresolved substructure at the same location.

Fig. 5.2 summarizes the contributions to the *intensity* APS of the different galactic components. The result refers to a single halo realization of the Monte Carlo simulation illustrated above. The main halo (solid black line) dominates the APS at all multipoles. The subhalos (dotted blue curve) constitute the second main contribution. The growth of the APS of an unclustered population would be $\propto \ell^2$, i.e. a Poissonian APS independent on multipole, as it is predicted for standard astrophysical populations. On the contrary, it has been suggested that DM substructures would show a specific behavior which departs from $\propto \ell^2$ at higher multipoles (Ando, 2009). In this case, the suppression at smaller angular scales compared with the noise-like spectrum is too mild to conclude that the internal structure of the subhalos may be proved with this analysis and that the DM contribution does not behave as a population of γ-ray point sources. The cross correlation term between the main halo and the clumps is instead subdominant (dashed red line). As expected the contribution due to clumps with mass smaller than $10^5 M_\odot$ is suppressed (dotted orange line).

We notice that our estimate is consistent with the results of (Fornasa et al., 2013) within the theoretical uncertainty band that we compute in the next section.

5.2.3 Uncertainties on the angular power spectrum of galactic Dark Matter

We here discuss the theoretical uncertainties that affect the prediction of the APS of galactic DM, namely (i) the intrinsic uncertainty due to the extrapolation to short distances of the DM distribution determined from numerical simulations, and (ii) the statistical fluctuations implied by the mass and spatial distributions of subhalos.

Extrapolation to short distances of the DM distribution. A fundamental limitation of N-body simulations has been shown to be its spatial resolution, e.g. $\sim$ 200 pc in the case of *Aquarius*. The fact that below this resolution aggressive extrapolations are required in order to make statements and predictions on small angular scales determines an important theoretical

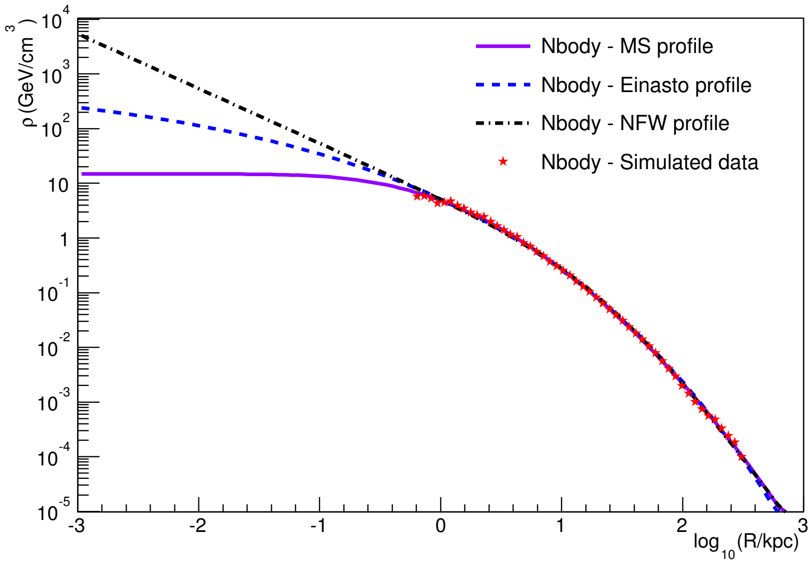

Figure 5.3: DM spatial profiles for the main halo in a typical N-body simulation. The same halo has been fitted using a NFW profile (dot-dashed black line), a Moore & Stadel – MS – (solid violet curve) and an Einasto profile (dashed blue curve). Red points refer to the simulation data.

uncertainty.

Indeed, for a source located at the GC, like the main halo of the Milky Way, the APS at multipoles $\ell > 100$ probes the DM distribution at $R < \pi/100 \cdot 8.5$ kpc$\sim$ 200pc. The study of the APS at $\ell \gtrsim 100$ requires therefore to extrapolate the DM profile to scales much below the resolution of current numerical simulations. Radial DM profiles differing in the center of the galaxy could then modify the predicted anisotropy level, as we will see in the following.

Moreover, the same extrapolation concerns also the individual subhalos and consequently impacts on the APS prediction.

By making use of results from numerical N-body simulations, we here study how the APS for galactic DM varies because of the extrapolation down to scales smaller than the resolution of the simulation of the DM density profiles of both the main halo and the substructures.

Our analysis is based on the g15784 PDM cosmological simulation which is part of the Making Galaxies in a Cosmological Context (MaGICC) project. This Milky Way-like galaxy has a total mass of $1.48 \times 10^{12} \mathrm{M}_\odot$ and spatial resolution of about 300 pc (Stinson et al., 2010; Stinson et al., 2012; Macciò et al., 2012).

The main halo has been fitted with three different parametrizations of

Table 5.2: Numerical values of the best-fit parameters for the different DM distributions (g15784 galaxy). Each profile is characterized by specific parameters, according to Eqs. 3.3, 3.4 and 3.5. The reduced χ^2 value of the fit is quoted as well.

Profile (Γ, Δ, Ω)	Γ (kpc)	Δ (ρ_{cr})	Ω	χ^2/d. o. f.
NFW (r_s, ρ_s, $-$)	16.8	$9.37 \cdot 10^4$	–	0.005
Einasto $(r_{-2}, \rho_{-2}, \alpha)$	19.6	$1.58 \cdot 10^4$	0.183	0.003
Moore & Stadel $(r_\lambda, \rho_0, \lambda)$	0.0541	$6.77 \cdot 10^6$	0.175	0.006

the total profile: NFW (Eq. 3.3 with $(\alpha, \beta, \gamma) = (1, 3, 1)$), Einasto (Eq. 3.4) and Moore & Stadel (Eq. 3.5). The best-fit values for the profile parameters are quoted in Tab. 5.2 and results of the fit are displayed in Fig. 5.3 together with the data points of the simulation. The three fitting formulae give a good fit to the data but they distinguish at small scales, below the resolution of the simulation $\sim$ 300 pc.

The simulation has resolved 27 subhalos in the mass range $M = 10^8 - 10^{10} M_\odot$. Each subhalo has then been fitted, as in the case of the main halo, by the three different profiles. In general the NFW profile leads to a χ^2 worse than the Einasto and Moore & Stadel profiles, indicating that the usage of such a cuspy profile might be questionable.

Fig. 5.4 represents the intensity maps of the γ-ray differential flux corresponding to the Einasto profile fit. The top panel corresponds to the smooth component of the main halo, whereas in the bottom panel the intensity due to the resolved substructures is shown. Analogously, we create γ-ray maps with the NFW and MS profile best-fit parameters. We notice that the integration of the NFW profile down to $R \to 0$ has been performed by imposing a constant value of the density profile below $R_{\rm cut} = 10^{-7} R_{\rm vir}$ after having tested the stability of the results by varying $R_{\rm cut}$ in the range $10^{-5} - 10^{-9} R_{\rm vir}$.

We now discuss the computation of the expected APS.

Firstly, we notice that computing the APS of the main DM halo (as well as of the substructures) requires to extrapolate the profiles down to scales smaller than the simulation resolution. Fig. 5.5 shows how the *fluctuation* APS (for a "test" galaxy) is affected by the resolution: a cut on the distance R corresponding to the length resolution of the simulation is applied on the profile, i.e. the profile is set to zero for distances smaller than the length resolution. By varying the cut, the APS departs from the full APS (i.e. without any cut on R) and starts to be dominated by shot noise. Although too much conservative, such a figure can give the idea of which is the impact of the finite resolution of the simulation.

By keeping in mind this caveat, in what follows we extrapolate the DM

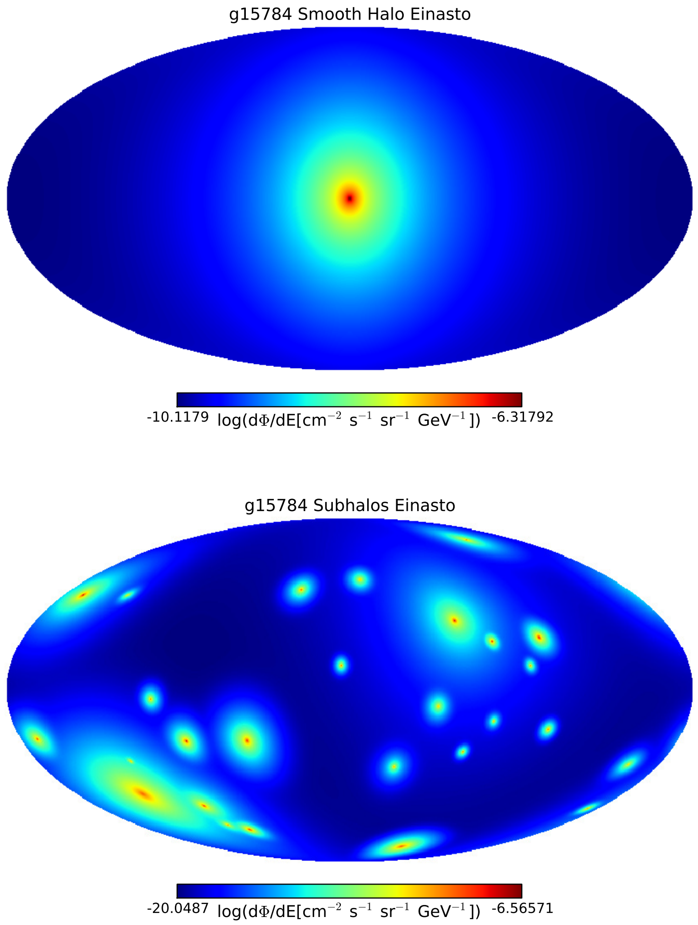
g15784 Smooth Halo Einasto

g15784 Subhalos Einasto

Figure 5.4: Intensity maps of the γ-ray differential flux ($\log_{10}(d\Phi/dE)$) for the g15784 galaxy according to the Einasto best-fit parameters. The top panel corresponds to the smooth component of the main halo, whereas the bottom panel refers to the flux from the resolved substructures.

profile down to short distances and we then compute the expected APS. Fig. 5.6 displays the *intensity* APS for the galactic DM distribution as predicted by the g15784 simulation when considering different halo profiles fitting formulae. Solid lines refer to the smooth halo fitted by the three profiles NFW (green), Einasto (red) and Moore & Stadel (blue). The three curves have the same power at large scales but differ at smaller scales, i.e. higher multipoles. At these scales, the most cored profile (i.e. Moore & Stadel) predicts the lowest anisotropy while the central cusp of the NFW profile results in a stronger anisotropy, which is almost constant at all multipoles. The different behavior of the main halo profiles at small scales affects the

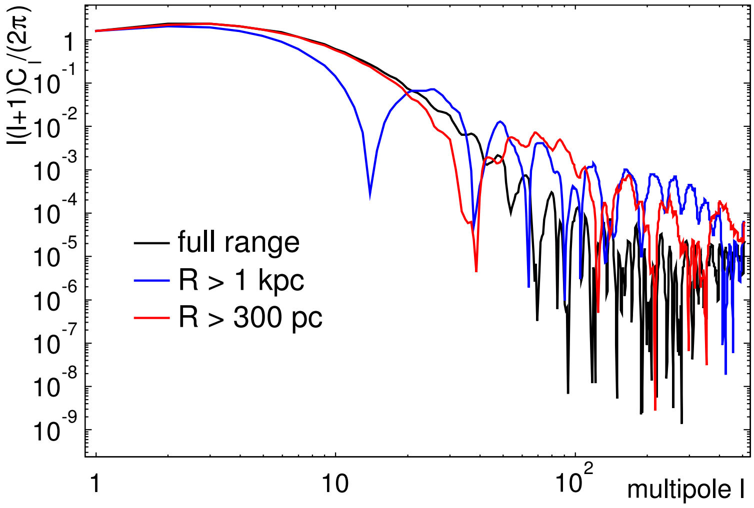

Figure 5.5: Impact of the finite resolution of the simulation on the *fluctuation* APS: the profile is set to zero for distances smaller than the length resolutions of 1 kpc and 300 pc. "Full" refers to the profile without any applied cut.

APS up to seven orders of magnitude at large multipoles ($\ell \sim 500$).

The same procedure, i.e. extrapolation to small scales, has been adopted also in computing the *intensity* APS for the substructures, displayed in Fig. 5.6 by dashed lines for the three different profiles. For the distribution of substructures with $M < 10^8 M_\odot$, that are not resolved in hydrodynamical simulations, we will resort to the results of the *Aquarius* simulation. We anyhow expect that drawing the distribution of individual clumps with $M = 10^5 - 10^8 M_\odot$ with the Monte Carlo procedure outlined in section 5.1 would not alter the main result of Fig. 5.6.

As to the subhalos contribution, Einasto and NFW profiles seems to indicate that (i) the anisotropy mildly depends on the choice of the subhalo inner profile (ii) the shape of the predicted APS is consistent with a Poisson-like APS as it is the case for an unclustered source population. On the other hand, the APS is much milder in the case of the cored MS profile and it clearly departs from the $\propto \ell^2$ behavior at high multipoles ($\ell \gtrsim 100$). Such a behavior, instead, is more consistent with predictions for galactic DM substructure APS dominated by the largest structures (i.e. $M \gtrsim 10^8 M_\odot$) (Ando, 2009).

Moreover, when considering both the smooth and subhalos contributions, the APS signal is dominated by the smooth halo component in the case of NFW and Einasto profiles in the whole multipole range, but if the

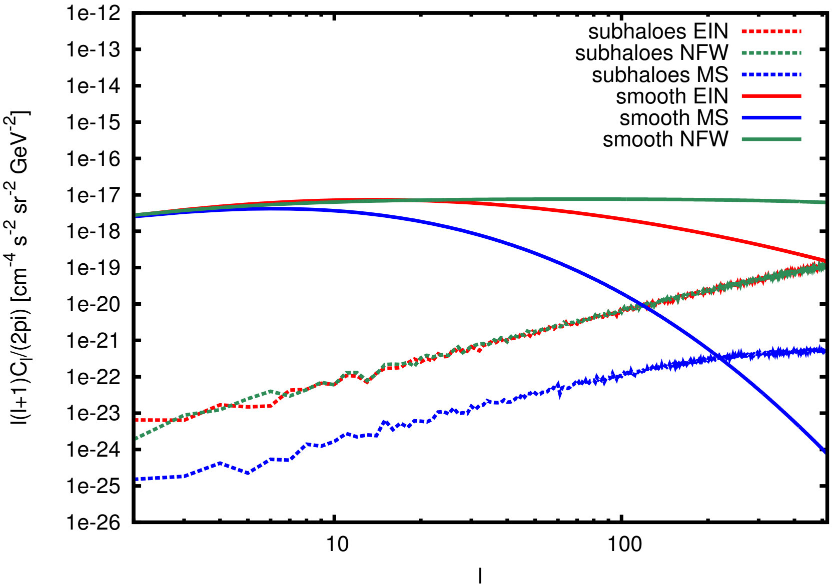

Figure 5.6: *Intensity* APS of the set of all-sky γ-ray maps from DM annihilation. Solid (dashed) lines indicate the smooth (clumps) contribution. Green lines stand for halos whose density distribution is fitted with a NFW profile; red lines refer to the Einasto profile whereas blue lines to the MS profile. The *intensity* APS gives a measure of the relative anisotropies of the smooth halo and subhalos components.

DM density profile inside halos is described by the cored profile of MS this conclusion is not valid anymore. In the latter case, indeed, the APS for the subhalos becomes dominant at $\ell \sim 200$.

With this analysis we demonstrate that the predicted APS is highly affected by the extrapolation to short distances of the DM profile in both the main halo and substructures. In the case of Einasto and NFW profiles similar conclusions can be derived: the smooth main halo would always (i.e. at all multipoles) dominate the subhalos APS. In a very optimistic perspective for future data, this can allow a discrimination of the shape of the smooth profile at small scales and can thus represent a powerful tool for relieving the “cusp/core” problem.

If, instead, the Moore & Stadel profile will be confirmed as best-fit of N-body simulation results (by the next high-resolution simulations), the substructures APS will show up at high multipoles and this can have important consequences on the detectability of the anisotropy DM signal since it would distinguish from the Poisson-like noise expected from other astrophysical sources.

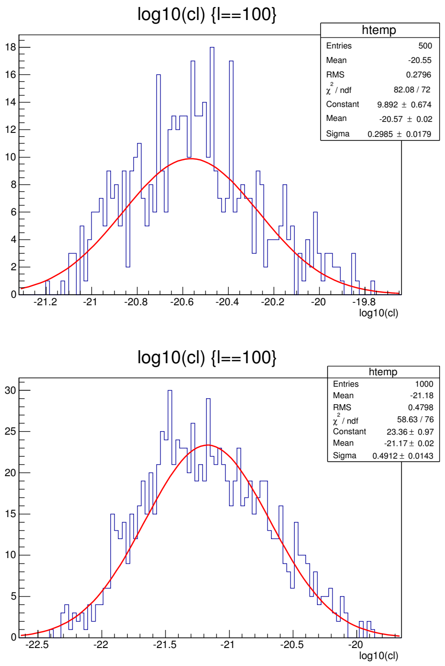

Figure 5.7: Distribution of C_ℓ for $\ell = 100$ of the two sets of Monte Carlo realizations: $10^5 < M/M_\odot < 10^{10}$ (500 realizations, top panel) and $10^8 < M/M_\odot < 10^{10}$ (1000 realizations, bottom panel). The C_ℓ distribution is well fitted by a log-normal function (red solid line) in both cases.

Statistical uncertainty of the single halo Monte Carlo realization. Substructures, notably the ones with large mass ($M \gtrsim 10^8\ M_\odot$), are expected to be only a few. This imply that the statistical fluctuations associated to their distribution can be large and predictions on anisotropy based on a single halo Monte Carlo realization could be strongly biased.

We therefore evaluate the uncertainty on the single halo Monte Carlo realization by performing several realizations of the substructure distribution. We perform 500 realizations in the mass range $10^5 < M/M_\odot < 10^{10}$ and 1000 in the range $10^8 < M/M_\odot < 10^{10}$ in order to assess the importance of the fluctuations due to heavier clumps.

For each ℓ the distribution of the C_ℓ is fitted with a log-normal function (as it is expected for a product of independent variables as the C_ℓ are). We display in Fig. 5.7 the C_ℓ distribution for $\ell = 100$, together with its best-fit function for the two sets of simulations. The low value of the χ^2 that we find in all our fits makes us confident that our distributions are statistically convergent, at least to percent precision.

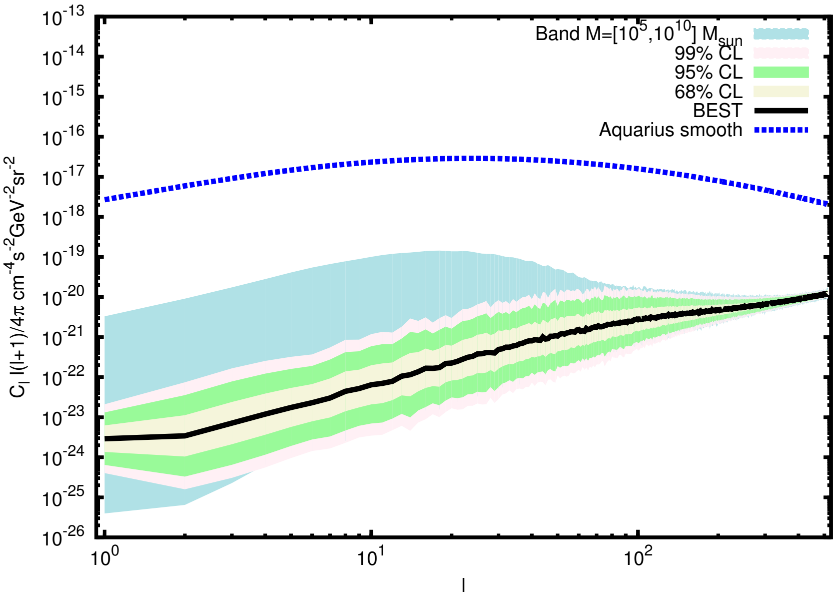

Figure 5.8: The shaded area represents the theoretical uncertainty band at 99% (light pink), 95% (green), 68% (light yellow) C.L. on the best-fit (solid black line) predicted APS for the subhalo distribution in the mass range $10^5 < M/M_\odot < 10^{10}$. The shaded light blue area represents all the 500 simulated Monte Carlo realizations. The dotted blue curve corresponds to the smooth halo APS contribution.

The statistical distribution of the C_ℓ for each ℓ allows us to draw the uncertainty band of the APS.

We show in Fig. 5.8 the best-fit, the 99%, 95%, 68% C.L. uncertainty band as resulting from our Monte Carlo for the range $10^5 < M/M_\odot < 10^{10}$. We checked the the main variation is due to the mass range $10^8 < M/M_\odot < 10^{10}$, whereas the statistical fluctuation for $10^5 < M/M_\odot < 10^8$ is reduced. While for high multipoles, in principle testable with *Fermi*-LAT or other future experiments, the uncertainty on the total APS is reduced to approximately a few %, for $\ell \lesssim 100$ it can exceed one order of magnitude. In no cases, however, the substructure contribution overshoot the main halo one.

For the sake of clarity, the predictions for the galactic DM APS performed in this chapter are not meant to be compared with *Fermi*-LAT measurements although they stand anyhow much below the current data. Indeed, such a comparison would require to mask the region of the sky at low galactic latitudes ($|b| \leq 30°$) as it has been done for the anisotropy analysis of the *Fermi*-LAT data (Ackermann, Ajello, Albert, Baldini, Ballet et al., 2012). Masking low galactic latitudes might alter the relative importance of the various components in the determination of the *intensity* APS. Moreover, *Fermi*-LAT anisotropy measurements correspond to finite energy bins and thus an additional integration over the energy range of interest would be required. Nevertheless, even in the case of a proper analysis aimed to set constraints on the DM anisotropy signal from data, the upper limits on *Fermi*-LAT anisotropy are about three orders of magnitude larger than predictions for DM as it has been demonstrated in (Ando & Komatsu, 2013).

This line of investigation deserves to be pursued not the least for the complementarity among angular and spectral DM searches.

Chapter 6

MAGN: a new relevant contribution to the IGRB

In Sec. 3.4 the MAGN population has been introduced in the framework of the AGN unification scheme (Urry & Padovani, 1995). MAGN are commonly defined as radio loud objects with steep radio spectra ($\alpha_{\rm r} > 0.5$) showing symmetrical extension in radio maps. Besides SSRQs, this class includes radio galaxies, non-aligned non-thermal dominated AGN with no broad emission lines and large emission angles, which can be classified in two classes accordingly to their radio morphology, FRI and FRII, (Fanaroff & Riley, 1974).

The FRI and FRII galaxies are strong emitting objects in a wide radio band, from hundreds of MHz up to tens of GHz. The radio emission is believed to originate from the synchrotron emission of highly relativistic electrons moving in the jets of the source. Measurements of the total radio flux are available for hundreds of FRI and FRII galaxies, while the emission from the central region of the source, the core, has been resolved on arcsecond scale for a smaller number of objects.

Since blazars are believed to dominate the IGRB and radio galaxies would represent the "parent population" of blazars, those MAGN could contribute significantly to the IGRB. Indeed, although they are less luminous given the lack of beaming effects, their expected number in the entire sky is higher than for blazars.

The aim of this chapter is to present the computation of the diffuse γ-ray flux originating from the MAGN unresolved population, Sec. 6.6. The fundamental quantity for this calculation is the so called γ-ray luminosity function (GLF) (already mentioned in Sec. 3.4). We will see in Sec. 6.4 how to derive indirectly such a quantity by correlating radio and γ-ray luminosities on the basis of a simple physical argument. The correlation is derived in Sec. 6.2 and supported by the computation of 95% C.L. flux upper limits of a sample of MAGN, Sec. 6.3. Also the source count distribution will represent an important test for our model, Sec. 6.5.

This chapter is based on (Di Mauro et al., 2013). The analysis makes use of a publicly available suite of tools for analyzing *Fermi*-LAT data. All the information concerning the *Fermi*-LAT tools are available online on the *Fermi* Science Support Center web page[i].

6.1 MAGN as γ-ray emitters

In the framework of the AGN unification model, mis-aligned AGN are sources with the jet mis-aligned with respect to the l.o.s..

Before the *Fermi* launch, radio loud AGN with a large inclination angle were not considered appealing γ-ray targets because of the relativistic beaming (i.e. the emission of a relativistic plasma results to be beamed in the forward direction for a fixed observer as a direct consequence of special relativity transformations). Indeed, the jet undergoes an amplification depending on its orientation with respect to the observer. Assuming isotropic emission in the comoving jet frame with a power-law spectrum of index α, the observed flux density $F_{\rm obs}(\nu)$ produced through synchrotron and SSC emission[ii] is related to the rest-frame flux density $F_{\rm rest}(\nu')$ through the relation: $F_{\rm obs}(\nu) = \delta^{3+\alpha} F_{\rm rest}(\nu')$ (Begelman, Blandford & Rees, 1984). δ is the Doppler factor defined by:

$$\delta = \frac{1}{\gamma(1-\beta\cos\theta)}\,, \tag{6.1}$$

with $\nu = \delta\nu'/(1+z)$, β the bulk velocity of the emitting plasma, $\gamma = 1/\sqrt{1-\beta^2}$ the corresponding Lorentz factor and θ the jet viewing angle namely the angle between the jet emission direction and the l.o.s. (Urry & Padovani, 1995). The flux enhancement is strongly dependent on the viewing angle and decreases very rapidly for $\theta > 8^\circ - 10^\circ$. If the emission is due to EC, the Doppler boosting is stronger and the γ-ray beaming cone narrower compared to synchrotron processes. The beaming factor of the flux density varies as $\delta^{4+2\alpha}$ (Dermer, 1995).

The *Fermi*-LAT detection of eleven objects (Abdo et al., 2010b) in the first 15 months of GeV sky exploration has confirmed MAGN to be a new class of γ-ray emitters and has provided a new insight into the structure of those high-energy sources. This sample includes seven FRI radio galaxies and four FRII radio sources. Among the FRII objects two of them are FRII radio galaxies (PKS 0943-354 and 3C 111) and two SSRQ (3C 207 and 3C 380). The latter SSRQs are classified as FRII radio galaxies because they have a radio luminosity comparable with FRII sources. Most of the sources

---

[i] http://fermi.gsfc.nasa.gov/ssc/

[ii] We notice that in those mechanisms electrons are assumed to be isotropically distributed in a randomly oriented field.

of the 15 month-MAGN sample are faint ($F(> 0.1\mathrm{GeV}) \sim 10^{-8}$ photons $\mathrm{cm}^{-2}\ \mathrm{s}^{1}$) and have steep power-law spectra ($\Gamma > 2.4$), in general agreement with the AGN unified model. After two years of mission 8 new misaligned sources have been detected and three sources present in the first catalog have not been confirmed (Ackermann et al., 2011b). Those sources are the 3C 111 and 3C 120 (probably high variable γ-ray sources) an the 3C 78 (found with a significance level lower than the threshold fixed by *Fermi*). Therefore, in total, *Fermi*-LAT has reported the detection of 15 MAGN, which can be classified into 10 FRI and 5 FRII galaxies; (Abdo et al., 2010b) report on the observation of 3C 78, PKS 0625-35, 3C 207, 3C 274, Centaurus A, NGC 6251, 3C 380, 3C 120, 3C 111, 3C 84, PKS 0943-76, while Centaurus B, Fornax A and IC 310 have been reported in the second LAT catalog (2FGL) (Nolan et al., 2012) – for Centaurus B see also (Katsuta et al., 2013) – and Pictor A identification has been discussed in (Brown & Adams, 2012).

The preference of data for FRI galaxies can be due to the different average distance of the two populations. FRI objects are indeed much more closer than FRII. Nevertheless, the abundance of FRI can also be interpreted in terms of different beaming factor. Indeed, assuming an EC origin of the γ-ray emission for FRII objects, and SSC for FRI, the stronger reduction in the EC flux for FRII radio galaxies viewed slightly away from the jet axis as compared to the SSC flux for off-axis FRI radio galaxies makes the detection of off-axis FRI galaxies more probable (Abdo et al., 2010b). Dedicated studies of M87 (Abdo et al., 2009), Centaurus A (Abdo et al., 2010) and NGC 1275 (Abdo, Ackermann, Ajello, Asano et al., 2009) show that the SSC process successfully fit the observed emission on a wide photon energy range.

However, the physical processes underlying the emission of γ-rays in MAGN are still an issue of debate. As an example of the complexity of the problem, variability studies of the NGC 1275 and other sources (Abdo, Ackermann, Ajello, Asano et al., 2009) seem to suggest a sub-pc scale ($<$ 1018 cm) emission region (thus corresponding to the core), but the discovery of γ-ray emission from the radio lobes of Centaurus A (Abdo et al., 2010a) shows that extranuclear extended kpc regions can also be sources of high energy photons.

Although the γ-ray emission from the extended region (the lobes) is unlikely, the lobes contribution has been evaluated in (Stawarz, Kneiske & Kataoka, 2006; Massaro & Ajello, 2011). Such a contribution comes from synchrotron radiation of ultra-relativistic electrons in the lobes that upscatter to higher energies photons through IC scattering, provided a high enough electron density is available. The dominant contribution is expected from CMB photons. The IC/CMB scattered emission in the lobes of distant galaxies is generally well observed in the X-ray band. The emission of Centaurus A, if interpreted in terms of IC scattering of electrons with ambient photons, requires high-energy electrons in the lobes, but it is unclear how common this electron population is in other RGs.

Throughout this chapter we assume that photons in MAGN originate from the inner region of the object although it is unclear whether the production mechanism is SSC or EC radiation. We notice that we neglect the contamination from the jet component.

6.2 Radio and γ-ray luminosity correlation

The number of detected γ-ray MAGN is low and does not allow to infer the main properties of the whole population on the basis of statistical arguments as it has been done for blazars (Abdo, Ackermann, Ajello, Antolini et al., 2010). Therefore, γ-ray properties of the population, e.g. its γ-ray luminosity function, its spectral index distribution, etc., cannot be inferred directly from γ-ray observations but may be derived indirectly by correlating the γ-ray luminosity with measurements of the same objects in the radio band. The radio luminosity is indeed phenomenologically much better established, given the high number of detected MAGN in the radio frequencies. The physical motivation of looking for a correlation is that the emission processes producing photons in different energy bands (γ and radio) are though to be correlated.

Looking for a correlation between different wavelengths is a well adopted practice that can be applied to different source classes. In the case of blazars, a correlation between radio and γ-ray luminosities has been suggested since the EGRET era although it was not firmly established because of flux limited samples (Padovani, Ghisellini, Fabian & Celotti, 1993; Stecker, Salamon & Malkan, 1993; Salamon & Stecker, 1994; Dondi & Ghisellini, 1995; Narumoto & Totani, 2006). Recently, using *Fermi* data, the correlation between the radio and γ-ray luminosities for blazars has been confirmed (Ghirlanda, Ghisellini, Tavecchio & Foschini, 2010; Ghirlanda, Ghisellini, Tavecchio, Foschini & Bonnoli, 2011a).

In the AGN unification scenario, all radio loud AGN are described by the same physical emission processes (and distinguished mainly by geometrical arguments). Therefore, the existence of a similar radio-γ correlation can be supposed and tested against data also for MAGN.

In the case of RG, such a correlation has been found (Ghisellini, Tavecchio & Chiaberge, 2005), based on the EGRET data sample (only three γ-ray detected RG). Recently, the radio-γ correlation for the sample of *Fermi* γ-ray detected MAGN has been confirmed by Inoue (Inoue, 2011). The analysis is based on the first *Fermi* catalog (11 objects) and links the radio luminosity at 5 GHz to the γ-ray luminosity.

Following those previous works, we extend such an analysis by including the new detected objects in the second catalog. We adopt the same choice of (Inoue, 2011) for what concerns the radio frequency. The band at 5 GHz has indeed a large statistics and multiple measurements of the same objects (both for the total and the core emission). The novelty of our approach is that we correlate the core radio luminosity to the γ-ray one, instead of looking for a correlation with the total radio luminosity as it has been done previously. Total and core radio luminosities are indeed two distinct measurements. The former refers to the radio luminosity of the whole object including the emission from the jet(s), core, and eventually lobes, whereas the latter only measures the intensity of the emission from the inner region (arcsecond scale), the core. Since typically both EC and SSC scenarios require that γ-ray radiation originates relatively close to the center of the AGN, we believe that a physically direct correlation should exist between the core radio luminosity and the γ-ray luminosity, while the correlation with the total radio luminosity should be an indirect effect of the first one. Indeed, as explained before the extended γ-ray emission from lobes seems to be unlikely. Nevertheless, a γ-ray component from jet(s), when present, is unavoidable and constitute a caveat for our reasoning. The compactness of the γ-ray source for FRI galaxies is supported by variability studies (Abdo et al., 2010b; Grandi & Torresi, 2012), even if a non-negligible γ-ray counterpart in radio lobes has been observed in Centaurus A (Abdo et al., 2010a). The situation for the FRII population is less definite. A recent *Fermi*-LAT analysis of the FRII 3C 111 galaxy (Grandi, Torresi & Stanghellini, 2012), together with a multi-frequency campaign conducted in the same period, localizes the GeV photons from 3C 111 in a compact, central region associated with the radio core.

The main radio and γ parameters of all the MAGN observed by *Fermi*-LAT are reported in Tab. 6.1.

The radio data have been chosen to be the closest in time to *Fermi*-LAT data taking in order to reduce spurious effects due to source variability. Radio data measurements come from the Very Large Array (VLA) for all the objects but NGC 6251, measured with the Very Long Baseline Interferometer (VLBI). The size scales of our sample variy from about 0.01 kpc to a few kpc, except for NGC 6251 (0.002 kpc) and 3C 380 and depend on the distance of the sources. Three sources have been excluded from our correlation analysis: the 3C 84 because of the very intense variability, the IC 310 which lacks measurements of the core at 5 GHz and whose total radio flux is very faint, and the PKS 0943-76 for which only upper limits for the core are given. *Fermi*-LAT measurements of the photon index Γ (between 0.1 and 10 GeV) and the integrated flux (above $E_\gamma > 0.1$ GeV) have been taken from (Abdo et al., 2010b) for 3C 78, 3C 111, 3C 120 and from (Nolan et al., 2012) for the remaining objects. From Table 6.1, the mean photon index Γ is 2.37, with spread 0.32. In Tab. 6.1 we also quote the radio and γ-ray luminosities we

Table 6.1: Properties of MAGN discovered to be γ-ray emitting objects by *Fermi*-LAT. Used radio and γ characteristics are quoted. Column 1: name of the MAGN (radio classification: FRI or FRII), 2: redshift, 3: Galactic latitude, 4: spectral index for radio core (total) spectrum in a range including 5 GHz, 5: measured radio core (total) flux at 5 GHz; 6: photon index for γ-ray spectrum between 100 MeV - 100 GeV; 7-γ-ray flux above 100 MeV; 8- Radio core luminosity at 5 GHz ; 9- γ-ray luminosity References: 1-(Morganti et al., 1993); 2-(Pauliny-Toth et al., 1972); 3-(Ekers et al., 1989); 4-(Kuehr et al., 1981); 5-(Spinrad et al., 1985); 6-(Mullin et al., 2006); 7-(Nagar et al., 2001); 8-(Giovannini et al., 1988); 9-(Laing et al., 1983); 10-(Israel et al., 2008); 11-(Burns et al., 1983); 12-(Wright et al., 1994); 13-(Evans et al., 2005); 14-(Mantovani et al., 2009); 15-(P. A. Jones et al., 2001); 16-(Massardi et al., 2008); 17-(Geldzahler & Fomalont, 1984); 18-(Becker et al., 1991); 19-(Perley et al., 1997); 20-(Linfield & Perley, 1984); 21-(Kadler et al., 2012); 22-(Burgess & Hunstead, 2006); 23-(Kadler et al., 2012); 24-(Gregory & Condon, 1991)

MAGN(FRI,FRII)	z	b [deg]	$\alpha_{\rm core}(\alpha_{\rm tot})$	$S^{\rm 5GHz}_{\rm core}$ [Jy] ($S^{\rm 5GHz}_{\rm tot}$) [Jy])	Γ	F_γ [10^{-9}ph cm^{-2} s^{-1}]	$L^{\rm 5GHz}_{r,\rm core}$ [erg s^{-1}]	L_γ [erg s^{-1}]
3C 78/NGC 1218(I)	0.0287	-44.6	0 (0.64 ^{1})	0.964 ± 0.164^1 (3.40 ± 0.11^2)	1.95 ± 0.14	4.7 ± 1.8	$(8.8 \pm 1.4) \cdot 10^{40}$	$(1.11 \pm 0.54) \cdot 10^{43}$
3C 274/M 87(I)	0.0038	74.5	0 (0.79 ^{8})	3.0971 ± 0.0300^7 (71.566 ± 0.993 ^{9})	2.17 ± 0.07	25.8 ± 3.5	$(4.90 \pm 0.05) \cdot 10^{39}$	$(6.2 \pm 1.1) \cdot 10^{41}$
Cen A(I)	0.0009	19.4	0.30^{10} (0.70^{10})	6.984 ± 0.210^{11} (62.837 ± 0.099 ^{12})	2.76 ± 0.05	175 ± 10	$(6.19 \pm 0.19) \cdot 10^{38}$	$(1.14 \pm 0.09) \cdot 10^{41}$
NGC 6251(I)	0.0247	31.2	0(0.72^9)	0.38 ± 0.04 ^{13} (0.510 ± 0.050 ^{13})	2.20 ± 0.07	18.2 ± 2.6	$(2.57 \pm 0.27) \cdot 10^{40}$	$(1.82 \pm 0.41) \cdot 10^{43}$
Cen B(I)	0.0129	1.68	0 (0.13^{16})	2.730^{15} (6.58 ± 1.04^{16})	2.33 ± 0.12	39.3 ± 11.4	$5.02 \cdot 10^{40}$	$(8.6 \pm 3.2) \cdot 10^{42}$
For A(I)	0.00587	-56.7	0.50^{17}(0.52 ^{1})	0.051^{17} (72^1)	2.16 ± 0.15	7.7 ± 2.4	$1.93 \cdot 10^{38}$	$(4.6 \pm 2.2) \cdot 10^{41}$
3C 120(I)	0.0330	-27.4	0 (0.44^{18})	3.458 ± 0.588 ^{1} (8.60 ± 1.46^1)	2.71 ± 0.35	29 ± 17	$(4.20 \pm 0.71) \cdot 10^{41}$	$(2.9 \pm 1.6) \cdot 10^{43}$
PKS 0625−35(I)	0.0546	-20.0	0 (0.65 ^{3})	0.600 ± 0.030 ^{3} (2.25 ± 0.09 ^{4})	1.93 ± 0.09	12.9 ± 2.6	$(2.02 \pm 0.10) \cdot 10^{41}$	$(1.21 \pm 0.43) \cdot 10^{44}$
Pictor A(II)	0.0351	-34.6	0 (1.07 ^{1})	1.15 ± 0.05^{19} (15.45 ± 0.47^4)	2.93 ± 0.03	21.9 ± 3.6	$(1.58 \pm 0.07) \cdot 10^{41}$	$(2.13 \pm 0.46) \cdot 10^{43}$
3C 111(II)	0.0485	-8.61	-0.20 (0.73^5)	1.14^{20} (6.637 ± 0.996^{18})	2.54 ± 0.19	40 ± 8	$2.98 \cdot 10^{41}$	$(1.01 \pm 0.38) \cdot 10^{44}$
3C 207(II))	0.681	30.1	0 (0.90 ^{5})	0.5391 ± 0.0030^6 (1.35 ± 0.04 ^{4})	2.36 ± 0.11	17.3 ± 3.3	$(3.32 \pm 0.02) \cdot 10^{43}$	$(2.41 \pm 0.61) \cdot 10^{46}$
3C 380(II))	0.692	23.5	0 (0.71^9)	5.073 ± 0.105 ^{14} (7.45 ± 0.37 ^{4})	2.34 ± 0.07	30.3 ± 3.7	$(3.12 \pm 0.07) \cdot 10^{44}$	$(4.44 \pm 0.73) \cdot 10^{46}$
IC 310(I)	0.0189	-13.7	n.a.(0.75^{23})	n.a. (0.258 ± 0.031^{24})	2.10 ± 0.19	11.1 ± 6.2	-	$(7.9 \pm 4.9) \cdot 10^{42}$
3C 84/NGC 1275(I)	0.0176	-13.2	(0.78^5)	high variability	2.00 ± 0.02	175 ± 8	-	$(1.22 \pm 0.07) \cdot 10^{44}$
PKS 0943−76(II)	0.270	-17.2	n.a.	upper limits(0.757^{22})	2.44 ± 0.14	19.5 ± 5.1	-	$(2.47 \pm 0.71) \cdot 10^{45}$

computed. The radio luminosity at a fixed frequency writes as:

$$L_r(\nu) = \frac{4\pi d_L^2(z)}{(1+z)^{1-\alpha_r}}\, S_r(\nu)\,, \tag{6.2}$$

where α_r is the radio spectral index ($\alpha_{\rm core}$ or $\alpha_{\rm tot}$), $\Gamma = \alpha_r + 1$ and $S_r(\nu)$ is the radio energy flux at a given energy. The γ-ray luminosity is:

$$L_\gamma(\epsilon_1, \epsilon_2) = 4\pi d_L^2(z) \frac{S_\gamma(\epsilon_1, \epsilon_2)}{(1+z)^{2-\Gamma}}, \tag{6.3}$$

where ϵ_1 and ϵ_2 are the energies between which L_γ is computed, $d_L(z)$ is the luminosity distance at the redshift z and $S(\epsilon_1, \epsilon_2)$ is the observed energy flux between ϵ_1 and ϵ_2. The factor $(1+z)^{2-\Gamma}$ is the so-called K-correction term that takes into account the redshift modification between emitted and observed energies. $S_\gamma(\epsilon_1, \epsilon_2)$ is related to the photon flux $F_\gamma = \int_{\epsilon_1}^{\epsilon_2} d\epsilon\, dN/d\epsilon$ (in units of photons cm^{-2} s^{-1}) by the relation:

$$S_\gamma(\epsilon_1, \epsilon_2) = \int_{\epsilon_1}^{\epsilon_2} \epsilon \frac{dN}{d\epsilon} d\epsilon\,, \tag{6.4}$$

where $dN/d\epsilon$ is the γ-ray spectrum of the source.

Single source γ-ray spectral distributions have been taken from the 2FGL. They are simple power-law or log-parabola spectra:

$$\frac{dN}{d\epsilon} = k \left(\frac{\epsilon}{\epsilon_{\rm Pivot}}\right)^{-\Gamma - \beta \log{(\epsilon/\epsilon_{\rm Pivot})}}, \tag{6.5}$$

the parameter β being zero for a power-law spectrum[iii]. In the computations we set $\epsilon_1 = 0.1$ GeV, $\epsilon_2 = 100$ GeV, while $\epsilon_{\rm Pivot}$ has been varied for each source except when dealing with average properties ($\epsilon_{\rm Pivot}$=0.1 GeV).

We show the result of the correlation in Fig. 6.1. The luminosities of the γ-ray detected MAGN of our sample are displayed in the L_γ and $L_{r,\rm core}$ (at 5 GHz) plane. The 12 objects are distinguished according to their FRI or FRII classification: blue squares (red open circles) refer to FRI (FRII) classification. Luminosities are computed from Eqs. 6.3 – 6.2, propagating errors on Γ and not those on the redshift, given their negligible effect. We find a correlation between $L_{r,\rm core}$ and L_γ for the 12 objects in the form:

$$\log{(L_\gamma)} = 2.00 \pm 0.98 + (1.008 \pm 0.025) \log{(L_{r,\rm core}^{\rm 5GHz})}\,, \tag{6.6}$$

represented by the solid black line in Fig. 6.1, while the relevant 1σ error band is shown as a shaded area. The band is obtained from the errors

---

[iii] Indeed for all the sources considered in our analysis β=0, as indicated in the 1FGL and 2FGL. The only source better reproduced by a log-parabola is 3C84, which is not included in our analysis.

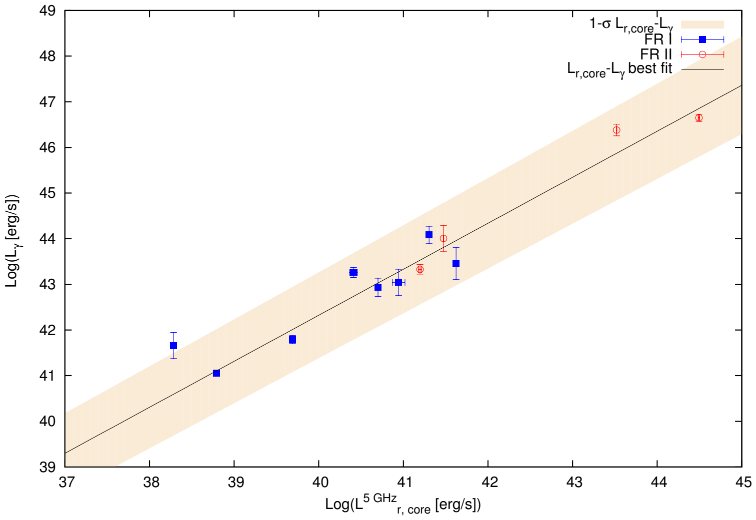

Figure 6.1: Correlation between γ-ray luminosity and radio core luminosity at 5 GHz for the MAGN of Tab. 6.1. The best-fit value for the correlation linear relation is displayed by the solid black line, while the light pink shaded area shows the corresponding 1σ error band. Blue squares (red open circles) refer to FRI (FRII) classifications.

on both the γ-ray and radio luminosities, although the former dominates the uncertainty. The uncertainty band of the γ-ray fluxes measured by the *Fermi*-LAT spans almost one order of magnitude around the best-fit.

We notice that in the sample three objects show non-standard MAGN properties. The radio morphology of 3C 380 is not unambiguously determined, as it shows some properties of a compact steep spectrum radio source (Abdo et al., 2010b; P. N. Wilkinson, Akujor, Cornwell & Saikia, 1991). The FRII 3C 207 behaves as a steep spectrum radio quasar in the optical band (Abdo et al., 2010b), while PKS 0625−35 has no clear association. We thus perform the analysis excluding those sources (3C 380, 3C 207 and PKS 0625−35) and we find that the correlation is not significantly altered. In this case, the linear relation is not very different from Eq. 6.6, if it were not for the increased spread in the fitted coefficients. Indeed, 3C 207 and PKS 0625−35 have large errors and 3C 380 is quite close to the correlation of Eq. 6.6.

For the sake of completeness, the correlation between the total radio luminosity at 5 GHz and the γ-ray luminosity is reported below for the whole sample of 12 sources:

$$\log\left(L_\gamma\right) = -2.5 \pm 1.1 + (1.095 \pm 0.026)\log\left(L^{5\mathrm{GHz}}_{r,\mathrm{tot}}\right). \tag{6.7}$$

The experimental values for the total radio luminosity are quoted in Tab. 6.1.

By comparing with the literature, the correlation of Eq. 6.6 agrees with the one obtained in (Ghisellini et al., 2005) for the sample of three EGRET γ-ray loud FRI galaxies. In the case of blazars the slope of the correlation between $L_\gamma(> 100$ MeV) and radio luminosity at different frequencies was found to be: 1.07± 0.05 at 20 GHz (Ghirlanda et al., 2010), 1.2 ± 0.1 at 5 GHz (Stecker et al., 1993) and 1.06 ± 0.02 at 8.4 GHz (Zeng, Yan, Sun & Zhang, 2012). Provided we test the robustness of the correlation by means of statistical methods (see next section), we can assume that the correlation in Eq. 6.6 is a good representation of the γ-ray luminosity of the cores of MAGN and we employ it in order to infer the emission of the unresolved MAGN population.

Another important phenomenological correlation exists between the radio total and radio core luminosities. Given the uncertainties affecting such a kind of studies, we display in the same plot, Fig. 6.2, three correlations, $L_{\nu,\rm tot}^{\rm 5GHz}$ and $L_{\nu,\rm core}^{\rm 5GHz}$, derived in the literature. The three lines refer to:

$$\log L_{\nu,\rm core}^{\rm 5GHz} = 4.2 \pm 2.1 + (0.77 \pm 0.08) \log L_{\nu,\rm tot}^{\rm 1.4GHz} \tag{6.8}$$

from (Lara et al., 2004) (black solid curve),

$$\log L_{\nu,\rm core}^{\rm 5GHz} = 7.6 \pm 1.1 + (0.62 \pm 0.04) \log L_{\nu,\rm tot}^{\rm 408MHz} \tag{6.9}$$

from (Giovannini, Cotton, Feretti, Lara & Venturi, 2001) (pink dot-dashed curve),

$$\log L_{\nu,\rm tot}^{\rm 408MHz} = 7.10 \pm 0.90 + (0.83 \pm 0.04) \log L_{\nu,\rm core}^{\rm 5GHz} \tag{6.10}$$

from (Yuan & Wang, 2012) (green dotted curve). Assuming a power-law dependence $L/\nu \propto \nu^{-\alpha}$, with $\alpha_{\rm tot} = 0.80$ for the total radio emission, we convert all the luminosities at 5 GHz. The data for our MAGN sample are also displayed and they seem to indicate a preference for the correlation proposed by (Lara et al., 2004).

6.3 Upper limits on unresolved MAGN γ-ray flux

In order to test the robustness of the $L_{r,\rm core}$-L_γ correlation of Eq. 6.6 we compute the 95% C.L. upper limits on the γ-ray flux of a sample of MAGN.

The sample is selected in order to include the most luminous sources in radio wavelength (at 5 GHz) and to cover almost homogeneously the radio interval corresponding to observable γ-ray fluxes (by assuming the correlation Eq. 6.6 is true). The sources in our sample (first column of Tab. 6.2) are extracted from radio galaxies in (Kataoka et al., 2011) and (Ghisellini et al., 2005) (first and second block in Tab. 6.2, respectively). From those two sets of objects we exclude sources already detected by *Fermi*-LAT (Pictor A, 3C 84, 3C 274, 3C 78), sources that do not show a clear FRI or FRII radio morphology classification (RGB J1722+246 and PKS 2251+11 being Seyfert galaxies, S5 2116+81 being a flat spectrum radio source with

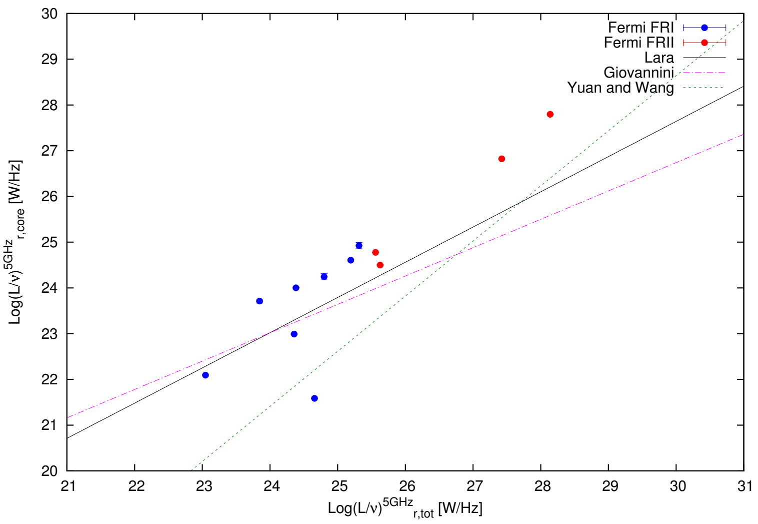

Figure 6.2: Correlation between radio core luminosity and total radio luminosity at 5 GHz taken from different analysis in the literature. Solid black line corresponds to Eq. 6.8, the pink dot-dashed and the green dotted correspond to Eq. 6.9 and Eq.6.10, respectively. Blue squares (red open circles) are the experimental data for our sample of FRI (FRII), Tab. 6.1.

a radio jet morphology, 3C 75), sources with latitudes below 10 ° in order to avoid the strong contamination from the galactic foreground (4C 50.55), and sources with a too intense variability (3C 317, (Venturi, Dallacasa & Stefanachi, 2004)). Four FRII RGs from the 3CRR catalogue (3C 245, 3C 109, 3C 212, DA 240) have been added to the sample so that our analysis will cover a wider range in radio luminosity (last block in Table 6.2). Our sample is therefore composed of 17 FRII and 22 FRI RGs.

We compute γ-ray flux upper limits for the listed galaxies by using the *Fermi*-LAT Science Tools[iv]. We extract the data and the corresponding spacecraft file from the *Fermi* Science Support Center data server[v] selecting photons within a circular region around the source and specifying object name, radius of the interested region, observation dates and energy range. Data are a list of counts that have been identified as resulting from astrophysical photons after the data selection. The LAT photon file contains the information about the energy of the event, the position, as well as information about the quality of the event reconstruction for each astrophysical photon. The spacecraft file contains the spacecraft position and orientation information. Data are stored as FITS files which stands for "Flexible Image

---

[iv] http://fermi.gsfc.nasa.gov/ssc/data/analysis/documentation, software version v9r27p1, Instrumental Response Functions (IRFs) P7_V6

[v] http://fermi.gsfc.nasa.gov/cgi-bin/ssc/LAT/LATDataQuery.cgi

Transport System". We make use of data taken from the starting time of the mission, 2008 August 4, until 2012 September 9. The Mission Elapsed Time (MET) interval runs from 239557414 to 368928003. Data are extracted from a region of interest (ROI) of radius equals to 8 ° centered at the position of the source. This radius has been found to be the best angular region for source analysis when sources are far from the galactic plane (Abdo, Ackermann, Ajello, Asano et al., 2009). We indeed neglect in this analysis sources that lie below 10 ° in latitude. We select γ-rays in the energy range 100 MeV - 100 GeV.

We adopt P7SOURCE_V6 photons[vi]. The preparation of the extracted data depends on the type of analysis one wishes to perform (e.g. point source, extended source, spectral analysis, timing analysis, etc.) and a series of *Fermi* tools is optimized for the data preparation. Event selection and time selection are the two main steps for data preparation performed by the *Fermi* tools gtselect and gtmktime respectively. Notably, gtselect allows to make user-defined cuts on the event file; the most common selections are those involving time range (minimum and maximum time) and energy range (minimum and maximum energy). Moreover further cuts on the zenith angle[vii], instrument coordinates, event class[viii] and rocking angle ($< 52°$) [ix] are applied according to software recommendations.

For each object in our sample, we look for the presence of the source in the ROI performing a likelihood analysis (see Appendix F for details about the statistics). The null hypothesis corresponds to a model without the source (i.e. only background events), while the alternative hypothesis considers a model with the additional source at a specified location.

The Test Statistic (TS) is defined as $TS = -2\ln(L_{\mathrm{max},0}/L_{\mathrm{max},1})$, where

---

[vi] Pass N (PN) refers to the version of the event reconstruction algorithms; Pass 7 is the currently used reconstruction algorithm. For a given reconstruction, the LAT team generates an accompanying set of parameterized instrument response functions (IRFs) that are designed for analysis of that particular dataset, these are labeled VN (where N is the version of the IRF). IRFs contains information about the efficiency in terms of the detector's effective area and the resolution as given by the point spread function (PSF) and energy dispersion.

[vii] The zenith angle is the angle between the reconstructed event direction and the zenith line which originates at the center of the Earth and passes through the center of mass of the spacecraft. The cut on the zenith angle is mandatory to prevent the contamination from albedo γ-rays and loss of exposure due to the presence of the Earth in the field of view. The Earth's limb lies at a zenith angle of 113°, so a suggested value of 100° provides protection against this source of background.

[viii] The event reconstruction relies on a series of cuts that will classify the events based on the probability that they result from photons and the quality of the reconstruction. The current event classes are ordered such that the higher probability photon selections are subsets of the less restrictive selections. For each event class exists a specific effective area and point spread function.

[ix] In survey mode the LAT's pointing relative to the sky changes constantly and uniformity of exposure is achieved by "rocking" the pointing perpendicular to the orbital motion. The maximum rocking angle is 60°.

$L_{\mathrm{max},0}$ is the maximum likelihood value for the null hypothesis and $L_{\mathrm{max},1}$ is the maximum likelihood value for the alternative hypothesis. TS is a monotonically increasing function of $L_{\mathrm{max},1}$, therefore maximizing TS is equivalent to maximizing the likelihood ratio. As explained in the Appendix F, in the limit of a large number of counts, Wilk's theorem states that the TS for the null hypothesis is asymptotically distributed as χ^2_x, where x is the number of parameters characterizing the additional source. A source results thus from a fluctuation in the TS distribution. A larger TS indicates that the null hypothesis has to be rejected and, in this case, the square root of the TS is approximately equal to the detection significance for the given source.

The number of expected counts in the ROI is derived by considering the emission from all sources in the 2FGL[x] inside a "source region" (distance from the target region) of 13° ($8^\circ + 5^\circ$). Additionally adopted backgrounds are the galactic diffuse emission and the isotropic diffuse model, which includes the true IGRB and the residual particle contamination[xi]. The diffuse models used in the analysis are: gal_2yearp7v6_v0.fits for the galactic diffuse model and iso_p7v6source.txt for the isotropic spectral template. We also take into account the presence of extended sources in the ROI by computing a user diffuse source response[xii]. The interested source is modeled as a point-like object with a power-law spectrum of index $\Gamma = 2.5$. This value has been chosen as nominal spectral index for all MAGN in analogy with (Kataoka et al., 2011).

The fitting procedure (i.e. the maximization of the TS) leaves the spectral parameters of all the sources inside the ROI free, whereas sources in the region $8^\circ < r < 13^\circ$ have spectral parameters fixed to the values of the 2FGL. All the relevant normalizations for the background model are left as free parameters during the fitting procedure. Fitting requires repeatedly calculating the likelihood for different trial parameter sets until a value sufficiently near the maximum is found and it is done through the MINUIT algorithm (James & Roos, 1975).

If the source is not statistically present, i.e. the TS is less than 25, a 95% C.L. upper limit (UL) is computed through a standard profile likelihood, which scans in normalization parameter values (see Appendix F for the definition of the profile likelihood). UL on the signal strength at the 95% C.L. are set by increasing the normalization from its best-fit value until the log-likelihood ratio has changed by 3.84 (for 1 degree of freedom). We verify that varying Γ of the source from 2.3 – 2.7 affects the limits by less than $\sim 10\%$.

We perform, when possible, an unbinned maximum-likelihood analysis. In the cases where the fit does not converge we adopt a binned analysis

---

[x] http://fermi.gsfc.nasa.gov/ssc/data/access/lat/2yr_catalog/

[xi] http://fermi.gsfc.nasa.gov/ssc/data/access/lat/BackgroundModels.html

[xii] The integral of the spectral part and the one over the instrument response function for the diffuse model components of the source model are called "diffuse responses".

although the unbinned likelihood would be most accurate since it does not average over a finite size bin. We therefore analyze the source region with both methods and derive the upper limits with the help of the LATAnalysisScripts[xiii], which make use of the UpperLimits.py module.

In Tab. 6.2 the flux upper limits are quoted together with the TS value for both unbinned and binned analysis. The differences in the TS values arise from different implemented algorithms for data analysis and processing, and are well within typical systematic uncertainties for spectral analysis. The unbinned analysis is much more computing intensive, and often technically hard to compute for very long time spans, and a binned analysis is therefore preferable as well as suggested by the Fermi Science Support Center. Given the systematic uncertainty arising from the different statistical methods, we adopt as *upper* limit the highest value for the flux bound. These *conservative* upper limits are shown in Fig. 6.3 together with the luminosity correlation from Eq. 6.6. The fact that the calculated upper limits do not fall below the uncertainty band, verifies the validity of the core radio and γ-ray correlation. We notice that our conclusions are unchanged if we adopts as upper limits the results from the unbinned analysis. It is worth saying that, on the other hand, with more statistics upper limits on undetected sources will represent a powerful method to further test the validity of the correlation.

Further statistical tests on the correlation of Eq. 6.6 are performed in order to check for a possible bias induced by distance dependence of the luminosity and flux-limited samples (Padovani, 1992; Ghirlanda, Ghisellini, Tavecchio, Foschini & Bonnoli, 2011b; Inoue, 2011). Indeed, in flux limited observations, luminosities of samples are strongly correlated with redshifts and this can lead to spurious luminosity correlations. In this case a double partial correlation analysis is used in order to test the correlation excluding the redshift dependence.

Partial correlation analysis is adopted in the case of multiple correlated variables in order to study the correlation between two variables after removing the effects of the others and reveals if such a correlation is true or due to spurious effects.

Typically, the partial correlation coefficient of two variables with respect to a third one, is computed from the pairwise values of the correlation between all the three variables (e.g. assuming linear relations). The correlation coefficient between e.g. x and y excluding the dependence on the third parameter z is evaluated as:

$$r_{xy,z} = \frac{r_{xy} - r_{xz} r_{yz}}{\sqrt{1 - r_{xz}^2}\sqrt{1 - r_{yz}^2}}\,, \tag{6.11}$$

[xiii] User contributions http://fermi.gsfc.nasa.gov/ssc/data/analysis/user/

Table 6.2: Flux upper limit at 95% C.L. derived for a sample of undetected MAGN. Column 1: name of the MAGN (radio classification: FRI or FRII), 2: redshift, 3: measured radio core flux at 5 GHz [Jy], 4: TS of unbinned analysis, 5: 95% C.L. upper limit from unbinned analysis on the flux above 100 MeV in units of 10^{-9} ph cm^{-2} s^{-1}, 6: TS of binned analysis, 7: 95% C.L. upper limit from binned analysis on the flux above 100 MeV in units of 10^{-9} ph cm^{-2} s^{-1}; 8: radio core luminosity at 5 GHz in units of erg s^{-1}.
References: 1-(Morganti et al., 1993); 2-(Henstock et al., 1995); 3-Third Cambridge Catalogue of Radio Sources ; 4-(Dodson et al., 2008); 5-(Neff et al., 1995); 6-(Pearson et al., 1992); 7-(Tingay et al., 2002).

MAGN(FRI,FRII)	z	$S^{\rm core}_{\rm 5GHz}$ [Jy]	TS$_{\rm unbinned}$	F$^{UL}_{\rm unbinned}$	TS$_{\rm binned}$	F$^{UL}_{\rm binned}$	$L^{\rm 5GHz}_{r,\rm core}$ [erg s^{-1}]
3C 18 (II)	0.188	0.083^{1}	< 1	2.7	2.6	6.0	$3.51 \cdot 10^{41}$
B3 0309+411B (II)	0.134	0.320^{2}	-	-	< 1	5.8	$6.73 \cdot 10^{41}$
3C 215 (II)	0.412	0.0164^{3}	<1	3.1	4.1	6.0	$3.56 \cdot 10^{41}$
3C 227 (II)	0.086	0.032^{1}	< 1	0.1	< 1	1.1	$2.70 \cdot 10^{40}$
3C 303 (II)	0.141	0.150^{3}	< 1	2.8	3.3	4.6	$3.50 \cdot 10^{41}$
3C 382 (II)	0.058	0.188^{3}	< 1	4.1	1.2	5.9	$7.12 \cdot 10^{40}$
3C 390.3 (II)	0.056	0.120^{4}	< 1	1.7	3.0	4.7	$4.26 \cdot 10^{40}$
3C 411(II)	0.467	0.078^{5}	-	-	< 1	6.1	$2.2 \cdot 10^{42}$
4C 74.26 (II)	0.104	0.100^{6}	1.1	5.4	<1	5.7	$1.25 \cdot 10^{41}$
PKS 2153-69 (II)	0.028	$0.300\ ^{7}$	4.2	6.6	<1	6.2	$2.67 \cdot 10^{40}$
3C 445 (II)	0.056	0.086^{1}	<1	0.8	<1	1.0	$3.06 \cdot 10^{40}$
3C 465 (I)	0.029	0.270^{3}	-	-	< 1	0.5	$2.5 \cdot 10^{40}$
3C 346 (I)	0.162	0.220^{3}	4.5	6.4	10.8	10.2	$1.39 \cdot 10^{39}$
3C 264 (I)	0.021	0.200^{3}	9.0	5.7	14.0	7.5	$9.58 \cdot 10^{39}$
3C 66B (I)	0.022	0.182^{3}	-	-	< 1	8.3	$9.31 \cdot 10^{39}$
3C 272.1(I)	0.003	0.180^{3}	5.2	5.6	5.3	6.8	$1.66 \cdot 10^{38}$
3C 315 (I)	0.1083	0.150^{3}	-	-	< 1	2.1	$2.04 \cdot 10^{41}$
3C 338 (I)	0.030	0.105^{3}	-	-	< 1	4.6	$1.07 \cdot 10^{40}$
3C 293 (I)	0.045	0.100^{1}	< 1	1.5	<1	1.8	$2.29 \cdot 10^{40}$
3C 29 (I)	0.045	0.093^{3}	< 1	1.5	<1	4.1	$2.11 \cdot 10^{40}$
3C 31(I)	0.017	0.092^{3}	-	-	< 1	4.0	$2.83 \cdot 10^{39}$
3C 310 (I)	0.054	0.080^{3}	< 1	1.2	<1	2.1	$2.63 \cdot 10^{40}$
3C 296 (I)	0.024	0.077^{3}	< 1	1.5	<1	2.3	$4.79 \cdot 10^{39}$
3C 89 (I)	0.1386	0.049^{3}	-	-	<1	1.8	$1.10 \cdot 10^{41}$
3C 449 (I)	0.017	0.037^{3}	< 1	0.5	<1	0.8	$1.19 \cdot 10^{39}$
3C 288 (I)	0.246	0.030^{3}	< 1	1.5	1.6	3.7	$2.22 \cdot 10^{41}$
3C 305 (I)	0.0414	0.0295^{3}	-	-	<1	2.1	$5.66 \cdot 10^{39}$
3C 83.1B (I)	0.026	0.040^{3}	10.0	19.7	16.5	23.2	$2.89 \cdot 10^{39}$
3C 424 (I)	0.1270	$0.0180\ ^{3}$	-	-	<1	1.6	$3.39 \cdot 10^{40}$
3C 438 (II)	0.290	0.0071^{3}	< 1	0.9	<1	3.2	$7.40 \cdot 10^{40}$
3C 386 (I)	0.018	0.120^{3}	-	-	<1	3.2	$4.15 \cdot 10^{39}$
3C 277.3 (I)	0.0857	0.0122^{3}	-	-	4.2	5.1	$1.03 \cdot 10^{40}$
3C 348 (I)	0.1540	0.010^{3}	-	-	<1	5.1	$2.80 \cdot 10^{40}$
3C 433 (II)	0.102	0.005^{3}	-	-	<1	1.9	$5.96 \cdot 10^{39}$
3C 442A (I)	0.027	0.002^{3}	<1	0.7	<1	0.9	$1.62 \cdot 10^{38}$
3C 245 (II)	1.029	0.910^{3}	< 1	2.0	<1	4.0	$1.30 \cdot 10^{44}$
3C 109 (II)	0.306	0.263^{3}	< 1	1.4	<1	3.5	$3.06 \cdot 10^{42}$
3C 212 (II)	1.049	0.150^{3}	6.4	7.1	10.11	8.8	$2.22 \cdot 10^{43}$
da 240 (II)	0.036	0.105^{3}	< 1	1.5	<1	2.8	$1.48 \cdot 10^{40}$

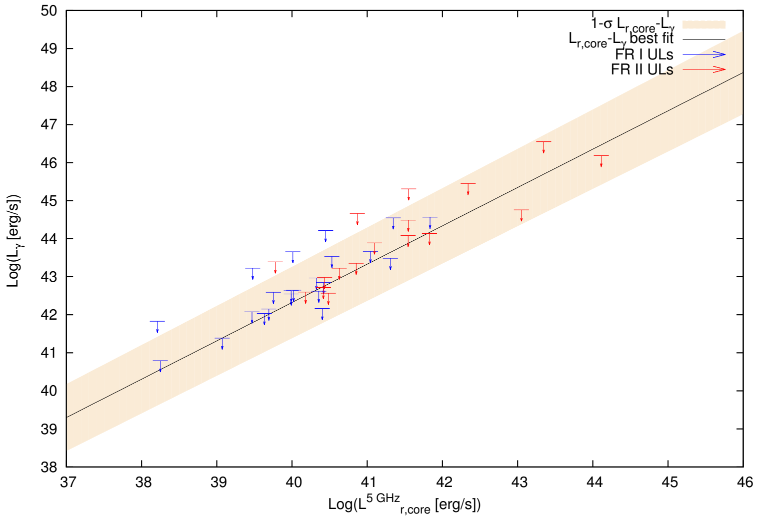

Figure 6.3: Correlation between γ-ray luminosity and radio core luminosity at 5 GHz for the MAGN of Tab. 6.1 (best-fit correlation – black solid line – and 1σ error band – light pink shaded area). We display the 95% C.L. γ-ray flux upper limits derived on a sample of *Fermi*-LAT undetected radio-loud MAGN.

where r_{xz} and r_{yz} are the correlation coefficients between x and z and between y and z, respectively. Those coefficients are computed by means of different methods, e.g. they can be defined as rank-order correlation coefficients.

The correlation coefficient is then used for rank correlation tests which are statistical tests making use of the statistical ranks of data points, i.e. the ordinal numbers of a value in a list arranged in a specified order (usually decreasing). We perform in what follows two different rank correlation tests on the correlation of Eq. 6.6.

Firstly, we calculate the Spearman rank-order correlation coefficient, see (Press, Teukolsky, Vetterling & Flannery, 1992) for details. The Spearman correlation coefficients are 0.94, 0.92, 0.98 between $\log{(L^{5\mathrm{GHz}}_{r,\mathrm{core}})}$ and $\log{(L_\gamma)}$, between $\log{(L^{5\mathrm{GHz}}_{r,\mathrm{core}})}$ and redshift, and between $\log{(L_\gamma)}$ and redshift, respectively. The partial correlation coefficient turns out to be 0.51 and the null hypothesis that the two luminosities are uncorrelated is rejected at the 95% C.L. (by performing T-Student test).

Secondly, we test the significance of the radio-γ correlation by using the modified Kendall τ rank correlation test proposed by (Akritas & Siebert, 1996), which is suitable for partially-censored datasets. By following the procedure highlighted in (Ackermann, Ajello, Allafort et al., 2012) – see Appendix therein for details – we perform a Monte Carlo simulation to compute the distribution of the τ correlation coefficient obtained under the

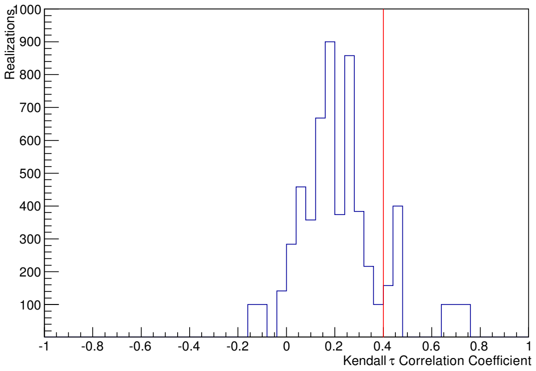

Figure 6.4: Null hypothesis distribution of τ correlation coefficients assuming independence between the γ and radio wavebands. The null hypothesis distributions are generated from 5800 permutations of γ-ray luminosities among the galaxies by requiring that the resultant γ-ray fluxes exceed the flux threshold of $7.7 \cdot 10^{-9}$ photons cm^{-2} s^{-1}. The mean value is 0.223 with the standard deviation of the distribution RMS=0.173. The correlation coefficient of the actual data is represented by the red solid line, $\tau = 0.397$.

null hypothesis of independence between the two wavebands. Starting from the detected sample of 12 sources we build several dataset realizations by scrambling the derived γ-ray luminosities among galaxies. For each galaxy we then compute the corresponding flux and we retain only galaxies with a flux above the minimal γ-ray flux of the detected sample ($7.7 \cdot 10^{-9}$ photons cm^{-2} s^{-1}). If the scrambled sample has fewer than 12 sources above the flux threshold, we randomly extract an additional source from the upper limit dataset (from Tab. 6.2) until the flux threshold is reached. For each scrambled dataset we then compute the Kendall coefficient and we build its distribution as shown in Fig. 6.4. The displayed distribution refers to 5800 realizations of scrambled samples and the red line represents the value of the τ correlation coefficient of the actual data, $\tau = 0.397$.

Finally, we compare the τ correlation coefficient of the actual data to the distribution of τ in Fig. 6.4 and we find that the integral of the distribution above $\tau = 0.397$ is 0.05. This is the probability to obtain the correlation by chance, i.e. the p-value of the correlation (the smaller the p-value, the greater the probability for the observed correlation of being true). As in the case of the Spearman test, we can exclude the correlation happening by chance at the 95% C.L.. The result indicates that a physical correlation between the core radio emission and the γ-ray flux of the *Fermi*-LAT detected MAGN is not affected by spurious effects.

6.4 The γ-ray luminosity function

In astrophysics the quantity used to describe the characteristics of a source population in terms of its distribution in luminosity and space is the so called "luminosity function". The luminosity function $\rho(L, z)$ is defined as the number of sources emitting at fixed energy per unit comoving volume, dV, and per unit (base 10) logarithm of luminosity, $d\log(L)$; it depends on the luminosity and on the redshift. The luminosity function writes as:

$$\rho(L, z) = \frac{d^2N}{d\log(L)\, dV}\,. \tag{6.12}$$

It is a statistical quantity obtained experimentally by fitting data of large source samples. Measurements of the total radio luminosity are available for hundreds of radio-loud MAGN, depending on the frequency of the survey, and thus it is possible to built directly from the data the corresponding luminosity function, i.e. the total radio luminosity function (RLF). Results on the total RLF are well established (Willott, Rawlings, Blundell, Lacy & Eales, 2001; Dunlop & Peacock, 1990; Yuan & Wang, 2012) and often adopted in literature, e.g. (Stawarz et al., 2006; Inoue, 2011). On the other hand, measurements of the core radio flux are available for a limited number of objects detected at low radio frequencies (around 0.1-few GHz). For this reason, computing the core RLF is difficult and the only result in literature about it is still not so well established (Yuan & Wang, 2012)[xiv].

In the case of γ-ray measurements of radio-loud MAGN, the limited sample (less than 20 objects) does not allow to construct the GLF through a statistical analysis of the detected population. Therefore, the GLF is derived indirectly from other wavelengths by assuming the existence of a correlation between luminosities. This practice is often adopted in astrophysics; we cite here some example for blazars (Stecker & Salamon, 1996; Kazanas & Perlman, 1997; Narumoto & Totani, 2006; Stecker & Venters, 2011) which should be compared with the experimentally derived GLF from *Fermi*-LAT detected sources (Abdo, Ackermann, Ajello, Antolini et al., 2010). Attempts of applying the same method to a population of RG have been performed as well (Ghisellini et al., 2005; Inoue, 2011).

Our aim is to derive the GLF for the unresolved (by *Fermi*) MAGN population. We adopt a phenomenological approach following the main idea of (Inoue, 2011), although we distinguish from this previous work for several

---

[xiv] The strong negative evolution of the core RLF found by those authors makes us wary of the result. It is expected that core and lobes should co-evolve. Lobes, at low frequency, evolve positively. In the literature there is very little evidence for the presence of radio galaxies with a "switched off" core, as it should be if lobes and cores have a different evolution. Moreover, the same authors report the positive evolution of total radio emission and derive a correlation between total radio flux and core flux, a simple transformation of their total RLF (using their correlation) would yield a positively-evolving core RLF.

aspects. The main original points of our analysis include (*i*) the correlation between the γ-ray and radio core luminosity instead of relating the γ-ray emission to the total radio emissivity; (*ii*) the propagation of the uncertainty on such a correlation throughout the analysis in order to estimate the theoretical uncertainty on our final prediction; (*iii*) the test of our hypothesis (i.e. the correlation) against the 1FGL and 2FGL sample.

The underlying ansatz is that the number of sources emitting in γ-ray is a fraction of the population shining in the radio band:

$$N_\gamma = k\ N_r, \tag{6.13}$$

where the normalization k is the fraction of radio emitting objects N_r having γ-ray counterpart N_γ.

From Eq. 6.12 it follows that the number of sources is related to the luminosity function by the relation:

$$N = \int dV \int \rho(L,z) d\log L\,. \tag{6.14}$$

By consequence, the GLF is defined through a RLF by:

$$\rho_\gamma(L_\gamma, z) = k\ \rho_r(L_r, z) \frac{d\log L_r}{d\log L_\gamma}\,. \tag{6.15}$$

Eq. 6.15 relies on the existence of a correlation $L_\gamma - L_r$ which allows to express $\rho_r(L_r, z)$ as $\rho_r(L_r(L_\gamma), z)$ and defines the Jacobian of the transformation $d\log L_r / d\log L_\gamma$.

Previous works (e.g. (Inoue, 2011)) derive the GLF by exploiting the correlation $L_\gamma - L_{r,\mathrm{tot}}$ (Eq. 6.7 in the case of our sample). In this case Eq. 6.15 takes the form:

$$\rho_\gamma(L_\gamma, z) = k\ \rho_{r,\mathrm{tot}}(L^{5\mathrm{GHz}}_{r,\mathrm{tot}}(L_\gamma), z) \frac{d\log L^{5\mathrm{GHz}}_{r,\mathrm{tot}}(L_\gamma)}{d\log L_\gamma}\,, \tag{6.16}$$

where $\rho_{r,\mathrm{tot}}$ refers to the total RLF, e.g. (Willott et al., 2001).

In the previous section we have already argued that the correlation $L_\gamma - L_{r,\mathrm{tot}}$ can be biased by spurious effects and we have motivated the existence of a correlation $L_\gamma - L_{r,\mathrm{core}}$ by means of a simple physical argument: if the bulk of the γ-ray emission is most likely originated by SSC or EC processes in the innermost region of the objects (as it is for blazars), γ-rays from MAGN should be directly related to the radio emission produced in the core via synchrotron emission.

We therefore derive the GLF from the $L_\gamma - L_{r,\mathrm{core}}$ correlation such that:

$$\rho_\gamma(L_\gamma, z) = k\ \rho_{r,\mathrm{core}}(L^{5\mathrm{GHz}}_{r,\mathrm{core}}(L_\gamma), z) \frac{d\log L^{5\mathrm{GHz}}_{r,\mathrm{core}}(L_\gamma)}{d\log L_\gamma}\,, \tag{6.17}$$

where $\rho_{r,\mathrm{core}}$ refers to the RLF of the cores of the MAGN.

Unfortunately, the lack of a well established and experimentally derived core RLF forces us to exploit a second correlation ($L_{r,\mathrm{core}} - L_{r,\mathrm{tot}}$) in order to derive an expression for $\rho_{r,\mathrm{core}}$. In this case, we make use of Eq. 6.8 and we build $\rho_{r,\mathrm{core}}$ as:

$$\rho_{r,\mathrm{core}}(L_{r,\mathrm{core}}, z) = \rho_{r,\mathrm{tot}}(L_{r,\mathrm{tot}}, z)\frac{d\log L_{r,\mathrm{tot}}}{d\log L_{r,\mathrm{core}}}\,. \tag{6.18}$$

We expect that the number of MAGN showing core and total emission is the same and therefore the fraction of radio sources emitting from the whole object (total emission) having an emitting core is equal to 1.

Finally, we obtain the GLF inserting Eq. 6.18 in Eq. 6.17:

$$\begin{aligned}\rho_\gamma(L_\gamma, z) \;&=\; k\;\rho_{r,\mathrm{tot}}\left(L^{5\mathrm{GHz}}_{r,\mathrm{tot}}(L^{5\mathrm{GHz}}_{r,\mathrm{core}}(L_\gamma)), z\right)\\ &\cdot\;\; \frac{d\log L^{5\mathrm{GHz}}_{r,\mathrm{core}}}{d\log L_\gamma}\,\frac{d\log L^{5\mathrm{GHz}}_{r,\mathrm{tot}}}{d\log L^{5\mathrm{GHz}}_{r,\mathrm{core}}}\,.\end{aligned} \tag{6.19}$$

$d\log L^{5\mathrm{GHz}}_{r,\mathrm{core}}/d\log L_\gamma$ is computed from Eq. 6.6, while the $d\log L^{5\mathrm{GHz}}_{r,\mathrm{tot}}/d\log L^{5\mathrm{GHz}}_{r,\mathrm{core}}$ derives from the total-core correlation, Eq. 6.8. The fraction k is a free parameter of our prediction. If our hypothesis of a correlation between the core radio and γ emission is physical, as supported by the results on the ULs (see previous section), we might expect k values not too far from 1. In other words, each MAGN with a bright radio core is expected to emit in the γ-ray band as well.

We notice that the further uncertainty introduced by using a second correlation is subdominant with respect to the error band coming from the $L_\gamma - L_{r,\mathrm{core}}$ correlation and it is likely compensated, at least to a good extent, by the fit to the cumulative number counts, Sec. 6.5.

For concrete calculations we adopt the total RLF at 151 MHz derived in (Willott et al., 2001) (Model C with Ω_M=0) and shift luminosities from 151 MHz to 5 GHz according to the power-law dependence of the radio luminosity. We convert the comoving volume to the standard ΛCDM cosmology by using the conversion factor $\eta(z)$:

$$\eta(z) = \frac{d^2V_W/dzd\Omega}{d^2V/dzd\Omega}, \tag{6.20}$$

where $d^2V_W/dzd\Omega$ is the comoving volume element used by (Willott et al., 2001):

$$\frac{d^2V_W}{dz\,d\Omega} = \frac{c^3z^2(2+z)^2}{4H^3_{0,W}(1+z)^3}, \tag{6.21}$$

c is the speed of light and $H_{0,W} = 50$ km s^{-1} Mpc^{-1}. In the cosmological model ΛCDM the comoving volume element is defined as:

$$\frac{d^2V}{dzd\Omega} = \frac{c\, d_L(z)^2}{H_0(1+z)^2\sqrt{(1-\Omega_\Lambda-\Omega_M)(1+z)^2+(1+z)^3\Omega_M+\Omega_\Lambda}}. \tag{6.22}$$

The values of cosmological parameters we use are: $H_0 = 70$ km s^{-1} Mpc^{-1}, $\Omega_M = 0.27$, $\Omega_\Lambda = 0.73$.

In the following sections, we will exploit the derived GLF Eq. 6.19 to predict relevant observable quantities: the source count distribution (Sec. 6.5) and the γ-ray diffuse flux from the MAGN unresolved population (Sec. 6.6).

6.5 The source count distribution

The source count distribution (known also as N-count or $\log N - \log S$ distribution) is the cumulative number of sources $N(> F_\gamma)$ detected above a threshold flux F_γ and it is directly related to the number density of sources. The theoretical N-count is derived from Eq. 6.12 as:

$$\begin{aligned} N_{\rm th}(> F_\gamma) &= 4\pi \int_{\Gamma_{\rm min}}^{\Gamma_{\rm max}} \frac{dN}{d\Gamma} d\Gamma \int_0^{z_{\rm max}} \frac{d^2V}{dzd\Omega}\, dz \\ &\int_{L_\gamma(F_\gamma,z,\Gamma)}^{L_\gamma^{\rm max}} \frac{dL_\gamma}{L_\gamma \ln(10)}\, \rho_\gamma(L_\gamma, z, \Gamma), \end{aligned} \tag{6.23}$$

where $L_\gamma(F_\gamma, z, \Gamma)$ is the γ-ray luminosity of a MAGN at redshift z, with photon spectral index Γ and photon flux F_γ (integrated above 100 MeV). The spectral index distribution, $dN/d\Gamma$, is assumed to be gaussian in analogy with blazars (Abdo, Ackermann, Ajello, Antolini et al., 2010). The comoving volume, $d^2V/(dzd\Omega)$, is computed according to Eq. 6.22. We set $\Gamma_{\rm min}$=1.0, $\Gamma_{\rm max}$=3.5, $z_{\rm max} = 6$ and $L_{\gamma,\rm max} = 10^{50}$ erg s^{-1}.

$\rho_\gamma(L_\gamma, z, \Gamma)$ is then computed accordingly to Eq. 6.19 and depends on the free parameter k. In order to constrain this parameter and confirm the validity of the correlation Eq. 6.6, we compare our prediction on the N-count with the experimental source count distribution.

The experimental source count distribution of the 12 MAGN of our sample is derived by following (Abdo et al., 2010c):

$$N(> F_\gamma) = \sum_{i=1}^{N(>F_{\gamma,i})} \frac{1}{\omega(F_{\gamma,i})}, \tag{6.24}$$

where the sum runs on all the i-sources with a γ-ray flux $F_{\gamma,i} > F_\gamma$, and $\omega(F_{\gamma,i})$ is the flux dependent detection efficiency compatible with our sample. The detection efficiency takes into account the fact that due to selection effects the intrinsic photon-index distribution is different from the observed one: for low fluxes *Fermi*-LAT detects more easy sources with harder spectra, as shown in (Abdo et al., 2009, 2010c). The detection efficiency is not available for the MAGN sample from the 2FGL and we reasonably assume it is the same as for blazars of the 1FGL and take it from (Abdo, Ackermann, Ajello, Antolini et al., 2010)[xv].

Black points in Fig. 6.5 display the experimental N-count for the sample of our 12 MAGN. The N-count is a cumulative quantity and therefore all the data points are highly correlated. It is anyhow useful to fit the theoretical $N_{\rm th}(> F_\gamma)$ to the experimental source count distribution to constrain the parameter k. We notice that the shape of the function predicting $N(> F_\gamma)$ is essentially driven by the RLF, and not by the fit to the experimental source count distribution.

In Fig. 6.5 we also show the predictions from Eq. 6.23 when using different correlations and imposing that the theoretical N-count fits the experimental data. The dashed back line and the dot-dashed red line refer to the source count distribution derived by adopting two different correlations for $\rho_\gamma(L_\gamma, z, \Gamma)$ in Eq. 6.23. The dashed back line exploits the correlation $L_\gamma - L_{r,\rm core}$ of Eq. 6.6, while the dot-dashed red line corresponds to the correlation $L_\gamma - L_{r,\rm tot}$ of Eq. 6.7[xvi]. The "best-fit" label in the legend refers in this case to the correlation best-fit of the respective Eqs. 6.6, 6.7. The fit to the experimental source count distribution gives $k = 3.05$ and $k = 0.156$ respectively, meaning that using the best-fit radio core-γ correlation function slightly under-predicts the distribution of MAGN observed by *Fermi*-LAT, whereas adopting the radio total-γ correlation leads to a lower number of sources at the lowest fluxes. Moreover, we compute the uncertainty on our prediction (colored bands) as follows:

[xv] Out of the 12 MAGN considered in our analysis, 8 galaxies (3C78, 3C274, Centaurus A, NGC 6521, PKS 0625-35, 3C111, 3C207, 3C380) are found in the 1FGL, 8 (3C274, Centaurus A, NGC 6521, Centaurus B, Fornax A, PKS 0625-35, 3C207, 3C380) are in the 2FGL, while 3C120 is listed in (Abdo, Ackermann, Ajello, Asano et al., 2009) and Pictor A has been revealed in (Brown & Adams, 2012). The efficiency employed in our analysis is taken from (Abdo, Ackermann, Ajello, Antolini et al., 2010), which refers to the 1FGL blazar catalog. We have also demonstrated in (Di Mauro et al., 2013) that an empirical estimation of the efficiency for the 2FGL blazars does not change the results of our analysis. We indeed conclude that the source number count for the 2FGL sample and with newly estimated efficiency is compatible with the results obtained for the whole MAGN treated with the 1FGL efficiency. This is expected as the distribution is dominated by faint sources below the detection threshold, following the radio source count distribution, and the LAT-detected sources are not really constraining the γ-ray logN-logS. Additionally, a slightly different normalization can be safely compensated by the free normalization parameter k and will not change the flux prediction derived in Sec. 6.6.

[xvi] The total radio-γ correlation is shown here merely for comparison with previous works, notably with (Inoue, 2011).

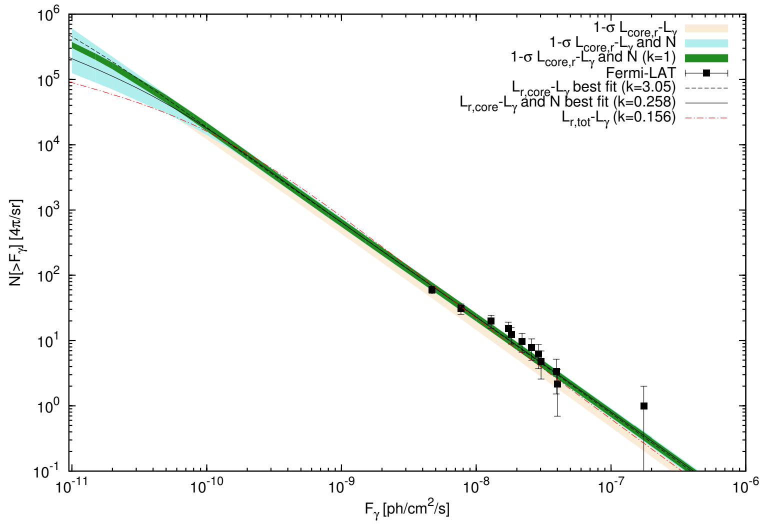

Figure 6.5: Source count distribution as a function of the integrated γ-ray flux. The experimental N-count derived from *Fermi*-LAT data is depicted by the black squares with their 1σ error bars. The black dashed line (pink shaded area) represents the N-count predicted by considering the the best-fit configuration (1σ uncertainty band) for the $L_{r,\text{core}}-L_\gamma$ correlation of Eq. 6.6. If we further constrain our model with the experimental N-count, we find the theoretical N-count to be described by the black solid line (cyan shaded area) which is obtained by performing the minimization on the $L_{r,\text{core}} - L_\gamma$ best-fit (1σ uncertainty band) correlation and k (see text for details). Finally, all the configurations with fixed k=1 are displayed by the green shaded area. The red dot-dashed curve has been obtained with the $L_{r,\text{tot}} - L_\gamma$ correlation according to Eq. 6.7.

- we calculate the $N(> F_\gamma)$ for all the correlation coefficients falling in the 1σ uncertainty band for the $L_{r,\mathrm{core}} - L_\gamma$ relationship (Fig. 6.1);
- for each combination of these coefficients we determine k by fitting the theoretical prediction with the experimental $\log N - \log S$ (pink shaded area);
- among all the best-fitted k values we select the configuration with the lowest χ^2 which predicts the best $N(> F_\gamma)$ (black solid line, k=0.258);
- all the configurations giving a 1σ variation from the lowest χ^2 (minimal χ^2 +3.53 as required by the estimation of three parameters) span the cyan shaded area.

Since, accordingly to our reasoning, we expect physically $k \sim 1$ we also make the same fitting exercise by fixing k to 1. The result corresponds to the green shaded band. This represents the ideal situation in which we predict that each MAGN has a radio-loud central region emitting in γ-rays as well. The band again refers to the 1σ uncertainty on the N-count fit by following the same procedure described above.

Comparing the theoretical and experimental source count distribution is important in testing the correctness of our assumption about the origin of the MAGN γ-ray emission. Nevertheless, we stress that every prediction is accompanied by its uncertainty band which cannot be neglected. Inside the error bands, the predictions represent a good fit to *Fermi*-LAT data. We notice that the most relevant discrepancies among predictions arise at low fluxes, where the theoretical N-count is unconstrained by present data. It is also worth mentioning that indeed the low-flux tail of the source count distribution gives the most important contribution to the unresolved γ-ray flux as we will see in the next section.

6.6 The contribution to the IGRB

In chapter 3 we have presented the IGRB as one of the most promising target for indirectly detect and constrain the DM γ-ray signal and we have already discussed the importance of the unavoidable astrophysical background which contributes to the IGRB through the contribution of multiple unresolved source classes.

We aim to compute the prediction for the contribution to the IGRB originating from the unresolved population of MAGN. In general, the diffuse γ-ray flux of an unresolved source class distribution is given by:

$$\frac{d^2F(\epsilon)}{d\epsilon d\Omega} = \int_{\Gamma_{\min}}^{\Gamma_{\max}} d\Gamma \frac{dN}{d\Gamma} \int_0^{z_{\max}} \frac{d^2V}{dzd\Omega}\, dz \int_{L_{\gamma,min}}^{L_{\gamma,max}} \frac{dF_\gamma}{d\epsilon} \tag{6.25}$$

$$\cdot \quad \frac{dL_\gamma}{L_\gamma \ln(10)}\, \rho_\gamma(L_\gamma, z)(1 - \omega(F_\gamma(L_\gamma, z)))\ \exp\left(-\tau_{\gamma,\gamma}(\epsilon, z)\right).$$

where $\omega(F_\gamma(L_\gamma, z))$ is the detection efficiency of *Fermi*-LAT for a photon flux F_γ, which is the flux from a source with a γ-ray luminosity L_γ at redshift z. $dN/d\Gamma$ is the photon spectral index distribution (see Eq. 6.23). The minimum γ-ray luminosity is set to 10^{41} erg s^{-1}, the maximum to 10^{50} erg s^{-1}. We check explicitly that the result does not depend on the maximal luminosity of integration, indicating that the main contribution to the γ-ray flux comes from very numerous and very faint sources. Indeed, we also test that shifting the lower luminosity limit from 10^{41} erg s^{-1} down to 10^{38} erg s^{-1} would lead to a 15% greater intensity. This means that the diffuse flux is very sensible to the low-flux end of the N-count where the constraints from data are weak. $dF_\gamma/d\epsilon$ is the intrinsic photon flux at energy ϵ, for a MAGN with γ-ray luminosity L_γ (Venters, Pavlidou & Reyes, 2009; Yan, Zeng & Zhang, 2012):

$$\frac{dF_\gamma}{d\epsilon} = \frac{(1+z)^{2-\Gamma}}{4\pi d_L(z)^2} \frac{(2-\Gamma)}{\left[\left(\frac{\epsilon_2}{\epsilon_1}\right)^{2-\Gamma} - 1\right]} \left(\frac{\epsilon}{\epsilon_1}\right)^{-\Gamma} \frac{L_\gamma}{\epsilon_1^2}. \tag{6.26}$$

When propagating in the universe high-energy γ-rays interact with the extragalactic background light (EBL), cosmic optical radiation and infrared background (Gould & Schréder, 1966; Jelley, 1966; Stecker, de Jager & Salamon, 1992; Salamon & Stecker, 1998; Stecker, Malkan & Scully, 2006; Mazin & Raue, 2007; Razzaque, Dermer & Finke, 2009; Gilmore, Madau, Primack, Somerville & Haardt, 2009; Finke, Razzaque & Dermer, 2010; Ackermann et al., 2012a; Abramowski et al., 2013) and they thus get absorbed by the EBL. This is encoded in the optical depth $\tau_{\gamma,\gamma}(\epsilon, z)$. We adopt here the attenuation model of (Finke et al., 2010). As a consequence of this interaction, electron-positron pairs are created and they scatter off the CMB photons yielding a secondary cascade emission in the γ-ray range. We here neglect the effect of cascade emission which is expected to be negligible for soft sources like MAGN (Inoue, 2011; Venters, 2010; Inoue & Ioka, 2012).

Our prediction on the diffuse γ-ray flux from the unresolved MAGN population as a function of γ-ray energy is displayed in Fig. 6.6 along with *Fermi*-LAT measurements and best-fit power-law of the IGRB (Abdo & al., 2010). Lines and bands follow the same color and style code of Fig. 6.5. The cyan shaded area corresponds to the 1σ uncertainty band on the $L_{r,\text{core}} - L_\gamma$ correlation and on the k parameter in the source count distribution. It is remarkable that the band nearly achieves the IGRB data points and it spans almost one order of magnitude. The green band is obtained by fixing $k = 1$ as described in the previous section for Fig. 6.5. The black dashed line refers to the flux derived by adopting the best-fit coefficients of the $L_{r,\text{core}} - L_\gamma$ correlation and k=3.05 (as it is required by the best-fit the N-count), while the dot-dashed red line represents the flux derived when the γ-ray luminosity is correlated with the total radio luminosity according to

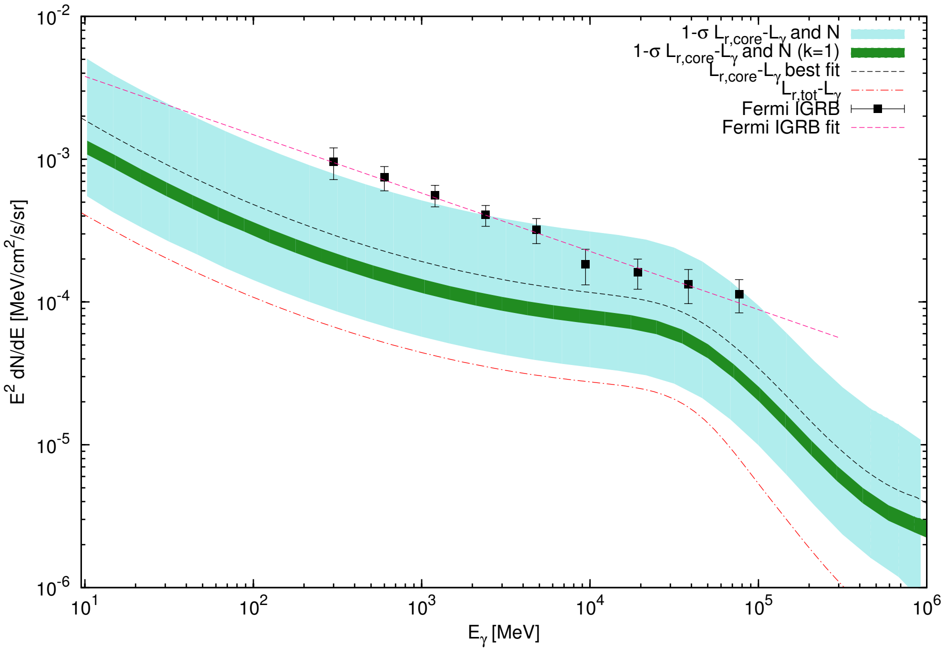

Figure 6.6: Contribution to the IGRB differential spectrum produced by the unresolved MAGN population as a function of γ-ray energy. IGRB measurements of *Fermi*-LAT (Abdo & al., 2010) are represented by black squares together with their best-fit power-law (magenta dashed curve). The prediction of the diffuse γ-ray flux from MAGN is displayed by the cyan shaded area which corresponds to the 1σ uncertainty band on the $L_{r,\mathrm{core}} - L_\gamma$ correlation once the constraint on the k parameter is imposed through the source count distribution. Results coming from best-fit expected values are shown for the $L_{r,\mathrm{core}} - L_\gamma$ (dashed black line) and $L_{r,\mathrm{tot}} - L_\gamma$ (red dot-dashed curve) correlation. Finally, the green band represents the configurations with k=1 at 1σ C.L. (see discussion on Fig. 6.5).

Eq. 6.7, and total RLF (Willott et al., 2001). The latter curve is not meant to be a prediction of our but it is shown for the sake of completeness. We have already stressed that we rely on the assumption that the γ-ray emission of the MAGN population is assumed to originate from the central region of the active galaxy, and modeled from the core RLF. Therefore, the prediction of this work is represented by the cyan band.

From the Fig. 6.6 we can see that below $\sim$ 30 GeV the flux does not follow a pure power-law. This deviation is due to the integration over the photon index distribution in Eq. 6.25. The attenuation of flux at high energies (i.e. above 50 GeV) is instead due to the effect of EBL absorption which depletes the γ-ray flux. The flux integrated above 100 MeV is $5.69 \cdot 10^{-7}$ cm^{-2}s^{-1}sr^{-1} for the lower bound of the cyan uncertainty band, and $4.91 \cdot 10^{-6}$ cm^{-2}s^{-1}sr^{-1} for the upper one. These values compare with $1.03 \cdot 10^{-5}$ cm^{-2}s^{-1}sr^{-1} derived from the experimental data (Abdo & al., 2010) and constitute about the 9.5% and 83% of the IGRB intensity respectively. At all *Fermi*-LAT energies, the best-fit MAGN contribution is 20%-30% of the measured IGRB flux. This result is compatible with the one reported by (Inoue, 2011), where the contribution of MAGN to the IGRB is found to range from 10% to 63%. Compared to the blazar population, our prediction shows almost the same slope although it is higher in normalization.

By having computed the contribution of unresolved MAGN to the IGRB, we conclude that this faint but numerous population gives a sizable diffuse γ-ray flux that participates in determining the origin of the IGRB together with other unavoidable astrophysical source classes. When added to the contribution from the other populations listed in Sec. 3.4 the flux from MAGN could even saturate the observed IGRB. Nonetheless, the prediction is affected by an important uncertainty which originates mostly from the correlation adopted to compute the GLF. If more γ-ray sources are detected in the next future, it will be possible to overcome such an uncertainty; only a larger MAGN detected sample would allow to build the GLF by means of statistical analysis instead of relying on the correlation with the radio wavelength.

The determination of this additional contribution to the IGRB impacts not only on astrophysics but also on DM indirect detection. Indeed, the IGRB measurements represent a powerful tool to constrain the DM parameter space. Taking into account the unavoidable astrophysical background is mandatory when constraining the DM γ-ray flux through the IGRB. Modeling the emission of unresolved γ-ray sources may leave very little room for more exotic sources, such as DM in the halo of our galaxy (Bringmann et al., 2013). On the other hand, the more accurately the astrophysical background is modeled, the more strong and reliable are the constraints on DM.

We will see in the next chapter 7 which is the effect of including the MAGN contribution to the IGRB for DM indirect searches.

Chapter 7

Dark Matter constraints and potential detection

In chapter 3 we have reported an overview about DM searches through γ-rays and the main results of the current research. We dedicate this chapter to present our contribution in this field.

This chapter is organized as follows: in section 7.1 we report our results about constraints on the DM annihilation cross section from an analysis of the IGRB, in section 7.2 we show the relevance of DM spectral features for indirect detection and we make prospects for the next generation of γ-ray telescopes. The two sections are based on (Bringmann et al., 2013) and (Bringmann et al., 2011) respectively.

7.1 Constraining Dark Matter through the IGRB

We have already introduced in chapter 3 the IGRB as a target for DM searches. Indeed, this faint and almost isotropic component of the γ-ray sky is believed to originate from the superposition of several sources of astrophysical or more exotic origin. Among other components, γ-rays produced by DM annihilation from galactic and cosmological distances can contribute to the IGRB intensity. The lack of any detected DM signal in the IGRB data[i] allows us only to set constraints on DM.

In the seminal work of (Calore et al., 2012) conservative upper limits on the DM annihilation cross section have been derived from the high-latitude diffuse component, by subtracting from the IGRB (Abdo & al., 2010) the minimum estimated fluxes for the most significant unresolved source pop-

---

[i] The 130 GeV feature described in chapter 3 does not show up in the IGRB as expected for the annihilation rate of $\langle\sigma_{\rm ann}v\rangle_{\gamma\gamma} \sim 10^{-27}{\rm cm}^3{\rm s}^{-1}$ inferred from the galactic center observation (Abdo, Ackermann, Ajello, Baldini et al., 2010). It is possible anyhow to enhance this signal in the IGRB if adopting optimistic models for the evolution and distribution of DM subhalos (Zavala, Springel & Boylan-Kolchin, 2010).

ulations. Indeed, subtracting the unavoidable contribution of standard astrophysical source classes, whose unresolved flux is firmly estimated in a non-negligible *Fermi*-LAT IGRB percentage, leads to a “residual” IGRB that can be used to set strong constraints on DM. The drawback of such an analysis is the dependence on the uncertainty of the estimates for the background fluxes, which can even span several orders of magnitude depending on the source class. Nevertheless, it is always possible to adopt a conservative point of view by considering all the astrophysical contributions at their minimal level, such that the ensuing constraints on DM cross section are “true” upper limits, in the sense that higher values of the cross section are unlikely compatible with the IGRB measurements.

Recently, motivated by our prediction that the faint but numerous population of unresolved MAGN contributes significantly to the total IGRB intensity (chapter 6), we evaluate the room left for galactic DM at high latitudes ($> 10^\circ$) and we set stringent constraints on the DM parameter space. In this context, we discuss in detail the uncertainty related to the modeling of the astrophysical background and we emphasize the potential that the IGRB has to be one of the most promising targets for DM ID once uncertainties on the background are even slightly reduced. We present adopted methods and results of (Bringmann et al., 2013) in the following.

7.1.1 Modeling the astrophysical background

The modeling of the astrophysical background follow the idea outlined in (Calore et al., 2012), where each source class with a non-negligible contribution to the IGRB has been considered at its minimal level. In the present work the astrophysical background is modeled by considering the contributions from different unresolved point-source populations, namely from MAGN (as presented in chapter 6), BL Lacs objects and FSRQs (as derived in (Abdo, Ackermann, Ajello, Antolini et al., 2010) and (Ajello et al., 2012) respectively), SF galaxies (Ackermann, Ajello, Allafort et al., 2012) and MSPs (Calore et al., 2012). All these source classes have been deeply illustrated in section 3.4. Also the diffuse emission from the interaction of ultra-high-energy CRs with the ISM can results in a non-negligible contribution to the IGRB. We here neglect such a contribution which produce a significant flux (% level) only at the high-energy end of the IGRB spectrum as shown in (Calore et al., 2012).

Fig. 7.1 displays the contributions to the IGRB that we consider in the present analysis. The uncertainty bands are shown as reported in the relevant references (roughly corresponding to 1σ deviations). The *Fermi*-LAT IGRB data (Abdo & al., 2010) and its power-law fit (solid black line) are depicted as well. The solid dark-green curve refers to the expected diffuse γ-ray flux from unresolved MAGN (Di Mauro et al., 2013), the light-green band bracketing the corresponding uncertainty. The other displayed components are: SF galaxies (the MW model is depicted by the dashed dark-(light-) blue line (area)[ii]), MSPs (dot-dashed red line and orange band), FSRQs (purple dotted line and pink band), and BL Lacs (dotted dark-grey line and light-grey band).

While BL Lacs induced spectrum is well described by a power-law, the FSRQs contribution shows a different behavior which is the result of a more detailed and recent analysis taking into account the spectral energy distribution and the evolution of the luminosity function for this source class (Ajello et al., 2012). BL Lacs dominate above 1 – 2 GeV, while FSRQs give an intense flux at low energies. Notice that for $E_\gamma \gtrsim 30\,\mathrm{GeV}$ the BL Lacs flux is actually expected to drop in the same way as the MAGN flux, due to EBL absorption, but this has not been taken into account in the flux estimate referred to here. The γ-ray spectrum from unresolved MSPs shows a distinctive exponential cutoff at few GeV, whose peak is due to the primary electron cooling from curvature radiation. This contribution dominates over the blazars spectra from 300 MeV up to 3 – 4 GeV. A bump spectrum is also expected from the SF population due to the hadronic emission of CRs with the ISM. Finally, MAGN lead to the dominant contribution at all energies.

In the following, we define Σ_{BMS} as the sum of the contributions from Blazars (both BL Lacs and FSRQs), MSPs and SF galaxies. By varying the contribution of each component within its uncertainty band, the IGRB data can be saturated by multiple combinations of the above fluxes, i.e. only little room is left to other unknown γ-ray sources as e.g. DM.

7.1.2 Modeling the Dark Matter contribution

We make here the common hypothesis that DM consists of WIMPs. The γ-ray flux produced by DM self-annihilations in our galaxy is expressed by Eq. 3.1. Additionally, we average Eq. 3.1 over the telescope viewing solid angle $\Delta\Omega$ when integrating in $d\Omega$. As already explained in chapter 3 the DM γ-ray flux factorizes in two terms: the particle physics term containing all the information about the nature of the particle DM candidate and the astrophysical factor encoding the information about the geometrical distribution of DM in the studied target.

The number of photons per annihilation is modeled by taking into account only the continuum γ-ray flux of secondary photons from two-body processes (section 3.1)[iii]. Namely, we consider the prompt γ-ray emission from final-state showers or hadronic decays of the two-body annihilation

---

[ii] We remind the reader that (Ackermann, Ajello, Allafort et al., 2012) adopts two possible γ-ray spectra for the SF emission which bracket the expected contribution from multiple-type SF galaxies. The first one refers to Milky Way-like SF galaxies (model MW), the second one assumes a power-law spectrum in accordance to the properties of the *Fermi*-LAT detected star-burst galaxies (model PL).

[iii] We here do not model the secondary from three-body processes as they result from EW corrected spectra (see chapter 4).

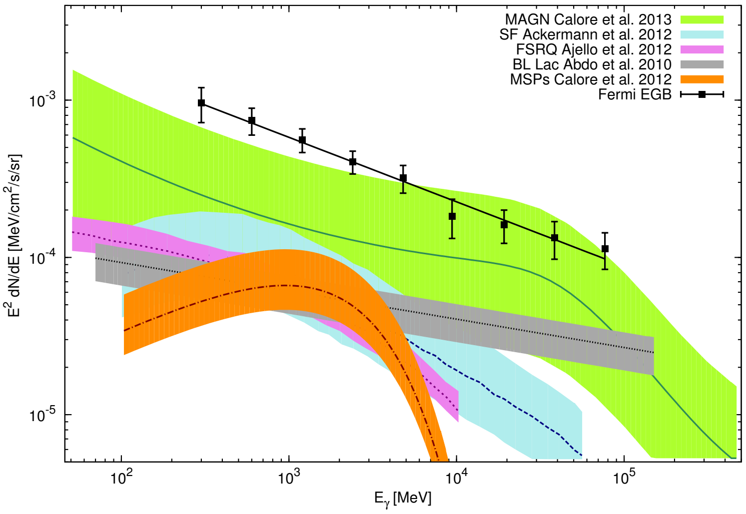

Figure 7.1: Contributions to the IGRB at high latitudes from classes of unresolved point-like sources described in the text. IGRB data at high galactic latitudes ($|b| > 10°$) are shown together with their power-law fit (Abdo & al., 2010). We display each standard astrophysical contribution and its corresponding uncertainty band: MAGN (Di Mauro et al., 2013) (solid dark-green curve and light-green band), MW model for SF galaxies (Ackermann, Ajello, Allafort et al., 2012) (dot-dashed red line and orange band), MSPs (Calore et al., 2012) (dot-dashed red line and orange band), BL Lacs (Abdo, Ackermann, Ajello, Antolini et al., 2010) (dotted dark-grey line and light-grey band), and FSRQs (Ajello et al., 2012) (purple dotted line and pink band).

products and the ICS photons by energetic electrons and positrons (produced by a chain of decays and hadronization processes as well) off the interstellar radiation field (ISRF). The spectrum for the prompt emission of both photons and $e^{\pm}$ as been computed by running the Pythia Montecarlo code (version 8.162) (Sjostrand, Mrenna & Skands, 2008). We study the annihilation into different final states by fixing the annihilation channel (branching ratio equal to one). This results in a rather model independent analysis.

The ICS has been computed from $e^{\pm}$ originated by DM annihilation and interacting with ambient photons, following the prescription in (Cirelli & Panci, 2009). Energetic electrons propagate in the galaxy as a consequence of the scattering on the inhomogeneities of the galactic magnetic field. While, as usually assumed in the literature (Regis & Ullio, 2008), diffusion can be safely neglected for GeV – TeV energies, the dominant processes are energy losses due to the interactions with ambient photons fields, i.e. with the ISRF, namely with CMB photons, infrared radiation (IR) emitted by absorption and re-emission of starlight by the galactic dust, and starlight (SL) produced by stars in the disk. We here include both electromagnetic energy losses and synchrotron radiation. The former are considered in the fully relativistic Klein-Nishina regime. Photon density distributions are modeled as average fields normalized differently according to the different sky regions, following (Cirelli & Panci, 2009). Notably, we take into account all the three fields (CMB, IR, SL) in the region between 10° and 20°, whereas SL and IR are neglected for $|b| > 20°$. Synchrotron is included in the region $10° < |b| < 20°$ because of the almost vanishing B at high-latitudes (Sun, Reich, Waelkens & Enßlin, 2008; J. L. Han & Qiao, 1994; Prouza & Šmída, 2003; Pshirkov, Tinyakov, Kronberg & Newton-McGee, 2011). The assumed mean value of the magnetic field is $B = 2\,\mu$G Increasing the total energy loss, the synchrotron radiation reduces the γ-ray flux from DM by ~30% and increases of the upper limits on $\langle\sigma_{\rm ann} v\rangle$ by 10%.

For the DM geometrical distribution we consider a Burkert profile, Eq. 3.6. We determine the values of its characterizing parameters, r_s and ρ_s, by fixing the local DM density $\rho(r = r_\odot) = 0.4$ GeV cm^{-3} ($r_\odot$=8.33 kpc) and fitting the halo DM mass $M(r < r_0)$ contained within a certain radius r_0. We use available $M(r < r_0)$ data for different values of r_0 (Deason et al., 2012; Gnedin, Brown, Geller & Kenyon, 2010; Irrgang, Wilcox, Tucker & Schiefelbein, 2013; Kafle, Sharma, Lewis & Bland-Hawthorn, 2012; Kochanek, 1996; Sakamoto, Chiba & Beers, 2003; Watkins et al., 2009; M. I. Wilkinson & Evans, 1999; Xue et al., 2008) and we find a best fit value of $r_s = 15$ kpc. We notice that the study of the high-latitude region does not suffer from uncertainties due to the choice of the DM profile as it would be for the GC region. Indeed, the astrophysical factor slightly depends on the DM profile at those latitudes. By defining:

$$I_{\Delta\Omega} = \frac{1}{\Delta\Omega}\int_0^{\Delta\Omega} {\rm d}\Omega \int_{\rm l.o.s} \rho^2(R(s,\phi,\theta))ds., \tag{7.1}$$

we find $I_{\Delta\Omega}(|b| > 10°) \cdot {\rm GeV}^{-2}{\rm cm}^6{\rm kpc}^{-1} = 2.4,\ 2.5,\ 2.8$ for the case of an isothermal sphere, a NFW (Navarro, Frenk & White, 1996), and an Einasto (Einasto, 1965) profile respectively (see section 3.2 for the profiles expressions).

To limit the uncertainties of our prediction, we do not include the existence of a dark disk (Read, Lake, Agertz & Debattista, 2008) as well as the contributions from galactic and extragalactic DM halos and subhalos (Diemand & Moore, 2011; Springel et al., 2008) that would increase the geometrical factor and result in stronger upper limits on DM.

A further source of uncertainty is the value of the local DM density. Its determination suffers from high systematic uncertainties and its value is found to range from 0.2 up to 0.7 GeV cm^{-3} (Salucci et al., 2010). If not explicitly stated differently, we will assume $\rho_\odot$=0.4 GeV cm^{-3}.

7.1.3 Updated constraints and future potential

Having improved the modeling of the standard astrophysical contributions to the IGRB and having included the ICS component in the computation of the DM expected γ-ray flux, we set upper limits on the DM annihilation cross section that result to significantly improve those in (Calore et al., 2012), given also the more detailed discussion about the impact of astrophysical uncertainties. We derive constraints on the DM annihilation cross section in function of the mass of the DM candidate. Given the assumptions illustrated above, our limits are meant to be conservative[iv] and slightly dependent on the underlying particle physics model. The main uncertainties come from the adopted astrophysical background as we discuss in the following.

We derive upper bounds on the DM annihilation cross section by imposing that the DM flux together with the sum of the different astrophysical background does not overproduce any of the IGRB data, considered at 2σ (Abdo & al., 2010). This method is commonly applied in the literature and allows us to compare our results with the current ones. We anyhow notice that when the total expected flux almost reach the IGRB we safely consider the *Fermi*-LAT data plus 3σ. From Fig. 7.1 we can deduce that the limits are set by the last data bins where the astrophysical background is very close to the data.

As discussed above, DM γ-rays come from the prompt emission and the $e^{\pm}$ ICS off ambient photon fields. The inclusion of the ICS results in an enhancement of the DM γ-ray flux and, as a consequence, in stronger limits on the annihilation cross section. We show in Fig. 7.2 the improvement on constraints due to the inclusion of the ICS for the $e^{\pm}$ leptonic channel. The blue dashed curve corresponds to upper limits on $\langle\sigma_{\rm ann}v\rangle$ when the DM spectrum originates only from the prompt γ-ray component, while the solid red line refers to the inclusion of ICS. Here, the astrophysical background is fixed at its minimal value, considering the sum of the minimal contributions for all the components described above and plotted in Fig. 7.1. The effect of ICS inclusion starts to be effective at high energies, i.e. at high DM masses, because the prompt only component of the DM flux is peaked at too higher energies with respect to the last data points whereas the ICS flux presents a much broader spectral distribution. "Prompt only" limits are about a factor of two weaker at $\simeq$ 10 TeV, meaning that ICS γ-rays is important for large DM masses ($m_\chi \gtrsim 1\,\text{TeV}$). This implies that IGRB constraints may be able to test the mass range which can justify the positron fraction excess (Adriani

---

[iv] The choice we made on the Burkert profile and a smooth halo is meant to be conservative and different assumptions on the DM profile would lower the upper bounds we find by up to about 30% In fact, considerably more for optimistic assumptions about DM substructure (Diemand, Kuhlen & Madau, 2007; Kuhlen, Diemand & Madau, 2008; Pieri et al., 2011).

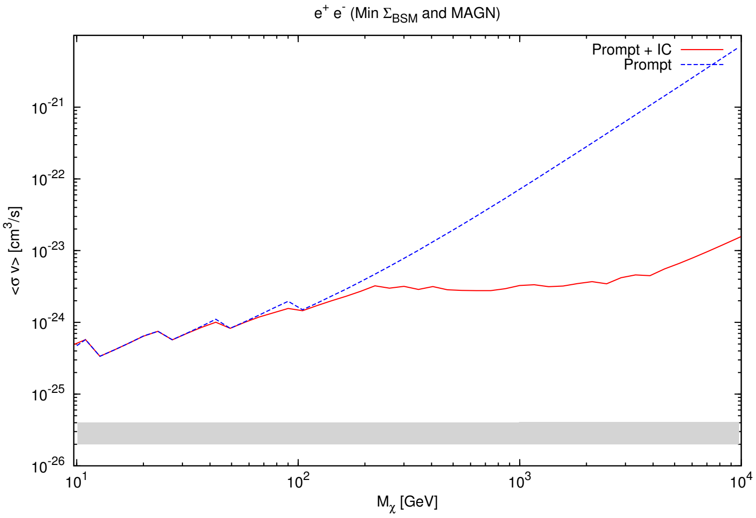

Figure 7.2: Upper limits on the DM annihilation cross section $\langle\sigma_{\rm ann}v\rangle$ into $e^{\pm}$ final states, as a function of the DM mass m_χ, derived by setting the astrophysical background to its minimal level for each considered class of sources (MAGN, blazars, SF and MSPs). The blue dashed curve corresponds to considering the DM γ-ray spectrum originated from the prompt component only, while the solid red line represents the effect of ICS. The grey area depicts the typically adopted value for the cross section of thermally produced WIMPs, $\langle\sigma_{ann}v\rangle \sim 3\cdot 10^{-26}$ cm^3 s^{-1}.

et al., 2009; Ackermann et al., 2012b; M. Aguilar et al., 2013) in terms of DM annihilation into leptonic final states (Bergstrom, Edsjo & Zaharijas, 2009; Yuan et al., 2013; Cholis & Hooper, 2013; Jin, Wu & Zhou, 2013).

For comparison, we also indicate in the same plot the thermal cross section of $\langle\sigma_{ann}v\rangle \sim 3\cdot 10^{-26}$ cm^3 s^{-1}.

The main source of uncertainty on our derived constraints is represented by the systematic uncertainty in the determination of the different unresolved source classes to the IGRB. Indeed, these astrophysical estimates suffer from large uncertainties due mainly to the poor statistics of detected γ-ray sources and the difficulty of theoretically modeling such contributions. Indeed, from Fig. 7.1 the narrower bands correspond to populations (BL Lacs and FSRQs) for which the detected sample is large and population studies in γ-rays are possible, while for e.g. MAGN and SF galaxies the estimate of the IGRB contribution relies on phenomenological approaches based on multi-wavelengths correlations that lead to a greater uncertainty on the final result.

Depending on the relative contributions of the different populations, the room left for a possible DM component can be severely constrained. In what follows, we discuss the effect of the various astrophysical backgrounds on DM limits. Given the high degeneracy of the different astrophysical classes, the scenarios presented here are meant to be illustrative examples of the fundamental importance of astrophysics in this kind of analysis and they emphasize the great potential of the IGRB in constraining the DM annihilation cross section.

Fig. 7.3 displays upper limits on the DM annihilation cross section into $b\bar{b}$. The left panel refers to the impact of the MAGN component as it has been derived in chapter 6 and considered here for the first time in the context of DM searches. $\Sigma_{\rm BMS}$ is fixed to the minimally allowed value (in order to be conservative), while the MAGN contribution varies from its minimal expected value up to the 70%[v] of its maximally expected value. Increasing the MAGN component results in an improvement of limits by at least one order of magnitude with respect to adopting a conservative choice for the astrophysical contributions, i.e. the one according which all the contributions are set to their minimal estimates.

We stress here that the conservative limits on the DM annihilation cross section are represented by the scenario in which all the astrophysical components are set to their minimally expected value, i.e. to the pink shaded area.

On the other hand, the constraints are affected, even if more slightly, by varying the other astrophysical contributions, notably the SF model component.

In the right panel of Fig. 7.3 the MAGN contribution is set to its best-fit value and $\Sigma_{\rm BMS}$ changes from its minimally to maximally predicted contribution according to the error bands described in Fig. 7.1. When all the astrophysical contributions but MAGN are included at their minimal level, the constraints on the $\langle\sigma_{\rm ann}v\rangle$ are very close to the ones derived in (Calore et al., 2012), where a similar modeling of the astrophysical background was considered. The constraints depend on the choice of the underlying SF galaxy model; indeed, while for E $\sim$ 2 GeV the two models predict a diffuse γ-ray flux which is comparable (the MW one slightly higher than the PL model), above this energy the MW model drops faster, and at $\sim$ 100 GeV it is about a factor of ten lower than the PL model. By consequence, $\langle\sigma_{\rm ann}v\rangle$ upper limits are directly affected by the different modeling of SF galaxies emission, notably when the maximally predicted $\Sigma_{\rm BMS}$ is considered. The flux calculated according to the PL model lowers the upper limits by a factor of about $\sim$3 for m_χ=10 TeV, while the MW SF spectrum reduces the room to DM at lower energies, thus for smaller WIMP masses. We notice that when $\Sigma_{\rm BMS}$ contributes at the minimal level, the difference between SF galaxy models is negligible since the MAGN contribution dominates the IGRB in

---

[v] We note that setting the γ-ray flux from MAGN to the maximally allowed value would exceed the *Fermi*-LAT data by more than 2σ.

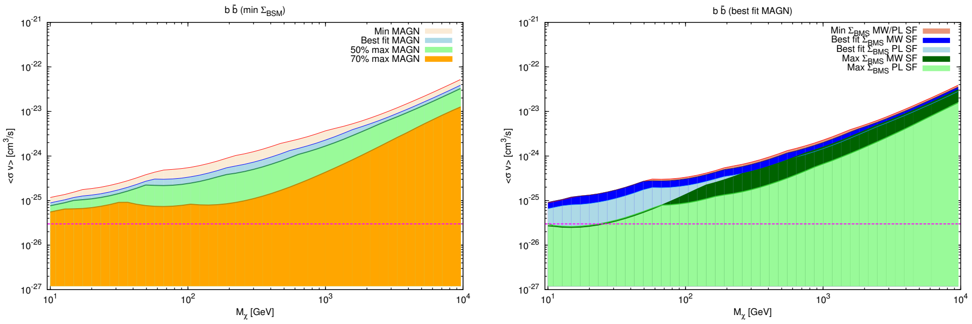

Figure 7.3: Upper limits on $\langle\sigma_{\rm ann}v\rangle$ as a function of the WIMP mass for different levels of $\Sigma_{\rm BMS}$ and MAGN. Shaded areas indicate the region of the parameter space allowed by γ-ray *Fermi*-LAT IGRB data (Abdo & al., 2010) with the modeling of astrophysical backgrounds here adopted. In the left panel, $\Sigma_{\rm BMS}$ is set to the minimal level of the different predictions and the contribution from MAGN is varied from its minimal up to 70% of its maximally expected level. The impact of various choices for $\Sigma_{\rm BMS}$ on the limits is shown in the right panel where the MAGN contribution has been fixed to its best-fit value as derived in chapter 6. The constant line at $3{\cdot}10^{-26}$ cm^3 s^{-1} represents the thermal DM cross section.

the whole energy range.

Upper limits of $\langle\sigma_{\rm ann}v\rangle$ for the various annihilation channels are presented in Fig. 7.4. We define four astrophysical scenarios depending on the contribution to the IGRB of the different source classes. In the top left panel, our most conservative scenario considers all the astrophysical backgrounds set to their minimal values. This "conservative" case can be directly compared with Fig. 3 of (Calore et al., 2012), where the displayed limits was derived by minimally modeling the IGRB contributions and considering DM prompt only photons. That figure shows "conservative" limits on $\langle\sigma_{\rm ann}v\rangle$ for $b\bar{b}$, $\mu^+\mu^-$ and $\tau^+\tau^-$ final states for two different "minimal" models of the IGRB (taking into account blazars and MSPs, Model I, and blazars, MSPs, star forming and ultra-high-energy CRs, Model II). The results of our "conservative" scenario, as expected, are well compatible with those of (Calore et al., 2012) for DM masses below ~100 TeV. For $m_\chi \gtrsim 100$ GeV the inclusion of ICS becomes important. This results in an improvement of limits on leptonic channels with respect to those of (Calore et al., 2012).

The right panel shows a more realistic scenario: all astrophysical backgrounds contribute at their expected "best-fit" values. The ensuing limits are stronger by about a factor of two compared to the conservative case.

Lower panels of Fig. 7.4 illustrate a more optimistic perspective showing how much the IGRB can be powerful in constraining galactic DM annihilation. $\Sigma_{\rm BMS}$ is set at the "best-fit" value in both panels, whereas the

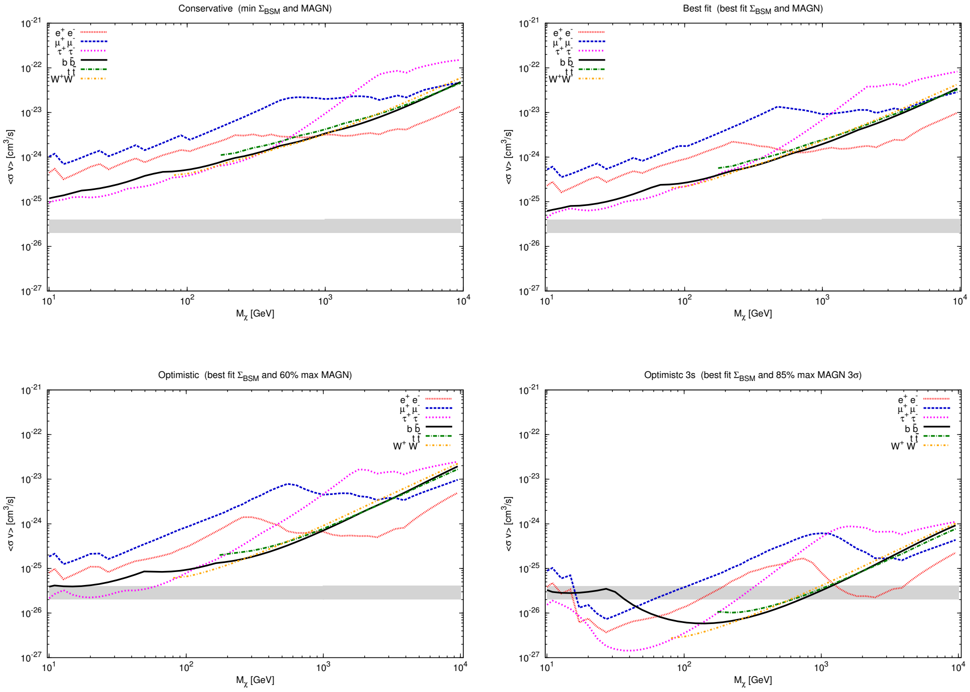

Figure 7.4: Upper limits on $\langle\sigma_{\rm ann}v\rangle$ for different modelings of the astrophysical background representing four illustrative scenarios. Constraints derived by assuming all sources contributing at their minimal level are displayed in the top left panel. Allowing sources to contribute at their expected "best-fit" level we obtain limits as depicted in the top right panel. In the bottom panels we fix $\Sigma_{\rm BMS}$ at the "best-fit" value, by varying the contribution of MAGN from 60% (left panel) to 85% (right panel) of the maximally expected flux. In each panel, we show limits for different DM annihilation channels by assuming a 100% BR. The grey band corresponds to the value for the "thermal" cross section for WIMPs, $\langle\sigma_{\rm ann}v\rangle\sim 3\cdot 10^{-26}$ cm^3 s^{-1}.

MAGN contribution varies from 60% (right bottom panel) to 85% (left bottom panel) of its maximally predicted value. The former assumption on the MAGN component would result in limits that start to probe the thermal cross section of $\langle\sigma_{\rm ann}v\rangle\sim 3\cdot 10^{-26}$ cm^3 s^{-1}. Since, at this level, a slight increase of the MAGN contribution rapidly skims the data impacting significantly on the room left of DM annihilation, we safely derive limits by considering the data plus their 3σ errors. The result is shown in the bottom right panel of Fig. 7.4 where we consider the MAGN contribution at 85% of the maximally predicted flux. Concerning the annihilation into leptons, our results allow to rule out a DM interpretation of the positron fraction rising at least for a relatively large contribution of the MAGN population as depicted in the bottom-left panel of Fig. 7.4. Indeed, while $e^{\pm}$ final states severely constrain the annihilation into e^+e^- with $\langle\sigma_{\rm ann}v\rangle\sim$ 0.3 (1)$\cdot 10^{-23}$ cm^3 s^{-1} for masses of about 1-3 (10) TeV, weaker bounds are derived by fixing the annihilation channel into muons or tau leptons. Limits for the latter channel are set close to the value required to fit the AMS-02 data (Yuan et al., 2013; Jin et al., 2013).

Moreover, our results improve the limits derived in (Calore et al., 2012) at DM masses above ~100 GeV due to the inclusion of ICS and the inclusion of MAGN contribution make those limits stronger by a factor of ~2 in the case of the "best-fit' scenario displayed in Fig. 7.4.

Compared to an analysis of preliminary *Fermi* data (Cirelli & Panci, 2009) taking into account the ICS contribution, our results are better for high masses. They also turn out to improve by a factor of about 4 (for $b\bar{b}$) the limits obtained for the analysis of 1-year IGRB data in a smaller sky region than considered here (Cirelli, Panci & Serpico, 2010).

We also compare our results to the ones derived by the *Fermi*-LAT Collaboration analysis of galactic DM contributions to the IGRB (Ackermann, Ajello, Atwood et al., 2012). In the case of no background modeling, we find that, in our conservative scenario, bounds are comparable for $b\bar{b}$ and $\tau^+\tau^-$ final states (for $m_\chi \sim 20$ GeV). If we compare with the outcome of that analysis when modeling the background, we obtain upper limits comparable with the MAGN best fit choice for $m_\chi \sim 100$ GeV. Instead, for the same scenario, higher masses $m_\chi \sim 1$ TeV are more severely constrained by the present study, i.e. the limits are a factor of roughly 3 stronger.

Furthermore, our results are also consistent with constraints from different targets (with very different astrophysical backgrounds and systematics uncertainties). Upper limits competitive with the joint likelihood analysis of 10 dwarf Spheroidal galaxies (Ackermann et al., 2011) are the ones derived by setting the MAGN flux at 60% of its maximal expectation value ("optimistic" limits). In the case of TeV masses and leptonic final states, even the scenario with a minimal MAGN contribution leads to comparable results. Low DM masses for leptonic channels from radio emission (Fornengo et al., 2012) are constrained comparably to this analysis, while for masses $m_\chi \sim$ 100 GeV we find stronger limits, regardless the amount of MAGN. Finally, our conservative constraints improve also the ones derived from galaxy cluster (Ackermann et al., 2010a) and observations of the CMB (Galli, Iocco, Bertone & Melchiorri, 2011).

The updated upper limits on DM annihilation cross section through the analysis of the IGRB astrophysical background are robust, mildly dependent on the choice of the DM density profile and conservative since we do not consider here the contribution of galactic and extragalactic substructures.

As we have seen, our constraints result to be competitive with current limits and they can likely be improved significantly by reducing even slightly the uncertainty on the astrophysical fluxes.

Indeed, WIMPs which have been thermally produced in the early universe can be severely constrained up to TeV masses by assuming that MAGN contribute at their maximal level as predicted in this work.

This means that the IGRB will represent a powerful target to constrain DM even more efficiently than other presently promising targets as the GC and dwarf galaxies which present a fundamental reach that will not allow to improve drastically the limits even with a greatly increased statistics (Bringmann & Weniger, 2012).

Therefore, we have shown that the IGRB can have a great potential in constraing the flux from DM annihilation. In order to fully exploit this possibility, an understanding of the astrophysical background is mandatory. Indeed, reducing the theoretical uncertainty affecting the predictions on the IGRB contributions will make the limits derived from this target more robust. In particular, the impact of MAGN prediction's uncertainty results to be the most significant on limits, since this population constitutes by now the most important contribution to the IGRB. As seen in chapter 6, reducing the uncertainty on the MAGN contribution will be possible in the next future by detecting other γ-ray emitting objects. For all the above mentioned reasons, the IGRB has a great future potential in constraining DM properties.

7.2 The relevance of Dark Matter spectral features

In chapter 3 we have learnt that one of the advantages of the γ-ray DM signal is to show distinct and unambiguous spectral features coming from higher order radiative corrections to the two-body annihilation cross section. While loop-suppressed line-like signals are always expected to occur, spectral features from electromagnetic corrections (notably from VIB) are a generic prediction for most models.

In what follows, we will illustrate how well pronounced spectral features, other than lines, can improve the sensitivity of current and future γ-ray telescopes to the DM signal. Indeed, so far, only line-like signal has been explicitly searched for regardless of the fact that it is $\mathcal{O}(\alpha^2)$ suppressed and therefore subdominant with respect to other spectral signatures (Bringmann et al., 2008). Moreover, since the energy resolution of current experiments does not allow a discrimination among line-, step-, or pronounced bump-like signals, it is mandatory to have a method suitable to look for any of these features which are equivalently more promising for signal discovery than the featureless spectrum of secondary photons. We thus present a general method to search for DM spectral features and we show that their inclusion can greatly help in disentangling the DM signal from the astrophysical background and improves DM constraints, as we demonstrate with a concrete application to IACTs[vi] for observations of the GC region.

7.2.1 Looking for spectral features

The defining aspect of a spectral feature is an abrupt change of the flux as a function of the energy near the kinematic endpoint of the spectrum, namely a sharp cutoff at $E_\gamma \sim m_\chi$. The corresponding energy range would be only limited by the energy resolution of the experiment. The idea is to concentrate the search for these kind of signals on a small "sliding" (with energy) energy window, defined by the limits E_0, E_1, with $E_0 < E_1$. The width of the energy window is defined as:

$$\epsilon \equiv \frac{E_0}{E_1}\,, \tag{7.2}$$

and it is centered on the value of the spectral cutoff, i.e. $\bar{E} \equiv \sqrt{E_0 E_1} \sim m_\chi$, such that:

$$E_0 \equiv \frac{\bar{E}}{\epsilon(E)}\,; \qquad E_1 \equiv \bar{E} \cdot \epsilon(E)\,. \tag{7.3}$$

The main advantage is that γ-ray fluxes of astrophysical origin can usually be very well described by a local power-law in such a small energy range. This effectively allows a determination of the background at the statistical limit and removes the uncertainties related to background modeling in a wider energy range.

The crucial point is the choice of the window size. Indeed, the validity of the power-law approximation for the background breaks down for too large ϵ and depends critically on the collected statistics and the curvature of the background with respect to the pure power-law,

$$k \equiv \frac{d^2 \log(dN_{\mathrm{bkg}}/dE)}{(d \log E)^2}\,, \tag{7.4}$$

representing the deviation from the pure power-law, i.e. $k \equiv 0$. Constraining the maximal allowed window size $\epsilon_{\max}$ is thus mandatory, as we will see in the case of concrete instrument and observation specifications.

The discrimination of the signal from the background is then performed by applying a binned likelihood method (see Appendix F for details), which allows to derive upper limits on the signal or its significance in case of a detection.

[vi] We recall that IACTs collect the Cherenkov light produced by very high energy γ-rays interacting with atmospheric nuclei and generating electromagnetic showers (a sizable fraction of charged secondary shower particles then emits Cherenkov light) and record the shower images.

We derive upper limits by defining the likelihood function $L(\boldsymbol{\mu}|\mathbf{c}) = \Pi_i P_{\mu_i}(c_i)$ for each energy bin ΔE_i, in which we have divided the energy range $[E_0, E_1]$; μ_i (c_i) indicates the expected (observed) count number in bin i and P_μ is the Poisson probability distribution with mean μ. The observed counts are defined as:

$$\frac{\mu_i}{t_{\rm obs}} = \int_{\Delta E_i} dE \int dE' \, \mathcal{D}_{E,E'} A_{\rm eff}(E') \left[\alpha \frac{dN_\chi}{dE'} + \beta E'^{-\gamma} \right] , \tag{7.5}$$

where $t_{\rm obs}$ is the time of observation, $A_{\rm eff}$ the effective area and $\mathcal{D}_{E,E'}$ the energy dispersion of the instrument (taken to be Gaussian throughout the analysis). The free parameters of the analysis are the background normalization β, its spectral slope γ and the normalization of the DM signal α. For a given data set $\mathbf{c}$, their best-fit estimates are derived by maximizing $L(\boldsymbol{\mu}|\mathbf{c})$ in the energy window $[E_0, E_1]$.

By imposing that the variation of the $-2 \log L$ is equal to 4 when increasing α from its best-fit value and maximizing the likelihood with respect to β and γ, we compute the 97.7% C.L. upper limits on the signal strength[vii] . In a very simplistic way, i.e. neglecting trial factors[viii], it is also possible to compute the value of the cross section that would lead to a more than 5σ detection. This is set by a discrepancy of the $-2 \log L$ values for background-only and background-plus-signal fits of at least 25.

To demonstrate the potential of the presented method, we apply it to a concrete example by specifying instrument and observation characteristics.

7.2.2 A concrete example: prospects for IACTs

Background and signal fluxes are modeled according to the considered experiment and signal looked for. We here present prospects on DM spectral features from the observation of the GC region with IACTs.

The DM Signal. The DM signal flux $dJ_{\rm DM}/dE$ from an angular region $\Delta\Omega$ is expressed by Eq. 3.1.

The differential number of photon per annihilation has been discussed in chapters 3 and 4. Here, we consider three types of typical endpoint features coming from higher order corrections to the tree-level annihilation process.

[vii] We notice that this is the correct C.L. corresponding to one-sided limits derived at 2σ.

[viii] When searching for a signal somewhere in a possible energy range, the significance of observing a local excess of events must take into account the probability of observing such an excess anywhere in the range. This is the so called "look elsewhere effect". The effect can be quantified in terms of a trial factor, which is usually defined as the ratio between the probability of observing the excess at some fixed energy point to the probability of observing it anywhere in the range. Analogously, the look elsewhere effect must be taken into account when scanning over different target regions.

Table 7.1: We here report the most relevant information of the benchmark models used as spectral templates for this analysis. Internal bremsstrahlung dominant annihilation channel is quoted with mass and total annihilation rate expected from thermally produced DM.

Model	DM particle	m_χ [TeV]	$\langle\sigma v\rangle$ [cm^{3}s^{-1}]	channel	spectral feature
KK	$B^{(1)}$	1.3	$1 \cdot 10^{-26}$	$\ell^+\ell^-\gamma$	FSR step
BM3	neutralino	0.23	$9 \cdot 10^{-29}$	$\ell^+\ell^-\gamma$	IB bump
BM4	neutralino	1.9	$3 \cdot 10^{-27}$	$W^+W^-\gamma$	IB bump

First order $\mathcal{O}(\alpha_{\rm em})$ QED corrections from the emission of collinear photons from FSR are predicted to lead to almost universal sharp step-like spectra, while when the additional photon is radiated off the virtual internal leg (VIB) the spectrum shows, for most models, a pronounced bump-like feature which can resemble the line-like one.

A prominent example of a model in which FSR dominates the electromagnetic bremsstrahlung is the case of KK DM in models of UED (Bergström et al., 2005b) (see section 2.4.3 for datails). In the minimal version of these models, the LKP corresponds to the first KK mode of the weak hypercharged gauge boson $B^{(1)}$, with the correct relic density obtained for $m_{B^{(1)}} \sim 1.3\,\mathrm{TeV}$ (Bélanger et al., 2011). $B^{(1)}$ pair annihilation goes mainly into charged leptons pair and the electromagnetic corrections are dominated by the logarithmic enhancement of FSR. The total γ-ray spectrum at high energies is thus dominated by FSR. It is worth noticing that the spectrum is indeed almost independent of $m_{B^{(1)}}$ and other model parameters.

In the framework of the MSSM, VIB corrections to neutralino annihilation might give a more important contribution than FSR to the total final spectrum. Indeed, it has been shown that for some classes of MSSM models VIB produces a pronounced bump at the high-energy end of the spectrum because of the lifting of helicity suppression, while FSR is still suppressed for helicity arguments. As benchmarks for VIB spectral features, we consider two MSSM models, BM3 and BM4, in which VIB from all leptons ($\tilde{\tau}$ co-annihilation region) and W^+W^- final states respectively dominates the total spectrum (Bringmann et al., 2008). Although VIB spectral features are highly model dependent, we here assume the simplified approach of considering the spectra for the above mentioned models as spectral templates (and independent on m_χ).

Finally, the most striking spectral feature is represented by the line signal originating from the direct annihilation of DM particles into two photons and generically suppressed at loop level.

Table 7.1 summarizes the benchmark models for spectral features adopted in this work. We include for completeness the DM mass and total annihilation rate required to obtain the observed relic density for thermally produced DM, although we treat these values as free parameters in our analysis.

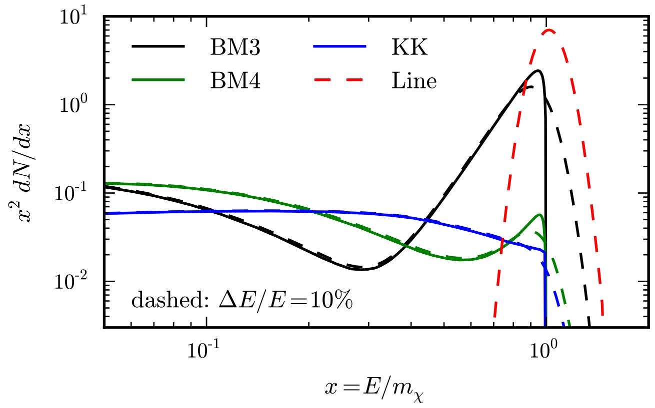

Figure 7.5: Typical examples of DM spectral features corresponding to models of Table 7.1. Photon spectra for line signal (red curve), step-like feature from KK annihilation (blue line) and pronounced bump-like feature from neutralino annihilation (black lines) are displayed together with their smearing due to a Gaussian energy resolution of width $\Delta x/x = 0.1$ (dashed lines).

Fig. 7.5 shows the total photon spectra corresponding to the these benchmarks and the effect of the smearing due to a finite energy resolution.

The Background. The main background of Cherenkov telescopes are CRs induced photons, i.e. photons produced by CRs interacting with the atmosphere, namely by protons and electrons. While electrons give origin to showers very similar to those induced by primary photons and hence constitute a practically irreducible background, proton-induced hadronic showers differ in the shape of profile and the photon energy density. They can currently be rejected with efficiencies $\epsilon_p \sim \mathcal{O}(10^{-2}\text{–}10^{-1})$. Charged CRs typically constitute the major background of IACT observations because of their large intrinsic fluxes.

In order to produce fake data for our ideal experiment, we model the background in the GC region as follows. The CR flux of electrons is:

$$\frac{dJ_{e^-}}{dEd\Omega} = 1.17 \times 10^{-11} \left(\frac{E}{\text{TeV}}\right)^{-3.9} \qquad (\text{GeV cm}^2 \text{ s sr})^{-1} \tag{7.6}$$

above 1 TeV, and it hardens below 1 TeV to a spectral index of −3.0 (Aharonian et al., 2008). The transition between the two slopes is assumed to be proportional to their generalized mean with exponent −2).

The proton flux is modeled as:

$$\frac{dJ_p}{dEd\Omega} = 8.73 \times 10^{-9} \left(\frac{E}{\text{TeV}}\right)^{-2.71} \qquad (\text{GeV cm}^2 \text{ s sr})^{-1} \tag{7.7}$$

Table 7.2: IACTs benchmark scenarios: instrumental characteristics representing the performances of the different IACTs (effective area, energy resolution, rejection efficiency and observation time). From top to bottom, they roughly correspond to the HESS (Aharonian et al., 2006c), the future CTA (Actis et al., 2011) and the proposed DMA (Bergström et al., 2011) telescope characteristics.

Scenario	$A_{\rm eff}$(1TeV)	$\Delta E/E$(1TeV)	ϵ_p	$t_{\rm obs}$
IACT1	0.18 km^2	15%	10^{-1}	50 h
IACT2	2.3 km^2	9%	10^{-2}	100 h
IACT3	23 km^2	7%	10^{-3}	5000 h

(Hoerandel, 2003)[ix].

Moreover, as we have already mentioned, observations of the GC are highly affected by the presence of the HESS source J1745-290 (Aharonian et al., 2006b). We consider its flux as a further background for our observations:

$$\frac{dJ_{\rm HESS}}{dE} = 2.3\times10^{-15}\left(\frac{E}{\rm TeV}\right)^{-2.25} \qquad ({\rm GeV\ cm^2\ s\ sr})^{-1}\,. \tag{7.8}$$

Finally, we take into account the diffuse photon emission measured by HESS in a $-0.8^\circ \leq \ell \leq 0.8^\circ$ and $|b| \leq 0.3^\circ$ region around the GC given by

$$\frac{dJ_{\rm diff}}{dE} = 5.1\times10^{-15}\left(\frac{E}{\rm TeV}\right)^{-2.29} \qquad ({\rm GeV\ cm^2\ s\ sr})^{-1} \tag{7.9}$$

(Aharonian et al., 2006a). In order to account for this emission in our target region ($2^\circ \times 2^\circ$), we rescale the flux by a factor of two.

To compute the number of events we define the different instrument specifications as represented by three benchmark observational scenarios that we summarize in Table 7.2. They correspond roughly to the currently operating HESS (Aharonian et al., 2006c), the future CTA (Actis et al., 2011) and the most optimistic choice of a dedicated experiment for indirect DM searches represented by the proposed Dark Matter Array (DMA) (Bergström et al., 2011). The effective area $A_{\rm eff}$ depends on energy for HESS (Aharonian et al., 2006c) and CTA [x], whereas we assume $A_{\rm eff}^{\rm DMA} = 10\cdot A_{\rm eff}^{\rm CTA}$. We allow a significant improvement in the energy resolution: from 15% of HESS down to 7% for DMA. The proton, γ-ray and electron efficiencies are ϵ_{p,γ,e^-}; ϵ_p is defined according to the Table 7.2, while $\epsilon_\gamma = \epsilon_{e^-} = 0.8$ in all three scenarios. We assume that the proposed DMA can have a protons rejection efficiency of $\approx 10^{-3}$.

[ix] Notice that a shift of the proton flux to lower energies by a factor of 3 takes into account the reduced Cherenkov light output of hadronic showers, $E_p^{\rm recon.} \approx E_p^{\rm true}/3$ (see e.g. (Fegan, 1993)).

[x] http://www-hess.physik.hu-berlin.de/public/trabajo.pdf

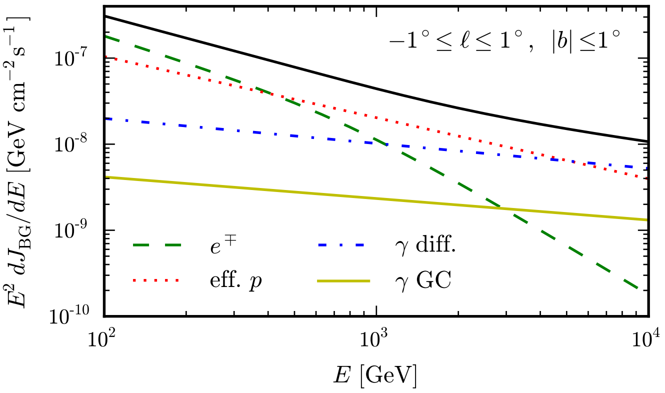

Figure 7.6: Background fluxes for IACTs in the $2^\circ \times 2^\circ$ target region around the Galactic center. The effective proton flux is set to $\epsilon_p = 10^{-2}$, as it is for the IACT2 scenario). The black solid line corresponds to the total background flux.

The overlaid of the backgrounds we consider is displayed in Fig. 7.6 in the case of IACT2 scenario (i.e. $\epsilon_p = 10^{-2}$). The total differential number of expected counts for the background is represented by the solid black line.

The target region of our analysis is chosen to be a $2^\circ \times 2^\circ$ angular region around the GC. The choice of the target region, i.e. of the solid angle $\Delta\Omega$, is crucial when looking for spectral features since the statistical significance of a spectral feature depends on the signal-to-noise ratio $\mathcal{S}/\mathcal{N}$ ($\mathcal{N} \simeq \sqrt{\mathcal{B}+\mathcal{S}}$) inside the considered target region. Indeed, although the DM annihilation flux is expected to be maximized at the GC, geometrical factors and the presence of a strong astrophysical background from point-like sources and diffuse emission make the determination of the best target region about the GC depend on the angular distribution of both the signal and the background (Serpico & Zaharijas, 2008). We thus choose $\Delta\Omega$ as the region in which the quantity $\mathcal{S}/\mathcal{N}$ is optimized. The number of expected background events $\mathcal{B}$ within a target region $\Delta\Omega$ and energy range ΔE is calculated from Eq. 7.5 by considering only the background fluxes and integrating over $\Delta\Omega$. In the same way, the number of signal events $\mathcal{S}$ is obtained from Eq. 3.1 for a line-like signal.

Fig. 7.7 shows how the $\mathcal{S}/\mathcal{N}$ ratio (thick lines) for a line-like spectral feature varies when increasing the target region, i.e. the radius θ of a circular region around the GC. We compare results for the Einasto and NFW DM profiles with parameters $r_s^{\rm NFW} = 21$ kpc, $r_s^{\rm Ein.} = 20$ kpc, $\alpha = 0.17$ and $\rho_\chi = 0.4$ GeV cm^{-3} at Sun's position $r_\odot = 8.5$ kpc (Pieri et al., 2011). Moreover, we also consider a profile boosted in a region concentrated around the GC by the effect of e.g. adiabatic compression (Blumenthal et al., 1986; Gnedin & Primack, 2004; Gustafsson, Fairbairn & Sommer-Larsen, 2006).

Adiabatic compression predicts a steepening of the inner DM profile due to the effect of baryons during the structure formation of the DM halo. The baryonic component is indeed able to cool (i.e. dissipate energy) and contract and thus can sink into the center of the galaxy enhancing the gravitational potential which DM is attracted by. To model this effect, adiabatic invariants are used, e.g. the quantity $R \cdot M(< R)$ (which is constant because of the conservation of angular momentum), in the context of dedicated hydrodynamical (i.e. with baryons) simulations where compressed DM profiles are found. In this case, we consider an Einasto profile (Ein.+AC) which is boosted by adiabatic contractions as modeled in (Gnedin & Primack, 2004). We adopt the best fit parameters derived from the hydrodynamical simulation S1 of (Gustafsson et al., 2006). In this case, the profile steepens in the central region as $\rho \sim r^{-1.12}$. For such an enhancement, DM self-annihilations may be non-negligible (Berezinsky & Zybin, 1992); however, we check that this effect does not alter our results[xi].

For standard profiles, as can be seen from the figure, radii of a few degree maximize the $\mathcal{S}/\mathcal{N}$ (see also (Serpico & Zaharijas, 2008)), while the boosted Einasto profile requires much smaller target regions. Therefore, we will reduce the target region for adiabatic compressed profiles 9 $0.2° \times 0.2°$).

It is worth noticing that, to determine the best target region in light of systematic instrumental effects, e.g. artefacts and uncertainties in the reconstructed energy spectrum of the instrument, it is convenient to consider also the signal-to-background ratio $\mathcal{S}/\mathcal{B}$. Such a ratio is shown in Fig. 7.7 for comparison (thin lines). Adopting a relatively small $\Delta\Omega = 2° \times 2°$ region around the GC is therefore a good compromise since the $\mathcal{S}/\mathcal{N}$ turns out to be optimized and the $\mathcal{S}/\mathcal{B}$ is not too small as it would be for larger regions.

The maximally allowed window size. In order to test the validity of the local power-law approximation for the background we assume the background to be described by a bended power-law with maximal curvature $k = k_{\rm max}$ fixed and we constrain the energy window size ϵ by requiring that average DM limits obtained when incorporating a (fixed) curvature k in the background fit change less than 50% with respect to limits obtained when the background is well described by a simple power-law. We thus derive the maximally allowed window size $\epsilon_{\rm max}$ for each observational scenarios and for different values of the background curvature.

Fig. 7.8 displays the values of $\epsilon_{\rm max}$ as function of the sliding energy window position $\bar{E} \equiv \sqrt{E_0 E_1}$, and for different curvatures $k_{\rm max}$, i.e. from top to bottom $k_{\rm max} = 0.1, 0.2, 0.3$. For IACT1 we also compute the values of

---

[xi] DM self-interactions are effective if the characterizing time of particles loss due to the annihilation at the position R, $\tau_{\rm loss}(R)$, is greater than the life time of the galaxy, $\tau_{\rm gal}$. A cutoff radius is thus defined by the condition $\tau_{\rm loss}(R_{\rm cutoff})/\tau_{\rm gal} = 1$. In our case, $R_{\rm cutoff} = 10^{-9}$ kpc and thus self-annihilations do not affect our results.

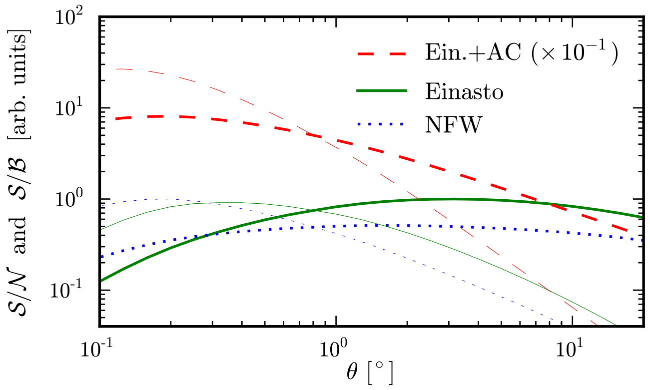

Figure 7.7: For the optimization of the target region we compare the $\mathcal{S}/\mathcal{N}$ (thick lines) and the $\mathcal{S}/\mathcal{B}$ (thin lines) of DM signal inside a circle around the GC with radius θ for different DM spatial profiles: NFW (dotted blue line), Einasto (solid green line) and Einasto with adiabatic compressions (dashed red line). We assume $\mathcal{S} \ll \mathcal{B}$. We set energy threshold is set to 200 GeV, although we find similar results varying the threshold from 100 GeV up to 5 TeV.

$\epsilon_{\max}$ for which at least 80% of the mock data sets show a p-value for the power-law fit is larger than 0.05. Those values are represented by dotted lines, which demonstrate that a statistically good quality of the power-law fit does not mean negligible effects on the DM limits. Therefore, *a priori* assumptions on $k_{\max}$ are indispensable; in our case, we determine the optimal logarithmic window size by employing $|k| \leq k_{\max} \approx 0.2$ for IACT1 and IACT2, according to Fig. 7.8. We of course check that this value is satisfied for the background we adopt here. As we can see from the figure, in the case of IACTs, the extremely good statistics make the spectrum with $k \sim \mathcal{O}(0.1)$ curvature deviate from a power-law background already for small sizes of the sliding energy window. We thus consider $k \neq 0$ as a free parameter of the fit to set reasonable limits and allow for energy windows larger than what shown in Fig. 7.8.

Upper limits on DM annihilation cross section. We derive projected limits on the spectral features described above. Fig. 7.9 shows the expected 2σ upper limits (thick lines) on the different DM models as well as their variance (shaded area) over 300 realizations of mock data sets.

Mock data are created in the hypothesis of background only events by using the definition of the IACTs background given above.

Upper limits on $\langle\sigma_{\rm ann}v\rangle$ are derived by defining

$$\frac{dJ_{\rm DM}}{dE} \equiv \alpha \frac{dN}{dE}\,, \tag{7.10}$$

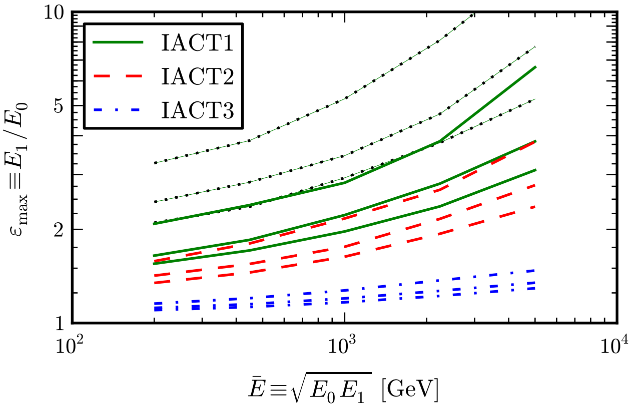

Figure 7.8: Maximal sliding energy window size $\epsilon_{\max}$ as function of the window position $\bar{E}$. For different intrinsic background curvatures $k_{\max} = 0.1, 0.2, 0.3$ (top to bottom), we show the window sizes above which DM limits are affected by more than 50% with respect to the pure power-law ansatz. The dotted lines correspond to $\epsilon_{\max}$ (IACT1 scenario) for which a power-law fit to the background is still statistically good, i.e. for which at least 80% of the mock data sets have a p-value larger than 0.05 when adopting a pure power-law fit.

with $dJ_{\rm DM}/dE$ as expressed in Eq. 3.1. For any photon spectrum and DM mass, limits on α (and thus on $\langle \sigma_{\rm ann} v \rangle$) are derived by scanning over all possible values of m_χ and applying the binned profile likelihood method as described above.

We notice that our limits are derived down to m_χ ~200 GeV, because we are interested in the IACTs energy range and we do not push our limits in the low-energy regime of the instruments where performances of IACTs are more model-dependent.

From left to right we present upper limits on the different spectral features: line-, step- and bump-like signals, corresponding to different DM models and different observational scenarios. Upper limits on $\langle \sigma_{\rm ann} v \rangle_{\chi\chi \to \gamma\gamma}$ are rescaled by $\alpha_{\rm em}^{-2}$ for a direct comparison with the other panels.

We can see that looking for IB (FSR or VIB) features in the spectrum (central and right panel) can constrain annihilation rates close to the “thermal” cross value even when considering standard DM spatial profiles (we notice that NFW and Einasto profiles lead to very compatible results). This implies that including such a spectral information can be more efficient than line-like signals in setting limits on DM annihilation. The constraining power of spectral features can be also deduced by comparing the results of Fig. 7.9 with the best current limits from Cherenkov telescopes that come from the HESS observation of the GC region and are imposed by assuming DM annihilation into two-body final states.

For conservative assumptions on the DM profile the constraints are about

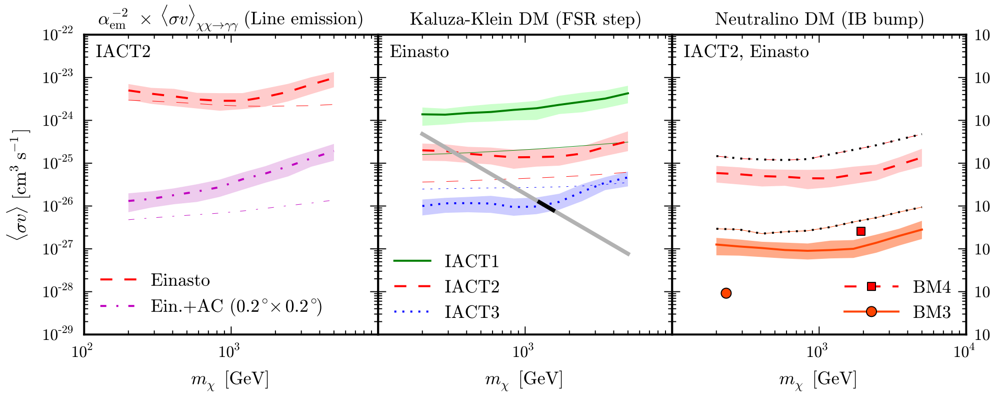

Figure 7.9: 2σ upper limits (thick lines) on $\langle\sigma_{\rm ann}v\rangle$ for the DM benchmark models assumed as spectral templates. Limits are derived by averaging over 300 mock-data sets and their 68% C.L. variance is depicted by the shaded bands. We also show the DM cross section values corresponding to $\mathcal{S}/\mathcal{B} \approx 1\%$ (thin lines). Upper bounds are reported for the different spectral features (from the left panel to right panel: line-like, step-like and bump-like signal), different DM spatial profile (left panel: comparison between Einasto profile and an Einasto profile boosted by adiabatic compression as described in the text) and different IACT scenarios (central panel: comparison among the performances of the IACTs of Table 7.2). In the case of the line-signal, results are rescaled by $\alpha_{\rm em}^{-2}$ in order to compare directly the three panels. We also display the expected value of $\langle\sigma_{\rm ann}v\rangle$ for thermally produced DM in the case of KK (grey band representing the generic prediction of $\langle\sigma_{\rm ann}v\rangle$ as a function of the mass and black square for a 1.3 TeV $\mathrm{B}^{(1)}$ candidate) and neutralino (colored markers) candidates. In the right panel we also show the projected sensitivity (dotted lines) to a neutralino internal bremsstrahlung signal.

$\mathcal{O}(10)$ too weak to exclude models. See e.g. the displayed values of cross sections (and masses) compatible with the relic density for the KK model (in the central panel the grey band indicates the expected $\langle\sigma_{\rm ann}v\rangle$, the black part being compatible with the observed relic density), BM3 and BM4 models (benchmark points in the right panel). Nevertheless, in case of an adiabatically compressed profile our limits could improve by about two orders of magnitude, as demonstrated for γ-ray lines in the left panel.

The comparison among observational scenarios is represented by the central panel. With respect to current operating telescopes, limits may be improved by about one order of magnitude with the future CTA and the most optimistic DMA could derive bounds stronger by another factor of ten. Moreover for DMA limits understanding the systematics of the instrument will be crucial. In all the panels, thin lines indicate the values of $\langle\sigma_{\rm ann}v\rangle$ corresponding to $\mathcal{S}/\mathcal{B} \approx 1\%$. As mentioned above, $\mathcal{S}/\mathcal{B} \approx 1\%$ is indeed a good measure of the level at which discrepancies in the energy reconstruction of the instrument must be understood. It is worth saying that our derived limits correspond to $\mathcal{S}/\mathcal{B}$ values of a few percent (except for IACT3), which should be in reach of current instruments.

Finally, we display by dotted lines in the right panel of Fig. 7.9 the projected sensitivity of a 5σ signal for the IACT2 scenario. We notice that prospects for detection require a more detailed analysis of e.g. systematics, trial factors and secondary γ-ray contributions which is beyond the scope of the present work.

Recently, a search for DM line-like signal has been performed with the HESS telescope for a 112-hour data set of observations of the central galactic halo, a 1° circular region around the GC with masked latitudes $|b| \leq 0.3°$ (Abramowski et al., 2013). With a binned maximum likelihood analysis, 95% C.L. upper limits on the DM flux expected from a monochromatic line as well as from spectral features due to electromagnetic corrections (adopting the same benchmark model BM4 as in this work) have been set. The CRs induced background is modeled in a more sophisticated way than what has been presented here so that the parameters of the fit are more than three. The ensuing constraints on DM annihilation cross section are well comparable with our limits for line signal (Einasto profile). Indeed, a value of $\langle \sigma_{\mathrm{ann}} v \rangle_{\chi\chi \to \gamma\gamma} \sim 2.5 \cdot 10^{-27} (3 \cdot 10^{-27})$ cm^3 s^{-1} for a DM candidate of 1 (10) TeV is reported. Those numbers are of the same order of our rescaled limits in the first panel of Fig. 7.9, while the case of electromagnetic internal bremsstrahlung leads to limits stronger by about a factor of two with respect to the present analysis (right panel, BM4 model).

Our results show that the traditional method applied for γ-ray line searches can successfully be extended to look for pronounced spectral feature at the endpoint of the spectrum and that including such a spectral information improves limits on DM annihilation cross section even more significantly than lines.

This method turns out to be almost background free (because of the validity of the local power-law background approximation) and it can be applied to different targets and instruments although we have presented here constraints for IACT observations of the GC region. Indeed, the same method (properly improved and optimized) has been successful in revealing a potential γ-ray DM signal from 43-month *Fermi*-LAT data of the GC region (see chapter 3). This excess can be interpret as due to a DM component from a VIB-like signal (3.1σ after trial factor correction) (Bringmann et al., 2012) or a line-like signal (3.3σ after trial factor correction) (Weniger, 2012) and a discrimination between the two type of features is not possible because of the limitation of the energy resolution.

Spectral features are complementary to the most often adopted rather model-independent spectrum for secondary DM γ-rays, that are usually more powerful in setting constraints on the total annihilation rate $\langle \sigma_{\mathrm{ann}} v \rangle$ with respect to line-like signal. Moreover, in the cases of a detection, such spectral signatures could provide a rather unambiguous evidence for the DM nature of the signal.

We finally notice that the secondary γ-ray component could significantly alter the upper limits on $\langle\sigma_{\rm ann}v\rangle$. Indeed, limits on γ-ray lines as shown in Fig. 7.9 are derived neglecting any secondary γ-ray component from DM annihilation. This approximation is no longer correct for very small branching ratio into lines since part of the secondary component will leak into the sliding energy window. This makes a naive application of standard line-search results on DM models with generic $\mathcal{O}(\alpha_{\rm em}^2)$ branching ratios into γ-ray lines controversial.

Chapter 8

Conclusions and Outlook

Indirect searches for WIMP DM, looking for the products of DM annihilation in the galactic halo or at cosmological distances, severely constrain the DM parameter space, namely the DM annihilation rate. In this respect, current operating and future experiments like *Fermi*, AMS or CTA are expected to explore a large part of the remaining parameter space and collect enough statistics to improve our knowledge about the astrophysical backgrounds.

Searches with γ-rays have been proven to be one of the most promising channels for DM ID and we have explored such an appealing possibility throughout this thesis. Our research has touched several aspects of DM ID through γ-rays. We here summarize the main results and possible future developments.

Modeling the expected γ-ray flux from DM annihilation is crucial when trying to unveil the nature of this elusive component. Spectral and spatial signatures can indeed help in identifying a possible excess in data as due to DM. In chapter 4, we have reported the first fully general calculation of leading EW corrections to the annihilation rate of supersymmetric neutralino DM, keeping not only all relevant diagrams but also the full mass dependence of both fermions and gauge bosons. While the most striking features are expected from EM bremsstrahlung, EW corrections have been shown to remarkably alter the low-energy tail of the total photon differential yield inducing a very sizable change of both total photon flux and spectral form. The photon count can be indeed enhanced by up to two orders of magnitude, in particular for models where the total annihilation rate at tree-level is smaller than the standard value for thermally produced DM, resulting in an enhanced discovery potential of neutralino DM with current and upcoming CRs experiments. EW corrections would modify predictions of the flux not only of the final γ-rays but also of other CR species. A possible development of the present work is therefore the detailed discussion of this "multi-messenger" signal and of the perspectives for the current and next generation of CRs experiments.

Distinctive spatial features from DM annihilating in the galaxy are expected to participate in determining the γ-ray anisotropy of the IGRB. Nevertheless, in chapter 5 we have shown that several uncertainties still limit the power of DM searches through γ-ray anisotropies. With this analysis we have demonstrated that the predicted APS is highly affected by the extrapolation to short distances of the DM profile in both the main halo and substructures. We expect such uncertainty to shrink with the next generation of high-resolution N-body simulations, which will be able to probe much smaller scales and hopefully to rule out some proposed DM profile. Moreover, we have shown that a statistical uncertainty on the single halo realization is due to the statistical fluctuations associated with the distribution of substructures with large mass ($M \gtrsim 10^8 M_\odot$). Although such uncertainty can be large at low multipoles and predictions on anisotropy based on a single halo realization could be strongly biased in this multipole range, the error is significantly reduced at high multipoles ($\ell \gtrsim 100$) which correspond to the region probed by *Fermi*-LAT and, in the future, by CTA.

This line of investigation deserves to be pursued in many directions. Firstly, a fair comparison with *Fermi*-LAT data requires to mask the region of the sky lying at low galactic latitudes. Moreover, a detailed discussion of the background and its anisotropy signal can not be neglected by a complete and exhaustive analysis. Finally, complementary constraints from the measured IGRB flux and its anisotropy can help in identifying the various contributions to this faint, almost isotropic, emission.

Concerning the origin of the IGRB, part of this thesis has been devoted to compute the contribution to the IGRB from the unresolved population of MAGN, discovered by *Fermi* as a new class of γ-ray emitters. We have predicted in chapter 6 the expected diffuse γ-ray flux of such a source class by correlating the radio and γ-ray luminosity of sources detected in both wavelengths. The robustness of the correlation has been tested by the computation of the 95% C.L. flux upper limits for a sample of radio loud AGN derived from the *Fermi*-LAT data over a four-year data taking period. The agreement between the theoretical source count distribution and the experimental one confirmed the reliability of our model. We thus have concluded that this faint but numerous population gives a sizable diffuse γ-ray flux that, when added to the contribution from the other populations, could even saturate the observed IGRB. Nonetheless, the prediction is affected by an important uncertainty which originates mostly from the correlation between the radio and γ-ray luminosity and can be reduced in the next years by an increased statistics in the number of detected sources.

Motivated by our prediction on the contribution to the IGRB of unresolved MAGN, in chapter 7, Sec. 7.1, we have derived constraints on the DM annihilation cross section and discussed in detail the uncertainty related to the modeling of the astrophysical background. Those updated upper limits on DM annihilation cross section are robust, mildly dependent on the choice of the DM density profile and conservative. As we have seen, our constraints resulted to be competitive with current limits and they can likely be improved significantly by reducing even slightly the uncertainty on the astrophysical fluxes. We therefore have emphasized the potential that the IGRB has got to be one of the most promising targets for testing the WIMP hypothesis once uncertainties on the background are even slightly reduced. In order to actually exploit the great potential of the IGRB, a reduction of the relatively large theoretical uncertainty on the diffuse γ-ray flux from unresolved MAGN, as well as from other astrophysical sources, is mandatory and is well in reach for *Fermi*-LAT and next generation of γ-ray telescopes.

Additionally, very strong constraints from the next generation of γ-ray experiments are expected when spectral features at the high-energy end of the predicted photon spectrum are looked for. In Sec. 7.2 we have indeed shown that extending and optimizing traditional methods for γ-ray line searches by including spectral features can greatly help in disentangling the DM signal from the poorly known background. Looking for spectral features represents a complementary search with respect to strategies considering the rather model-independent spectrum for secondary DM γ-rays and, in the cases of a detection, would provide a rather unambiguous evidence for the DM nature of the signal as well as allow to determine important parameters like the DM mass.

Our prospects for IACTs observations of the GC region have demonstrated that including such a spectral information has the potential to constrain the annihilation rate at least down to values typically expected for thermal production already for modest assumptions about the DM distribution and remarkable improvements are expected with optimistic choices of instrument specifications. Nonetheless, the presented method is much more general and can be applied to both other targets and other instruments.

Extending such a discussion to prospects for detection will be a natural follow-up of this work.

All the various aspects of DM ID discussed in this thesis emphasize the primary role of γ-rays as DM messengers. In the next decade, progresses in γ-ray astrophysics are expected from a new generation of experiments that will provide a better insight into the γ-ray sky. As far as DM ID is concerned, this will raise the probability of discovering a DM signal by exploiting both its spectral and angular signatures or, in a less optimistic case, it will allow to set stronger limits on the DM parameter space due also to an improved knowledge of the astrophysical background. Nonetheless, any claim of DM detection will require to be supported by correlated searches in other wavelengths and with other messengers as well as by the outcomes from other detection strategies. Even in the case in which no detection will take place and constraints will be pushed so down as to make questionable the WIMP hypothesis, only the complementarity among different messengers and techniques can achieve a comprehensive understanding of the implications for particle physics and cosmology.

Appendices

Appendix A

Four-spinors in Dirac representation

Whenever an explicit representation of the four-component spinors is required, we work in the Dirac representation. In Dirac representation gamma matrices take the form:

$$\gamma_0 = \begin{pmatrix} 1 & 0 & 0 & 0 \\ 0 & 1 & 0 & 0 \\ 0 & 0 & -1 & 0 \\ 0 & 0 & 0 & -1 \end{pmatrix} \qquad \gamma_1 = \begin{pmatrix} 0 & 0 & 0 & 1 \\ 0 & 0 & 1 & 0 \\ 0 & -1 & 0 & 0 \\ -1 & 0 & 0 & 0 \end{pmatrix}$$

$$\gamma_2 = \begin{pmatrix} 0 & 0 & 0 & -i \\ 0 & 0 & i & 0 \\ 0 & i & 0 & 0 \\ -i & 0 & 0 & 0 \end{pmatrix} \qquad \gamma_3 = \begin{pmatrix} 0 & 0 & 1 & 0 \\ 0 & 0 & 0 & -1 \\ -1 & 0 & 0 & 0 \\ 0 & 1 & 0 & 0 \end{pmatrix}$$

Four-component spinors in Dirac representation write as:

$$u_h(p) = \begin{pmatrix} \sqrt{E+m}\,\chi_h(\hat{p}) \\ h\,\sqrt{E-m}\,\chi_h(\hat{p}) \end{pmatrix} \tag{A.1}$$

$$v_h(p) = \begin{pmatrix} \sqrt{E-m}\,\chi_{-h}(\hat{p}) \\ -h\,\sqrt{E+m}\,\chi_{-h}(\hat{p}) \end{pmatrix} \tag{A.2}$$

where χ_h is the two-component spinor (i.e. Pauli's spinor) and h is the helicity. Eq. A.2 is derived by using the relation:

$$(\chi_h(\hat{p}))^C = h\,\chi_{-h}(\hat{p}) \tag{A.3}$$

For each spinor, by fixing the quantization axis S_z, we can always choose the two-component spinor with positive/negative helicity in the S_z direction:

$$\chi_+ = \begin{pmatrix} 1 \\ 0 \end{pmatrix} \qquad \chi_- = \begin{pmatrix} 0 \\ 1 \end{pmatrix} \tag{A.4}$$

Often, the Chiral/Weyl representation is used:

$$u_h^{\mathrm{Weyl}}(p) = \begin{pmatrix} \sqrt{p\cdot\sigma}\,\chi_h(\hat{p}) \\ \sqrt{p\cdot\bar{\sigma}}\,\chi_h(\hat{p}) \end{pmatrix} = \begin{pmatrix} \sqrt{E-h\,p}\,\chi_h(\hat{p}) \\ \sqrt{E+h\,p}\,\chi_h(\hat{p}) \end{pmatrix} \tag{A.5}$$

$$v_h^{\mathrm{Weyl}}(p) = \begin{pmatrix} \sqrt{p\cdot\sigma}\,(\chi_h(\hat{p}))^C \\ -\sqrt{p\cdot\bar{\sigma}}\,(\chi_h(\hat{p}))^C \end{pmatrix} = \begin{pmatrix} \sqrt{E+h\,p}\,(\chi_h(\hat{p}))^C \\ -\sqrt{E-h\,p}\,(\chi_h(\hat{p}))^C \end{pmatrix} \tag{A.6}$$

the following relations being valid:

$$\begin{aligned} p\cdot\sigma &= E-\vec{\sigma}\cdot\vec{p} && \text{(A.7)}\\ p\cdot\bar{\sigma} &= E+\vec{\sigma}\cdot\vec{p} && \text{(A.8)}\\ \vec{\sigma}\cdot\hat{p}\,\chi_h(\hat{p}) &= h\,\chi_h(\hat{p}) && \text{(A.9)}\\ \vec{\sigma}\cdot\hat{p}\,(\chi_h(\hat{p}))^C &= -h\,(\chi_h(\hat{p}))^C && \text{(A.10)}\\ & && \text{(A.11)} \end{aligned}$$

Here $\sigma \equiv (\mathbb{1}, \vec{\sigma})$ and $\bar{\sigma} \equiv (\mathbb{1}, -\vec{\sigma})$, where $\vec{\sigma}$ are the well known Pauli's sigma matrices:

$$\sigma^1 = \begin{pmatrix} 0 & 1 \\ 1 & 0 \end{pmatrix} \qquad \sigma^2 = \begin{pmatrix} 0 & -i \\ i & 0 \end{pmatrix} \qquad \sigma^3 = \begin{pmatrix} 1 & 0 \\ 0 & -1 \end{pmatrix} \tag{A.12}$$

Notice that Dirac representation is connected to the Chiral/Weyl one through a unitary matrix:

$$U = \frac{1}{\sqrt{2}} \begin{pmatrix} \mathbb{1} & -\mathbb{1} \\ \mathbb{1} & \mathbb{1} \end{pmatrix} \tag{A.13}$$

such that:

$$U\,(\psi_h(p))_{\mathrm{Dirac}} = (\psi_h(p))_{\mathrm{Weyl}}\,. \tag{A.14}$$

We quote here the explicit representation of spinors for a particle antiparticle pair, with momenta p_1 and p_2 respectively. We always work in the CMS of the two particles, where we fix the z-axis parallel to the particle's momentum $\vec{p}_1$. Therefore, in the CMS $\vec{p}_2 = -\vec{p}_1$ and we can exploit the relation (Jacob & Wick, 1959):

$$\chi_h(\hat{p}) = \chi_{-h}(-\hat{p}) \tag{A.15}$$

We report below the particle's four-component spinors:

$$u_+(p_1) = \begin{pmatrix} \sqrt{E_1+m_1} \\ 0 \\ \sqrt{E_1-m_1} \\ 0 \end{pmatrix} \qquad u_-(p_1) = \begin{pmatrix} 0 \\ \sqrt{E_1+m_1} \\ 0 \\ -\sqrt{E_1-m_1} \end{pmatrix} \tag{A.16}$$

The antiparticle's four-component spinors write as:

$$v_+(p_2) = \begin{pmatrix} \sqrt{E_2 - m_2} \\ 0 \\ -\sqrt{E_2 + m_2} \\ 0 \end{pmatrix} \qquad v_-(p_2) = \begin{pmatrix} 0 \\ \sqrt{E_2 - m_2} \\ 0 \\ \sqrt{E_2 + m_2} \end{pmatrix} \tag{A.17}$$

Considering the pair of incoming DM particles, from the expressions above is easy to get the explicit expression of four-component spinors in the non-relativistic limit. In the zero-velocity limit in the CMS of the two incoming particles ($\vec{p}_1 = -\vec{p}_2$):

$$E_1 = E_2 = m_\chi \tag{A.18}$$

$$m_1 = m_2 = m_\chi \,. \tag{A.19}$$

We will use the explicit representation of four-component spinors of the pair of incoming DM particles in the non-relativistic limit in Appendix B in order to build the spin singlet projector. In Appendix C such an explicit representation will be used in the framework of the *helicity amplitude* method.

Appendix B

Initial state projector for Majorana particles

The annihilation of two Majorana fermions at zero velocity implies that the quantum numbers of the initial state are: $J = L = S = 0$ ($P_{^1S_0}$ state).

It is possible to build explicitly the $P_{^1S_0}$ projector for Majorana particles.

By definition, in the CMS of the two incoming particles the $P_{^1S_0}$ projector is:

$$P_{^1S_0} = \frac{u_+(p_1)\,\bar{v}_+(p_2) - u_-(p_1)\,\bar{v}_-(p_2)}{\sqrt{2}} = -\frac{u_-(p_2)\,\bar{v}_-(p_1) - u_+(p_2)\,\bar{v}_+(p_1)}{\sqrt{2}}\,. \tag{B.1}$$

By using the explicit expressions of the four-component spinors, Appendix A, we derive the $P_{^1S_0}$ projector in the CMS frame:

$$(P_{^1S_0})_0 = \frac{\gamma_5\, m_\chi(\mathbb{1} - \gamma_0)}{\sqrt{2}} = \sqrt{2}m_\chi \begin{pmatrix} 0 & \mathbb{1} \\ 0 & 0 \end{pmatrix} \tag{B.2}$$

The Lorentz invariant expression of the $P_{^1S_0}$ projector in an arbitrary frame is then derived by applying a Lorentz boost to the $(P_{^1S_0})_0$. The transformation of the spinors from the CMS to an arbitrary frame being:

$$u_\pm = S(\Lambda)u^0_\pm \qquad \bar{u}_\pm = \bar{u}^0_\pm S^{-1}(\Lambda) \tag{B.3}$$

$$v_\pm = S(\Lambda)v^0_\pm \qquad \bar{v}_\pm = \bar{v}^0_\pm S^{-1}(\Lambda) \tag{B.4}$$

the projector writes as:

$$P_{^1S_0} = S(\Lambda)(P_{^1S_0})_0 S^{-1}(\Lambda) = \frac{\gamma_5\,(m_\chi - \not{p}/2)}{\sqrt{2}}\,, \tag{B.5}$$

where $p = p_1 + p_2$ and $S(\Lambda)$ is the boost transformation:

$$S(\Lambda) = \exp\left(-\frac{i}{2}\omega_{\mu\nu}S^{\mu\nu}\right), \qquad S^{\mu\nu} \equiv \frac{i}{4}[\gamma^\mu, \gamma^\nu] \tag{B.6}$$

We consider the boost transformation $\mu = 0$, $\nu = i$ with the rapidity $\omega_{0i} = -\omega_{i0} \equiv \eta_i$, such that

$$S^{0i} = \frac{i}{4}[\gamma^0, \gamma^i] = \frac{i}{2} \begin{pmatrix} 0 & \sigma^i \\ \sigma^i & 0 \end{pmatrix} \qquad \text{Dirac representation}\,. \tag{B.7}$$

Then

$$\begin{aligned} S(\Lambda) &= \exp\left(-i\,\eta_i\, S^{0i}\right) \\ &= \exp\left(\frac{\eta_i}{2} \begin{pmatrix} 0 & \sigma^i \\ \sigma^i & 0 \end{pmatrix}\right) \\ &= ... = \mathbb{1}\, \cosh\left(\frac{|\vec{\eta}|}{2}\right) + \frac{\eta_i}{|\vec{\eta}|} \begin{pmatrix} 0 & \sigma^i \\ \sigma^i & 0 \end{pmatrix} \sinh\left(\frac{|\vec{\eta}|}{2}\right)\,, \end{aligned}$$

having used the relation $\sigma_i\,\sigma_j = \delta_{ij} + i\,\epsilon^{ijk}\,\sigma_k$, and analogously

$$\begin{aligned} S^{-1}(\Lambda) &= \exp\left(-\frac{\eta_i}{2} \begin{pmatrix} 0 & \sigma^i \\ \sigma^i & 0 \end{pmatrix}\right) \\ &= \mathbb{1}\, \cosh\left(\frac{|\vec{\eta}|}{2}\right) - \frac{\eta_i}{|\vec{\eta}|} \begin{pmatrix} 0 & \sigma^i \\ \sigma^i & 0 \end{pmatrix} \sinh\left(\frac{|\vec{\eta}|}{2}\right)\,. \end{aligned}$$

Therefore

$$\begin{aligned} P_{^1S_0} &= S(\Lambda)(P_{^1S_0})_0 S^{-1}(\Lambda) \\ &= \left[\mathbb{1}\, \cosh\left(\frac{|\vec{\eta}|}{2}\right) + \frac{\eta_i}{|\vec{\eta}|} \begin{pmatrix} 0 & \sigma^i \\ \sigma^i & 0 \end{pmatrix} \sinh\left(\frac{|\vec{\eta}|}{2}\right)\right] \\ &\quad (P_{^1S_0})_0 \left[\mathbb{1}\, \cosh\left(\frac{|\vec{\eta}|}{2}\right) - \frac{\eta_i}{|\vec{\eta}|} \begin{pmatrix} 0 & \sigma^i \\ \sigma^i & 0 \end{pmatrix} \sinh\left(\frac{|\vec{\eta}|}{2}\right)\right] \\ &= \sqrt{2}\, m_\chi \gamma^5 \left[\gamma^i\, \frac{\eta_i}{|\vec{\eta}|} \cosh\left(\frac{|\vec{\eta}|}{2}\right) \sinh\left(\frac{|\vec{\eta}|}{2}\right) + \frac{1}{2} - \gamma^0 \left(\frac{1}{2} + \sinh^2\left(\frac{|\vec{\eta}|}{2}\right)\right)\right] \\ &= \frac{m_\chi}{\sqrt{2}}\gamma^5 \left[\gamma^i\, \frac{\eta_i}{|\vec{\eta}|} \sinh\left(|\vec{\eta}|\right) + \mathbb{1} - \gamma^0 \cosh\left(|\vec{\eta}|\right)\right]\,. \end{aligned}$$

By having used the relations: $\cosh(\frac{x}{2})\,\sinh(\frac{x}{2}) = \frac{1}{2}\,\sinh(x)$, $\frac{1}{2} + \sinh(\frac{x}{2}) = \frac{1}{2}\,\cosh(x)$. Finally, exploiting $\sinh\left(|\vec{\eta}|\right) \equiv \beta = \frac{p}{E}$ and $\cosh\left(|\vec{\eta}|\right) \equiv \gamma \equiv$

$(\sqrt{1-\beta^2})^{-1} = \frac{E}{2\,m_\chi}$:

$$
\begin{aligned}
P_{{}^1S_0} &= \frac{m_\chi}{\sqrt{2}}\gamma^5 \left[\gamma^i \,\frac{p^i}{2\,m_\chi} + \mathbb{1} - \gamma^0 \,\frac{E}{2\,m_\chi}\right] \\
&= \frac{m_\chi}{\sqrt{2}}\gamma^5 \left[\mathbb{1} - \gamma^\mu \,\frac{p_\mu}{2\,m_\chi}\right] \\
&= \frac{1}{\sqrt{2}}\gamma^5 \left(m_\chi - \frac{\not{p}}{2}\right) .
\end{aligned}
$$

In Appendix C we will see that the fundamental requirement of the method we use for the calculations, i.e. the *helicity amplitude* method, is that fermion chains should contain only either initial or final state particles.

As discussed in chapter 4, in the case of s-channel, the amplitude is already in the desired form, whereas for t- and u-channel Fierz transformations would be required in order to separate initial and final states into different fermion chains.

The use of the Fierz transformations is circumvented by applying the initial state projector $P_{{}^1S_0}$. In practice, the projector replaces the Majorana spinors $\bar{v}(p_2)$ and $u(p_1)$ in the amplitude. The following practical replacements are possible (we here explicit spinor indices):

$$
\bar{v}_r(p_2)\,(\Gamma_{\text{initial}})_{rs}\,u_s(p_1) = (\Gamma_{\text{initial}})_{rs}\,(P_{{}^1S_0})_{sr} = \mathrm{Tr}\left(\Gamma_{\text{initial}}\,P_{{}^1S_0}\right) \,, \qquad \text{(B.8)}
$$

in the s-channel case, and:

$$
\begin{aligned}
u_r(p_1)\,\bar{v}_s(p_2) &= (P_{{}^1S_0})_{rs} && \text{(B.9)} \\
u_r(p_2)\,\bar{v}_s(p_1) &= -(P_{{}^1S_0})_{rs} \,, && \text{(B.10)}
\end{aligned}
$$

in the case of t- and u topology respectively[i].

We notice that the potential ambiguity in the sign of the projector for the s-channel is solved by preserving the correct relative sign among topologies (which is defined once for all before applying the projector) even once the projector has been applied.

---

[i] We remind that the general structure of a t-channel diagram is: $\bar{u}_i(k_1)\Gamma_{ij}u_j(p_1)\bar{v}_m(p_2)\tilde{\Gamma}_{mn}v_n(k_2)$.

Appendix C

The helicity amplitude method

C.1 From Dirac bilinears to helicity vectors

We dedicate the present Appendix to the *helicity amplitude* method introduced in 4.2.2. Namely we explain how to transform standard amplitudes, expressed in terms of fundamental Dirac bilinears, into helicity amplitudes, expressed in terms of helicity vectors linear combinations.

In general, the amplitude for the the process $\chi(p_1)\chi(p_2) \to f_1(k_1)\bar{f}_2(k_2)V(k_3)$ contains, besides the polarization vector $\epsilon^*_\mu(\lambda)$, fermion chains in the form $\bar{\psi}\Gamma\psi$, where ψ can be either the u or v spinor – as introduced in Appendix A – according to the different topologies (s, t and u), and Γ is a combination of γ-matrices.

Γ can be decomposed in terms of the basis of sixteen 4×4 matrices that have definite transformation properties under the Lorentz group. One possible choice is represented by the following antisymmetric combinations of γ-matrices: $\tilde{\Gamma} = \{1, \gamma^\mu, \gamma^{\mu\nu} \equiv \gamma^{[\mu}\gamma^{\nu]}, \gamma^{\mu\nu\rho} \equiv \gamma^{[\mu}\gamma^\nu\gamma^{\rho]}, \gamma^{\mu\nu\rho\sigma} \equiv \gamma^{[\mu}\gamma^\nu\gamma^\rho\gamma^{\sigma]}\}$. They can be re-written as: $\tilde{\Gamma} = \{1, \gamma^\mu, \sigma^{\mu\nu} \equiv \frac{i}{2}[\gamma^\mu, \gamma^\nu], \gamma^\mu\gamma^5, \gamma^5\}$, which transform respectively as a scalar, vector, tensor, pseudo-vector and pseudo-scalar under Lorentz transformations. Notice the term *pseudo* refer to the fact that the corresponding quantities transform with an additional sign change under parity transformations.

The *helicity amplitude* method relies on the possibility to manipulate fermion chains in which only either initial or final particles appear, e.g. fermion chains in the form $\bar{v}(p_2)\,\Gamma\,u(p_1)$ for the initial state and $\bar{u}(k_1)\,\Gamma\,v(k_2)$ for the final state (according to the momenta assignation specified in Fig. 4.2).

In the case of s-channel, the amplitude is already in the form $\bar{v}(p_2)\,(\Gamma_{\text{initial}})\,u(p_1)\bar{u}(k_1)\,(\Gamma_{\text{final}})\,v(k_2)$, whereas for t- and u-channel Fierz transformations would be required in order to separate initial/final states. However, as we have seen in Appendix B, the initial state projector can effectively replace the initial Majorana spinors for all the three topologies and thus Fierz transformations are not required.

For each two-particle system (initial/final fermions), we always work in the system in which the sum of the momenta of the two particles is zero. In our case, the initial particles' system coincides with the CMS ($\vec{p}_1 = -\vec{p}_2$), while for the final state fermion-antifermion pair (where the outgoing particle, f, has momentum k_1 and mass m_1, whereas the outgoing antiparticle $\bar{f}$ has momentum k_2 and mass m_2) we work in the back-to-back system defined by the condition $\vec{k}_1 = -\vec{k}_2 \equiv \vec{k}$. In these two systems, the explicit Dirac representation of four-components spinors derived in Appendix A applies.

According to such an explicit representation, for each two-particle system we can define four states of definite helicity.

We quote below the definition of helicity states in terms of the four-component spinors with definite helicity both for initial and final fermion chains, although in the computation we deal explicitly only with final fermion chains because the initial chain is removed by applying the projector (Appendix B).

$$(\bar{v}(p_2)\,\Gamma\,u(p_1))_{(0,0)} = \frac{(\bar{v}_+(p_2)\,\Gamma\,u_+(p_1) - \bar{v}_-(p_2)\,\Gamma\,u_-(p_1))}{\sqrt{2}} \tag{C.1}$$

$$(\bar{v}(p_2)\,\Gamma\,u(p_1))_{(1,-1)} = \bar{v}_+(p_2)\,\Gamma\,u_-(p_1) \tag{C.2}$$

$$(\bar{v}(p_2)\,\Gamma\,u(p_1))_{(1,0)} = \frac{(\bar{v}_+(p_2)\,\Gamma\,u_+(p_1) + \bar{v}_-(p_2)\,\Gamma\,u_-(p_1))}{\sqrt{2}} \tag{C.3}$$

$$(\bar{v}(p_2)\,\Gamma\,u(p_1))_{(1,1)} = \bar{v}_-(p_2)\,\Gamma\,u_+(p_1) \tag{C.4}$$

$$\tag{C.5}$$

and

$$(\bar{u}(k_1)\,\Gamma\,v(k_2))_{(0,0)} = \frac{(\bar{u}_+(k_1)\,\Gamma\,v_+(k_2) - \bar{u}_-(k_1)\,\Gamma\,v_-(k_2))}{\sqrt{2}} \tag{C.6}$$

$$(\bar{u}(k_1)\,\Gamma\,v(k_2))_{(1,-1)} = \bar{u}_-(k_1)\,\Gamma\,v_+(k_2) \tag{C.7}$$

$$(\bar{u}(k_1)\,\Gamma\,v(k_2))_{(1,0)} = \frac{(\bar{u}_+(k_1)\,\Gamma\,v_+(k_2) + \bar{u}_-(k_1)\,\Gamma\,v_-(k_2))}{\sqrt{2}} \tag{C.8}$$

$$(\bar{u}(k_1)\,\Gamma\,v(k_2))_{(1,1)} = \bar{u}_+(k_1)\,\Gamma\,v_-(k_2) \tag{C.9}$$

where $\Gamma \equiv \Gamma^{\mu\ldots\nu}$. The label (s,η) refers to the helicity configuration of the two-particle system with respect to the fixed quantization axis: $(0,0)$ is the singlet spin configuration, whereas the three configurations for the triplet $S = 1$ are $(1,0),(1,-1)$ and $(1,1)$. The subscript $\pm$ corresponds to the helicity h of the Pauli's spinors as introduced in Appendix A.

The helicity states are defined in analogy to the spin states of a two $1/2$ spin particles system, for which the states with $S_z = 0$ are defined only to within a global phase factor.

The decomposition of Dirac bilinears (with definite helicity) in terms of helicity vectors results in a standard basis transformations from the $\mathcal{R}^4$ canonical basis to the helicity basis. We report here the fundamentals of basis transformations that the reader can find in any text book of linear algebra.

We are interested in the components of the Dirac field bilinears, $\bar{\psi}\Gamma\psi$, with respect to the helicity basis, an orthonormal basis of $\mathcal{R}^4$ constructed from the $\mathcal{R}^3$ polar basis vectors properly extended to $\mathcal{R}^4$ by adding the temporal vector. We thus perform a transformation from the canonical $\mathcal{R}^4$ basis,

$$B = \{(1,0,0,0),(0,1,0,0),(0,0,1,0),(0,0,0,1)\} = \{e_i\} \tag{C.10}$$

to the helicity basis,

$$\begin{aligned} B' &= \{(1,0,0,0), \frac{1}{\sqrt{2}}(0,-1,-i,0), \frac{1}{\sqrt{2}}(0,1,-i,0),(0,0,0,1)\} \\ &= \{e_u, e_+, e_-, e_0\} = \{e'_i\}\,. \end{aligned} \tag{C.11}$$

The unitary matrix, A,

$$A_{ij} = e'_i \cdot e_j \tag{C.12}$$

defines the transformation of the vector basis in the matrix representation as:

$$\mathbf{e}' = \mathbf{A}\mathbf{e} \tag{C.13}$$

$$\mathbf{e} = \mathbf{A^{-1}}\mathbf{e}' \tag{C.14}$$

For the sake of completeness the matrix representation of A is:

$$\begin{pmatrix} 1 & 0 & 0 & 0 \\ 0 & -\frac{1}{\sqrt{2}} & -\frac{i}{\sqrt{2}} & 0 \\ 0 & \frac{1}{\sqrt{2}} & -\frac{i}{\sqrt{2}} & 0 \\ 0 & 0 & 0 & 1 \end{pmatrix}$$

Vector and tensor components transform as follows. Given the vector

$$v = c_i e_i = c'_j e'_j \tag{C.15}$$

its components transform as:

$$c_i = c'_j A_{ji} \ ; \ c'_j = c_i A^{-1}_{ij} \tag{C.16}$$

i. e. in matrix representation:

$$\mathbf{C} = \mathbf{A^T}\mathbf{C}' \ ; \ \mathbf{C}' = (\mathbf{A^T})^{-1}\mathbf{C} \tag{C.17}$$

Analogously, for the tensor

$$T = c_{ij} e_i \otimes e_j = c'_{mn} e'_m \otimes e'_n \tag{C.18}$$

it follows

$$\begin{aligned}
c_{ij}(e_i \otimes e_j) \cdot e'_l &= c'_{mn}(e'_m \otimes e'_n) \cdot e'_l && \text{(C.19)}\\
c_{ij} e_i (e_j \cdot e'_l) &= c'_{mn} e'_m (e'_n \cdot e'_l) && \text{(C.20)}\\
c_{ij} e_i A^{-1}_{jl} &= c'_{mn} e'_m \delta_{nl} && \text{(C.21)}\\
c_{ij}(e_i \cdot e'_p) A^{-1}_{jl} &= c'_{mn}(e'_m \cdot e'_p) \delta_{nl} && \text{(C.22)}\\
c_{ij} A^{-1}_{ip} A^{-1}_{jl} &= c'_{mn} \delta_{ip} \delta_{nl} && \text{(C.23)}\\
(A^{-1})^T_{pi} c_{ij} A^{-1}_{jl} &= c'_{il} \, . && \text{(C.24)}
\end{aligned}$$

Thus, in matrix representation:

$$\mathbf{C}' = (\mathbf{A}^{-1})^{\mathbf{T}} \mathbf{C} \mathbf{A}^{-1} \ ; \ \mathbf{C} = \mathbf{A}^{\mathbf{T}} \mathbf{C}' \mathbf{A} \tag{C.25}$$

By means of the above reported basis transformations, we reduce each Dirac fermion bilinear to a linear combination of helicity basis vectors. The result of the basis transformation is quoted in table C.1 and C.2 for the case of initial and final fermion chain respectively. The differences arises from the different combination of u and v spinors, i.e. $\bar{v}(p_2)\,\Gamma\, u(p_1)$ for the initial state and $\bar{u}(p_1)\,\Gamma\, v(p_2)$ for the final state; since the explicit representation of four-component spinors is different for $\bar{\psi}$ and ψ spinor, the two states already has already different linear coefficients with respect to the canonical basis vectors.

The kinematical quantities involved are:

$$\begin{aligned}
E_{+} &= \frac{1}{2}(\sqrt{E_1+m_1}\sqrt{E_2+m_2}+\sqrt{E_1-m_1}\sqrt{E_2-m_2}) \\
&\equiv \sqrt{\frac{E_1\,E_2+m_1\,m_2+|\tilde{k}|^2}{2}} \qquad \text{(C.26)} \\
E_{-} &= \frac{1}{2}(\sqrt{E_1+m_1}\sqrt{E_2+m_2}-\sqrt{E_1-m_1}\sqrt{E_2-m_2}) \\
&\equiv \sqrt{\frac{E_1\,E_2+m_1\,m_2-|\tilde{k}|^2}{2}} \qquad \text{(C.27)} \\
p_{+} &= \frac{1}{2}(\sqrt{E_1+m_1}\sqrt{E_2-m_2}+\sqrt{E_1-m_1}\sqrt{E_2+m_2}) \\
&\equiv \sqrt{\frac{E_1\,E_2-m_1\,m_2+|\tilde{k}|^2}{2}} \qquad \text{(C.28)} \\
p_{-} &= \frac{1}{2}(\sqrt{E_1+m_1}\sqrt{E_2-m_2}-\sqrt{E_1-m_1}\sqrt{E_2+m_2}) \\
&\equiv \mathrm{sign}(E_2\,m_1-E_1\,m_2)\sqrt{\frac{E_1\,E_2-m_1\,m_2-|\tilde{k}|^2}{2}}\,, \qquad \text{(C.29)}
\end{aligned}$$

where $\tilde{k}$ stays for either p or k. The columns of table C.1 and C.2 refer to the definite helicity configurations of the fermion chain.

We have tested the correctness of such decompositions by considering simple matrix element of the form $\bar{\psi}\Gamma\psi$, computing the squared amplitude with the helicity amplitudes method, and comparing with the results from the standard method.

Table C.1: Dirac field bilinear decomposition for initial fermion chain: the columns refer to the definite helicity states as defined in Eqs. C.1 - C.4

Dirac Field Bilinear	$\delta^{s,\eta}_{0,0}$	$\delta^{s,\eta}_{1,-1}$	$\delta^{s,\eta}_{1,0}$	$\delta^{s,\eta}_{1,1}$
$\bar{v}(p_2)u(p_1)$	0	0	$2\sqrt{2}\,p_+$	0
$\bar{v}(p_2)\gamma^\mu u(p_1)$	0	$-2\sqrt{2}\,E_+\,e^\mu_-$	$\sqrt{2}\,(2\,p_-\,e^\mu_u - 2\,E_-\,e^\mu_0)$	$-2\sqrt{2}\,E_+\,e^\mu_+$
$\bar{v}(p_2)\sigma^{\mu\nu}u(p_1)$	$2i\sqrt{2}p_+(e^\mu_-e^\nu_+ - e^\mu_+e^\nu_-)$	$2i\sqrt{2}(p_-(e^\mu_-e^\nu_0 - e^\mu_0e^\nu_-) + E_-(e^\mu_ue^\nu_- - e^\mu_-e^\nu_u))$	$2i\sqrt{2}E_+(e^\mu_ue^\nu_0 - e^\mu_0e^\nu_u)$	$2i\sqrt{2}(p_-(e^\mu_+e^\nu_0 - e^\mu_0e^\nu_+) + E_-(e^\mu_ue^\nu_+ - e^\mu_+e^\nu_u))$
$\bar{v}(p_2)\gamma^\mu\gamma^5u(p_1)$	$\sqrt{2}\,(2\,p_-\,e^\mu_0 - 2\,E_-\,e^\mu_u)$	$2\sqrt{2}\,p_+\,e^\mu_-$	0	$-2\sqrt{2}\,p_+\,e^\mu_+$
$\bar{v}(p_2)\gamma^5u(p_1)$	$2\sqrt{2}\,E_+$	0	0	0

Table C.2: Dirac field bilinear decomposition for final fermion chain: the columns refer to the definite helicity states as defined in Eqs. C.6 - C.9

Dirac Field Bilinear	$\delta^{s,\eta}_{0,0}$	$\delta^{s,\eta}_{1,-1}$	$\delta^{s,\eta}_{1,0}$	$\delta^{s,\eta}_{1,1}$
$\bar{u}(k_1)v(k_2)$	0	0	$2\sqrt{2}\,p_+$	0
$\bar{u}(k_1)\gamma^\mu v(k_2)$	0	$2\sqrt{2}\,E_+\,e^\mu_+$	$\sqrt{2}\,(2\,p_-\,e^\mu_u - 2\,E_-\,e^\mu_0)$	$2\sqrt{2}\,E_+\,e^\mu_-$
$u(\bar{k}_1)\sigma^{\mu\nu}v(k_2)$	$2i\sqrt{2}p_+(e^\mu_-e^\nu_+ - e^\mu_+e^\nu_-)$	$2i\sqrt{2}(p_-(e^\mu_+e^\nu_0 - e^\mu_0e^\nu_+) + E_-(e^\mu_ue^\nu_+ - e^\mu_+e^\nu_u))$	$2i\sqrt{2}E_+(e^\mu_0e^\nu_u - e^\mu_ue^\nu_0)$	$2i\sqrt{2}(p_-(e^\mu_-e^\nu_0 - e^\mu_0e^\nu_-) + E_-(e^\mu_ue^\nu_- - e^\mu_-e^\nu_u))$
$\bar{u}(k_1)\gamma^\mu\gamma^5v(k_2)$	$\sqrt{2}\,(2\,p_-\,e^\mu_0 - 2\,E_-\,e^\mu_u)$	$-2\sqrt{2}\,p_+\,e^\mu_+$	0	$2\sqrt{2}\,p_+\,e^\mu_-$
$\bar{u}(k_1)\gamma^5v(k_2)$	$-2\sqrt{2}\,E_+$	0	0	0

Appendix D

Kinematics of three-body final state

We present here the kinematical relations we adopt for all the computations.

The general relations hold:

$$p^\mu = p_1^\mu + p_2^\mu = k_1^\mu + k_2^\mu + k_3^\mu \tag{D.1}$$

$$p^2 = 4\,m_\chi^2\,, \tag{D.2}$$

since the initial state of DM particle is annihilating at rest: $|p_1| = |p_2| = m_\chi$. We define the CMS energies as:

$$E_1 \equiv m_\chi x_1 \tag{D.3}$$

$$E_2 \equiv m_\chi x_2 \tag{D.4}$$

$$E_3 \equiv m_\chi x_3 \tag{D.5}$$

Thus:

$$x_1 + x_2 + x_3 = 2\,. \tag{D.6}$$

In the BB system of the final fermion-antifermion pair, we define energies as:

$$\tilde{E}_1 \equiv m_\chi \omega_1 \tag{D.7}$$

$$\tilde{E}_2 \equiv m_\chi \omega_2 \tag{D.8}$$

$$\tilde{E}_3 \equiv m_\chi \omega_3 \tag{D.9}$$

where $i = 1, 2, 3$ labels the final state particle: $i = 1$ indicates the fermion; $i = 2$ indicates the antifermion; $i = 3$ indicates the gauge boson. Momenta are defined as:

$$q_i \equiv \sqrt{\omega_i - \mu_i^2}\,, \tag{D.10}$$

where

$$\mu_i^2 \equiv \frac{m_i^2}{m_\chi^2}\,. \tag{D.11}$$

The momenta contractions are the following:

$$\begin{aligned}
k_i^2 &= m_i^2 \equiv m_\chi^2\,\mu_i^2 && \text{(D.12)}\\
k_1\cdot k_2 &= m_\chi^2\left[2\,(x_1+x_2-1)+\frac{\mu_3^2-\mu_1^2-\mu_2^2}{2}\right] && \\
&\equiv \omega_1\omega_2+\omega_1^2-m1^2 && \text{(D.13)}\\
k_1\cdot k_3 &= m_\chi^2\left[2\,(1-x_2)+\frac{\mu_2^2-\mu_1^2-\mu_3^2}{2}\right] && \\
&\equiv \omega_1\,\omega_3-\cos\theta\,q_3\,q_1 && \text{(D.14)}\\
k_2\cdot k_3 &= m_\chi^2\left[2\,(1-x_1)+\frac{\mu_1^2-\mu_2^2-\mu_3^2}{2}\right] && \\
&\equiv \omega_2\omega_3+\cos\theta\,q_3\,q_1 && \text{(D.15)}
\end{aligned}$$

In the BB system by definition $\vec{q}_1=-\vec{q}_2$ and $q_1=q_2$. After some algebra, we can list the following relations holding among the kinematical quantities in the BB and the CMS:

$$(\omega_1+\omega_2)^2 = 4\,(x_1+x_2-1)+\mu_3^2 \tag{D.16}$$

$$\begin{aligned}
\omega_1 &= \frac{x_1+x_2-1+\frac{\mu_3^2-\mu_2^2+\mu_1^2}{4}}{\sqrt{x_1+x_2-1+\frac{\mu_3^2}{4}}} && \text{(D.17)}\\
\omega_2 &= \frac{x_1+x_2-1+\frac{\mu_3^2-\mu_1^2+\mu_2^2}{4}}{\sqrt{x_1+x_2-1+\frac{\mu_3^2}{4}}} && \text{(D.18)}\\
\omega_3 &= \frac{2-x_1-x_2+\frac{\mu_3^2}{4}}{\sqrt{x_1+x_2-1+\frac{\mu_3^2}{4}}} && \text{(D.19)}
\end{aligned}$$

Moreover, we can work out the expression for the cosine of the angle θ between the momenta k_1 and k_3:

$$\cos\theta = \frac{-2\,(1-x_2)+\frac{\mu_1^2+\mu_3^2-\mu_2^2}{2}+\omega_1\,\omega_3}{q_1\,q_3} \tag{D.20}$$

The kinematical quantities E_+, E_-, p_+, p_-, Eq. C.26 - C.29, of the final fermion-antifermion pair write as:

$$E_{+} = m_\chi \left[\sqrt{x_1 + x_2 - 1 + \frac{\mu_3^2 - (\mu_1 - \mu_2)^2}{4}}\right] \tag{D.21}$$

$$E_{-} = m_\chi \left[\sqrt{\frac{(\mu_1 + \mu_2)^2}{4} - \frac{(\mu_1^2 - \mu_2^2)^2}{16\,(x_1 + x_2 - 1 + \mu_3^2/4)}}\right] \tag{D.22}$$

$$p_{+} = m_\chi \left[\sqrt{x_1 + x_2 - 1 + \frac{\mu_3^2 - (\mu_1 + \mu_2)^2}{4}}\right] \tag{D.23}$$

$$\begin{aligned} p_{-} &= m_\chi \,\mathrm{sign}(\mu_1\,\omega_2 - \mu_2\,\omega_1) \\ &\times \left[\sqrt{\frac{(\mu_1 - \mu_2)^2}{4} - \frac{(\mu_1^2 - \mu_2^2)^2}{16\,(x_1 + x_2 - 1 + \mu_3^2/4)}}\right] \end{aligned} \tag{D.24}$$

We have seen that working into BB system allows to use the helicity amplitude method as described in Appendix C. The transformation from the CMS to the BB is thus required by the method. Moreover, working with dimensionless quantities simplifies the calculations and results to be more useful than keeping the fully dimensional kinematical quantities.

Concerning the number of kinematical invariants involved in the process, since the DM pair annihilating acts as a pseudo scalar particle decaying at rest (with energy in the CMS equal to twice m_χ) the annihilation into three-body final state is kinematically equivalent to the decay process into a three-body final state of a particle at rest with CMS energy $2m_\chi$. This decay depends on two independent variables. Indeed, the nine components of the final three-vectors are constrained by four energy-momentum conservation equations so that 5 kinematical invariants are left; they can be chosen as two final state momenta e.g. k_1 and k_3 and three angles describing the orientation of the final state with respect to the initial state plane.

Furthermore, because of the annihilation at rest, the final state is independent on the three Euler angles describing its orientation as a whole since the initial state is isotropic in the rest frame of p so that there are only two remaining kinematic invariants.

We choose these two independent kinematical quantities to be the CMS energies of the fermion x_1 and the vector x_3 since the differential cross section in terms of those two energies is directly related to the spectra of final state particles and thus it has a directly physical meaning.

D.1 Vector-contractions

We quote here the definition of kinematical vectors involved in the calculations together with the contractions we apply. The conventions for the kinematics are depicted by Fig. 4.2. In the particular frame we work in, fermion and antifermion are emitted back-to-back and the components of the vectors used for the calculations are the following:

$$\begin{aligned}
k_1 &= \{\omega_1, 0, 0, q_1\} && \text{(D.25)}\\
k_2 &= \{\omega_2, 0, 0, -q_1\} && \text{(D.26)}\\
k_3 &= \{\omega_3, 0, \sin\theta\, q_3, \cos\theta\, q_3\} && \text{(D.27)}\\
\epsilon_0^* &= \frac{1}{\mu_3}\{q_3, 0, \omega_3\,\sin\theta, \omega_3\cos\theta\} && \text{(D.28)}\\
\epsilon_+^* &= \frac{1}{\sqrt{2}}\{0, -1, i\,\cos\theta, -i\,\sin\theta\} && \text{(D.29)}\\
\epsilon_-^* &= \frac{1}{\sqrt{2}}\{0, 1, i\,\cos\theta, -i\,\sin\theta\} && \text{(D.30)}\\
e_u &= \{1, 0, 0, 0\} && \text{(D.31)}\\
e_0 &= \{0, 0, 0, 1\} && \text{(D.32)}\\
e_+ &= \frac{1}{\sqrt{2}}\{0, -1, -i, 0\} && \text{(D.33)}\\
e_- &= \frac{1}{\sqrt{2}}\{0, 1, -i, 0\} && \text{(D.34)}
\end{aligned}$$

We make notice the polarization vectors of the emitted gauge boson appear always as complex conjugated quantities. The kinematical relations of the momenta with the helicity basis vectors which enter in the computation of the amplitudes are:

$$\begin{aligned}
e_u\cdot k_1 &= \omega_1\,, \qquad e_u\cdot k_2 = \omega_2\,, \qquad e_u\cdot k_3 = \omega_3 && \text{(D.35)}\\
e_0\cdot k_1 &= -q_1\,, \qquad e_0\cdot k_2 = q_1\,, \qquad e_0\cdot k_3 = -\cos\theta\, q_3 && \text{(D.36)}\\
e_+\cdot k_1 &= e_-\cdot k_1 = e_+\cdot k_2 = e_-\cdot k_2 = 0 && \text{(D.37)}\\
e_+\cdot k_3 &= e_-\cdot k_3 = \frac{i}{\sqrt{2}}\sin\theta\, q_3 && \text{(D.38)}
\end{aligned}$$

Analogously, the kinematical contractions involving polarization vectors turn out to be:

$$k_1 \cdot \epsilon_0^* = \frac{\omega_1\, q_3 - \omega_3\, q_1\, \cos\theta}{\mu_3} \tag{D.39}$$

$$k_2 \cdot \epsilon_0^* = \frac{\omega_2\, q_3 - \omega_3\, q_1\, \cos\theta}{\mu_3} \tag{D.40}$$

$$k_1 \cdot \epsilon_+^* = k_1 \cdot \epsilon_-^* = \frac{i}{\sqrt{2}} \sin\theta\, q_1 \tag{D.41}$$

$$k_2 \cdot \epsilon_+^* = k_2 \cdot \epsilon_-^* = -\frac{i}{\sqrt{2}} \sin\theta\, q_1 \tag{D.42}$$

$$k_3 \cdot \epsilon_0^* = k_3 \cdot \epsilon_+^* = k_3 \cdot \epsilon_-^* = 0 \tag{D.43}$$

$$e_u \cdot \epsilon_0^* = \frac{q_3}{\mu_3}, \qquad e_u \cdot \epsilon_+^* = e_u \cdot \epsilon_-^* = 0 \tag{D.44}$$

$$e_0 \cdot \epsilon_0^* = -\frac{\omega_3\, \cos\theta}{\mu_3}, \qquad e_0 \cdot \epsilon_+^* = e_0 \cdot \epsilon_-^* = \frac{i}{\sqrt{2}} \sin\theta \tag{D.45}$$

$$e_+ \cdot \epsilon_0^* = e_- \cdot \epsilon_0^* = \frac{i}{\sqrt{2}} \frac{\sin\theta\, \omega_3}{\mu_3} \tag{D.46}$$

$$e_+ \cdot \epsilon_-^* = e_- \cdot \epsilon_+^* = \frac{1 - \cos\theta}{2} \tag{D.47}$$

$$e_+ \cdot \epsilon_+^* = e_- \cdot \epsilon_-^* = \frac{-1 - \cos\theta}{2} \tag{D.48}$$

D.2 Kinematical boundaries

In general, invariant kinematic variables are conveniently defined as (Byckling & Kajantie, 1973):

$$s_{12} \equiv s_1 = (k_1 + k_2)^2 = (p - k_3)^2\,, \tag{D.49}$$

$$s_{23} \equiv s_2 = (k_2 + k_3)^2 = (p - k_1)^2\,, \tag{D.50}$$

$$s_{31} \equiv s_3 = (k_3 + k_1)^2 = (p - k_2)^2\,, \tag{D.51}$$

which satisfy the relation

$$s_1 + s_2 + s_3 = s + m_1^2 + m_2^2 + m_3^2\,. \tag{D.52}$$

The physically allowed region in the $s_i - s_j$ plane is called the *Dalitz plot.* Namely the plot in the $s_1 - s_2$ plane is defined by the boundaries:

$$s_2^{\max} = (\sqrt{s} - m_1)^2 \tag{D.53}$$

$$s_2^{\min} = (m_2 + m_3)^2 \tag{D.54}$$

$$\begin{aligned} s_1^{\max/\min}(s_2) &= m_1^2 + m_2^2 - \frac{1}{2\, s_2}\{(s_2 - s + m_1^2)(s_2 + m_2^2 - m_3^2) \\ &\mp \lambda^{\frac{1}{2}}(s_2, s, m_1^2)\lambda^{\frac{1}{2}}(s_2, m_2^2, m_3^2)\} \end{aligned} \tag{D.55}$$

where

$$\lambda(x,y,z) = (x-y-z)^2 - 4\,x\,y\,. \tag{D.56}$$

The equation giving s_2 boundaries in terms of s_1 is obtained by applying the transformations $m_1 \leftrightarrow m_3$ and $s_2 \leftrightarrow s_1$, and s_1 boundaries:

$$s_1^{\max} = (\sqrt{s} - m_3)^2 \tag{D.57}$$

$$s_1^{\min} = (m_1 + m_2)^2 \tag{D.58}$$

We express everything in terms of the two independent quantities x_1 and x_3: x_1 corresponds to the energy of the fermion divided by the mass of the neutralino and depends on s_2, while x_3 refers to the energy of the emitted vector boson divided by the mass of the neutralino and depends on s_1. The boundaries of x_1 and x_3 are:

$$x_1^{\min} = \mu_1 \tag{D.59}$$

$$x_1^{\max} = (4 + \mu_1^2 - (\mu_3 + \mu_2)^2)/4 \tag{D.60}$$

$$x_3^{\min} = \mu_3 \tag{D.61}$$

$$x_3^{\max} = (4 + \mu_3^2 - (\mu_1 + \mu_2)^2)/4 \tag{D.62}$$

By exploiting the dependence $x_1 = x_1(s_2)$ and $x_3 = x_3(s_1)$, we derive the relative kinematical boundaries:

$$
\begin{aligned}
x_1^{\min}(x_3) &= \frac{1}{2\left(-\mu_3^2+4x_3-4\right)} \\
&\cdot \sqrt{(x_3-\mu_3)(\mu_3+x_3)\left((\mu_1-\mu_2)^2-\mu_3^2+4x_3-4\right)} \\
&\cdot \sqrt{\left((\mu_1+\mu_2)^2-\mu_3^2+4x_3-4\right)} \\
&- \frac{(x_3-2)\left(-\mu_1^2+\mu_2^2-\mu_3^2+4x_3-4\right)}{2\left(-\mu_3^2+4x_3-4\right)} \qquad \text{(D.63)} \\
x_1^{\max}(x_3) &= -\frac{(x_3-2)\left(-\mu_1^2+\mu_2^2-\mu_3^2+4x_3-4\right)}{2\left(-\mu_3^2+4x_3-4\right)} \\
&+ \frac{1}{2\left(-\mu_3^2+4x_3-4\right)} \\
&\cdot \sqrt{(x_3-\mu_3)(\mu_3+x_3)\left((\mu_1-\mu_2)^2-\mu_3^2+4x_3-4\right)} \\
&\cdot \sqrt{\left((\mu_1+\mu_2)^2-\mu_3^2+4x_3-4\right)} \qquad \text{(D.64)} \\
x_3^{\min}(x_1) &= \frac{1}{24\left(-\mu_1^2+4x_1-4\right)} \\
&\cdot \sqrt{(x_1-\mu_1)(\mu_1+x_1)} \\
&\cdot \sqrt{\left(\mu_3^4+2\mu_3^2\left(-\mu_1^2-\mu_2^2+4x_1-4\right)+\left(\mu_1^2-\mu_2^2-4x_1+4\right)^2\right)} \\
&- \frac{(x_1-2)\left(-\mu_1^2+\mu_2^2-\mu_3^2+4x_1-4\right)}{24\left(-\mu_1^2+4x_1-4\right)} \qquad \text{(D.65)} \\
x_3^{\max}(x_1) &= -\frac{2\left(\mu_1^2-\mu_2^2+\mu_3^2+4\right)+4x_1^2-x_1\left(\mu_1^2-\mu_2^2+\mu_3^2+12\right)}{8x_1-2\left(\mu_1^2+4\right)} \\
&+ \frac{1}{8x_1-2\left(\mu_1^2+4\right)} \\
&\cdot \sqrt{(x_1-\mu_1)(\mu_1+x_1)} \\
&\cdot \sqrt{\left(\mu_3^4+2\mu_3^2\left(-\mu_1^2-\mu_2^2+4x_1-4\right)+\left(\mu_1^2-\mu_2^2-4x_1+4\right)^2\right)} \\
& \qquad \text{(D.66)}
\end{aligned}
$$

The kinematical bounds are used when performing the integration over the phase space.

Appendix E

Supersymmetry, a brief compendium

We have already discussed in chapter 2 the main motivations for the existence of physics beyond the SM and we have introduced SUSY as one of the most appealing solution to SM open issues. In this Appendix we overview the MSSM which constitutes the theoretical framework of calculations performed in chapter 4. In the following we adopt the notation of (Haber & Kane, 1985; Gunion & Haber, 1993) and we refer the interested reader to some good review on the MSSM e.g. (Peskin, 2008). The collection of Feynman rules used throughout the text is listed in (Edsjö, 1997). By means of generic coupling, they are suitable for numerical implementation and match DarkSUSY conventions.

The construction of an exact supersymmetric extension of the SM assigns to each SM particle a super partner such that for each fermionic degree of freedom there is a bosonic degree of freedom and vice-versa. The SM vector fields are assigned to supermultiplets and the matter fields to chiral supermultiplets. The supersymmetric partners of the SM gauge bosons are dubbed gauginos, while the scalar particles in the chiral supermultiplets are called sfermions. Concerning the Higgs sector, the SM Higgs is identified with a complex scalar component of a chiral supermultiplet. Moreover, two Higgs doublets are required in order to obtain all the couplings in the superpotential[i] and maintain the gauge invariance of the model by canceling gauge anomalies. The particle content of the MSSM is given in table E.1, which has been adapted from (Edsjö, 1997).

Although writing the full Lagrangian of the MSSM is beyond the scope of this Appendix, we here present its main features.

The kinetic terms and MSSM gauge couplings are completely determined by supersymmetry, the choice of the gauge group $SU(3) \times SU_L(2) \times U(1)$,

---

[i] It is the most generic dimension-three, gauge invariant, polynomial holomorphic function of superfields and it is e.g. the source of quarks and leptons masses.

SM particles		Supersymmetric partners			
		Interaction eigenstates		Mass eigenstates	
Symbol	Name	Symbol	Name	Symbol	Name
q	quark	$\tilde{q}_L$, $\tilde{q}_R$	squark	$\tilde{q}_1$, $\tilde{q}_2$	squark
l	lepton	$\tilde{l}_L$, $\tilde{l}_R$	slepton	$\tilde{l}_1$, $\tilde{l}_2$	slepton
ν	neutrino	$\tilde{\nu}$	sneutrino	$\tilde{\nu}$	sneutrino
g	gluon	$\tilde{g}$	gluino	$\tilde{g}$	gluino
$W^\pm$	W-boson	$\tilde{W}^\pm$	wino	$\tilde{\chi}^\pm_{1,2}$	chargino
H^-	Higgs boson	$\tilde{H}^-_1$	higgsino		
H^+	Higgs boson	$\tilde{H}^+_2$	higgsino		
B	B-field	$\tilde{B}$	bino	$\tilde{\chi}^0_{1,2,3,4}$	neutralino
W^3	W^3-field	$\tilde{W}^3$	wino		
H	Higgs boson	$\tilde{H}^0_1$	higgsino		
h	Higgs boson	$\tilde{H}^0_2$	higgsino		
A	Higgs boson				

Table E.1: MSSM particle content. Table adapted from (Edsjö, 1997).

the choice of the quantum numbers of the matter fields, and the SM gauge couplings g_1, g_2 and g_3.

As we have already seen in chapter 2, the superpotential W is responsible for generating the Higgs Yukawa couplings needed to give mass to the quarks and leptons. The superpotential writes as:

$$W = \epsilon_{ij}\left(-\hat{\mathbf{e}}^*_R\mathbf{Y}_E\hat{\mathbf{l}}^i_L\hat{H}^j_1 - \hat{\mathbf{d}}^*_R\mathbf{Y}_D\hat{\mathbf{q}}^i_L\hat{H}^j_1 + \hat{\mathbf{u}}^*_R\mathbf{Y}_U\hat{\mathbf{q}}^i_L\hat{H}^j_2 - \mu\hat{H}^i_1\hat{H}^j_2\right) \tag{E.1}$$

where i and j are $SU_L(2)$ indices, the Yukawa couplings $\mathbf{Y}$ are matrices in generation space and $\hat{\mathbf{e}}$, $\hat{\mathbf{l}}$, $\hat{\mathbf{u}}$, $\hat{\mathbf{d}}$ and $\hat{\mathbf{q}}$ are the superfields of the leptons and sleptons and of the quarks and squarks. The Yukawa couplings $\mathbf{Y}$ are general 3×3 complex-valued matrices, that can be diagonalized using two unitary transformations. One of these unitary transformations is identified with the Cabibbo-Kobayashi-Maskawa weak interaction mixing matrix. Therefore, the superpotential contains the remaining SM parameters: 9 quark and lepton masses (derived from the diagonalized Yukawa couplings) and the 4 mixing angles of the Cabibbo-Kobayashi-Maskawa weak interaction mixing matrix. The last term in the W, is related to the supersymmetric contribution to the masses of the Higgs bosons and it depends on the μ parameter. μ is a new beyond the SM parameter. An additional new parameter from the Higgs sector is the ratio of the Higgs vacuum expectation values,

$$\tan\beta = v_2/v_1\,. \tag{E.2}$$

Furthermore, the superpotential can contain terms which are consistent with the SM gauge symmetry and quantum numbers but can violate either baryon or lepton number. One way to forbid such terms is imposing a new discrete symmetry: the R-parity. By construction, SM particles have R =

+1 and superpartners R = -1. In this thesis we will assume that R-parity is conserved. We already noticed that the most important implication for cosmology of R-parity conservation is the prediction of the LSP which represents a viable DM candidate in the MSSM framework.

All the above mentioned terms exactly preserve supersymmetry. The lack of observational evidence of superparticles forces SUSY to be a broken symmetry. SUSY is broken explicitly and “softly” in order to not spoil the SUSY’s solution to the hierarchy problem, i.e. to not reintroduce dangerous UV divergencies. This is called “soft supersymmetry-breaking” (SSB). A subset of SUSY breaking terms whose couplings (with positive mass dimension) are dubbed “soft parameters”, includes all allowed terms that do not introduce quadratic divergencies in the theory. Several models of SSB can be worked out and thus the theory is defined by its SSB.

The generic soft SUSY-breaking terms in the Lagrangian takes the form:

$$\begin{aligned}
V_{\text{soft}} = \epsilon_{ij} \Big(& \tilde{\mathbf{e}}^*_R \mathbf{A}_E \mathbf{Y}_E \tilde{\mathbf{l}}^i_L H^j_1 + \tilde{\mathbf{d}}^*_R \mathbf{A}_D \mathbf{Y}_D \tilde{\mathbf{q}}^i_L H^j_1 \\
& - \tilde{\mathbf{u}}^*_R \mathbf{A}_U \mathbf{Y}_U \tilde{\mathbf{q}}^i_L H^j_2 - B\mu H^i_1 H^j_2 + \text{h.c.} \Big) \\
& + H^{i*}_1 m^2_1 H^i_1 + H^{i*}_2 m^2_2 H^i_2 \\
& + \tilde{\mathbf{q}}^{i*}_L \mathbf{M}^2_Q \tilde{\mathbf{q}}^i_L + \tilde{\mathbf{l}}^{i*}_L \mathbf{M}^2_L \tilde{\mathbf{l}}^i_L + \tilde{\mathbf{u}}^*_R \mathbf{M}^2_U \tilde{\mathbf{u}}_R + \tilde{\mathbf{d}}^*_R \mathbf{M}^2_D \tilde{\mathbf{d}}_R + \tilde{\mathbf{e}}^*_R \mathbf{M}^2_E \tilde{\mathbf{e}}_R \\
& + \frac{1}{2} M_1 \tilde{B}\tilde{B} + \frac{1}{2} M_2 \left(\tilde{W}^3 \tilde{W}^3 + 2\tilde{W}^+ \tilde{W}^- \right) + \frac{1}{2} M_3 \tilde{g}\tilde{g}
\end{aligned} \tag{E.3}$$

where the matrices $\mathbf{A}$ and $\mathbf{M}$ represent the soft trilinear couplings and sfermion masses respectively; $\tilde{\mathbf{e}}$, $\tilde{\mathbf{l}}$, $\tilde{\mathbf{u}}$, $\tilde{\mathbf{d}}$ and $\tilde{\mathbf{q}}$ correspond to scalar super partners of SM fields. The L and R subscripts on the sfermion fields refer to the chirality of the fermion they are superpartners of. Finally, $\tilde{B}$, $\tilde{W}^3$ and $\tilde{W}^{\pm}$ are the fermionic superpartners of the $U(1)$ and $SU_L(2)$ gauge fields and $\tilde{g}$ is the gluino. M_1, M_2 and M_3 are the gaugino masses, B the soft bilinear coupling and $m_{1,2}$ are Higgs mass parameters. Additional free-parameters of the theory coming from the SSB terms are thus: gaugino masses for each gauge group; squark, slepton and Higgs m^2 terms; and triple scalar couplings. Beside the 19 SM parameters, MSSM adds 105 new parameters for a total of 124 parameters. They likely are not all fundamental parameters because they are embedded in a more fundamental theory. Nevertheless, knowing the values of these parameters can allow to infer the properties of the new fundamental scale.

Usually, in order to reduce the number of free parameters of the theory, the unification of SM gauge couplings at the GUT scale is assumed:

$$\frac{M_1}{g_1^2} = \frac{M_2}{g_2^2} = \frac{M_3}{g_3^2} \tag{E.4}$$

where g_i are the SM gauge couplings.

Besides the parameters μ (the higgsino mass parameter), $\tan\beta$ (the ratio of vacuum expectation values of the two Higgs doublets) and M_1 (connected to M_2 and M_3), one possible (not the unique) choice of phenomenological MSSM parameter space, MSSM-7, can be defined by specifying 4 additional free parameters: m_A (the CP-odd Higgs boson mass [ii]), A_t, A_b, m_0 which come from a simplification of the soft SUSY breaking parameters (i.e. from the assumption that A matrices in Eq. E.3 are diagonal) and represent the soft trilinear couplings and the soft sfermion masses respectively [iii].

A further "constrained" MSSM (cMSSM) parameter space is obtained by imposing that the soft parameters unify at some high energy scale and, as a consequence, all spin-0 scalars receive m_0 mass and all the gauginos $M_{1/2}$, such as occurs in mSUGRA models. In this way, the effective number of parameters is reduced to 5: m_0, the universal scalar mass, $M_{1/2}$, the universal gaugino mass (both defined at $M_{GUT} \sim 2 \cdot 10^{16}$ GeV), A_0, related to the cubic scalar particles interaction, and parameters defining the Higgs boson potential, $\tan\beta$ and sign(μ).

In this case parameters are defined at GUT scale and the values at the low energy scale are obtained by solving the renormalization group equation[iv].

For the large scans over the SUSY parameter space performed in chapter 4 we have adopted samples from both the MSSM-7 and cMSSM models.

We here overview the mass spectrum of the MSSM, focusing mostly on the Higgs sector and on neutralino/chargino masses (for more details please refer to (Edsjö, 1997)).

Higgs masses. The MSSM accommodates five physical Higgs bosons: three neutral scalar H, h and the CP-odd A (in DarkSUSY conventions referred to as H_1^0, H_2^0, H_3^0 respectively) and the charged $H^{\pm}$. The CP-even Higgs bosons are generally mixtures of the interaction eigenstates and the mixing angle is denoted by α where $-\pi/2 \leq \alpha \leq 0$.

The soft SUSY-breaking term depends on three parameters in the Higgs sector, m_1, m_2 and B. Out of them, only two are independent and they can be chosen to be $\tan\beta$ and the mass of the CP-odd Higgs boson, m_A. At

---

[ii] The constraints coming from minimizing the Higgs potential remove one of the three parameters in this sector and we are left with two independent parameters.

[iii] Notice that such an ansatz does not introduce any tree-level flavour changing neutral currents (FCNCs).

[iv] Notice that in the case of MSSM-7 the parameters are defined already at the low-energy scale.

tree-level [v] the Higgs bosons mass spectrum is:

$$m^2_{h,H} = \frac{1}{2}\left[m^2_A + m^2_Z \mp \sqrt{(m^2_A + m^2_Z)^2 - 4m^2_Z m^2_A \cos^2 2\beta}\right] \quad (E.5)$$

$$m^2_{H^\pm} = m^2_A + m^2_W. \quad (E.6)$$

Thus, the mass of the lightest Higgs boson m_h at tree-level is bounded from above:

$$m_h \leq m_Z|\cos 2\beta|. \quad (E.7)$$

Neutralino and Chargino masses. The most appealing DM candidate in the MSSM is the lightest neutralino. Neutralinos arise from the linear combination of the superpartners of the gauge bosons and the Higgs bosons, $\tilde{B}, \tilde{W}_3, \tilde{H}^0_1, \tilde{H}^0_2$.

The mass matrix for gauginos and Higgsinos is non-diagonal and thus a mixing among states is present and encoded in the neutralino mass matrix:

$$\mathcal{M}_{\tilde{\chi}^0} = \begin{pmatrix} M_1 & 0 & -\frac{g' v_1}{\sqrt{2}} & +\frac{g' v_2}{\sqrt{2}} \\ 0 & M_2 & +\frac{g v_1}{\sqrt{2}} & -\frac{g v_2}{\sqrt{2}} \\ -\frac{g' v_1}{\sqrt{2}} & +\frac{g v_1}{\sqrt{2}} & 0 & -\mu \\ +\frac{g' v_2}{\sqrt{2}} & -\frac{g v_2}{\sqrt{2}} & -\mu & 0 \end{pmatrix}. \quad (E.8)$$

The same occurs for Dirac chargino fields, whose mass matrix is in the form:

$$\mathcal{M}_{\tilde{\chi}^\pm} = \begin{pmatrix} M_2 & g v_2 \\ g v_1 & \mu \end{pmatrix}, \quad (E.9)$$

The mass eigenstates of neutralinos, $\tilde{\chi}^0_i$ (i = 1,4), and charginos, $\tilde{\chi}^\pm$, are obtained by diagonalizating the corresponding mass matrices. The mass eigenstates are then:

$$\tilde{\chi}^0_i = N_{i1}\tilde{B} + N_{i2}\tilde{W}^3 + N_{i3}\tilde{H}^0_1 + N_{i4}\tilde{H}^0_2, \quad (E.10)$$

for neutralinos, and:

$$\tilde{\chi}^-_i = U_{i1}\tilde{W}^- + U_{i2}\tilde{H}^-_1 \quad (E.11)$$

$$\tilde{\chi}^+_i = V_{i1}\tilde{W}^+ + V_{i2}\tilde{H}^+_2 \quad (E.12)$$

for charginos[vi].

Depending on its gaugino fraction,

$$Z^i_g = |N_{i1}|^2 + |N_{i2}|^2, \quad (E.13)$$

---

[v] We make notice that Higgs boson masses get large radiative corrections, e.g. implemented together with their decay widths in FeynHiggsFast (Heinemeyer, Hollik & Weiglein, 2000).

[vi] We notice that in DarkSUSY conventions $\det(U) = 1$ and $U^* \mathcal{M}_{\tilde{\chi}^\pm} V^\dagger = \mathrm{diag}(m_{\tilde{\chi}^\pm_1}, m_{\tilde{\chi}^\pm_2})$ with non-negative chargino masses.

the lightest neutralino can be: higgsino-like e.g. when $Z_g^1 < 0.01$, mixed e.g. when $0.01 \leq Z_g^1 < 0.99$ and gaugino-like e.g. when $Z_g^1 \geq 0.99$.

We mention here that the neutralino mass matrix, Eq. E.8, valid at tree level, receives higher order corrections due to dominantly quark-squark (t, b) loops.

Appendix F

Statistics

F.1 The method of Maximum Likelihood

In chapters 6 and 7 we make use of the maximum likelihood (ML) method for parameter(s) estimation. We here give an overview of this important method. We refer to (Bohm & Zech, 2010) as a good introductory book to statistics and to the statistics review of the Particle Data Group[i].

The value of a true parameter θ is "estimated" by an estimator $\hat{\theta}$ which is a function of the data. The main requirement for a good estimator is to be consistent, i.e. the estimate $\hat{\theta}$ converges to the true value θ when increasing the statistics.

Consider a set of n unknown parameters $\boldsymbol{\theta} = (\theta_1, ..., \theta_n)$ that have to be estimated from a set of N measurements $\mathbf{x} = (x_1, ..., x_N)$, described by the probability distribution function (p.d.f.) $f(\mathbf{x}; \boldsymbol{\theta})$. The likelihood function is defined as the p.d.f. viewed as a function of the parameters:

$$L(\boldsymbol{\theta}) \equiv f(\mathbf{x}; \boldsymbol{\theta})\,. \tag{F.1}$$

In the case of N independent measurements following each the p.d.f. $f(x; \boldsymbol{\theta})$ the likelihood writes as the product of each p.d.f.:

$$L(\boldsymbol{\theta}) = \prod_{i=1}^{N} f(x_i; \boldsymbol{\theta})\,. \tag{F.2}$$

This is the so called "unbinned likelihood" function and the estimators $\hat{\boldsymbol{\theta}}$ are those values of $\boldsymbol{\theta}$ maximizing $L(\boldsymbol{\theta})$ (unbinned ML method). Since $\ln L$ is maximized by the same set of parameters $\boldsymbol{\theta}$, it is useful to work with the so calle "log-likelihood". The ML estimators are defined by solving the "likelihood equations":

$$\frac{\partial \ln L}{\partial \theta_i} = 0 \tag{F.3}$$

---

[i] http://pdg.lbl.gov/2011/reviews/rpp2011-rev-statistics.pdf

with $i = 1, ...n$. ML estimators are almost unbiased (i.e. the difference between the expectation value of the estimator and the true value of the parameter is small).

In the case of large data samples it is convenient to bin the data in an histogram. By considering an histogram with k bins, we define n_i the number of events in the i^{th} bin, $\mathbf{n} = (n_1, ..., n_k)$ the corresponding vector of data and N the total number of events ($N = \sum_{i=1}^{k} n_i$). The number of events predicted by the model in the i^{th} bin is y_i and it is a function of the parameters $\boldsymbol{\theta}$. The total number of events predicted by the model is $N_{\mathrm{th}} = \sum_{i=1}^{k} y_i$. The p.d.f. per bin is then $f(n_i, y_i(\boldsymbol{\theta}))$. In the case of a counting experiments, designed to measure N, the independent Poisson statistics applies, i.e. the probability of detecting n_i counts with average rate per bin y_i is:

$$P_i = y_i^{n_i} \frac{\exp(-y_i)}{n_i!} \,. \tag{F.4}$$

The likelihood thus writes as:

$$\begin{aligned} L(\boldsymbol{\theta}) &= \prod_{i=1}^{k} f(n_i; y_i(\boldsymbol{\theta})) \qquad \text{(F.5)} \\ &= \prod_{i=1}^{k} y_i^{n_i} \frac{\exp(-y_i)}{n_i!} \equiv \exp(-N_{\mathrm{th}}) \prod_{i=1}^{k} \frac{y_i^{n_i}}{n_i!} \end{aligned}$$

By using the log-likelihood, we get:

$$\ln L(\boldsymbol{\theta}) = \sum_{i=1}^{k} (n_i \ln(y_i(\boldsymbol{\theta})) - y_i(\boldsymbol{\theta}) - \ln(n_i!) \,. \tag{F.6}$$

Since for likelihood inference only derivative of the likelihood function contribute to the ML estimator, factors independent on $\boldsymbol{\theta}$ can be omitted and thus:

$$\ln L(\boldsymbol{\theta}) \equiv \sum_{i=1}^{k} (n_i \ln(y_i(\boldsymbol{\theta})) - y_i(\boldsymbol{\theta})) \,. \tag{F.7}$$

Typically the maximum of this function is computed with numerical methods, that require the evaluation of the likelihood for each variation of of the parameters until the maximum of the function is reached.

In the case in which the events per bin is large, we know that the Poisson distribution asymptotically approaches a normal distribution. Thus for high statistics histograms we can use a normal distribution for the number of events n in a bin with prediction $y(\boldsymbol{\theta})$:

$$f(n) = \frac{1}{\sqrt{2\pi y}} \exp(-\frac{(n-y)^2}{2y}) \,. \tag{F.8}$$

The log-likelihood writes as:

$$\ln L = -\frac{(n-y)^2}{2y} - \frac{1}{2}\ln(2\pi) - \frac{1}{2}\ln y \tag{F.9}$$

Since for large y the logarithmic term is a slowly varying function of y, we can neglect the last term:

$$\ln L = -\frac{1}{2}\sum_{i}^{k}\frac{(n_i - y_i)^2}{y_i} \equiv -\frac{1}{2}\chi^2\,, \tag{F.10}$$

with k the number of bins. The sum corresponds to the χ^2 definition:

$$\chi^2 \equiv \sum_{i}^{k}\frac{(n_i - y_i)^2}{y_i} \tag{F.11}$$

Therefore, the likelihood estimation of the parameters may be replaced by a χ^2 fit in the large sample limit. Maximizing the log-likelihood is thus equivalent to minimizing the χ^2. The standard error (for single parameter estimation) on the estimators $\boldsymbol{\theta}$ are given by an increase of χ^2 by one unit or, equivalently, the error of the estimates $\boldsymbol{\theta}$ is obtained when the likelihood changes by 1/2 [ii]. If there are k bins and m fitted parameters, then the number of degree of freedom for the χ^2 distribution is $k - m$ (in the case data are treated as Poisson-distributed).

F.2 Statistical Tests

In order to assess the validity of a certain statement concerning data's underlying distribution, one has to perform e.g. frequentist hipothesis tests, which provide a rule for accepting or rejecting hypothesis depending on the outcome of the measurements.

A statistical test is a rule that states for which values of the data a given hypothesis (the null hypothesis, H_0) is rejected with a certain confidence level (C.L.). The rejection is done with respect to some alternative hypothesis H_1. Concretely, H_0 could represent the hypothesis of background events only, while the alternative hypothesis represents a mixture of background and signal. In each case the set of parameters $\boldsymbol{\theta}$ is defined to maximize the likelihood for the two hypothesis, e.g. $H_0 : \boldsymbol{\theta} = \boldsymbol{\theta}_0$ and $H_1 : \boldsymbol{\theta} = \boldsymbol{\theta}_1$.

Type-I errors occur when rejecting H_0 when it is true, while type-II errors correspond to not rejecting H_0 if an alternative hypothesis H_1 is true.

[ii] When the sample size is very large (i.e. more than 40 entries per bin) the likelihood function approaches a Gaussian and becomes proportional to the p.d.f. of the parameter(s). Then, the error limit corresponds to the standard deviation of the p.d.f., i.e. the square root of the variance of the Gaussian; s-standard deviation errors correspond to the contour given by: $\ln L(\boldsymbol{\theta}') = \ln L_{\max} - s^2/2$.

According to the Neyman-Pearson lemma, the optimal test statistic is defined by the likelihood ratio:

$$\lambda(\mathbf{x}) \equiv \frac{f(\mathbf{x}|H_0)}{f(\mathbf{x}|H_1)} = \frac{L(\boldsymbol{\theta}_0|\mathbf{x})}{L(\boldsymbol{\theta}_1|\mathbf{x})} \,. \tag{F.12}$$

where $\mathbf{x}$ are the data and the the parameters are chosen to maximize the likelihoods for the given observation $\mathbf{x}$ under the two hypothesis. Accordingly to the Wilk's theorem (for sufficiently large samples), the minimum of $-2\ln\lambda$ follows a χ^2 distribution, distributed with degrees of freedom equal to the difference in dimensionality of $\boldsymbol{\theta}_0$ and $\boldsymbol{\theta}_1$ (Wilk, 1983). This implies that, as a practical rule, one can compute the likelihood ratio for the data and compare $-2\ln\lambda$ to the χ^2 value corresponding to a desired statistical significance.

F.3 The Profile Likelihood

In the presence of multidimensional likelihood depending on parameters which are not of primary interest (the so called nuisance parameters), it is possible to reduce the number of effective parameters by defining the "profile likelihood". By considering $\boldsymbol{\pi}$ the nuisance parameters and $\boldsymbol{\theta}$ the parameters of interest, the profile likelihood is defined as:

$$L_p(\boldsymbol{\theta}) = L(\boldsymbol{\theta}, \hat{\boldsymbol{\pi}}(\boldsymbol{\theta}))\,, \tag{F.13}$$

where $\hat{\boldsymbol{\pi}}(\boldsymbol{\theta})$ corresponds to $\boldsymbol{\pi}$ that maximizes the likelihood for a given $\boldsymbol{\theta}$.

Confidence intervals for the parameters of interest, i.e. intervals in which a measurement or trial falls corresponding to a given probability, can then be constructed by using the "profile likelihood ratio":

$$\lambda_p(\boldsymbol{\theta}) = \frac{L(\boldsymbol{\theta})}{L(\hat{\boldsymbol{\theta}}, \hat{\boldsymbol{\pi}})}\,, \tag{F.14}$$

where $\hat{\boldsymbol{\theta}}$ and $\hat{\boldsymbol{\pi}}$ are ML estimators.

Bibliography

Aad, G., Abajyan, T., Abbott, B., Abdallah, J., Abdel Khalek, S., Abdelalim, A. A. et al. (2012, September). Observation of a new particle in the search for the Standard Model Higgs boson with the ATLAS detector at the LHC. *Physics Letters B*, *716*, 1-29.

Aad, G., Abbott, B., Abdallah, J., Abdelalim, A. A., Abdesselam, A., Abdinov, O. et al. (2012, März). Search for squarks and gluinos using final states with jets and missing transverse momentum with the ATLAS detector in s=7 TeV proton-proton collisions. *Physics Letters B*, *710*, 67-85.

Aalseth, C. E., Barbeau, P. S., Colaresi, J., Collar, J. I., Diaz Leon, J., Fast, J. E. et al. (2011, September). Search for an Annual Modulation in a p-Type Point Contact Germanium Dark Matter Detector. *Physical Review Letters*, *107* (14), 141301.

Aaronson, M. (1983, März). Accurate radial velocities for carbon stars in Draco and Ursa Minor - The first hint of a dwarf spheroidal mass-to-light ratio. *Astrophys. J. Lett.*, *266*, L11-L15.

Aarssen, L. G. van den, Bringmann, T. & Goedecke, Y. C. (2012). Thermal decoupling and the smallest subhalo mass in dark matter models with Sommerfeld-enhanced annihilation rates. *Phys.Rev.*, *D85*, 123512.

Aartsen, M. G., Abbasi, R., Abdou, Y., Ackermann, M., Adams, J., Aguilar, J. A. et al. (2013, März). Search for Dark Matter Annihilations in the Sun with the 79-String IceCube Detector. *Physical Review Letters*, *110* (13), 131302.

Abazajian, K., Acero, M., Agarwalla, S., Aguilar-Arevalo, A., Albright, C. et al. (2012). Light Sterile Neutrinos: A White Paper. *arXiv:1204.5379*.

Abazajian, K. N., Adelman-McCarthy, J. K., Agüeros, M. A., Allam, S. S., Allende Prieto, C., An, D. et al. (2009, Juni). The Seventh Data Release of the Sloan Digital Sky Survey. *Astrophys. J. Supplement*, *182*, 543-558.

Abazajian, K. N., Blanchet, S. & Harding, J. P. (2011, November). Contribution of blazars to the extragalactic diffuse gamma-ray background and their future spatial resolution. *Phys. Rev. D*, *84* (10), 103007.

Abbott, L. F. & Sikivie, P. (1983, Januar). A cosmological bound on the invisible axion. *Physics Letters B*, *120*, 133-136.

Abdo, A. et al. (2009). Fermi Large Area Telescope Gamma-Ray Detection of the Radio Galaxy M87. *Astrophys.J.*, *707*, 55-60.

Abdo, A. et al. (2010). Fermi Large Area Telescope View of the Core of the Radio Galaxy Centaurus A. *Astrophys.J.*, *719*, 1433-1444.

Abdo, A. A., Ackermann, M., Agudo, I., Ajello, M., Aller, H. D., Aller, M. F. et al. (2010, Juni). The Spectral Energy Distribution of Fermi Bright Blazars. *Astrophys. J.*, *716*, 30-70.

Abdo, A. A., Ackermann, M., Ajello, M., Allafort, A., Antolini, E., Atwood, W. B. et al. (2010, Juni). Fermi Large Area Telescope First Source Catalog. *Astrophys. J. S.S.*, *188*, 405-436.

Abdo, A. A., Ackermann, M., Ajello, M., Antolini, E., Baldini, L., Ballet, J. et al. (2010, September). The Fermi-LAT High-Latitude Survey: Source Count Distributions and the Origin of the Extragalactic Diffuse Background. *Astrophys. J.*, *720*, 435-453.

Abdo, A. A., Ackermann, M., Ajello, M., Asano, K., Baldini, L., Ballet, J. et al. (2009, Juli). Fermi Discovery of Gamma-ray Emission from NGC 1275. *Astrophys. J.*, *699*, 31-39.

Abdo, A. A., Ackermann, M., Ajello, M., Atwood, W. B., Axelsson, M., Baldini, L. et al. (2009a, Mai). Measurement of the Cosmic Ray $e^{+}+e^{-}$ Spectrum from 20GeV to 1TeV with the Fermi Large Area Telescope. *Physical Review Letters*, *102* (18), 181101.

Abdo, A. A., Ackermann, M., Ajello, M., Atwood, W. B., Axelsson, M., Baldini, L. et al. (2009b, August). A Population of Gamma-Ray Millisecond Pulsars Seen with the Fermi Large Area Telescope. *Science*, *325*, 848-.

Abdo, A. A., Ackermann, M., Ajello, M., Atwood, W. B., Baldini, L., Ballet, J. et al. (2009, Dezember). Fermi large area telescope observations of the cosmic-ray induced γ-ray emission of the Earth's atmosphere. *Phys. Rev. D*, *80* (12), 122004.

Abdo, A. A., Ackermann, M., Ajello, M., Atwood, W. B., Baldini, L., Ballet, J. et al. (2010, März). Observations of Milky Way Dwarf Spheroidal Galaxies with the Fermi-Large Area Telescope Detector and Constraints on Dark Matter Models. *Astrophys. J.*, *712*, 147-158.

Abdo, A. A., Ackermann, M., Ajello, M., Baldini, L., Ballet, J., Barbiellini, G. et al. (2010, April). Constraints on cosmological dark matter annihilation from the Fermi-LAT isotropic diffuse gamma-ray measurement. *JCAP*, *4*, 14.

Abdo, A. A. & al. et. (2010, März). Spectrum of the Isotropic Diffuse Gamma-Ray Emission Derived from First-Year Fermi Large Area Telescope Data. *Phys. Rev. Lett.*, *104* (10), 101101.

Abdo, A. A. et al. (2009, Juli). Bright Active Galactic Nuclei Source List from the First Three Months of the Fermi Large Area Telescope All-Sky Survey. *Astrophys. J.*, *700*, 597–622.

Abdo, A. A. et al. (2010a, Mai). Fermi Gamma-Ray Imaging of a Radio

Galaxy. *Science*, *328*, 725–.

Abdo, A. A. et al. (2010b, September). Fermi Large Area Telescope Observations of Misaligned Active Galactic Nuclei. *Astrophys. J.*, *720*, 912–922.

Abdo, A. A. et al. (2010c, Mai). The First Catalog of Active Galactic Nuclei Detected by the Fermi Large Area Telescope. *Astrophys. J.*, *715*, 429–457.

Abramowski, A., Acero, F., Aharonian, F., Akhperjanian, A. G., Anton, G., Balenderan, S. et al. (2013, Februar). Measurement of the extragalactic background light imprint on the spectra of the brightest blazars observed with H.E.S.S. *A&A*, *550*, A4.

Abramowski, A., Acero, F., Aharonian, F., Akhperjanian, A. G., Anton, G., Barnacka, A. et al. (2011, April). Search for a Dark Matter Annihilation Signal from the Galactic Center Halo with H.E.S.S. *Physical Review Letters*, *106* (16), 161301.

Abramowski, A. et al. (2013). Search for photon line-like signatures from Dark Matter annihilations with H.E.S.S. *Phys.Rev.Lett.*, *110*, 041301.

Achterberg, A., Ackermann, M., Adams, J., Ahrens, J., Andeen, K., Atlee, D. W. et al. (2006, Oktober). First year performance of the IceCube neutrino telescope. *Astroparticle Physics*, *26*, 155-173.

Ackermann, M., Ahrens, J., Bai, X., Bartelt, M., Barwick, S. W., Bay, R. C. et al. (2006, Januar). Limits to the muon flux from neutralino annihilations in the Sun with the AMANDA detector. *Astroparticle Physics*, *24*, 459-466.

Ackermann, M., Ajello, M., Albert, A., Atwood, W. B., Baldini, L., Ballet, J. et al. (2011, Dezember). Constraining Dark Matter Models from a Combined Analysis of Milky Way Satellites with the Fermi Large Area Telescope. *Physical Review Letters*, *107* (24), 241302.

Ackermann, M., Ajello, M., Albert, A., Baldini, L., Ballet, J., Barbiellini, G. et al. (2012, April). Anisotropies in the diffuse gamma-ray background measured by the Fermi LAT. *Phys. Rev. D*, *85* (8), 083007.

Ackermann, M., Ajello, M., Albert, A., Baldini, L., Barbiellini, G., Bechtol, K. et al. (2012, Juli). Fermi LAT search for dark matter in gamma-ray lines and the inclusive photon spectrum. *Phys. Rev. D*, *86* (2), 022002.

Ackermann, M., Ajello, M., Allafort, A., Baldini, L., Ballet, J., Barbiellini, G. et al. (2010a, Mai). Constraints on dark matter annihilation in clusters of galaxies with the Fermi large area telescope. *JCAP*, *5*, 25.

Ackermann, M., Ajello, M., Allafort, A., Baldini, L., Ballet, J., Barbiellini, G. et al. (2010b, Juli). GeV Gamma-ray Flux Upper Limits from Clusters of Galaxies. *Astrophys. J. Lett.*, *717*, L71-L78.

Ackermann, M., Ajello, M., Allafort, A., Baldini, L., Ballet, J., Bastieri, D. et al. (2012, August). GeV Observations of Star-forming Galaxies with the Fermi Large Area Telescope. *Astrophys. J.*, *755*, 164.

Ackermann, M., Ajello, M., Atwood, W. B., Baldini, L., Barbiellini, G., Bastieri, D. et al. (2012, Dezember). Constraints on the Galactic Halo Dark Matter from Fermi-LAT Diffuse Measurements. *Astrophys. J.*, *761*, 91.

Ackermann, M. et al. (2011). Constraining Dark Matter Models from a Combined Analysis of Milky Way Satellites with the Fermi Large Area Telescope. *Phys.Rev.Lett.*, *107*, 241302.

Ackermann, M. et al. (2011a). The radio/gamma-ray connection in Active Galactic Nuclei in the era of the Fermi Large Area Telescope. *Astrophys. J.*, *741*, 30.

Ackermann, M. et al. (2011b, Dezember). The Second Catalog of Active Galactic Nuclei Detected by the Fermi Large Area Telescope. *Astrophys. J.*, *743*, 171.

Ackermann, M. et al. (2012a). The Imprint of The Extragalactic Background Light in the Gamma-Ray Spectra of Blazars. *Science*, *338*, 1190–1192.

Ackermann, M. et al. (2012b). Measurement of separate cosmic-ray electron and positron spectra with the Fermi Large Area Telescope. *Phys.Rev.Lett.*, *108*, 011103.

Actis, M., Agnetta, G., Aharonian, F., Akhperjanian, A., Aleksić, J., Aliu, E. et al. (2011, Dezember). Design concepts for the Cherenkov Telescope Array CTA: an advanced facility for ground-based high-energy gamma-ray astronomy. *Experimental Astronomy*, *32*, 193-316.

Ade, P. A. R., Aghanim, N., Armitage-Caplan, C., Arnaud, M., Ashdown, M., Atrio-Barandela, F. et al. (2013, März). Planck 2013 results. XVI. Cosmological parameters. *arXiv:1303.5076*.

Adriani, O., Barbarino, G. C., Bazilevskaya, G. A., Bellotti, R., Boezio, M., Bogomolov, E. A. et al. (2010, September). PAMELA Results on the Cosmic-Ray Antiproton Flux from 60 MeV to 180 GeV in Kinetic Energy. *Physical Review Letters*, *105* (12), 121101.

Adriani, O. et al. (2009). An anomalous positron abundance in cosmic rays with energies 1.5-100 GeV. *Nature*, *458*, 607–609.

Agnese, R., Ahmed, Z., Anderson, A. J., Arrenberg, S., Balakishiyeva, D., Basu Thakur, R. et al. (2013, April). Dark Matter Search Results Using the Silicon Detectors of CDMS II. *arXiv:1304.4279*.

Aguilar, J. et al. (2004). Status of the ANTARES Project. *Eur.Phys.J.*, *C33*, S971-S974.

Aguilar, M. et al. (2013). First Result from the Alpha Magnetic Spectrometer on the International Space Station: Precision Measurement of the Positron Fraction in Primary Cosmic Rays of 0.5 ˘350 GeV. *Phys.Rev.Lett.*, *110* (14), 141102.

Aharonian, F., Akhperjanian, A. G., Anton, G., Barres de Almeida, U., Bazer-Bachi, A. R., Becherini, Y. et al. (2009, September). Spectrum and variability of the Galactic center VHE γ-ray source HESS J1745-290. *A&A*, *503*, 817-825.

Aharonian, F., Akhperjanian, A. G., Aye, K.-M., Bazer-Bachi, A. R., Beilicke, M., Benbow, W. et al. (2004, Oktober). Very high energy gamma rays from the direction of Sagittarius A*. *A&A*, *425*, L13-L17.

Aharonian, F., Khangulyan, D. & Malyshev, D. (2012, November). Cold ultrarelativistic pulsar winds as potential sources of galactic gamma-ray lines above 100 GeV. *A&A*, *547*, A114.

Aharonian, F. et al. (2006a). Discovery of very-high-energy gamma-rays from the galactic centre ridge. *Nature*, *439*, 695-698.

Aharonian, F. et al. (2006b). H.E.S.S. observations of the Galactic Center region and their possible dark matter interpretation. *Phys.Rev.Lett.*, *97*, 221102.

Aharonian, F. et al. (2006c). Observations of the Crab Nebula with H.E.S.S. *Astron.Astrophys.*, *457*, 899-915.

Aharonian, F. et al. (2008). The energy spectrum of cosmic-ray electrons at TeV energies. *Phys.Rev.Lett.*, *101*, 261104.

Ahlen, S., Balebanov, V. M., Battiston, R., Becker, U., Burger, J., Capell, M. et al. (1994, Oktober). An antimatter spectrometer in space. *Nuclear Instruments and Methods in Physics Research A*, *350*, 351-367.

Ahlers, M., Anchordoqui, L. A., Gonzalez - Garcia, M. C., Halzen, F. & Sarkar, S. (2010, September). GZK neutrinos after the Fermi-LAT diffuse photon flux measurement. *Astroparticle Physics*, *34*, 106-115.

Ahmed, Z., Akerib, D. S., Arrenberg, S., Bailey, C. N., Balakishiyeva, D., Baudis, L. et al. (2010, März). Dark Matter Search Results from the CDMS II Experiment. *Science*, *327*, 1619-.

Ajello, M., Shaw, M. S., Romani, R. W., Dermer, C. D., Costamante, L., King, O. G. et al. (2012, Juni). The Luminosity Function of Fermi-detected Flat-spectrum Radio Quasars. *Astrophys. J.*, *751*, 108.

Akritas, M. G. & Siebert, J. (1996, Februar). A test for partial correlation with censored astronomical data. *MNRAS*, *278*, 919–924.

Albert, J., Aliu, E., Anderhub, H., Antoranz, P., Armada, A., Asensio, M. et al. (2006, Februar). Observation of Gamma Rays from the Galactic Center with the MAGIC Telescope. *Astrophys. J. Lett.*, *638*, L101-L104.

Albert, J. et al. (2008). VHE Gamma-Ray Observation of the Crab Nebula and Pulsar with MAGIC. *Astrophys.J.*, *674*, 1037-1055.

Alvarez, H., Aparici, J., May, J. & Reich, P. (2000, März). The radio continuum spectrum of Centaurus A's large-scale components. *A&A*, *355*, 863–872.

Amsler, C. et al. (2008). Review of Particle Physics. *Phys.Lett.*, *B667*, 1-1340.

Ando, S. (2009, Juli). Gamma-ray background anisotropy from Galactic dark matter substructure. *Phys. Rev. D*, *80* (2), 023520.

Ando, S. & Komatsu, E. (2006, Januar). Anisotropy of the cosmic gamma-ray background from dark matter annihilation. *Phys. Rev. D*, *73* (2), 023521.

Ando, S. & Komatsu, E. (2013, Januar). Constraints on the annihilation cross section of dark matter particles from anisotropies in the diffuse gamma-ray background measured with Fermi-LAT. *arXiv:1301.5901*.

Ando, S., Komatsu, E., Narumoto, T. & Totani, T. (2007). Angular power spectrum of gamma-ray sources for GLAST: Blazars and clusters of galaxies. *Mon.Not.Roy.Astron.Soc.*, *376*, 1635-1647.

Ando, S., Komatsu, E., Narumoto, T. & Totani, T. (2007, März). Dark matter annihilation or unresolved astrophysical sources? Anisotropy probe of the origin of the cosmic gamma-ray background. *Phys. Rev. D*, *75* (6), 063519.

Ando, S., Nakar, E. & Sari, R. (2008, Dezember). GeV Emission from Prompt and Afterglow Phases of Gamma-Ray Bursts. *Astrophys. J.*, *689*, 1150-1160.

Ando, S. & Pavlidou, V. (2009, Dezember). Imprint of galaxy clustering in the cosmic gamma-ray background. *MNRAS*, *400*, 2122-2127.

Angloher, G., Bauer, M., Bavykina, I., Bento, A., Bucci, C., Ciemniak, C. et al. (2012, April). Results from 730 kg days of the CRESST-II Dark Matter search. *European Physical Journal C*, *72*, 1971.

Appelquist, T., Cheng, H.-C. & Dobrescu, B. A. (2001, August). Bounds on universal extra dimensions. *Phys. Rev. D*, *64* (3), 035002.

Aprile, E., Arisaka, K., Arneodo, F., Askin, A., Baudis, L., Behrens, A. et al. (2011, September). Dark Matter Results from 100 Live Days of XENON100 Data. *Physical Review Letters*, *107* (13), 131302.

Arina, C., Hambye, T., Ibarra, A. & Weniger, C. (2010, März). Intense gamma-ray lines from hidden vector dark matter decay. *JCAP*, *3*, 24.

Arkani-Hamed, N., Finkbeiner, D. P., Slatyer, T. R. & Weiner, N. (2009, Januar). A theory of dark matter. *Phys. Rev. D*, *79* (1), 015014.

Arnowitt, R., Dutta, B. & Santoso, Y. (2001, Juli). Coannihilation effects in supergravity and D-brane models. *Nuclear Physics B*, *606*, 59-83.

Arrenberg, S., Baudis, L., Kong, K., Matchev, K. T. & Yoo, J. (2008, September). Kaluza-Klein dark matter: Direct detection vis-a-vis CERN LHC. *Phys. Rev. D*, *78* (5), 056002.

Asano, M., Bringmann, T. & Weniger, C. (2012, März). Indirect dark matter searches as a probe of degenerate particle spectra. *Physics Letters B*, *709*, 128-132.

Atwood, W. B., Abdo, A. A., Ackermann, M., Althouse, W., Anderson, B., Axelsson, M. et al. (2009, Juni). The Large Area Telescope on the Fermi Gamma-Ray Space Telescope Mission. *Astrophys. J.*, *697*, 1071-1102.

Backer, D. C., Kulkarni, S. R., Heiles, C., Davis, M. M. & Goss, W. M. (1982, Dezember). A millisecond pulsar. *Nature*, *300*, 615-618.

Baer, H., Barger, V., Huang, P., Mickelson, D., Mustafayev, A. & Tata, X. (2013, Februar). Post-LHC7 fine-tuning in the minimal supergravity/CMSSM model with a 125 GeV Higgs boson. *Phys. Rev. D*, *87* (3), 035017.

Baer, H., Barger, V. & Mustafayev, A. (2012, Mai). Neutralino dark matter in mSUGRA/CMSSM with a 125 GeV light Higgs scalar. *Journal of High Energy Physics*, *5*, 91.

Baer, H. & Brhlik, M. (1998, Januar). Neutralino dark matter in minimal supergravity: Direct detection versus collider searches. *Phys. Rev. D*, *57*, 567-577.

Baltz, E. A., Berenji, B., Bertone, G., Bergström, L., Bloom, E., Bringmann, T. et al. (2008, Juli). Pre-launch estimates for GLAST sensitivity to dark matter annihilation signals. *JCAP*, *7*, 13.

Baltz, E. A. & Bergström, L. (2003, Februar). Detection of leptonic dark matter. *Phys. Rev. D*, *67* (4), 043516.

Baltz, E. A. & Edsjö, J. (1999, Januar). Positron propagation and fluxes from neutralino annihilation in the halo. *Phys. Rev. D*, *59* (2), 023511.

Baltz, E. A. & Wai, L. (2004, Juli). Diffuse inverse Compton and synchrotron emission from dark matter annihilations in galactic satellites. *Phys. Rev. D*, *70* (2), 023512.

Barbieri, R. (1999, September). What is the limit on the Higgs mass? *Physics Letters B*, *462*, 144-149.

Barthel, P. D. (1989, Januar). Is every quasar beamed? *Astrophys. J.*, *336*, 606–611.

Baum, S. A., Heckman, T. M., Bridle, A., van Breugel, W. J. M. & Miley, G. K. (1988, Dezember). Extended optical-line-emitting gas in radio galaxies - Broad-band optical, narrow-band optical, and radio imaging of a representative sample. *Astrophys. J. Supplement*, *68*, 643–714.

Becker, R. H., White, R. L. & Edwards, A. L. (1991, Januar). A new catalog of 53,522 4.85 GHz sources. *Astrophys. J. Supplement*, *75*, 1–229.

Begelman, M. C., Blandford, R. D. & Rees, M. J. (1984, Apr). Theory of extragalactic radio sources. *Rev. Mod. Phys.*, *56*, 255–351.

Bélanger, G., Belyaev, A., Brown, M., Kakizaki, M. & Pukhov, A. (2013, Januar). Testing minimal universal extra dimensions using Higgs boson searches at the LHC. *Phys. Rev. D*, *87* (1), 016008.

Bélanger, G., Kakizaki, M. & Pukhov, A. (2011, Februar). Dark matter in UED: the role of the second KK level. *JCAP*, *2*, 9.

Bell, N. F., Dent, J. B., Galea, A. J., Jacques, T. D., Krauss, L. M. & Weiler, T. J. (2011, November). W/Z bremsstrahlung as the dominant annihilation channel for dark matter, revisited. *Physics Letters B*, *706*, 6-12.

Bell, N. F., Dent, J. B., Jacques, T. D. & Weiler, T. J. (2008, Oktober). Electroweak bremsstrahlung in dark matter annihilation. *Phys. Rev. D*, *78* (8), 083540.

Bell, N. F., Dent, J. B., Jacques, T. D. & Weiler, T. J. (2011a, November). Dark matter annihilation signatures from electroweak bremsstrahlung. *Phys. Rev. D*, *84* (10), 103517.

Bell, N. F., Dent, J. B., Jacques, T. D. & Weiler, T. J. (2011b, Januar). W/Z bremsstrahlung as the dominant annihilation channel for dark matter. *Phys. Rev. D*, *83* (1), 013001.

Bell, N. F., Galea, A. J., Dent, J. B., Jacques, T. D., Krauss, L. M. & Weiler, T. J. (2012, November). Searching for dark matter at the LHC with a mono-Z. *Phys. Rev. D*, *86* (9), 096011.

Berezhiani, Z. G., Dolgov, A. D. & Mohapatra, R. N. (1996, Februar). Asymmetric inflationary reheating and the nature of mirror universe. *Physics Letters B*, *375*, 26-36.

Berezinskii, V. S., Bulanov, S. V., Dogiel, V. A. & Ptuskin, V. S. (1990). *Astrophysics of cosmic rays.*

Berezinsky, G. A., V. S. & Zybin, K. (1992). Distribution of dark matter in the galaxy and the lower limits for the masses of supersymmetric particles. *Phys. Lett. B*, *294*, 221.

Berezinsky, V., Bottino, A., Ellis, J., Fornengo, N., Mignola, G. & Scopel, S. (1996, Oktober). Searching for relic neutralinos using neutrino telescopes. *Astroparticle Physics*, *5*, 333-352.

Berezinsky, V., Gazizov, A., Kachelrieß, M. & Ostapchenko, S. (2011, Januar). Restricting UHECRs and cosmogenic neutrinos with Fermi-LAT. *Physics Letters B*, *695*, 13-18.

Bergström, L. (1989, Juli). Radiative processes in dark matter photino annihilation. *Physics Letters B*, *225*, 372-380.

Bergström, L. (2000, Mai). Non-baryonic dark matter: observational evidence and detection methods. *Reports on Progress in Physics*, *63*, 793-841.

Bergström, L. (2012, Oktober). Dark matter evidence, particle physics candidates and detection methods. *Annalen der Physik*, *524*, 479-496.

Bergström, L., Bertone, G., Bringmann, T., Edsjö, J. & Taoso, M. (2009, April). Gamma-ray and radio constraints of high positron rate dark matter models annihilating into new light particles. *Phys. Rev. D*, *79* (8), 081303.

Bergstrom, L., Bringmann, T., Cholis, I., Hooper, D. & Weniger, C. (2013, Juni). New limits on dark matter annihilation from AMS cosmic ray positron data. *arXiv:1306.3983*.

Bergström, L., Bringmann, T. & Edsjö, J. (2008, November). New positron spectral features from supersymmetric dark matter: A way to explain the PAMELA data? *Phys. Rev. D*, *78* (10), 103520.

Bergström, L., Bringmann, T. & Edsjö, J. (2011, Februar). Complementarity of direct dark matter detection and indirect detection through gamma rays. *Phys. Rev. D*, *83* (4), 045024.

Bergström, L., Bringmann, T., Eriksson, M. & Gustafsson, M. (2005a, Dezember). Gamma Rays from Heavy Neutralino Dark Matter. *Physical Review Letters*, *95* (24), 241301.

Bergström, L., Bringmann, T., Eriksson, M. & Gustafsson, M. (2005b, April). Gamma Rays from Kaluza-Klein Dark Matter. *Physical Review Letters*, *94* (13), 131301.

Bergström, L., Edsjö, J. & Ullio, P. (1999, November). Cosmic Antiprotons as a Probe for Supersymmetric Dark Matter? *Astrophys. J.*, *526*, 215-235.

Bergström, L., Edsjö, J. & Ullio, P. (2001, Dezember). Spectral Gamma-Ray Signatures of Cosmological Dark Matter Annihilations. *Physical Review Letters*, *87* (25), 251301.

Bergstrom, L., Edsjo, J. & Zaharijas, G. (2009). Dark matter interpretation of recent electron and positron data. *Phys.Rev.Lett.*, *103*, 031103.

Bergström, L., Ullio, P. & Buckley, J. H. (1998, August). Observability of gamma rays from dark matter neutralino annihilations in the Milky Way halo. *Astroparticle Physics*, *9*, 137-162.

Bernabei, R., Belli, P., Cappella, F., Cerulli, R., Dai, C. J., D'Angelo, A. et al. (2008, August). First results from DAMA/LIBRA and the combined results with DAMA/NaI. *European Physical Journal C*, *56*, 333.

Bernabei, R., Belli, P., Cappella, F., Cerulli, R., Dai, C. J., D'Angelo, A. et al. (2010, Mai). New results from DAMA/LIBRA. *European Physical Journal C*, *67*, 39-49.

Bertone, G. (2010). *Particle Dark Matter: Observations, Models and Searches.* Cambridge University Press.

Bertone, G., Cerdeño, D. G., Fornasa, M., Ruiz de Austri, R. & Trotta, R. (2010, September). Identification of dark matter particles with LHC and direct detection data. *Phys. Rev. D*, *82* (5), 055008.

Bertone, G., Cirelli, M., Strumia, A. & Taoso, M. (2009, März). Gamma-ray and radio tests of the $e^{\pm}$ excess from DM annihilations. *JCAP*, *3*, 9.

Bertone, G., Hooper, D. & Silk, J. (2005, Januar). Particle dark matter: evidence, candidates and constraints. *Physics Reports*, *405*, 279-390.

Bertone, G., Sigl, G. & Silk, J. (2002, November). Annihilation radiation from a dark matter spike at the Galactic Centre. *MNRAS*, *337*, 98-102.

Bhattacharya, D., Sreekumar, P. & Mukherjee, R. (2009, November). Contribution from unresolved discrete sources to the extragalactic gamma-ray background (EGRB). *Research in Astronomy and Astrophysics*, *9*, 1205-1214.

Bhattacharya, D. & Srinivasan, G. (1991, März). Gamma rays from millisecond pulsars. *Journal of Astrophysics and Astronomy*, *12*, 17-25.

Bhattacharya, D. & van den Heuvel, E. P. J. (1991). Formation and evolution of binary and millisecond radio pulsars. *Physics Reports*, *203*, 1-124.

Bird, S., Harris, W. E., Blakeslee, J. P. & Flynn, C. (2010, Dezember). The inner halo of M 87: a first direct view of the red-giant population. *A&A*, *524*, A71.

Birkedal, A., Matchev, K. & Perelstein, M. (2004, Oktober). Dark matter at colliders: A model-independent approach. *Phys. Rev. D*, *70* (7), 077701.

Birkedal, A., Matchev, K. T., Perelstein, M. & Spray, A. (2005, Juli). Robust Gamma Ray Signature of WIMP Dark Matter. *arXiv:hep-ph/0507194*.

Blasi, P., Gabici, S. & Brunetti, G. (2007). Gamma Rays from Clusters of Galaxies. *International Journal of Modern Physics A*, *22*, 681-706.

Błażejowski, M., Sikora, M., Moderski, R. & Madejski, G. M. (2000, Dezember). Comptonization of Infrared Radiation from Hot Dust by Relativistic Jets in Quasars. *Astrophys. J.*, *545*, 107–116.

Bloch, F. & Nordsieck, A. (1937, Juli). Note on the Radiation Field of the Electron. *Physical Review*, *52*, 54-59.

Bloom, E., Charles, E., Izaguirre, E., Snyder, A., Albert, A. et al. (2013). Search of the Earth Limb Fermi Data and Non-Galactic Center Region Fermi Data for Signs of Narrow Lines.

Blumenthal, G. R., Faber, S. M., Flores, R. & Primack, J. R. (1986, Februar). Contraction of dark matter galactic halos due to baryonic infall. *Astrophys. J.*, *301*, 27-34.

Boer, W. de. (1994). Grand unified theories and supersymmetry in particle physics and cosmology. *Prog.Part.Nucl.Phys.*, *33*, 201-302.

Bohm, G. & Zech, G. (2010). *Introduction to Statistics and Data Analysis for Physicists.* Verlag Deutsches Elektronen-Synchrotron.

Bottino, A., Donato, F., Fornengo, N. & Salati, P. (1998, Dezember). Which fraction of the measured cosmic-ray antiprotons might be due to neutralino annihilation in the galactic halo? *Phys. Rev. D*, *58* (12), 123503.

Bottino, A., Donato, F., Fornengo, N. & Scopel, S. (2004, Februar). Light neutralinos and WIMP direct searches. *Phys. Rev. D*, *69* (3), 037302.

Bottino, A., Donato, F., Fornengo, N. & Scopel, S. (2008, Oktober). Interpreting the recent results on direct searches for dark matter particles in terms of relic neutralinos. *Phys. Rev. D*, *78* (8), 083520.

Boylan-Kolchin, M., Springel, V., White, S. D. M., Jenkins, A. & Lemson, G. (2009, September). Resolving cosmic structure formation with the Millennium-II Simulation. *MNRAS*, *398*, 1150-1164.

Bradač, M., Allen, S. W., Treu, T., Ebeling, H., Massey, R., Morris, R. G. et al. (2008, November). Revealing the Properties of Dark Matter in the Merging Cluster MACS J0025.4-1222. *Astrophys. J.*, *687*, 959-967.

Braun, I., Bolz, O., van Eldik, C., Hermann, G., Hinton, J. & Hofmann, W.

(2008, Mai). Localising the HESS galactic centre point source. *Journal of Physics Conference Series*, *110* (6), 062003.

Bringmann, T. (2009, Oktober). Particle models and the small-scale structure of dark matter. *New Journal of Physics*, *11* (10), 105027.

Bringmann, T., Bergström, L. & Edsjö, J. (2008, Januar). New gamma-ray contributions to supersymmetric dark matter annihilation. *Journal of High Energy Physics*, *1*, 49.

Bringmann, T. & Calore, F. (2013). Significant Enhancement of Neutralino Dark Matter Annihilation. *arXiv:1308.1089*.

Bringmann, T., Calore, F., Di Mauro, M. & Donato, F. (2013, März). Constraining dark matter annihilation with the isotropic γ-ray background: updated limits and future potential. *arXiv:1303.3284*.

Bringmann, T., Calore, F., Vertongen, G. & Weniger, C. (2011, November). Relevance of sharp gamma-ray features for indirect dark matter searches. *Phys. Rev. D*, *84* (10), 103525.

Bringmann, T., Huang, X., Ibarra, A., Vogl, S. & Weniger, C. (2012, Juli). Fermi LAT search for internal bremsstrahlung signatures from dark matter annihilation. *JCAP*, *7*, 54.

Bringmann, T. & Salati, P. (2007, April). Galactic antiproton spectrum at high energies: Background expectation versus exotic contributions. *Phys. Rev. D*, *75* (8), 083006.

Bringmann, T. & Weniger, C. (2012, November). Gamma ray signals from dark matter: Concepts, status and prospects. *Physics of the Dark Universe*, *1*, 194-217.

Brown, A. M. & Adams, J. (2012, April). Discovery of γ-ray emission from the broad-line radio galaxy Pictor A. *MNRAS*, *421*, 2303–2309.

Brunetti, G. & Bondi, M. (2001, September). Chandra discovery of large scale non-thermal emission in the radio loud quasar 3C 207. In *Two years of science with chandra.*

Bugaev, V. (2011, Februar). Different concepts of next generation IACT arrays. *Astrophysics and Space Sciences Transactions*, *7*, 53-59.

Bulik, T., Rudak, B. & Dyks, J. (2000, September). Spectral features in gamma-rays expected from millisecond pulsars. *MNRAS*, *317*, 97-104.

Bullock, J. S., Kolatt, T. S., Sigad, Y., Somerville, R. S., Kravtsov, A. V., Klypin, A. A. et al. (2001, März). Profiles of dark haloes: evolution, scatter and environment. *MNRAS*, *321*, 559-575.

Burgess, A. M. & Hunstead, R. W. (2006, Januar). The Molonglo Southern 4 Jy Sample (MS4). II. ATCA Imaging and Optical Identification. *Astrophys. J.*, *131*, 114–132.

Burles, S., Nollett, K. M. & Turner, M. S. (2001, März). What is the big-bang-nucleosynthesis prediction for the baryon density and how reliable is it? *Phys. Rev. D*, *63* (6), 063512.

Burns, J. O., Feigelson, E. D. & Schreier, E. J. (1983, Oktober). The inner radio structure of Centaurus A - Clues to the origin of the jet X-ray emission. *Astrophys. J.*, *273*, 128–153.

Byckling, E. & Kajantie, K. (1973). *Particle Kinematics.* John Wiley & Sons.

Calore, F., De Romeri, V., Di Mauro, M., Donato, F., Herpich, J., Maccio', A. V. et al. (2013). Uncertainties on γ-ray anisotropy from dark matter in the Milky Way. *Work in progress.*

Calore, F., de Romeri, V. & Donato, F. (2012, Januar). Conservative upper limits on WIMP annihilation cross section from Fermi-LAT γ rays. *Phys. Rev. D*, *85* (2), 023004.

Cara, M. & Lister, M. L. (2008, Februar). MOJAVE: Monitoring of Jets in AGN with VLBA Experiments. IV. The Parent Luminosity Function of Radio-Loud Blazars. *Astrophys. J.*, *674*, 111–121.

Carena, M., Tait, T. T. M. & Wagner, C. E. M. (2002, September). Branes and Orbifolds are Opaque. *Acta Physica Polonica B*, *33*, 2355.

Casanova, S., Dingus, B. L. & Zhang, B. (2007, Februar). Contribution of GRB Emission to the GeV Extragalactic Diffuse Gamma-Ray Flux. *Astrophys. J.*, *656*, 306-312.

Catena, R., Fornengo, N., Masiero, A., Pietroni, M. & Schelke, M. (2008, Oktober). Enlarging minimal-supergravity parameter space by decreasing pre-nucleosynthesis Hubble rate in scalar-tensor cosmologies. *Journal of High Energy Physics*, *10*, 3.

Cayrel, R., Steffen, M., Bonifacio, P., Ludwig, H.-G. & Caffau, E. (2008). Overview of the Li problem in metal-poor stars and new results on 6Li. In *Nuclei in the cosmos (nic x).*

Cembranos, J. A. R., de La Cruz-Dombriz, A., Dobado, A., Lineros, R. A. & Maroto, A. L. (2011, April). Photon spectra from WIMP annihilation. *Phys. Rev. D*, *83* (8), 083507.

Chamseddine, A. H., Arnowitt, R. & Nath, P. (1982, Oktober). Locally supersymmetric grand unification. *Physical Review Letters*, *49*, 970-974.

Chatrchyan, S., Khachatryan, V., Sirunyan, A. M., Tumasyan, A., Adam, W., Aguilo, E. et al. (2012a, September). Observation of a new boson at a mass of 125 GeV with the CMS experiment at the LHC. *Physics Letters B*, *716*, 30-61.

Chatrchyan, S., Khachatryan, V., Sirunyan, A. M., Tumasyan, A., Adam, W., Aguilo, E. et al. (2012b, September). Search for dark matter and large extra dimensions in monojet events in pp collisions at sqrt {s} = {7} TeV. *Journal of High Energy Physics*, *9*, 94.

Chatrchyan, S., Khachatryan, V., Sirunyan, A. M., Tumasyan, A., Adam, W., Bergauer, T. et al. (2011, November). Search for Supersymmetry at the LHC in Events with Jets and Missing Transverse Energy. *Physical Review Letters*, *107* (22), 221804.

Cheng, H.-C., Feng, J. L. & Matchev, K. T. (2002, Oktober). Kaluza-Klein

Dark Matter. *Physical Review Letters*, *89* (21), 211301.

Cheng, H.-C., Matchev, K. T. & Schmaltz, M. (2002a, September). Bosonic supersymmetry? Getting fooled at the CERN LHC. *Phys. Rev. D*, *66* (5), 056006.

Cheng, H.-C., Matchev, K. T. & Schmaltz, M. (2002b, August). Radiative corrections to Kaluza-Klein masses. *Phys. Rev. D*, *66* (3), 036005.

Cheng, K. S., Ho, C. & Ruderman, M. (1986, Januar). Energetic radiation from rapidly spinning pulsars. I - Outer magnetosphere gaps. II - VELA and Crab. *Astrophys. J.*, *300*, 500-539.

Chiaberge, M., Capetti, A. & Celotti, A. (1999, September). The HST view of FR I radio galaxies: evidence for non-thermal nuclear sources. *A&A*, *349*, 77–87.

Cholis, I. & Hooper, D. (2013). Dark Matter and Pulsar Origins of the Rising Cosmic Ray Positron Fraction in Light of New Data From AMS.

Ciafaloni, M., Ciafaloni, P. & Comelli, D. (2000, Mai). Bloch-Nordsieck Violating Electroweak Corrections to Inclusive TeV Scale Hard Processes. *Physical Review Letters*, *84*, 4810-4813.

Ciafaloni, P., Cirelli, M., Comelli, D., De Simone, A., Riotto, A. & Urbano, A. (2011a, Oktober). Initial state radiation in Majorana Dark Matter annihilations. *JCAP*, *10*, 34.

Ciafaloni, P., Cirelli, M., Comelli, D., De Simone, A., Riotto, A. & Urbano, A. (2011b, Juni). On the importance of electroweak corrections for Majorana dark matter indirect detection. *JCAP*, *6*, 18.

Ciafaloni, P. & Comelli, D. (1999, Januar). Sudakov effects in electroweak corrections. *Physics Letters B*, *446*, 278-284.

Ciafaloni, P., Comelli, D., De Simone, A., Riotto, A. & Urbano, A. (2012, Juni). Electroweak bremsstrahlung for wino-like Dark Matter annihilations. *JCAP*, *6*, 16.

Ciafaloni, P., Comelli, D., Riotto, A., Sala, F., Strumia, A. & Urbano, A. (2011, März). Weak corrections are relevant for dark matter indirect detection. *JCAP*, *3*, 19.

Ciafaloni, P. & Urbano, A. (2010, August). TeV scale dark matter and electroweak radiative corrections. *Phys. Rev. D*, *82* (4), 043512.

Cirelli, M. & Panci, P. (2009, November). Inverse Compton constraints on the Dark Matter e excesses. *Nuclear Physics B*, *821*, 399–416.

Cirelli, M., Panci, P. & Serpico, P. D. (2010, November). Diffuse gamma ray constraints on annihilating or decaying Dark Matter after Fermi. *Nuclear Physics B*, *840*, 284–303.

Clowe, D., Bradač, M., Gonzalez, A. H., Markevitch, M., Randall, S. W., Jones, C. et al. (2006, September). A Direct Empirical Proof of the Existence of Dark Matter. *Astrophys. J. Lett.*, *648*, L109-L113.

Colafrancesco, S., Profumo, S. & Ullio, P. (2006). Multi-frequency analysis of neutralino dark matter annihilations in the Coma cluster. *Astron.Astrophys.*, *455*, 21.

Combi, J. A. & Romero, G. E. (1997, Januar). The large-scale radio spectral index distribution of Centaurus A. *Astronomy and Astrophysics, Supplement*, *121*, 11–14.

Cumberbatch, D. T., López-Fogliani, D. E., Roszkowski, L., Ruiz de Austri, R. & Tsai, Y.-L. S. (2011, Juli). Is light neutralino as dark matter still viable? *arXiv:1107.1604*.

Daugherty, J. K. & Harding, A. K. (1994, Juli). Polar CAP models of gamma-ray pulsars: Emision from single poles of nearly aligned rotators. *Astrophys. J.*, *429*, 325-330.

Deason, A. J., Belokurov, V., Evans, N. W., Koposov, S. E., Cooke, R. J., Peñarrubia, J. et al. (2012, Oktober). The cold veil of the Milky Way stellar halo. *Mon.Not.R.Astron.Soc.*, *425*, 2840–2853.

Delahaye, T., Lineros, R., Donato, F., Fornengo, N., Lavalle, J., Salati, P. et al. (2009, Juli). Galactic secondary positron flux at the Earth. *A&A*, *501*, 821-833.

Dent, J. B., Scherrer, R. J. & Weiler, T. J. (2008, September). Toward a minimum branching fraction for dark matter annihilation into electromagnetic final states. *Phys. Rev. D*, *78* (6), 063509.

Dermer, C. D. (1995, Juni). On the Beaming Statistics of Gamma-Ray Sources. *Astrophys. J. Lett.*, *446*, L63.

Dermer, C. D. & Schlickeiser, R. (1993, Oktober). Model for the High-Energy Emission from Blazars. *Astrophys. J.*, *416*, 458.

Dermer, C. D. & Schlickeiser, R. (2002, August). Transformation Properties of External Radiation Fields, Energy-Loss Rates and Scattered Spectra, and a Model for Blazar Variability. *Astrophys. J.*, *575*, 667-686.

Desai, S., Ashie, Y., Fukuda, S., Fukuda, Y., Ishihara, K., Itow, Y. et al. (2004, Oktober). Search for dark matter WIMPs using upward through-going muons in Super-Kamiokande. *Phys. Rev. D*, *70* (8), 083523.

Di Bernardo, G., Evoli, C., Gaggero, D., Grasso, D., Maccione, L. & Mazziotta, M. N. (2011, Februar). Implications of the cosmic ray electron spectrum and anisotropy measured with Fermi-LAT. *Astroparticle Physics*, *34*, 528-538.

Di Mauro, M., Calore, F., Donato, F., Ajello, M. & Latronico, L. (2013, April). Diffuse γ-ray emission from misaligned active galactic nuclei. *arXiv:1304.0908*.

Diaferio, A., Schindler, S. & Dolag, K. (2008, Februar). Clusters of Galaxies: Setting the Stage. *Space Sci. Rev.*, *134*, 7-24.

Diemand, J., Kuhlen, M. & Madau, P. (2007). Dark matter substructure and gamma-ray annihilation in the Milky Way halo. *Astrophys.J.*, *657*, 262-270.

Diemand, J., Kuhlen, M., Madau, P., Zemp, M., Moore, B., Potter, D. et al. (2008, August). Clumps and streams in the local dark matter distribution. *Nature*, *454*, 735-738.

Diemand, J. & Moore, B. (2011, Februar). The Structure and Evolution of Cold Dark Matter Halos. *Advanced Science Letters*, *4*, 297–310.

Diemand, J., Moore, B. & Stadel, J. (2005, Januar). Earth-mass dark-matter haloes as the first structures in the early Universe. *Nature*, *433*, 389-391.

Dine, M. & Fischler, W. (1983, Januar). The not-so-harmless axion. *Physics Letters B*, *120*, 137-141.

Dodelson, S. & Widrow, L. M. (1994, Januar). Sterile neutrinos as dark matter. *Physical Review Letters*, *72*, 17-20.

Dodson, R., Fomalont, E. B., Wiik, K., Horiuchi, S., Hirabayashi, H., Edwards, P. G. et al. (2008, April). The VSOP 5 GHz Active Galactic Nucleus Survey. V. Imaging Results for the Remaining 140 Sources. *Astrophys. J. Supplement*, *175*, 314–355.

Donato, F., Fornengo, N. & Maurin, D. (2008, August). Antideuteron fluxes from dark matter annihilation in diffusion models. *Phys. Rev. D*, *78* (4), 043506.

Donato, F., Fornengo, N., Maurin, D., Salati, P. & Taillet, R. (2004, März). Antiprotons in cosmic rays from neutralino annihilation. *Phys. Rev. D*, *69* (6), 063501.

Donato, F., Fornengo, N. & Salati, P. (2000, August). Antideuterons as a signature of supersymmetric dark matter. *Phys. Rev. D*, *62* (4), 043003.

Donato, F., Gentile, G., Salucci, P., Frigerio Martins, C., Wilkinson, M. I., Gilmore, G. et al. (2009, August). A constant dark matter halo surface density in galaxies. *MNRAS*, *397*, 1169-1176.

Donato, F., Maurin, D., Brun, P., Delahaye, T. & Salati, P. (2009, Februar). Constraints on WIMP Dark Matter from the High Energy PAMELA $\bar{p}$/p Data. *Physical Review Letters*, *102* (7), 071301.

Donato, F., Maurin, D., Salati, P., Barrau, A., Boudoul, G. & Taillet, R. (2001, Dezember). Antiprotons from Spallations of Cosmic Rays on Interstellar Matter. *Astrophys. J.*, *563*, 172-184.

Dondi, L. & Ghisellini, G. (1995, April). Gamma-ray-loud blazars and beaming. *MNRAS*, *273*, 583–595.

Doro, M., Conrad, J., Emmanoulopoulos, D., Sànchez-Conde, M. A., Barrio, J. A., Birsin, E. et al. (2013, März). Dark matter and fundamental physics with the Cherenkov Telescope Array. *Astroparticle Physics*, *43*, 189-214.

Drees, M. & Nojiri, M. M. (1993, Januar). Neutralino relic density in minimal N=1 supergravity. *Phys. Rev. D*, *47*, 376-408.

Drukier, A. K., Freese, K. & Spergel, D. N. (1986, Juni). Detecting cold dark-matter candidates. *Phys. Rev. D*, *33*, 3495-3508.

Du, Y. J., Qiao, G. J. & Chen, D. (2013, Januar). Radio and Gamma-Ray Pulsed Emission from Millisecond Pulsars. *Astrophys. J.*, *763*, 29.

Du, Y. J., Xu, R. X., Qiao, G. J. & Han, J. L. (2009, November). The formation of submillisecond pulsars and the possibility of detection. *MNRAS*, *399*, 1587-1596.

Dudas, E., Mambrini, Y., Pokorski, S. & Romagnoni, A. (2009, August). (In)visible Z' and dark matter. *Journal of High Energy Physics*, *8*, 14.

Dunlop, J. S. & Peacock, J. A. (1990, November). The Redshift Cut-Off in the Luminosity Function of Radio Galaxies and Quasars. *MNRAS*, *247*, 19.

Duperray, R., Baret, B., Maurin, D., Boudoul, G., Barrau, A., Derome, L. et al. (2005, April). Flux of light antimatter nuclei near Earth, induced by cosmic rays in the Galaxy and in the atmosphere. *Phys. Rev. D*, *71* (8), 083013.

Dutton, A. A., Conroy, C., van den Bosch, F. C., Simard, L., Mendel, J. T., Courteau, S. et al. (2011, September). Dark halo response and the stellar initial mass function in early-type and late-type galaxies. *MNRAS*, *416*, 322-345.

Edelhäuser, L., Flacke, T. & Krämer, M. (2013, Februar). Constraints on models with universal extra dimensions from dilepton searches at the LHC. *ArXiv e-prints*.

Edsjö, J. (1997). Aspects of Neutrino Detection of Neutralino Dark Matter. *arXiv:hep-ph/9704384*.

Edsjö, J. & Gondolo, P. (1997, August). Neutralino relic density including coannihilations. *Phys. Rev. D*, *56*, 1879-1894.

Einasto, J. (1965). On the Construction of a Composite Model for the Galaxy and on the Determination of the System of Galactic Parameters. *Trudy Astrofizicheskogo Instituta Alma-Ata*, *5*, 87–100.

Ekers, R. D., Wall, J. V., Shaver, P. A., Goss, W. M., Fosbury, R. A. E., Danziger, I. J. et al. (1989, Februar). A complete sample of radio galaxies. I - The radio data. *MNRAS*, *236*, 737–777.

Ellis, J., Falk, T. & Olive, K. A. (1998, Dezember). Neutralino-stau coannihilation and the cosmological upper limit on the mass of the lightest supersymmetric particle. *Physics Letters B*, *444*, 367-372.

Ellis, J., Falk, T., Olive, K. A. & Srednicki, M. (2000, Mai). Calculations of neutralino-stau coannihilation channels and the cosmologically relevant region of MSSM parameter space. *Astroparticle Physics*, *13*, 181-213.

Ellis, J., Hagelin, J. S., Nanopoulos, D. V., Olive, K. & Srednicki, M. (1984, Juni). Supersymmetric relics from the big bang. *Nuclear Physics B*, *238*, 453-476.

Ellis, J. & Ross, D. (2001, Mai). A light Higgs boson would invite supersymmetry. *Physics Letters B*, *506*, 331-336.

Ellis, J. R., Kelley, S. & Nanopoulos, D. V. (1991). Probing the desert using gauge coupling unification. *Phys.Lett.*, *B260*, 131-137.

Evans, D. A., Hardcastle, M. J., Croston, J. H., Worrall, D. M. & Birkinshaw,

M. (2005, Mai). Chandra and XMM-Newton observations of NGC 6251. *MNRAS*, *359*, 363–382.

Evoli, C., Cholis, I., Grasso, D., Maccione, L. & Ullio, P. (2012). Antiprotons from dark matter annihilation in the Galaxy: astrophysical uncertainties. *Phys.Rev.*, *D85*, 123511.

Evoli, C., Gaggero, D., Grasso, D. & Maccione, L. (2010). Dragon code. Verfügbar unter `http://dragon.hepforge.org/DRAGON/Home.html`

Faber, S. M. & Gallagher, J. S. (1979). Masses and mass-to-light ratios of galaxies. *Annual Review of Astron. and Astrophys.*, *17*, 135-187.

Falco, E. E., Kochanek, C. S. & Munoz, J. A. (1998, Februar). Limits on Cosmological Models from Radio-selected Gravitational Lenses. *Astrophys. J.*, *494*, 47.

Fanaroff, B. L. & Riley, J. M. (1974, Mai). The morphology of extragalactic radio sources of high and low luminosity. *MNRAS*, *167*, 31P-36P.

Farrar, G. R. & Fayet, P. (1978). Phenomenology of the Production, Decay, and Detection of New Hadronic States Associated with Supersymmetry. *Phys.Lett.*, *B76*, 575-579.

Faucher-Giguère, C.-A. & Loeb, A. (2010, Januar). The pulsar contribution to the gamma-ray background. *JCAP*, *1*, 5.

Fayet, P. (1976, September). Supersymmetry and weak, electromagnetic and strong interactions. *Physics Letters B*, *64*, 159-162.

Fayet, P. (1977). Spontaneously broken supersymmetric theories of weak, electromagnetic and strong interactions. *Physics Letters B*, *69*, 489-494.

Fayet, P. (1979, Juli). Relations between the masses of the superpartners of leptons and quarks, the goldstino coupling and the neutral currents. *Physics Letters B*, *84*, 416-420.

Fegan, D. J. (1993). gamma/hadron separation at TeV energies. *J. Phys. G*, *23*, 1013.

Feng, J. L. (2013, Februar). Naturalness and the Status of Supersymmetry. *arXiv:1302.6587*.

Feng, J. L., Matchev, K. T. & Wilczek, F. (2000, Juni). Neutralino dark matter in focus point supersymmetry. *Physics Letters B*, *482*, 388-399.

Feng, J. L., Rajaraman, A. & Takayama, F. (2003a, September). Superweakly interacting massive particle dark matter signals from the early Universe. *Phys. Rev. D*, *68* (6), 063504.

Feng, J. L., Rajaraman, A. & Takayama, F. (2003b, Juli). Superweakly Interacting Massive Particles. *Physical Review Letters*, *91* (1), 011302.

Feng, L., Yuan, Q., Yin, P.-F., Bi, X.-J. & Li, M. (2012, April). Search for dark matter signals with Fermi-LAT observation of globular clusters NGC 6388 and M 15. *JCAP*, *4*, 30.

Fermi-LAT Collaboration. (2013, Mai). Search for Gamma-ray Spectral

Lines with the Fermi Large Area Telescope and Dark Matter Implications. *arXiv:1305.5597*.

Fichtel, C. E., Hartman, R. C., Kniffen, D. A., Thompson, D. J., Ogelman, H., Ozel, M. E. et al. (1975, Mai). High-energy gamma-ray results from the second small astronomy satellite. *Astrophys. J.*, *198*, 163-182.

Fields, B. D., Pavlidou, V. & Prodanović, T. (2010, Oktober). Cosmic Gamma-ray Background from Star-forming Galaxies. *Astrophys. J. Lett.*, *722*, L199-L203.

Finkbeiner, D. P., Su, M. & Weniger, C. (2013, Januar). Is the 130 GeV line real? A search for systematics in the Fermi-LAT data. *JCAP*, *1*, 29.

Finke, J. D., Razzaque, S. & Dermer, C. D. (2010, März). Modeling the Extragalactic Background Light from Stars and Dust. *Astrophys. J.*, *712*, 238–249.

Flores, R., Olive, K. A. & Rudaz, S. (1989, Dezember). Radiative processes in LSP annihilation. *Physics Letters B*, *232*, 377-382.

Fornasa, M., Pieri, L., Bertone, G. & Branchini, E. (2009). Anisotropy probe of galactic and extra-galactic Dark Matter annihilations. *Phys.Rev.*, *D80*, 023518.

Fornasa, M., Zavala, J., Sánchez-Conde, M. A., Siegal-Gaskins, J. M., Delahaye, T., Prada, F. et al. (2013, Februar). Characterization of dark-matter-induced anisotropies in the diffuse gamma-ray background. *MNRAS*, *429*, 1529-1553.

Fornengo, N., Lineros, R. A., Regis, M. & Taoso, M. (2012, Januar). Galactic synchrotron emission from WIMPs at radio frequencies. *JCAP*, *1*, 5.

Fornengo, N., Maccione, L. & Vittino, A. (2013). Dark matter searches with cosmic antideuterons: status and perspectives.

Fornengo, N., Pieri, L. & Scopel, S. (2004, November). Neutralino annihilation into γ rays in the Milky Way and in external galaxies. *Phys. Rev. D*, *70* (10), 103529.

Freedman, W. L., Madore, B. F., Gibson, B. K., Ferrarese, L., Kelson, D. D., Sakai, S. et al. (2001, Mai). Final Results from the Hubble Space Telescope Key Project to Measure the Hubble Constant. *Astrophys. J.*, *553*, 47-72.

Funk, S. & Hinton, J. A. (2013, März). Comparison of Fermi-LAT and CTA in the region between 10-100 GeV. *Astroparticle Physics*, *43*, 348-355.

Gabici, S. & Blasi, P. (2003, September). The gamma ray background from large scale structure formation. *Astroparticle Physics*, *19*, 679-689.

Galli, S., Iocco, F., Bertone, G. & Melchiorri, A. (2011, Juli). Updated CMB constraints on dark matter annihilation cross sections. *Phys. Rev. D*, *84*, 027302.

Galper, A. M., Adriani, O., Aptekar, R. L., Arkhangelskaja, I. V., Arkhangelskiy, A. I., Boezio, M. et al. (2013, Februar). Design and performance of the GAMMA-400 gamma-ray telescope for dark matter searches. In J. F. Ormes (Hrsg.), *American institute of physics conference series* (Bd. 1516, S. 288-292).

Gao, L., Frenk, C. S., Jenkins, A., Springel, V. & White, S. D. M. (2012, Januar). Where will supersymmetric dark matter first be seen? *MNRAS*, *419*, 1721-1726.

Garny, M., Ibarra, A. & Vogl, S. (2011, Juli). Antiproton constraints on dark matter annihilations from internal electroweak bremsstrahlung. *JCAP*, *7*, 28.

Garny, M., Ibarra, A. & Vogl, S. (2012, April). Dark matter annihilations into two light fermions and one gauge boson: general analysis and antiproton constraints. *JCAP*, *4*, 33.

Gates, E. I., Gyuk, G. & Turner, M. S. (1995, Mai). Microlensing and Halo Cold Dark Matter. *Physical Review Letters*, *74*, 3724-3727.

Geldzahler, B. J. & Fomalont, E. B. (1984, November). Radio observations of the jet in Fornax A. *Astron. J.*, *89*, 1650–1657.

Gentile, G., Salucci, P., Klein, U. & Granato, G. L. (2007, Februar). NGC 3741: the dark halo profile from the most extended rotation curve. *MNRAS*, *375*, 199-212.

Geringer-Sameth, A. & Koushiappas, S. M. (2011, Dezember). Exclusion of Canonical Weakly Interacting Massive Particles by Joint Analysis of Milky Way Dwarf Galaxies with Data from the Fermi Gamma-Ray Space Telescope. *Physical Review Letters*, *107* (24), 241303.

Geringer-Sameth, A. & Koushiappas, S. M. (2012, Juli). Dark matter line search using a joint analysis of dwarf galaxies with the Fermi Gamma-ray Space Telescope. *Phys. Rev. D*, *86* (2), 021302.

Ghirlanda, G., Ghisellini, G., Tavecchio, F. & Foschini, L. (2010, September). Correlation of Fermi Large Area Telescope sources with the 20-GHz Australia Telescope Compact Array radio survey. *MNRAS*, *407*, 791–803.

Ghirlanda, G., Ghisellini, G., Tavecchio, F., Foschini, L. & Bonnoli, G. (2011a, Mai). The radio-γ-ray connection in Fermi blazars. *MNRAS*, *413*, 852–862.

Ghirlanda, G., Ghisellini, G., Tavecchio, F., Foschini, L. & Bonnoli, G. (2011b, Mai). The radio-γ-ray connection in Fermi blazars. *MNRAS*, *413*, 852-862.

Ghisellini, G. & Maraschi, L. (1989, Mai). Bulk acceleration in relativistic jets and the spectral properties of blazars. *Astrophys. J.*, *340*, 181-189.

Ghisellini, G., Tavecchio, F. & Chiaberge, M. (2005, März). Structured jets in TeV BL Lac objects and radiogalaxies. Implications for the observed properties. *A&A*, *432*, 401–410.

Gilmore, R. C., Madau, P., Primack, J. R., Somerville, R. S. & Haardt, F. (2009, November). GeV gamma-ray attenuation and the high-redshift UV background. *MNRAS*, *399*, 1694–1708.

Giovannini, G., Cotton, W. D., Feretti, L., Lara, L. & Venturi, T. (2001, Mai). VLBI Observations of a Complete Sample of Radio Galaxies: 10 Years Later. *Astrophys. J.*, *552*, 508–526.

Giovannini, G., Feretti, L., Gregorini, L. & Parma, P. (1988, Juni). Radio nuclei in elliptical galaxies. *A&A*, *199*, 73–84.

Giunti, C., Kim, C. W. & Lee, U. W. (1991). Running Coupling Constants and Grand Unification Models. *Modern Physics Letters A*, *6*, 1745-1755.

Gleeson, L. J. & Axford, W. I. (1968, Dezember). Solar Modulation of Galactic Cosmic Rays. *Astrophys. J.*, *154*, 1011.

Gnedin, O. Y., Brown, W. R., Geller, M. J. & Kenyon, S. J. (2010, September). The Mass Profile of the Galaxy to 80 kpc. *Astrophys. J.*, *720*, L108–L112.

Gnedin, O. Y., Kravtsov, A. V., Klypin, A. A. & Nagai, D. (2004, November). Response of Dark Matter Halos to Condensation of Baryons: Cosmological Simulations and Improved Adiabatic Contraction Model. *Astrophys. J.*, *616*, 16-26.

Gnedin, O. Y. & Primack, J. R. (2004). Dark Matter Profile in the Galactic Center. *Phys.Rev.Lett.*, *93*, 061302.

Gnedin, O. Y., Weinberg, D. H., Pizagno, J., Prada, F. & Rix, H.-W. (2007, Dezember). Dark Matter Halos of Disk Galaxies: Constraints from the Tully-Fisher Relation. *Astrophys. J.*, *671*, 1115-1134.

Goldberg, H. (1983, Mai). Constraint on the photino mass from cosmology. *Physical Review Letters*, *50*, 1419-1422.

Golse, G., Kneib, J.-P. & Soucail, G. (2002, Juni). Constraining the cosmological parameters using strong lensing. *A&A*, *387*, 788-803.

Gondolo, P., Edsjö, J., Ullio, P., Bergström, L., Schelke, M. & Baltz, E. A. (2004, Juli). DarkSUSY: computing supersymmetric dark matter properties numerically. *JCAP*, *7*, 8.

Gondolo, P. & Gelmini, G. (1991, August). Cosmic abundances of stable particles: improved analysis. *Nuclear Physics B*, *360*, 145-179.

Gondolo, P. & Silk, J. (1999). Dark matter annihilation at the galactic center. *Phys.Rev.Lett.*, *83*, 1719-1722.

Goodman, M. W. & Witten, E. (1985, Juni). Detectability of certain dark-matter candidates. *Phys. Rev. D*, *31*, 3059-3063.

Górski, K. M., Hivon, E., Banday, A. J., Wandelt, B. D., Hansen, F. K., Reinecke, M. et al. (2005, April). HEALPix: A Framework for High-Resolution Discretization and Fast Analysis of Data Distributed on the Sphere. *Astrophys. J.*, *622*, 759-771.

Gould, R. J. & Schréder, G. (1966, Februar). Opacity of the Universe to High-Energy Photons. *Physical Review Letters*, *16*, 252-254.

Grandi, P. (2012). Gamma Rays from Radio Galaxies: FERMI/LAT Observations. *International Journal of Modern Physics Conference Series*, *8*, 25-30.

Grandi, P. & Torresi, E. (2012, Mai). Exploring the FRI/FRII radio dichotomy with the Fermi satellite. *arXiv:1205.1686*.

Grandi, P., Torresi, E. & Stanghellini, C. (2012, Mai). The γ-Ray Emission Region in the Fanaroff-Riley II Radio Galaxy 3C 111. *Astrophys. J. Lett.*, *751*, L3.

Grcevich, J. & Putman, M. E. (2009, Mai). H I in Local Group Dwarf Galaxies and Stripping by the Galactic Halo. *Astrophys. J.*, *696*, 385-395.

Green, A. M., Hofmann, S. & Schwarz, D. J. (2004). The power spectrum of SUSY - CDM on sub-galactic scales. *Mon.Not.Roy.Astron.Soc.*, *353*, L23.

Green, A. M., Hofmann, S. & Schwarz, D. J. (2005). The First wimpy halos. *JCAP*, *0508*, 003.

Grégoire, T. & Knödlseder, J. (2013, Mai). Constraining the Galactic millisecond pulsar population using Fermi Large Area Telescope. *arXiv:1305.1584*.

Gregory, P. C. & Condon, J. J. (1991, April). The 87GB catalog of radio sources covering delta between O and + 75 deg at 4.85 GHz. *Astrophys. J. Supplement*, *75*, 1011–1291.

Gregory, P. C., Vavasour, J. D., Scott, W. K. & Condon, J. J. (1994, Januar). The Parkes-MIT-NRAO (PMN) map catalog of radio sources covering -88 deg less than delta less than -37 deg at 4.85GHz. *Astrophys. J. Supplement*, *90*, 173–177.

Griffith, M., Heflin, M., Conner, S., Burke, B. & Langston, G. (1991, März). The fourth MIT-Green Bank 5 GHz survey. *Astrophys. J. Supplement*, *75*, 801–833.

Guedes, J., Callegari, S., Madau, P. & Mayer, L. (2011). Forming Realistic Late-Type Spirals in a LCDM Universe: The Eris Simulation. *Astrophys.J.*, *742*, 76.

Guillemot, L., Johnson, T. J., Venter, C., Kerr, M., Pancrazi, B., Livingstone, M. et al. (2012, Januar). Pulsed Gamma Rays from the Original Millisecond and Black Widow Pulsars: A Case for Caustic Radio Emission? *Astrophys. J.*, *744*, 33.

Gunion, J. F. & Haber, H. E. (1993, August). Higgs bosons in supersymmetric models (I) [Nucl. Phys. B272 (1986) 1]. *Nuclear Physics B*, *402*, 567-568.

Gustafsson, M., Fairbairn, M. & Sommer-Larsen, J. (2006). Baryonic Pinching of Galactic Dark Matter Haloes. *Phys.Rev.*, *D74*, 123522.

Gustafsson, M., Lundström, E., Bergström, L. & Edsjö, J. (2007, Juli). Significant Gamma Lines from Inert Higgs Dark Matter. *Physical Review Letters*, *99* (4), 041301.

Haber, H. E. & Kane, G. L. (1985). The search for supersymmetry: Probing physics beyond the standard model. *Phys.Rep.*, *117*, 75.

Hahn, T. (2001). Generating Feynman diagrams and amplitudes with FeynArts 3. *Comput.Phys.Commun.*, *140*, 418-431.

Hahn, T. (2008). FormCalc 6. *PoS*, *ACAT08*, 121.

Han, J., Frenk, C. S., Eke, V. R., Gao, L., White, S. D. M., Boyarsky, A. et al. (2012, Dezember). Constraining extended gamma-ray emission from galaxy clusters. *MNRAS*, *427*, 1651-1665.

Han, J. L. & Qiao, G. J. (1994, August). The magnetic field in the disk of our Galaxy. *A&A*, *288*, 759–772.

Harding, A. K. & Stecker, F. W. (1981, März). Pulsar and diffuse contributions to observed galactic gamma radiation. *Nature*, *290*, 316-318.

Harding, A. K., Usov, V. V. & Muslimov, A. G. (2005, März). High-Energy Emission from Millisecond Pulsars. *Astrophys. J.*, *622*, 531-543.

Harris, D. E., Cheung, C. C., Stawarz, Ł., Biretta, J. A. & Perlman, E. S. (2009, Juli). Variability Timescales in the M87 Jet: Signatures of E ^{2} Losses, Discovery of a Quasi Period in HST-1, and the Site of TeV Flaring. *Astrophys. J.*, *699*, 305–314.

Heinemeyer, S., Hollik, W. & Weiglein, G. (2000, Februar). FeynHiggsFast: a program for a fast calculation of masses and mixing angles in the Higgs Sector of the MSSM. *ArXiv High Energy Physics - Phenomenology e-prints*.

Heister, A. et al. (2002). Search for gauge mediated SUSY breaking topologies in e^+e^- collisions at center-of-mass energies up to 209-GeV. *Eur.Phys.J.*, *C25*, 339-351.

Hensley, B. S., Siegal-Gaskins, J. M. & Pavlidou, V. (2010, November). The Detectability of Dark Matter Annihilation with Fermi Using the Anisotropy Energy Spectrum of the Gamma-ray Background. *Astrophys. J.*, *723*, 277-284.

Henstock, D. R., Browne, I. W. A., Wilkinson, P. N., Taylor, G. B., Vermeulen, R. C., Pearson, T. J. et al. (1995, September). The Second Caltech–Jodrell Bank VLBI Survey. II. Observations of 102 of 193 Sources. *Astrophys. J. Supplement*, *100*, 1.

Hisano, J., Matsumoto, S., Nojiri, M. M. & Saito, O. (2005). Nonperturbative effect on dark matter annihilation and gamma ray signature from galactic center. *Phys.Rev.*, *D71*, 063528.

Hodges, H. M. (1993, Jan). Mirror baryons as the dark matter. *Phys. Rev. D*, *47*, 456–459.

Hoerandel, J. R. (2003). On the knee in the energy spectrum of cosmic rays. *Astropart.Phys.*, *19*, 193-220.

Hogbom, J. A. (1979, Mai). A study of the radio galaxies 3C111, 192, 219, 223, 315 and 452. *Astronomy and Astrophysics, Supplement*, *36*, 173–192.

Hooper, D., Blasi, P. & Dario Serpico, P. (2009, Januar). Pulsars as the sources of high energy cosmic ray positrons. *JCAP*, *1*, 25.

Hooper, D., Kelso, C. & Queiroz, F. S. (2012, September). Stringent and

Robust Constraints on the Dark Matter Annihilation Cross Section From the Region of the Galactic Center. *arXiv:1209.3015*.

Hooper, D. & Linden, T. (2011, Dezember). Origin of the gamma rays from the Galactic Center. *Phys. Rev. D*, *84* (12), 123005.

Horiuchi, S., Fomalont, E. B., Taylor, W. K., Scott, A. R., Lovell, J. E. J., Moellenbrock, G. A. et al. (2004, November). The VSOP 5 GHz Active Galactic Nucleus Survey. IV. The Angular Size/Brightness Temperature Distribution. *Astrophys. J.*, *616*, 110–122.

Hough, D. H. & Readhead, A. C. S. (1989, Oktober). A complete sample of double-lobed radio quasars for VLBI tests of source models - Definition and statistics. *Astron. J.*, *98*, 1208–1225.

Huang, X., Vertongen, G. & Weniger, C. (2012, Januar). Probing dark matter decay and annihilation with Fermi LAT observations of nearby galaxy clusters. *JCAP*, *1*, 42.

Huang, X., Yuan, Q., Yin, P.-F., Bi, X.-J. & Chen, X. (2012, November). Constraints on the dark matter annihilation scenario of Fermi 130 GeV gamma-ray line emission by continuous gamma-rays, Milky Way halo, galaxy clusters and dwarf galaxies observations. *JCAP*, *11*, 48.

Ibarra, A. & Wild, S. (2013, Februar). Prospects of antideuteron detection from dark matter annihilations or decays at AMS-02 and GAPS. *JCAP*, *2*, 21.

Inoue, Y. (2011, Mai). Contribution of Gamma-Ray-loud Radio Galaxies' Core Emissions to the Cosmic MeV and GeV Gamma-Ray Background Radiation. *Astrophys. J.*, *733*, 66.

Inoue, Y. & Ioka, K. (2012, Juli). Upper limit on the cosmological gamma-ray background. *Phys. Rev. D*, *86* (2), 023003.

Inoue, Y. & Totani, T. (2009, September). The Blazar Sequence and the Cosmic Gamma-ray Background Radiation in the Fermi Era. *Astrophys. J.*, *702*, 523–536.

Irrgang, A., Wilcox, B., Tucker, E. & Schiefelbein, L. (2013, Januar). Milky Way mass models for orbit calculations. *A&A*, *549*, A137.

Israel, F. P., Raban, D., Booth, R. S. & Rantakyrö, F. T. (2008, Juni). The millimeter-wave continuum spectrum of Centaurus A and its nucleus. *A&A*, *483*, 741–748.

Jacob, M. & Wick, G. (1959). On the general theory of collisions for particles with spin. *Annals Phys.*, *7*, 404-428.

James, F. & Roos, M. (1975, Dezember). Minuit - a system for function minimization and analysis of the parameter errors and correlations. *Computer Physics Communications*, *10*, 343-367.

Jelley, J. V. (1966, März). High-Energy γ-Ray Absorption in Space by a 3.5degK Microwave Field. *Physical Review Letters*, *16*, 479-481.

Jeltema, T. E., Kehayias, J. & Profumo, S. (2009). Gamma Rays from Clusters and Groups of Galaxies: Cosmic Rays versus Dark Matter. *Phys.Rev.*, *D80*, 023005.

Jin, H.-B., Wu, Y.-L. & Zhou, Y.-F. (2013). Implications of the first AMS-02 measurement for dark matter annihilation and decay.

Jones, D. L., Unwin, S. C., Readhead, A. C. S., Sargent, W. L. W., Seielstad, G. A., Simon, R. S. et al. (1986, Juni). High dynamic range VLBI observations of NGC 6251. *Astrophys. J.*, *305*, 684–697.

Jones, P. A., Lloyd, B. D. & McAdam, W. B. (2001, August). The radio galaxy Centaurus B. *MNRAS*, *325*, 817–825.

Jones, T. W., O'dell, S. L. & Stein, W. A. (1974, März). Physics of Compact Nonthermal Sources. I. Theory of Radiation Processes. *Astrophys. J.*, *188*, 353-368.

Jungman, G., Kamionkowski, M. & Griest, K. (1996, März). Supersymmetric dark matter. *Physics Reports*, *267*, 195-373.

Junkes, N., Haynes, R. F., Harnett, J. I. & Jauncey, D. L. (1993, März). Radio polarization surveys of Centaurus A (NGC 5128). I - The complete radio source at 6.3 CM. *A&A*, *269*, 29–38.

Kachelrieß, M. & Serpico, P. D. (2007, September). Model-independent dark matter annihilation bound from the diffuse gamma ray flux. *Phys. Rev. D*, *76* (6), 063516.

Kachelrieß, M., Serpico, P. D. & Solberg, M. A. (2009, Dezember). Role of electroweak bremsstrahlung for indirect dark matter signatures. *Phys. Rev. D*, *80* (12), 123533.

Kadler, M., Eisenacher, D., Ros, E., Mannheim, K., Elsässer, D. & Bach, U. (2012, Februar). The blazar-like radio structure of the TeV source IC 310. *A&A*, *538*, L1.

Kafle, P. R., Sharma, S., Lewis, G. F. & Bland-Hawthorn, J. (2012, Dezember). Kinematics of the Stellar Halo and the Mass Distribution of the Milky Way Using Blue Horizontal Branch Stars. *Astrophys. J.*, *761*, 98.

Kalashev, O. E., Semikoz, D. V. & Sigl, G. (2009, März). Ultrahigh energy cosmic rays and the GeV-TeV diffuse gamma-ray flux. *Phys. Rev. D*, *79* (6), 063005.

Kaluza, T. (1921). On the Problem of Unity in Physics. *Sitzungsber.Preuss.Akad.Wiss.Berlin (Math.Phys.)*, *1921*, 966-972.

Kamionkowski, M. & Turner, M. S. (1991, März). Distinctive positron feature from particle dark-matter annihilations in the galactic halo. *Phys. Rev. D*, *43*, 1774-1780.

Kataoka, J. et al. (2010, Mai). γ-ray Spectral Evolution of NGC 1275 Observed with Fermi Large Area Telescope. *Astrophys. J.*, *715*, 554–560.

Kataoka, J. et al. (2011, Oktober). Broad-line Radio Galaxies Observed with Fermi-LAT: The Origin of the GeV γ-Ray Emission. *Astrophys. J.*, *740*, 29.

Katsuta, J., Tanaka, Y. T., Stawarz, Ł., O'Sullivan, S. P., Cheung, C. C., Kataoka, J. et al. (2013, Februar). Fermi-LAT and Suzaku observations of the radio galaxy Centaurus B. *A&A*, *550*, A66.

Kazanas, D. & Perlman, E. (1997, Februar). Low-State Gamma-Ray Emission from Blazars and the Gamma-Ray Background. *Astrophys. J.*, *476*, 7.

Kellermann, K. I., Pauliny-Toth, I. I. K. & Williams, P. J. S. (1969, Juli). The Spectra of Radio Sources in the Revised 3c Catalogue. *Astrophys. J.*, *157*, 1.

Keshet, U., Waxman, E. & Loeb, A. (2004, April). The case for a low extragalactic gamma-ray background. *JCAP*, *4*, 6.

Keshet, U., Waxman, E., Loeb, A., Springel, V. & Hernquist, L. (2003, März). Gamma Rays from Intergalactic Shocks. *Astrophys. J.*, *585*, 128-150.

Klein, O. (1926). Quantum Theory and Five-Dimensional Theory of Relativity. (In German and English). *Z.Phys.*, *37*, 895-906.

Kochanek, C. S. (1996, Januar). The Mass of the Milky Way. *Astrophys. J.*, *457*, 228.

Kolb, E. W. & Turner, M. S. (1990). *The early universe.* Redwood City: Addison-Wesley.

Komatsu, E., Smith, K. M., Dunkley, J., Bennett, C. L., Gold, B., Hinshaw, G. et al. (2011, Februar). Seven-year Wilkinson Microwave Anisotropy Probe (WMAP) Observations: Cosmological Interpretation. *Astrophys. J. Supplement*, *192*, 18.

Kosack, K., Badran, H. M., Bond, I. H., Boyle, P. J., Bradbury, S. M., Buckley, J. H. et al. (2004, Juni). TeV Gamma-Ray Observations of the Galactic Center. *Astrophys. J. Lett.*, *608*, L97-L100.

Kuehr, H., Witzel, A., Pauliny-Toth, I. I. K. & Nauber, U. (1981, September). A catalogue of extragalactic radio sources having flux densities greater than 1 Jy at 5 GHz. *Astronomy and Astrophysics, Supplement*, *45*, 367–430.

Kuhlen, M., Diemand, J. & Madau, P. (2008). The Dark Matter Annihilation Signal from Galactic Substructure: Predictions for GLAST. *Astrophys.J.*, *686*, 262.

Kuhlen, M., Guedes, J., Pillepich, A., Madau, P. & Mayer, L. (2013). An Off-center Density Peak in the Milky Way's Dark Matter Halo? *Astrophys.J.*, *765*, 10.

Kuhlen, M., Vogelsberger, M. & Angulo, R. (2012). Numerical Simulations of the Dark Universe: State of the Art and the Next Decade. *Phys.Dark Univ.*, *1*, 50-93.

Kusenko, A. & Voloshin, M. B. (2012, Januar). A gamma-ray signature of energetic sources of cosmic-ray nuclei. *Physics Letters B*, *707*, 255-258.

Laing, R. A. & Peacock, J. A. (1980, März). The relation between radio luminosity and spectrum for extended extragalactic radio sources. *MNRAS*, *190*, 903–924.

Laing, R. A., Riley, J. M. & Longair, M. S. (1983, Juli). Bright radio sources at 178 MHz - Flux densities, optical identifications and the cosmological evolution of powerful radio galaxies. *MNRAS*, *204*, 151–187.

Lara, L., Giovannini, G., Cotton, W. D., Feretti, L., Marcaide, J. M., Márquez, I. et al. (2004, Juli). A new sample of large angular size radio galaxies. III. Statistics and evolution of the grown population. *A&A*, *421*, 899–911.

Lavalle, J., Manseri, H., Jacholkowska, A., Brion, E., Britto, R., Bruel, P. et al. (2006, April). Indirect search for dark matter in M 31 with the CELESTE experiment. *A&A*, *450*, 1-8.

Ledlow, M. J. & Owen, F. N. (1996, Juli). 20 CM VLA Survey of Abell Clusters of Galaxies. VI. Radio/Optical Luminosity Functions. *Astron. J.*, *112*, 9.

Lee, S. K., Ando, S. & Kamionkowski, M. (2009, Juli). The gamma-ray-flux PDF from galactic halo substructure. *JCAP*, *7*, 7.

Lehmann, E. L. & D'Abrera, H. J. M. (2008). *Nonparametrics: Statistical Methods Based on Ranks.* Englewood Cliffs.

Linfield, R. & Perley, R. (1984, April). 3C 111 - A luminous radio galaxy with a highly collimated jet. *Astrophys. J.*, *279*, 60–73.

Linford, J. D., Taylor, G. B., Romani, R. W., Helmboldt, J. F., Readhead, A. C. S., Reeves, R. et al. (2012, Januar). Contemporaneous VLBA 5 GHz Observations of Large Area Telescope Detected Blazars. *Astrophys. J.*, *744*, 177.

Longair, M. S. (1998). *Galaxy formation.* Springer.

Lucchin, F. & Coles, P. (1992). *Cosmology: The origin and evolution of cosmic structure* (2nd Aufl.). Chichester, UK: John Wiley and Sons.

Macciò, A. V., Stinson, G., Brook, C. B., Wadsley, J., Couchman, H. M. P., Shen, S. et al. (2012, Januar). Halo Expansion in Cosmological Hydro Simulations: Toward a Baryonic Solution of the Cusp/Core Problem in Massive Spirals. *Astrophys. J. Lett.*, *744*, L9.

Maccione, L. (2013, Februar). Low Energy Cosmic Ray Positron Fraction Explained by Charge-Sign Dependent Solar Modulation. *Physical Review Letters*, *110* (8), 081101.

Makiya, R., Totani, T. & Kobayashi, M. A. R. (2011, Februar). Contribution from Star-forming Galaxies to the Cosmic Gamma-ray Background Radiation. *Astrophys. J.*, *728*, 158.

Mambrini, Y. (2009). A Clear Dark Matter gamma ray line generated by the Green-Schwarz mechanism. *JCAP*, *0912*, 005.

Mantovani, F., Mack, K.-H., Montenegro-Montes, F. M., Rossetti, A. & Kraus, A. (2009, Juli). Effelsberg 100-m polarimetric observations of a sample of compact steep-spectrum sources. *A&A*, *502*, 61–65.

Maraschi, L., Ghisellini, G. & Celotti, A. (1992, September). A jet model for the gamma-ray emitting blazar 3C 279. *Astrophys. J. Lett.*, *397*, L5–L9.

Marshall, H. L., Schwartz, D. A., Lovell, J. E. J., Murphy, D. W., Worrall, D. M., Birkinshaw, M. et al. (2005, Januar). A Chandra Survey of Quasar Jets: First Results. *Astrophys. J. Supplement*, *156*, 13–33.

Martizzi, D., Teyssier, R. & Moore, B. (2013, Mai). Cusp-core transformations induced by AGN feedback in the progenitors of cluster galaxies. *MNRAS*.

Mashchenko, S., Couchman, H. M. P. & Wadsley, J. (2006, August). The removal of cusps from galaxy centres by stellar feedback in the early Universe. *Nature*, *442*, 539-542.

Mashchenko, S., Wadsley, J. & Couchman, H. M. P. (2008, Januar). Stellar Feedback in Dwarf Galaxy Formation. *Science*, *319*, 174-.

Massardi, M., Ekers, R. D., Murphy, T., Ricci, R., Sadler, E. M., Burke, S. et al. (2008, Februar). The Australia Telescope 20-GHz (AT20G) Survey: the Bright Source Sample. *MNRAS*, *384*, 775–802.

Massaro, F. & Ajello, M. (2011, März). Fueling Lobes of Radio Galaxies: Statistical Particle Acceleration and the Extragalactic γ-ray Background. *Astrophys. J. Lett.*, *729*, L12.

Mateo, M. L. (1998). Dwarf Galaxies of the Local Group. *Annual Review of Astron. and Astrophys.*, *36*, 435-506.

Maurin, D., Donato, F., Taillet, R. & Salati, P. (2001, Juli). Cosmic Rays below Z=30 in a Diffusion Model: New Constraints on Propagation Parameters. *Astrophys. J.*, *555*, 585-596.

Mazin, D. & Raue, M. (2007, August). New limits on the density of the extragalactic background light in the optical to the far infrared from the spectra of all known TeV blazars. *A&A*, *471*, 439–452.

Mazziotta, M. N., Loparco, F., de Palma, F. & Giglietto, N. (2012, September). A model-independent analysis of the Fermi Large Area Telescope gamma-ray data from the Milky Way dwarf galaxies and halo to constrain dark matter scenarios. *Astroparticle Physics*, *37*, 26-39.

Milgrom, M. (1983, Juli). A modification of the Newtonian dynamics as a possible alternative to the hidden mass hypothesis. *Astrophys. J.*, *270*, 365-370.

Miniati, F., Koushiappas, S. M. & Di Matteo, T. (2007, September). Angular Anisotropies in the Cosmic Gamma-Ray Background as a Probe of Its Origin. *Astrophys. J. Lett.*, *667*, L1-L4.

Morganti, R., Killeen, N. E. B. & Tadhunter, C. N. (1993, August). The Radio Structures of Southern 2-JY Radio Sources. *MNRAS*, *263*, 1023.

Moskalenko, I. V. & Porter, T. A. (2009, Februar). Isotropic Gamma-Ray Background: Cosmic-Ray-Induced Albedo from Debris in the Solar System? *Astrophys. J. Lett.*, *692*, L54-L57.

Moskalenko, I. V., Porter, T. A. & Digel, S. W. (2006, November). Inverse Compton Scattering on Solar Photons, Heliospheric Modulation, and Neutrino Astrophysics. *Astrophys. J. Lett.*, *652*, L65-L68.

Moskalenko, I. V. & Strong, A. W. (1998, Januar). Production and Propagation of Cosmic-Ray Positrons and Electrons. *Astrophys. J.*, *493*, 694.

Mullin, L. M., Hardcastle, M. J. & Riley, J. M. (2006, Oktober). High-resolution observations of radio sources with 0.6 ¡ z ¡ 1.0. *MNRAS*, *372*, 113–135.

Nagar, N. M., Wilson, A. S. & Falcke, H. (2001, Oktober). Evidence for Jet Domination of the Nuclear Radio Emission in Low-Luminosity Active Galactic Nuclei. *Astrophys. J. Lett.*, *559*, L87–L90.

Narumoto, T. & Totani, T. (2006, Mai). Gamma-Ray Luminosity Function of Blazars and the Cosmic Gamma-Ray Background: Evidence for the Luminosity-Dependent Density Evolution. *Astrophys. J.*, *643*, 81–91.

Nath, P. & Arnowitt, R. (1993, Juni). Predictions in SU(5) supergravity grand unification with proton stability and relic density constraints. *Physical Review Letters*, *70*, 3696-3699.

Navarro, J. F., Eke, V. R. & Frenk, C. S. (1996, Dezember). The cores of dwarf galaxy haloes. *MNRAS*, *283*, L72-L78.

Navarro, J. F., Frenk, C. S. & White, S. D. M. (1996, Mai). The Structure of Cold Dark Matter Halos. *Astrophys. J.*, *462*, 563.

Navarro, J. F., Hayashi, E., Power, C., Jenkins, A. R., Frenk, C. S., White, S. D. M. et al. (2004, April). The inner structure of ΛCDM haloes - III. Universality and asymptotic slopes. *MNRAS*, *349*, 1039-1051.

Neff, S. G., Roberts, L. & Hutchings, J. B. (1995, August). VLA Maps of Radio Galaxies to Z = 1. *Astrophys. J. Supplement*, *99*, 349.

Nolan, P. L., Abdo, A. A., Ackermann, M., Ajello, M., Allafort, A., Antolini, E. et al. (2012, April). Fermi Large Area Telescope Second Source Catalog. *Astrophys. J. S.S.*, *199*, 31.

Nolan, P. L. et al. (2012, Juni). Fermi LAT second source catalog (2FGL) (Nolan+, 2012). *VizieR Online Data Catalog*, *219*, 90031.

Nomura, Y. & Thaler, J. (2009, April). Dark matter through the axion portal. *Phys. Rev. D*, *79* (7), 075008.

Noordam, J. E. & de Bruyn, A. G. (1982, Oktober). High dynamic range mapping of strong radio sources, with application to 3C84. *Nat*, *299*, 597.

Ogiya, G. & Mori, M. (2011, Juli). The Core-Cusp Problem in Cold Dark Matter Halos and Supernova Feedback: Effects of Mass Loss. *Astrophys. J. Lett.*, *736*, L2.

Oh, S.-H., de Blok, W. J. G., Brinks, E., Walter, F. & Kennicutt, R. C., Jr. (2011, Juni). Dark and Luminous Matter in THINGS Dwarf Galaxies. *Astron. J.*, *141*, 193.

Padovani, P. (1992, März). A statistical analysis of complete samples of BL Lacertae objects. *A&A*, *256*, 399-407.

Padovani, P., Ghisellini, G., Fabian, A. C. & Celotti, A. (1993, Februar). Radio-loud AGN and the extragalactic gamma-ray background. *MNRAS*, *260*, L21-L24.

Pagels, H. & Primack, J. R. (1982, Jan). Supersymmetry, cosmology, and new physics at teraelectronvolt energies. *Phys. Rev. Lett.*, *48*, 223–226. Verfügbar unter `http://link.aps.org/doi/10.1103/PhysRevLett.48.223`

Pauliny-Toth, I. I. K., Kellermann, K. I., Davis, M. M., Fomalont, E. B. & Shaffer, D. B. (1972, Mai). The NRAO 5-GHz radio source survey. II. The 140-ft "strong", "intermediate", and "deep" source surveys. *Astron. J.*, *77*, 265–284.

Pavlidou, V. & Fields, B. D. (2002, August). The Guaranteed Gamma-Ray Background. *Astrophys. J. Lett.*, *575*, L5-L8.

Pearson, T. J., Blundell, K. M., Riley, J. M. & Warner, P. J. (1992, November). A jet in the nucleus of the giant quasar 4C 74.26. *MNRAS*, *259*, 13P–16P.

Peccei, R. D. & Quinn, H. R. (1977, Juni). CP conservation in the presence of pseudoparticles. *Physical Review Letters*, *38*, 1440-1443.

Peebles, P. J. E. (1982, Dezember). Large-scale background temperature and mass fluctuations due to scale-invariant primeval perturbations. *Astrophys. J. Lett.*, *263*, L1-L5.

Perley, R. A., Dreher, J. W. & Cowan, J. J. (1984, Oktober). The jet and filaments in Cygnus A. *Astrophys. J. Lett.*, *285*, L35–L38.

Perley, R. A., Roser, H.-J. & Meisenheimer, K. (1997, Dezember). The radio galaxy PictorA – a study with the VLA. *A&A*, *328*, 12–32.

Perlmutter, S., Aldering, G., Goldhaber, G., Knop, R. A., Nugent, P., Castro, P. G. et al. (1999, Juni). Measurements of Omega and Lambda from 42 High-Redshift Supernovae. *Astrophys. J.*, *517*, 565-586.

Peskin, M. E. (2008). Supersymmetry in Elementary Particle Physics. In S. Dawson & R. N. Mohapatra (Hrsg.), *Colliders and neutrinos: the window into physics beyond the standard model* (S. 609). World Scientific.

Pieri, L., Lavalle, J., Bertone, G. & Branchini, E. (2011). Implications of High-Resolution Simulations on Indirect Dark Matter Searches. *Phys.Rev.*, *D83*, 023518.

Pinzke, A., Pfrommer, C. & Bergström, L. (2011, Dezember). Prospects of detecting gamma-ray emission from galaxy clusters: Cosmic rays and dark matter annihilations. *Phys. Rev. D*, *84* (12), 123509.

Pontzen, A. & Governato, F. (2012, April). How supernova feedback turns dark matter cusps into cores. *MNRAS*, *421*, 3464-3471.

Preskill, J., Wise, M. B. & Wilczek, F. (1983, Januar). Cosmology of the invisible axion. *Physics Letters B*, *120*, 127-132.

Press, W. H., Teukolsky, S. A., Vetterling, W. T. & Flannery, B. P. (1992). *Numerical recipes in FORTRAN. The art of scientific computing.*

Prieto, M. A., Reunanen, J., Beckert, T., Tristram, K., Neumayer, N., Fernandez, J. A. et al. (2007, Oktober). The Spectral Energy Distribution of the Central Parsecs Region of Galaxies. In L. C. Ho & J.-W. Wang (Hrsg.), *The central engine of active galactic nuclei* (Bd. 373, S. 600).

Profumo, S. (2012, Februar). Dissecting cosmic-ray electron-positron data with Occam's razor: the role of known pulsars. *Central European Journal of Physics*, *10*, 1-31.

Prouza, M. & Šmída, R. (2003, Oktober). The Galactic magnetic field and propagation of ultra-high energy cosmic rays. *A&A*, *410*, 1–10.

Pshirkov, M. S., Tinyakov, P. G., Kronberg, P. P. & Newton-McGee, K. J. (2011, September). Deriving the Global Structure of the Galactic Magnetic Field from Faraday Rotation Measures of Extragalactic Sources. *Astrophys. J.*, *738*, 192.

Razzaque, S., Dermer, C. D. & Finke, J. D. (2009, Mai). The Stellar Contribution to the Extragalactic Background Light and Absorption of High-Energy Gamma Rays. *Astrophys. J.*, *697*, 483–492.

Read, J. I., Lake, G., Agertz, O. & Debattista, V. P. (2008, September). Thin, thick and dark discs in ΛCDM. *Mon. Not. R. Astron. Soc.*, *389*, 1041-1057.

Regis, M. & Ullio, P. (2008). Multi-wavelength signals of dark matter annihilations at the Galactic center. *Phys.Rev.*, *D78*, 043505.

Reid, B. A., Percival, W. J., Eisenstein, D. J., Verde, L., Spergel, D. N. et al. (2010). Cosmological Constraints from the Clustering of the Sloan Digital Sky Survey DR7 Luminous Red Galaxies. *Mon.Not.Roy.Astron.Soc.*, *404*, 60-85.

Riess, A. G., Filippenko, A. V., Challis, P., Clocchiatti, A., Diercks, A., Garnavich, P. M. et al. (1998, September). Observational Evidence from Supernovae for an Accelerating Universe and a Cosmological Constant. *Astron. J.*, *116*, 1009-1038.

Ripken, J., Cuoco, A., Zechlin, H.-S., Conrad, J. & Horns, D. (2012, November). The sensitivity of Cherenkov telescopes to dark matter and astrophysically induced anisotropies in the diffuse gamma-ray background. *arXiv:1211.6922*.

Ritz, S. & Seckel, D. (1988). Detailed neutrino spectra from cold dark-matter annihilations in the sun. *Nuclear Physics B*, *304*, 877-908.

Rodighiero, G., Vaccari, M., Franceschini, A., Tresse, L., Le Fevre, O., Le Brun, V. et al. (2010, Juni). Mid- and far-infrared luminosity functions and galaxy evolution from multiwavelength Spitzer observations up to z ˜ 2.5. *A&A*, *515*, A8.

Rolke, W. A., López, A. M. & Conrad, J. (2005, Oktober). Limits and confidence intervals in the presence of nuisance parameters. *Nuclear Instruments and Methods in Physics Research A*, *551*, 493-503.

Rubin, V. C., Ford, W. K. J. & Thonnard, N. (1980, Juni). Rotational properties of 21 SC galaxies with a large range of luminosities and radii, from NGC 4605 /R = 4kpc/ to UGC 2885 /R = 122 kpc/. *Astrophys. J.*, *238*, 471-487.

Saikia, D. J., Subrahmanya, C. R., Patnaik, A. R., Unger, S. W., Cornwell, T. J., Graham, D. A. et al. (1986, April). Radio observations of the S0 galaxy NGC 1218 (3C 78). *MNRAS*, *219*, 545–553.

Sakamoto, T., Chiba, M. & Beers, T. C. (2003, Januar). The mass of the Milky Way: Limits from a newly assembled set of halo objects. *A&A*, *397*, 899–911.

Salamon, M. H. & Stecker, F. W. (1994, Juli). The blazar gamma-ray luminosity function and the diffuse extragalactic gamma-ray background. *Astrophys. J. Lett.*, *430*, L21–L24.

Salamon, M. H. & Stecker, F. W. (1998, Januar). Absorption of High-Energy Gamma Rays by Interactions with Extragalactic Starlight Photons at High Redshifts and the High-Energy Gamma-Ray Background. *Astrophys. J.*, *493*, 547.

Salucci, P. & Borriello, A. (2003). The Intriguing Distribution of Dark Matter in Galaxies. In J. Trampeti & J. Wess (Hrsg.), *Particle physics in the new millennium* (Bd. 616, S. 66-77).

Salucci, P. & Burkert, A. (2000, Juli). Dark Matter Scaling Relations. *Astrophys. J. Lett.*, *537*, L9-L12.

Salucci, P., Nesti, F., Gentile, G. & Frigerio Martins, C. (2010, November). The dark matter density at the Sun's location. *A&A*, *523*, A83.

Schwetz, T. & Zupan, J. (2011, August). Dark matter attempts for CoGeNT and DAMA. *JCAP*, *8*, 8.

Scopel, S., Fornengo, N. & Bottino, A. (2013, Juli). Embedding the 125 GeV Higgs boson measured at the LHC in an effective MSSM: Possible implications for neutralino dark matter. *Phys. Rev. D*, *88* (2), 023506.

Serpico, P. D. & Bertone, G. (2010, September). Astrophysical limitations to the identification of dark matter: Indirect neutrino signals vis-à-vis direct detection recoil rates. *Phys. Rev. D*, *82* (6), 063505.

Serpico, P. D., Sefusatti, E., Gustafsson, M. & Zaharijas, G. (2012, März). Extragalactic gamma-ray signal from dark matter annihilation: a power spectrum based computation. *MNRAS*, *421*, L87-L91.

Serpico, P. D. & Zaharijas, G. (2008). Optimal angular window for observing Dark Matter annihilation from the Galactic Center region: the case of γ^- ray lines. *Astropart.Phys.*, *29*, 380-385.

Servant, G. & Tait, T. M. P. (2003, Februar). Is the lightest Kaluza-Klein particle a viable dark matter candidate? *Nuclear Physics B*, *650*, 391-419.

Shen, C. S. (1970, Dezember). Pulsars and Very High-Energy Cosmic-Ray Electrons. *Astrophys. J. Lett.*, *162*, L181.

Siegal-Gaskins, J. M. (2008, Oktober). Revealing dark matter substructure with anisotropies in the diffuse gamma-ray background. *JCAP*, *10*, 40.

Siegal-Gaskins, J. M., Reesman, R., Pavlidou, V., Profumo, S. & Walker, T. P. (2011, August). Anisotropies in the gamma-ray sky from millisecond pulsars. *MNRAS*, *415*, 1074-1082.

Siegal-Gaskins, J. M., Reesman, R., Pavlidou, V., Profumo, S. & Walker, T. P. (2011). Anisotropies in the gamma-ray sky from millisecond pulsars. *Mon.Not.Roy.Astron.Soc.*, *415*, 1074S.

Sikora, M., Begelman, M. C. & Rees, M. J. (1994, Januar). Comptonization of diffuse ambient radiation by a relativistic jet: The source of gamma rays from blazars? *Astrophys. J.*, *421*, 153-162.

Silk, J. (1968, Februar). Cosmic Black-Body Radiation and Galaxy Formation. *Astrophys. J.*, *151*, 459.

Simon, J. D., Bolatto, A. D., Leroy, A., Blitz, L. & Gates, E. L. (2005, März). High-Resolution Measurements of the Halos of Four Dark Matter-Dominated Galaxies: Deviations from a Universal Density Profile. *Astrophys. J.*, *621*, 757-776.

Sjöstrand, T., Mrenna, S. & Skands, P. (2006, Mai). PYTHIA 6.4 physics and manual. *Journal of High Energy Physics*, *5*, 26.

Sjostrand, T., Mrenna, S. & Skands, P. Z. (2008). A Brief Introduction to PYTHIA 8.1. *Comput.Phys.Commun.*, *178*, 852–867.

Sokolov, A. & Marscher, A. P. (2005, August). External Compton Radiation from Rapid Nonthermal Flares in Blazars. *Astrophys. J.*, *629*, 52–60.

Spekkens, K., Giovanelli, R. & Haynes, M. P. (2005, Mai). The Cusp/Core Problem in Galactic Halos: Long-Slit Spectra for a Large Dwarf Galaxy Sample. *Astron. J.*, *129*, 2119-2137.

Spinrad, H., Marr, J., Aguilar, L. & Djorgovski, S. (1985, Oktober). A third update of the status of the 3CR sources - Further new redshifts and new identifications of distant galaxies. *PASP*, *97*, 932–961.

Springel, V., Wang, J., Vogelsberger, M., Ludlow, A., Jenkins, A., Helmi, A. et al. (2008, Dezember). The Aquarius Project: the subhaloes of galactic haloes. *MNRAS*, *391*, 1685-1711.

Sreekumar, P., Bertsch, D. L., Dingus, B. L., Esposito, J. A., Fichtel, C. E., Hartman, R. C. et al. (1998, Februar). EGRET Observations of the Extragalactic Gamma-Ray Emission. *Astrophys. J.*, *494*, 523.

Stadel, J., Potter, D., Moore, B., Diemand, J., Madau, P., Zemp, M. et al. (2009, September). Quantifying the heart of darkness with GHALO - a multibillion particle simulation of a galactic halo. *MNRAS*, *398*, L21-L25.

Stawarz, Ł., Kneiske, T. M. & Kataoka, J. (2006, Februar). Kiloparsec-Scale Jets in FR I Radio Galaxies and the γ-Ray Background. *Astrophys. J.*, *637*, 693–698.

Stecker, F. W., de Jager, O. C. & Salamon, M. H. (1992, Mai). TeV gamma rays from 3C 279 - A possible probe of origin and intergalactic infrared radiation fields. *Astrophys. J. Lett.*, *390*, L49-L52.

Stecker, F. W., Malkan, M. A. & Scully, S. T. (2006, September). Intergalactic Photon Spectra from the Far-IR to the UV Lyman Limit for 0 ¡ z ¡ 6 and the Optical Depth of the Universe to High-Energy Gamma Rays. *Astrophys. J.*, *648*, 774–783.

Stecker, F. W. & Salamon, M. H. (1996, Juni). The Gamma-Ray Background from Blazars: A New Look. *Astrophys. J.*, *464*, 600.

Stecker, F. W., Salamon, M. H. & Malkan, M. A. (1993, Juni). The high-energy diffuse cosmic gamma-ray background radiation from blazars. *Astrophys. J. Lett.*, *410*, L71–L74.

Stecker, F. W. & Venters, T. M. (2011, Juli). Components of the Extragalactic Gamma-ray Background. *Astrophys. J.*, *736*, 40.

Stinson, G., Brook, C., Maccio, A., Wadsley, J., Quinn, T. et al. (2012). Making Galaxies in a Cosmological Context: The Need for Early Stellar Feedback.

Stinson, G. S., Bailin, J., Couchman, H., Wadsley, J., Shen, S., Nickerson, S. et al. (2010, Oktober). Cosmological galaxy formation simulations using smoothed particle hydrodynamics. *MNRAS*, *408*, 812-826.

Strigari, L. E., Koushiappas, S. M., Bullock, J. S., Kaplinghat, M., Simon, J. D., Geha, M. et al. (2008, Mai). The Most Dark-Matter-dominated Galaxies: Predicted Gamma-Ray Signals from the Faintest Milky Way Dwarfs. *Astrophys. J.*, *678*, 614-620.

Sun, X. H., Reich, W., Waelkens, A. & Enßlin, T. A. (2008, Januar). Radio observational constraints on Galactic 3D-emission models. *A&A*, *477*, 573–592.

Susskind, L. (1979, Nov). Dynamics of spontaneous symmetry breaking in the weinberg-salam theory. *Phys. Rev. D*, *20*, 2619–2625. Verfügbar unter `http://link.aps.org/doi/10.1103/PhysRevD.20.2619`

Taylor, G. B., Gugliucci, N. E., Fabian, A. C., Sanders, J. S., Gentile, G. & Allen, S. W. (2006, Juni). Magnetic fields in the centre of the Perseus cluster. *MNRAS*, *368*, 1500–1506.

Tempel, E., Hektor, A. & Raidal, M. (2012). Fermi 130 GeV gamma-ray excess and dark matter annihilation in sub-haloes and in the Galactic centre. *JCAP*, *1209*, 032.

Thompson, T. A., Quataert, E. & Waxman, E. (2007, Januar). The Starburst Contribution to the Extragalactic γ-Ray Background. *Astrophys. J.*, *654*, 219-225.

Tingay, S. J., Jauncey, D. L., King, E. A., Tzioumis, A. K., Lovell, J. E. J. & Edwards, P. G. (2003, April). ATCA Monitoring Observations of 202 Compact Radio Sources in Support of the VSOP AGN Survey. *pasj*, *55*, 351–384.

Tingay, S. J., Reynolds, J. E., Tzioumis, A. K., Jauncey, D. L., Lovell, J. E. J., Dodson, R. et al. (2002, August). VSOP Space VLBI and

Geodetic VLBI Investigations of Southern Hemisphere Radio Sources. *Astrophys. J. Supplement*, *141*, 311–335.

Tsuchiya, K., Enomoto, R., Ksenofontov, L. T., Mori, M., Naito, T., Asahara, A. et al. (2004, Mai). Detection of Sub-TeV Gamma Rays from the Galactic Center Direction by CANGAROO-II. *Astrophys. J. Lett.*, *606*, L115-L118.

Tyson, J. A., Kochanski, G. P. & dell'Antonio, I. P. (1998, Mai). Detailed Mass Map of CL 0024+1654 from Strong Lensing. *Astrophys. J. Lett.*, *498*, L107.

Ullio, P., Bergström, L., Edsjö, J. & Lacey, C. (2002, Dezember). Cosmological dark matter annihilations into γ rays: A closer look. *Phys. Rev. D*, *66* (12), 123502.

Ullio, P., Zhao, H. & Kamionkowski, M. (2001, August). Dark-matter spike at the galactic center? *Phys. Rev. D*, *64* (4), 043504.

Unger, S. W., Booler, R. V. & Pedlar, A. (1984, April). A kiloparsec radio jet in the nucleus of the S0 galaxy NGC 1218 (3C78). *MNRAS*, *207*, 679–684.

Urry, C. M. & Padovani, P. (1995, September). Unified Schemes for Radio-Loud Active Galactic Nuclei. *PASP*, *107*, 803.

Valenzuela, O., Rhee, G., Klypin, A., Governato, F., Stinson, G., Quinn, T. et al. (2007, März). Is There Evidence for Flat Cores in the Halos of Dwarf Galaxies? The Case of NGC 3109 and NGC 6822. *Astrophys. J.*, *657*, 773-789.

Venters, T. M. (2010, Februar). Contribution to the Extragalactic Gamma-Ray Background from the Cascades of very High Energy Gamma Rays from Blazars. *Astrophys. J.*, *710*, 1530–1540.

Venters, T. M., Pavlidou, V. & Reyes, L. C. (2009, Oktober). The Extragalactic Background Light Absorption Feature in the Blazar Component of the Extragalactic Gamma-ray Background. *Astrophys. J.*, *703*, 1939–1946.

Venturi, T., Dallacasa, D. & Stefanachi, F. (2004, August). Radio galaxies in cooling core clusters. Renewed activity in the nucleus of 3C 317? *A&A*, *422*, 515–522.

Venturi, T., Morganti, R., Tzioumis, T. & Reynolds, J. (2000, November). Parsec-scale structures of radio galaxies in the 2-Jy sample. *A&A*, *363*, 84–92.

Vladimirov, A. E., Digel, S. W., Jóhannesson, G., Michelson, P. F., Moskalenko, I. V., Nolan, P. L. et al. (2011, Mai). GALPROP WebRun: An internet-based service for calculating galactic cosmic ray propagation and associated photon emissions. *Computer Physics Communications*, *182*, 1156-1161.

Walker, M., Combet, C., Hinton, J., Maurin, D. & Wilkinson, M. (2011). Dark matter in the classical dwarf spheroidal galaxies: a robust constraint on the astrophysical factor for gamma-ray flux calculations.

Astrophys.J., *733*, L46.

Watkins, L. L., Evans, N. W., Belokurov, V., Smith, M. C., Hewett, P. C., Bramich, D. M. et al. (2009, Oktober). Substructure revealed by RRLyraes in SDSS Stripe 82. *Mon.Not.R.Astron.Soc.*, *398*, 1757–1770.

Waxman, E. & Loeb, A. (2000, Dezember). Fluctuations in the Radio Background from Intergalactic Synchrotron Emission. *Astrophys. J. Lett.*, *545*, L11-L14.

Weinberg, D. H., Croft, R. A. C., Hernquist, L., Katz, N. & Pettini, M. (1999, September). Closing In on Omega_M: The Amplitude of Mass Fluctuations from Galaxy Clusters and the Lyalpha Forest. *Astrophys. J.*, *522*, 563-568.

Weinberg, S. (1976, Feb). Implications of dynamical symmetry breaking. *Phys. Rev. D*, *13*, 974–996. Verfügbar unter `http://link.aps.org/doi/10.1103/PhysRevD.13.974`

Weniger, C. (2012, August). A tentative gamma-ray line from Dark Matter annihilation at the Fermi Large Area Telescope. *JCAP*, *8*, 7.

Weniger, C., Su, M., Finkbeiner, D. P., Bringmann, T. & Mirabal, N. (2013, Mai). Closing in on the Fermi Line with a New Observation Strategy. *arXiv:1305.4710*.

Whiteson, D. (2012, November). Disentangling instrumental features of the 130 GeV Fermi line. *JCAP*, *11*, 8.

Wilk, S. S. (1983). The Large-Sample Distribution of the Likelihood Ratio for Testing Composite Hypotheses. *Ann. Math. Statist.*, *9*, 60-62.

Wilkinson, M. I. & Evans, N. W. (1999, Dezember). The present and future mass of the Milky Way halo. *Mon.Not.R.Astron.Soc.*, *310*, 645–662.

Wilkinson, P. N., Akujor, C. E., Cornwell, T. J. & Saikia, D. J. (1991, Januar). 3C380 - A powerful radio source seen end-on? *MNRAS*, *248*, 86–90.

Willick, J. A., Strauss, M. A., Dekel, A. & Kolatt, T. (1997, September). Maximum Likelihood Comparisons of Tully-Fisher and Redshift Data: Constraints on Omega and Biasing. *Astrophys. J.*, *486*, 629.

Willott, C. J., Rawlings, S., Blundell, K. M., Lacy, M. & Eales, S. A. (2001, April). The radio luminosity function from the low-frequency 3CRR, 6CE and 7CRS complete samples. *MNRAS*, *322*, 536–552.

Witten, E. (1981, Oktober). Mass hierarchies in supersymmetric theories. *Physics Letters B*, *105*, 267-271.

Wright, A. E., Griffith, M. R., Burke, B. F. & Ekers, R. D. (1994, März). The Parkes-MIT-NRAO (PMN) surveys. 2: Source catalog for the southern survey (delta greater than -87.5 deg and less than -37 deg). *Astrophys. J. Supplement*, *91*, 111–308.

Xue, X. X., Rix, H. W., Zhao, G., Re Fiorentin, P., Naab, T., Steinmetz, M. et al. (2008, September). The Milky Way's Circular Velocity Curve to 60 kpc and an Estimate of the Dark Matter Halo Mass from the

Kinematics of ˜2400 SDSS Blue Horizontal-Branch Stars. *Astrophys. J.*, *684*, 1143–1158.

Yan, D., Zeng, H. & Zhang, L. (2012, Mai). Contribution from blazar cascade emission to the extragalactic gamma-ray background: what role does the extragalactic magnetic field play? *MNRAS*, *422*, 1779–1784.

Yuan, Q., Bi, X.-J., Chen, G.-M., Guo, Y.-Q., Lin, S.-J. et al. (2013). Implications of the AMS-02 positron fraction in cosmic rays.

Yuan, Z. & Wang, J. (2012, Januar). On the Evolution of the Cores of Radio Sources and Their Extended Radio Emission. *Astrophys. J.*, *744*, 84.

Zavala, J., Springel, V. & Boylan-Kolchin, M. (2010). Extragalactic gamma-ray background radiation from dark matter annihilation. *Mon.Not.Roy.Astron.Soc.*, *405*, 593.

Zechlin, H.-S., Fernandes, M. V., Elsässer, D. & Horns, D. (2012, Februar). Dark matter subhaloes as gamma-ray sources and candidates in the first Fermi-LAT catalogue. *A&A*, *538*, A93.

Zechlin, H.-S. & Horns, D. (2012, November). Unidentified sources in the Fermi-LAT second source catalog: the case for DM subhalos. *JCAP*, *11*, 50.

Zeng, H. D., Yan, D. H., Sun, Y. Q. & Zhang, L. (2012, April). γ-Ray Luminosity Function and the Contribution to Extragalactic γ-Ray Background for Fermi-detected Blazars. *Astrophys. J.*, *749*, 151.

Zhao, H. (1996, Januar). Analytical models for galactic nuclei. *MNRAS*, *278*, 488-496.

Zhou, M. & Wang, J. (2013, Juni). A New Result on the Origin of the Extragalactic Gamma-Ray Background. *Astrophys. J.*, *769*, 153.

Zimmer, S., Conrad, J., for the Fermi-LAT Collaboration & Pinzke, A. (2011, Oktober). A Combined Analysis of Clusters of Galaxies - Gamma Ray Emission from Cosmic Rays and Dark Matter. *arXiv:1110.6863*.

Zwicky, F. (1933). Die Rotverschiebung von extragalaktischen Nebeln. *Helvetica Physica Acta*, *6*, 110-127.

Acknowledgements

The work done during these three years in Hamburg has been possible also thanks to the support of many people who accompanied me along this road and to whom I am very grateful.

Firstly, I would like to thank my supervisors. Torsten Bringmann, who gave me the opportunity to grow scientifically and personally during my PhD. He always encouraged me to think with my head and to be independent and accurate. And Fiorenza Donato, who was always present during this time and willing to support me whenever I needed a good advise. In working with her I learnt a lot. I am thankful to both for having led me to this goal.

I also thank all my colleagues and collaborators who made pleasant and stimulating my experience at DESY. Among them a special thanks goes to Martin and Andrey who helped me in the very last stage of this work.

During this time, I received the support from a lot of friends: those who I met here, in Hamburg, as well as those who I left in my home town, in Turin. I want to thank in particular Ninetta, Giulia and Irene for their constant presence and love.

Everything I have done so far has been possible thanks to my parents. They always supported my choice since the beginning even if it was hard, even if it hurt. They constantly let me feel they were close to me although living far away.

Finally, I am grateful to the person who open my heart and participated in making this time unforgettable. Francesco has been an invaluable supporter of mine since the very first stages of this thesis and he encouraged me to do always my best. With his critical judgment and stimulating questions he contributed substantially in improving this work.

Eidesstattliche Versicherung
Declaration on Oath

Hiermit erkläre ich an Eides statt, dass ich die vorliegende Dissertationsschrift selbst verfasst und keine anderen als die angegebenen Quellen und Hilfsmittel benutzt habe.

I hereby declare, on oath, that I have written the present dissertation by my own and have not used other than the acknowledged resources and aids.

Hamburg, den 2nd of October 2013 Francesca Calore